UNIVERSITÀ
DEGLI STUDI
FIRENZE

DOTTORATO DI RICERCA IN FISICA E ASTRONOMIA

CICLO XXXI

COORDINATORE Prof. Raffaello D'Alessandro

The impact of galactic outflows on their host galaxies through spatially resolved spectroscopy

Settore Scientifico Disciplinare: FIS/05 Astronomia e Astrofisica

Dottorando	**Tutore**
Dott. Giacomo Venturi	Prof. Alessandro Marconi

Coordinatore
Prof. Raffaello D'Alessandro

Anni 2015/2018

Contents

Abstract

The observed properties of galaxies and supermassive black holes (BH) at their centers suggest that there must be a non-gravitational feedback mechanism regulating their evolution. These are the discrepancy at low and high masses between the observed stellar mass function of galaxies and that predicted by ΛCDM models, the scaling relations between the mass of BHs and the velocity dispersion, mass and luminosity of the host galaxy spheroid and the similarity between BH growth and star formation cosmic histories. Models of galaxy formation and evolution in fact routinely include feedback from active galactic nuclei (AGN) and supernovae (SNe), which can successfully reproduce the observed properties cited above. Models consider the following two types of AGN feedback: the radiative mode (or quasar mode), that operates during a luminous AGN phase through winds powered by radiation pressure, and the kinetic (or radio) mode, in which kinetic energy is released by the AGN on longer timescales through relativistic jets, which heat the surrounding halo in galaxy clusters, thus preventing cooling and further accretion on the central galaxy, and consequently further star formation.

So far, the clearest observational evidence of AGN feedback comes from the kinetic mode in massive central cluster galaxies. Radiative feedback is instead more elusive, and has been recently revealed in action only in a few luminous quasars around the peak of AGN activity history ($z \sim 2$), where most powerful outflows are observed. However, it is not possible to study high-z quasar outflows on small spatial scales ($\lesssim 100$ pc), being poorly-resolved or even unresolved in observations, due to their large distances. This can lead to systematics and uncertainties in the determination of outflow properties and forces to make some assumptions on them, which further increases the uncertainties on the outflow energetics and complicates the evaluation of the impact of outflows on host galaxies and the comparison with models. On the contrary, due to their vicinity, nearby active galaxies are ideal laboratories to explore in detail outflow properties, their formation and acceleration mechanisms, as well as the effects of AGN activity on host galaxies.

This work focuses on investigating the properties of outflows in nearby Seyfert galaxies, the physical conditions of the ionized gas and the interplay between nuclear activity and star formation in the galaxy, thanks to the unprecedented combination of spatial and spectral coverage provided by the integral field spectrograph MUSE at the Very Large Telescope (VLT). We introduce our optically- and X-ray selected sample of nearby Seyferts, called MAGNUM survey. We present our MUSE emission-line flux and kinematic maps of the 10 objects we have analyzed so far, including a star-forming galaxy, NGC 6810, to study the properties of a starburst outflow

for comparison as well. We map the ionized gas down to spatial scales as low as ∼10 pc. We find ubiquitous ionization cones and outflows with various morphologies and extensions, from a few hundred pc to several kpc. We detect peculiar kinematic features suggestive of outflows with hollow-conical structures. We also identify enhanced linewidths perpendicular to radio jets, which point to a correlation between the presence of jets and perpendicular turbulent or outflowing gas motions.

We then focus on a detailed multi-wavelength study of the ionized gas and outflow, in terms of physical properties, kinematics, and ionization mechanisms, in one specific galaxy of our sample, NGC 1365, from MUSE in optical band and *Chandra* satellite in X-rays. Here we map a kpc-scale biconical outflow ionized by the AGN prominent in [O III], while Hα emission traces star formation in a circumnuclear ring and along the bar of the galaxy. Soft X-rays are mostly due to thermal emission from the star-forming regions, but we manage to isolate the AGN photoionized component which matches the [O III] emission from MUSE. We map the mass outflow rate of the galactic ionized outflow, which matches that of the nuclear X-ray wind and then decreases with radius. The integrated mass outflow rate, kinetic energy rate, and outflow velocity are broadly consistent with the typical relations observed in more luminous AGN.

We extend our analysis to the nearby star-forming galaxy NGC 6810, whose bipolar galactic ionized outflow we map with MUSE. We determine the dominant ionization mechanism in the outflow, its density and ionization parameter, discovering the first case of star formation occurring within an outflow in an unambiguously star-forming galaxy.

We finally investigate with MUSE also the kinetic AGN feedback, by studying the ionized gas enshrouding the X-ray cavity inflated by radio jets around the massive radio-galaxy 3C 317 at the center of the local cluster Abell 2052. Thanks to MUSE capabilities, by mapping the warm gas filaments enshrouding the bubble we are able to directly measure the expansion velocity of the cavity, which usually is instead assumed or derived from indirect and model-dependent methods.

Declaration

The work described in this PhD thesis was undertaken between 1 November 2015 and 30 October 2018 under the supervision of Prof. Alessandro Marconi, at the Department of Physics and Astronomy of Università degli Studi di Firenze, in collaboration with INAF - Osservatorio Astrofisico di Arcetri and with Prof. Roberto Maiolino and Dr. Stefano Carniani at the Kavli Institute for Cosmology, University of Cambridge (UK).

Portions of this work have appeared (or are to appear) in the following papers:

- Chapter 2: **Venturi, G.** et al., in prep., *MAGNUM survey: mapping galactic ionized outflows in nearby Seyferts with MUSE*; **Venturi, G.**, Marconi, A., Mingozzi, M., Carniani, S., Cresci, G., Risaliti, G., and Mannucci, F., 2017, FrASS, 4, 46, *Ionized gas outflows from the MAGNUM survey: NGC 1365 and NGC 4945.*

- Chapter 3: **Venturi, G.**, Nardini, E., Marconi, A., Carniani, S., Mingozzi, M., Cresci, G., Mannucci, F., Risaliti, G., Maiolino, R., Balmaverde, B., Bongiorno, A., Brusa, M., Capetti, A., Cicone, C., Ciroi, S., Feruglio, C., Fiore, F., Gallazzi, A., La Franca, F., Mainieri, V., Matsuoka, K., Nagao, T., Perna, M., Piconcelli, E., Sani, E., Tozzi, P., and Zibetti, S., 2018, A&A, 619, A74, *MAGNUM survey: A MUSE-Chandra resolved view on ionized outflows and photoionization in the Seyfert galaxy NGC 1365.*

- Chapter 4: **Venturi, G.** et al., in prep., *Star formation within galactic outflow in starforming galaxy NGC 6810.* The work presented in this chapter is the result of the visit of the author at the Kavli Institute for Cosmology at the University of Cambridge in collaboration with Prof. Roberto Maiolino and Dr. Stefano Carniani.

- Chapter 5: Balmaverde, B., Capetti, A., Marconi, A., and **Venturi, G.**, 2018, A&A, 612, A19, *The VLT/MUSE view of the central galaxy in Abell 2052. Ionized gas swept by the expanding radio source.*

In addition to the work presented in this thesis, the author has also contributed to the following papers:

- Cresci, G., Marconi, A., Zibetti, S., Risaliti, G., Carniani, S., Mannucci, F., Gallazzi, A., Maiolino, R., Balmaverde, B., Brusa, M., Capetti, A., Cicone, C., Feruglio, C., Bland-Hawthorn, J., Nagao, T., Oliva, E., Salvato, M., Sani, E., Tozzi, P., Urrutia, T., and **Venturi, G.**, 2015, A&A, 582, A63, *The MAGNUM survey: positive feedback in the nuclear region of NGC 5643 suggested by MUSE.*

- Balmaverde, B., Capetti, A., Marconi, A., **Venturi, G.**, Chiaberge, M., Baldi, R. D., Baum, S., Gilli, R., Grandi, P., Meyer, E., Miley, G., O'Dea, C., Sparks, W., Torresi, E., and Tremblay, G., 2018, A&A, 619, A83, *The MURALES survey. I. A dual AGN in the radio galaxy 3C459?*

- Mingozzi M., Cresci, G., **Venturi, G.**, Marconi, A., Mannucci, F., Perna, M., Belfiore, F., Carniani, S., Balmaverde, B., Brusa, M., Cicone, C., Feruglio, C., Gallazzi, A., Mainieri, V., Maiolino, R., Nagao, T., Nardini, E., Sani, E., Tozzi, P., and Zibetti, S., 2018, A&A in press, arXiv:1811.07935, *The MAGNUM survey: different gas properties in the outflowing and disk components in nearby active galaxies with MUSE.*

- Fluetsch, A., Maiolino, R., Carniani, S., Marconi, A., Cicone, C., Bourne, M. A., Costa, T., Fabian, A. C., Ishibashi, W., and **Venturi, G.**, 2018, submitted to MNRAS and reviewed with moderate revision requested, arXiv:1805.05352, *Cold Molecular Outflows in the Local Universe.*

A brief description of these works can be found in Appendix.

List of Acronyms

AGN: Active Galactic Nucleus/i

BCG: Brightest Cluster Galaxy

BLR: Broad Line Region

BH: (supermassive) Black Hole

BPT: Baldwin-Phillips-Terlevich (diagram)

CGM: Circumgalactic Medium

FIR: Far-Infrared

IFU: Integral Field Unit

IFS: Integral Field Spectroscopy

IGM: Intergalactic Medium

IR: Infrared

ISM: Interstellar Medium

MIR: Mid-Infrared

NLR: Narrow Line Region

SF: Star Formation

SFR: Star Formation Rate

SN: Supernova

UFO: Ultra-fast Outflow

ULIRG: Ultra-Luminous Infrared Galaxy

UV: Ultraviolet

WA: Warm Absorber

1 Background: Feedback and outflows

1.1 The need for feedback in galaxy evolution

The feedback mechanism, both due to AGN and SNe, is considered a key ingredient in galaxy evolution to explain many properties of galaxies observed over cosmic time. Nowadays feedback is indeed always taken into account in theoretical, semianalytic and numerical simulations of galaxy formation and evolution[1]. In the following we report the main observational evidences which point to the need of an AGN and SN feedback on galaxies to explain some observed properties of galaxies. These are 1) the observed discrepancy in the luminosity function of galaxies between observations and models (without feedback) both at low and high masses, 2) the scaling relations observed between the mass of the BHs and the properties of the galaxies at whose center they reside, 3) the similarity between the BH accretion history and the star formation history throughout cosmic time.

1.1.1 The stellar mass function of galaxies

A first key observational aspect which can be explained by invoking feedback, both from SNe and from AGN, comes out by inspecting the masses of galaxies. In fact, by comparing the observed stellar mass function of galaxies[2] (i.e. the number density of galaxies having a certain stellar mass) with that predicted from Λ-CDM models of galaxy evolution, a large discrepancy emerges both at low and at high masses, as shown in Fig. 1.1. The former is reproduced by including in the models the stellar feedback due to SNe (Dekel & Silk 1986), which acts through stellar and SN-driven winds that progressively heat and eject the gas out of the galaxy, consequently reducing the gas reservoir to form stars (details in Sect. 1.2.1). Such mechanism becomes inefficient at higher masses. At $\sim 3 \times 10^{10}\,M_\odot$ the observed galaxy mass function reaches its minimum discrepancy from Λ-CDM models. Above this value, at the highest masses, the gap dramatically increases again. Such lack of high-mass galaxies is explained by the AGN feedback mechanism, suppressing star formation in the galaxy through the action of outflows and jets (details in Sect. 1.2.1), which allows to reconcile models with observations if taken into account.

---

[1] E.g. Kauffmann & Haehnelt (2000), Granato et al. (2004), Di Matteo et al. (2005), Springel et al. (2005), Bower et al. (2006), Croton et al. (2006), Hopkins et al. (2006, 2018), Ciotti et al. (2010), Scannapieco et al. (2012), Vogelsberger et al. (2014), Sijacki et al. (2015), Schaye et al. (2015).

[2] Alternatively, it is common to refer to the luminosity function of galaxies instead of the mass function, as stellar mass and luminosity scale together.
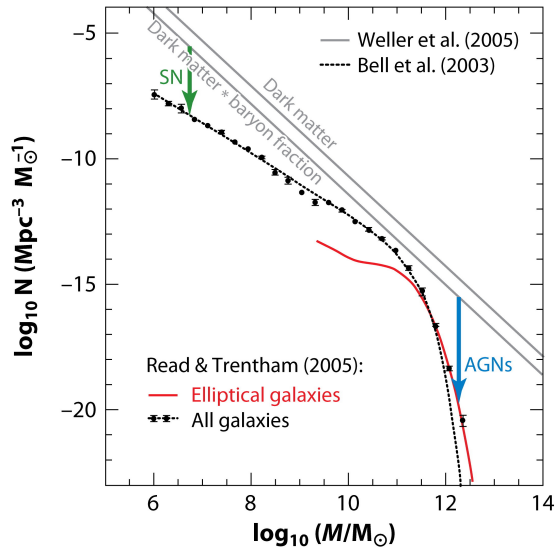
Fig. 1.1: Galaxy barionic mass function (black points for all galaxies, red curve for ellipticals only) from Read & Trentham (2005) fitted with a Schechter (1976) function (Bell et al. 2003; dotted curve), compared to the mass function of cold dark matter halos from numerical simulations (Weller et al. 2005) and to the same dark matter mass function multiplied by the universal baryon fraction of 0.163 (Hinshaw et al. 2013). Green and blue arrows indicate the effect of stellar (SN) and AGN feedback, respectively, without which semi-analytic models fail to reproduce the observed stellar mass function. Figure from Kormendy & Ho (2013).

1.1.2   BH-host galaxy scaling relations

The discovery of scaling relations between the masses of BHs and the properties of their host galaxy bulges (or spheroids) dates back about 30 years in time, after which such relations have been deeply investigated and progressively refined with increasing statistics and better-quality observations. BH masses are found to correlate with the luminosity of the host spheroid ($M_{\rm BH} \sim L_{\rm sph}^{1.1}$)[3], with its mass ($M_{\rm BH} \sim 10^{-3}\ M_{\rm sph}$)[4] and with the velocity dispersion of the stars in the spheroid ($M_{\rm BH} \sim \sigma_{\rm sph}^{4-5}$)[5]. The spheroid here both indicates the spheroidal component of the galaxy in case of spiral galaxies or the entire galaxy itself in case of ellipticals. Nowadays the BH-galaxy scaling relations are strongly established, as shown by the large number of works produced over the years.

The relations span several orders of magnitudes in mass, luminosity and velocity dispersion, and are quite tight, especially the $M_{\rm BH}$-$\sigma_{\rm sph}$ one. They thus imply the existence of a causal

---

[3]   E.g. Dressler (1989), Kormendy (1993), Magorrian et al. (1998), Ho (1999), Merritt & Ferrarese (2001), Laor (2001), Kormendy & Gebhardt (2001), McLure & Dunlop (2002), Marconi & Hunt (2003), Ferrarese & Ford (2005), Graham (2007), Gültekin et al. (2009), Sani et al. (2011), Kormendy & Bender (2011), Vika et al. (2012), Graham & Scott (2013), McConnell & Ma (2013).

[4]   E.g. Merritt & Ferrarese (2001), Kormendy & Gebhardt (2001), McLure & Dunlop (2002), Marconi & Hunt (2003), Häring & Rix (2004), Kormendy & Bender (2009).

[5]   E.g. Ferrarese & Merritt (2000), Gebhardt et al. (2000), Merritt & Ferrarese (2001), Kormendy & Gebhardt (2001), Tremaine et al. (2002), Marconi & Hunt (2003), Ferrarese & Ford (2005), Wyithe (2006), Graham (2007, 2008a,b), Hu (2008), Gültekin et al. (2009), Greene et al. (2010), Graham et al. (2011), Sani et al. (2011), Kormendy & Bender (2011), McConnell et al. (2011), Beifiori et al. (2012), Graham & Scott (2013), McConnell & Ma (2013), Kormendy & Ho (2013).
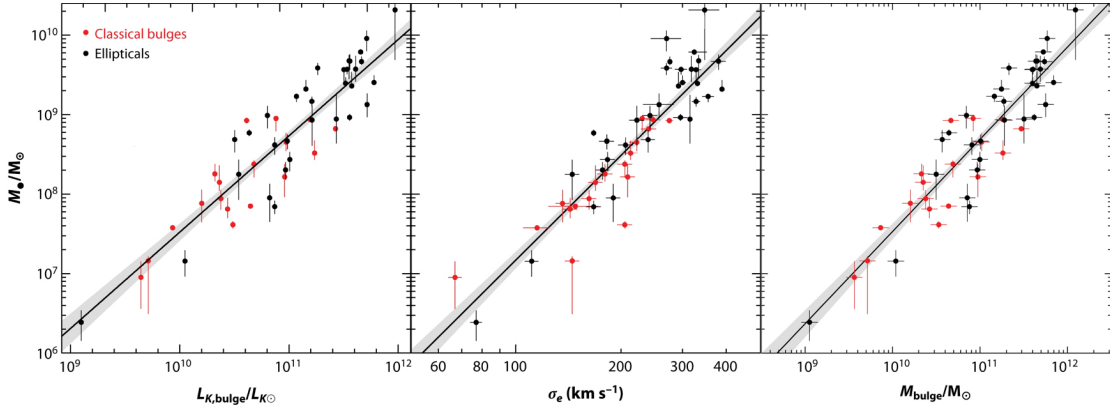
Fig. 1.2: From left to right: BH mass versus host galaxy bulge K-band luminosity, stellar velocity dispersion and bulge mass, respectively. Red and black points indicate classical bulges and elliptical galaxies, respectively. The black line is the best fit, together with its 1σ range (grey shading). Figure from Kormendy & Ho (2013).

connection between the central BH and the host galaxy, mutually shaping their physical properties. As the sphere of gravitational influence of a BH is negligible compared to the size of the host spheroid (of about a factor $\sim 5 \times 10^{-3}$), the mechanism responsible for the relations must have a non-gravitational origin, which is identified in the AGN feedback process. These scaling relations naturally arise in fact by considering simple models of feedback acting through outflows accelerated by the AGN (details later in Sect. 1.2.1.1).

1.1.3 BH and star formation history

The observed cosmic histories of BH growth and star formation are similar, as shown in Fig. 1.3. This suggests a coevolution of the two processes during the past of the Universe. There must then be a mechanism which self-regulates the star formation activity in the galaxy and the growth of the BH, coupling their evolution, and which cannot have a gravitational origin since BH and galactic gravitational scales differ by several orders of magnitude, as previously illustrated. The scale factor by which the BH accretion history is multiplied in Fig. 1.3 to match the star formation history is ~1500, which is consistent with the ~10^{-3} factor of the M_{BH}-M_{sph} local scaling relation (see Sect. 1.1.2). This provides a further clue that BH and host galaxy growth and evolution may be strictly connected by some mechanism. Both BH growth and star formation history peak at $z \sim 2$ (see also e.g. Madau et al. 1996, Lilly et al. 1999, Madau & Dickinson 2014), indicating that the bulk of BH growth and star formation took place between $z \sim$ 1-3 (e.g. Ueda et al. 2003, Marconi et al. 2004, Shankar et al. 2009, Aird et al. 2010, 2015). Powerful quasars were in fact much more numerous above $z \sim 1$ than below (e.g. Boyle et al. 2000, Richards et al. 2006). Moreover, if BHs had grown at the average rate observed for local AGN, they would have taken more than the age of the Universe to reach their present mass, implying that local BHs must have grown at much higher rates in the past giving rise to more powerful
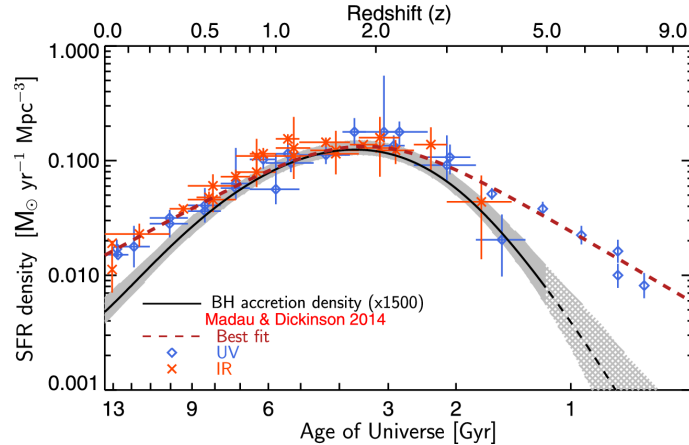
Fig. 1.3: Star formation rate (SFR) density compared to the BH mass accretion density, as a function of redshift (or age of the Universe). The points are the measurements of the SFR density from Madau & Dickinson (2014) from rest-frame UV (blue diamonds) and IR (orange crosses) observations, together with their best fit (dashed red curve). The black curve is the estimate of the BH mass accretion density from Aird et al. (2015) scaled by a factor of 1500, together with its uncertainties in shaded grey; dashed black line and grey hatching mark the extrapolation of the model outside the coverage of the data used. Figure taken from Aird et al. (2015).

AGN compared to local ones, as indeed observed. The mechanism considered responsible for the parallel cosmic history of BH growth and star formation is the AGN feedback.

1.2 "Flavours" of feedback

1.2.1 Negative feedback

We call "negative" feedback the mechanism through which AGN or SNe reduce or suppress the star formation in the galaxy, which we have called simply feedback up to now. The adjective "negative" is meant to distinguish it from another kind of feedback, called "positive", which is discussed later in Sect. 1.2.2.

Stellar feedback, through the reheating of cold disk gas and/or heating of the diffuse halo surrounding the galaxy by SNe and stellar winds, is able to suppress the formation of faint galaxies and is thus successful in reproducing the flattening observed at low masses in the galaxy mass function compared to Λ-CDM evolutionary models. Stellar feedback from SNe and stellar winds has been in fact routinely included in models and simulations of galaxy formation and evolution since many years (e.g. Kauffmann et al. 1993, Cole et al. 2000, Benson et al. 2003, Granato et al. 2004, Springel et al. 2005, Bower et al. 2012). However, SN feedback is unable to reproduce the observed lack of high-mass galaxies compared to models. In fact the more likely mechanism to explain such discrepancy, acting through starburst superwinds driven by SN explosions, is not feasible, since the total energy output required to match the observed galaxy mass function largely exceeds the energy available from SN explosions.

AGN feedback is invoked instead in order to reconcile models with observations at the high-

mass end of the galaxy mass function. From simple energetic considerations (see e.g. Fabian 2012) it follows that AGN powered by BH accretion are capable of having a profound impact on the host galaxy. The binding energy of a galaxy can be written as $E_{\mathrm{gal}} \sim M_{\mathrm{gal}}\sigma^2$ from the virial theorem, being M_{gal} and σ the mass and velocity dispersion of the galaxy, respectively. The energy released by the growth of a BH is $E_{\mathrm{BH}} = 0.1 M_{\mathrm{BH}}c^2$, assuming a radiative efficiency due to accretion of 10%, typical for a Shakura & Sunyaev (1973) accretion disk. Since the BH masses are typically $M_{\mathrm{BH}} \sim 10^{-3} M_{\mathrm{gal}}$ (see BH-galaxy scaling relations in Sect. 1.1.2), it follows that $E_{\mathrm{BH}}/E_{\mathrm{gal}} \sim 10^{-4}(c/\sigma)^2$. Since galaxies generally have $\sigma \lesssim 400$ km s^{-1}, we have that $E_{\mathrm{BH}}/E_{\mathrm{gal}} \gtrsim 50$. So, also if only a small fraction of the energy released by the BH during its activity can be transferred to the gas, an AGN is capable of deeply influencing its host galaxy from an energetic point of view.

In the standard picture AGN feedback is believed to act in two different modes. A first one, called radiative mode (also known as quasar or wind mode), in which the BH accretes material at high rates and accelerate powerful outflows which expel the gas out of the galaxy. A second one, called kinetic (also radio or maintenance) mode, operating at a later stage and acting on longer timescales, in which jets produced by the AGN (having low accretion rates in this phase) keep the gas in the galactic halo hot and prevent reaccretion on the galaxy and consequent reignition of star formation. The radiative mode of feedback is predicted to be effective at producing high mass outflow rates, shutting down star formation in the host galaxy and expelling the gas reservoir (necessary to carry on star formation) out of it, successfully reproducing many observed properties, such as the M_{BH}-σ_{sph} relation (see Sect. 1.2.1.1 in the following for details). The kinetic mode is required at a second stage to prevent the gas to fall back onto the galaxy and reignite star formation processes, successfully reproducing the galaxy mass function. The cartoon in Fig. 1.4 illustrates the two phases of AGN feedback.

1.2.1.1. Radiative mode

Radiative mode feedback, firstly proposed by Silk & Rees (1998), is predicted to act through winds of gas accelerated by the AGN radiation pressure. Differently from the kinetic one, this mode operates on much shorter timescales during phases of intense BH accretion, close to the Eddington limit, giving rise to strong AGN emission and powerful outflows of material ejected by the AGN. It is a destructive process, with gas being pushed out of the galaxy and away from the BH surroundings, thus depleting the reservoir to form stars in the galaxy and, at the same time, to carry on intense BH accretion and AGN activity. The sources in which this mechanism is believed to act are called "radiative-mode" AGN (Heckman & Best 2014), as they emit most of their energy in the form of radiation as result of BH accretion.

The radiative mode AGN feedback is, according to analytical models, the most likely ex-
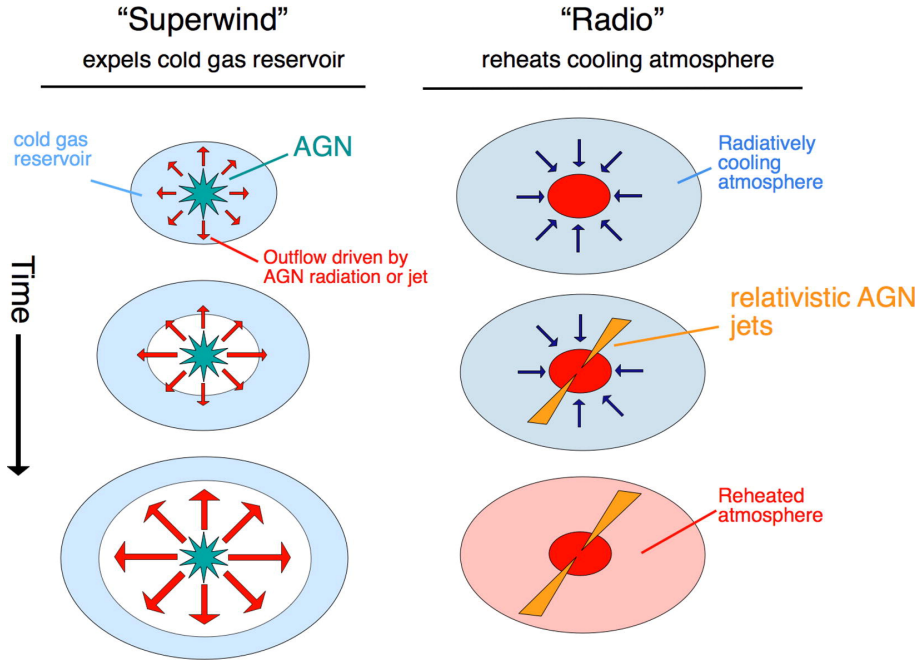
Fig. 1.4: Cartoon illustrating the two modes of negative AGN feedback, radiative (superwind) to the left, kinetic (radio) to the right. From Alexander & Hickox (2012).

planation for the M_{BH}-σ_{sph} and M_{BH}-M_{sph} relations[6] (introduced in Sect. 1.1.2). It was probably most effective back at $z \sim$ 1-3, around the peak of AGN activity and star formation history (see Sect. 1.1.3), when powerful quasars operated (that is why the radiative mode is also called quasar mode). It is indeed at these redshifts that evidence for AGN feedback from powerful outflows, capable of deeply influencing the host galaxy, is sought. Powerful outflows have been extensively observed both at low and high redshift (e.g. Maiolino et al. 2012, Swinbank et al. 2015, Carniani et al. 2016; other references later in Sect. 1.3). Still, observational evidence that they have a relevant impact on the star formation of their host galaxies remains elusive.

Models predict that the radiative mode feedback can act in three ways in producing galactic-wide outflows, 1) through momentum-conserving outflows (momentum-driven), 2) through energy-conserving outflows (energy-driven), or 3) through outflows directly accelerated by the AGN radiation pressure on dust grains (radiation pressure-driven). Details on each of the above modes are given in the following.

Momentum-driven   In this mode the BH radiation pressure accelerates a fast wind which impacts directly on the interstellar medium (ISM) in the galaxy, generating a shock which accelerates the ISM (e.g. King & Pounds 2015). If the shocked gas efficiently cools through radiation on a timescale shorter than its flow time, most of the pre-shock kinetic energy gets lost and we

---

[6]   E.g. Silk & Rees (1998), Fabian (1999, 2012), Granato et al. (2004), Murray et al. (2005), King et al. (2011), Faucher-Giguère & Quataert (2012), Alexander & Hickox (2012), King & Pounds (2015).

speak of a "momentum-driven" outflow, which transfers only its ram pressure to the host ISM to conserve its momentum. A momentum-driven outflow injects in the bulge gas an amount of energy which is only about 10% of the bulge binding energy (King & Pounds 2015). This mechanism is then not capable of destroying the bulge of the host galaxy and then represent a stable environment for BH mass growth. In this mode outflowing gas can efficiently cool only up to ~kpc distances, above which momentum-driven mode is not feasible anymore (e.g. King et al. 2011, Costa et al. 2014, King & Pounds 2015).

Energy-driven If cooling is negligible the shocked ISM gas retains all the mechanical energy of the AGN wind and expands adiabatically. We speak of an "energy-driven" outflow in this case. The energy-driven scenario is more violent than the momentum-driven one. A BH operating in the energy-driven mode only would blow out the bulge of the host galaxy before reaching the mass of observed BHs (e.g. King & Pounds 2015). Moreover, the energy-driven scenario is unable to reproduce the observed M_{BH}-σ_{sph} relation, giving $M_{BH} \propto \sigma_{sph}^5$ and a normalization which is too low of a factor 50-100 compared to the observed one (e.g. Silk & Rees 1998, King & Pounds 2015). Despite these problems in explaining observed properties, models predict that above distances of ~kpc the cooling time of the expanding gas is longer than its flow time and that large-scale outflows should be energy-driven (e.g. King 2003, 2005, King et al. 2011). Nevertheless, recent models and simulations of both starburst-driven (e.g. Zhang & Thompson 2012) and AGN-driven outflows (e.g. Zubovas & King 2014, Costa et al. 2015, Richings & Faucher-Giguère 2018) have also shown that in the energy-conserving scenario part of the outflow is still able to sufficiently cool to form molecules, explaining the fast molecular outflows observed (e.g. Feruglio et al. 2010, Sturm et al. 2011, Cicone et al. 2014; see Sect. 1.3.3).

According to models, in a first phase AGN outflows are momentum-driven and, as long as the BH mass is not large enough, the wind is not able to outcome the bulge gravitational potential and falls back, remaining confined within a distance of ~kpc. When the BH mass has grown sufficiently, so that the radiation force of the AGN photons accelerating the wind balances the inward gravitational force, the M_{BH}-σ_{sph} has been established. This can be shown with the following simple calculation (e.g. Fabian 1999, 2012, Fabian et al. 2002, King 2003, 2005, Costa et al. 2014, King & Pounds 2015). We consider an AGN emitting at the Eddington limit (i.e. the maximum luminosity above which the radiation pressure clears out the accreting gas around the BH, stopping accretion) which has swept the gas to the edge of the galaxy. By balancing the outward radiation force (F_{out}) with the inward force due to gravity (F_{in}) we obtain

$$\frac{4\pi G M_{BH} m_p}{\sigma_T} = \frac{L_{Edd}}{c} = F_{out} = F_{in} = \frac{G M_{gal} M_{gas}}{r^2}, \tag{1.1}$$

being L_{Edd} the Eddington luminosity, G the gravitational constant, m_p the proton mass and σ_T

the Thomson cross section for electron scattering. Considering that the gas mass is a fraction f of the total galaxy mass ($M_{gas} = f M_{gal}$) and approximating the galaxy spheroid as an isothermal sphere $M_{gal} = 2\sigma_{sph}^2 r / G$, gives

$$\frac{4\pi G M_{BH} m_p}{\sigma_T} = \frac{G f M_{gal}^2}{r^2} = \frac{G f 4 \sigma_{sph}^4 r^2}{r^2 G^2}, \tag{1.2}$$

from which it follows that

$$M_{BH} = \frac{f \sigma_T \sigma_{sph}^4}{\pi G^2 m_p} \simeq 3.2 \times 10^8 \, \mathrm{M_\odot} \, \sigma_{sph,200}^4, \tag{1.3}$$

being $\sigma_{sph,200}$ in unit of 200 km s^{-1} and having considered a typical gas fraction $f \sim 0.1$. This is in striking good agreement with the observed M_{BH}-σ_{sph} relation (e.g. Gültekin et al. 2009, Kormendy & Ho 2013 and other references in Sect. 1.1.2). After the M_{BH}-σ_{sph} relation has been established, the outflow is powerful enough to win against the gravitational pull and expands on $\gtrsim$kpc distances. At this point cooling is not efficient anymore and the outflow passes in the energy-driven regime and can blow away the gas from the host galaxy.

However, this is a very simplicistic view of the subject. It is in fact not well understood yet which mechanism is actually the main driver of galactic outflows and which is the role of the AGN feedback in establishing the BH-galaxy scaling relations (e.g. Peng 2007, Kormendy & Ho 2013, Anglés-Alcázar et al. 2017).

Radiation pressure-driven   Another way to accelerate galactic outflows, according to models, is through direct radiation pressure from AGN photons on dust grains in the ISM (e.g. Fabian 1999, Ishibashi & Fabian 2012, Thompson et al. 2015, Ishibashi et al. 2018). A large fraction of AGN luminosity by accretion is emitted in the form of UV photons, which are efficiently absorbed by dust, that can be then consequently pushed away and, being partially ionized by the radiation, drag the gas along with it. The cross section for dust absorption is ~1000 times larger than the Thompson cross section σ_T (Fabian et al. 2008) resulting in a critical luminosity L'_{Edd} smaller of the same factor than the classical Eddington luminosity L_{Edd} due to electron scattering (Eq. 1.1). This implies that an AGN emitting at L_{Edd}, Eddington limit for the ionized gas surrounding the BH, is at the same time at the effective Eddington limit for dusty gas L'_{Edd} for an object ~1000 times more massive (e.g. Fabian 2012). This factor corresponds to the (inverse of the) observed ratio between BH and galaxy bulge masses, $M_{BH}/M_{sph} \sim 10^{-3}$ (see Sect. 1.1.2), which could be only a coincidence or indicate that this mechanism, through radiation pressure on ISM dusty clouds, can directly affect the galaxy spheroid and shape the M_{BH}-M_{sph} relation. Models predict that direct radiation pressure on dust is able to drive outflows on ~kpc scales and above (Ishibashi & Fabian 2012, 2015, Ishibashi et al. 2018).

1.2.1.2. Kinetic mode

The clearest observational evidence of AGN feedback is found in the local Universe in the most massive galaxies (>10^{11} M$_\odot$), the brightest cluster galaxies (BCGs) in cool core clusters of galaxies. Here feedback operates in its kinetic (or radio or maintenance) mode. Without energy input through this mechanism, a large fraction of BCGs would appear as brilliant, giant starbursts instead of red objects with almost no star formation, and would be even more massive then they are, populating the high-mass end of the galaxy mass function (Fig. 1.1). It is in fact the kinetic AGN feedback which allows to reconcile models with observations at high masses in the galaxy mass function (e.g. Benson et al. 2003, Granato et al. 2004, Croton et al. 2006, Gabor et al. 2011, Bower et al. 2012).

In this mode the AGN injects energy in the gas surrounding the BCG at a rate balancing the energy loss through cooling (e.g. Peterson & Fabian 2006, McNamara & Nulsen 2007, Cattaneo et al. 2009). In fact, without a source of energy keeping the gas in the halo hot, the gas would radiatively cool in a short time considered its observed X-ray emission and collapse on the galaxy, so that a cooling flow of up to thousands of solar masses per year should be occurring, resulting in intense star formation in the galaxy (Fabian 2012). This is instead not seen from observations, which instead show cavities in the X-ray emitting hot ionized medium (10^6-10^7 K), filled by radio jets propagating from the active nucleus (e.g. Boehringer et al. 1993, Carilli et al. 1994, Rizza et al. 2000, McNamara et al. 2000, Bîrzan et al. 2004, 2012). The jets mechanically transfer their kinetic power (compared to which their radiative power is really low, with radiative efficiencies between 10^{-2} and 10^{-4}) to the gas in the halo. Such kinetic power is found to be generally consistent with the energy loss by X-ray radiation from the hot gas, thus giving the needed balance between radiative cooling and mechanical heating by feedback (e.g. Bîrzan et al. 2004, Dunn & Fabian 2008, Rafferty et al. 2006, 2008, McNamara & Nulsen 2007, 2012, Fabian 2012, Hlavacek-Larrondo et al. 2012, 2013). Differently from the radiative mode, AGN operating in the kinetic mode have low accretion rates, due to the low gas reservoir, and emit most of their energy through jets rather than radiation (they are also called "jet-mode" AGN in fact; Heckman & Best 2014). Moreover, kinetic mode acts on much longer timescales compared to radiative mode, and is thus also called maintenance mode.

1.2.2 Positive feedback

Up to this point we discussed AGN feedback only in relation to the reduction and quenching of the star formation in the host galaxy (negative feedback), which is indeed the reason why it is invoked in many galaxy formation and evolution models to explain the observed galaxy properties. However, some recent models have predicted that feedback from outflows, by overcompressing the molecular gas in the ISM, might also trigger star formation in the host rather than damping it ("positive" feedback; e.g. Silk & Norman 2009, Nayakshin & Zubovas 2012, Silk

2013, Zubovas et al. 2013b, Nayakshin 2014).

Observational evidence of AGN jets triggering star formation in companion galaxies was found for instance by Croft et al. (2006), Feain et al. (2007), Elbaz et al. (2009). Jet-induced star formation has also been observed by Crockett et al. (2012), Santoro et al. (2015, 2016), who found star-forming clumps triggered by jet compression around Centaurus A.

Evidence of positive feedback from AGN outflows has been recently found both at high- and low-z. Cresci et al. (2015b) found evidence in a $z \simeq 1.6$ quasar for star formation being quenched in the direction of outflowing gas (negative feedback) but at the same time being boosted at the edges of the outflow (positive feedback). Further evidence of positive feedback in action was found by Cresci et al. (2015a) in a nearby Seyfert, NGC 5643, as part of our MAGNUM survey (see Chapter 2). Here two bright clumps hosting intense star formation are observed in the direction of the outflow, being the result of the compression of the cold material in the dust lane exerted by the outflow. Such studies have been made possible thanks to the advent of integral field spectroscopy (IFS), which allowed to spatially resolve the outflows and to study more in detail their impact on the properties of the host galaxies.

Up to now we only have evidence of episodic positive feedback occurring in a few objects in single clumps or limited regions. Further observational efforts are then needed to quantify the prevalence of positive feedback and its actual impact on host galaxies and on their evolution. We stress that positive feedback does not rule out the effect of negative feedback (as demonstrated by the observation of both phenomena occurring in the same object by Cresci et al. 2015a), but it has to be considered as an additional effect that outflows might produce on the star formation in host galaxies.

1.2.2.1. Star formation within galactic outflows

Besides star formation being triggered by outflows and jets by compression of the cold gas in the host, recent models predict a new mode of star formation, in which stars form directly within the outflow itself as a consequence of compression, cooling and fragmentation of the outflowing gas (e.g. Ishibashi & Fabian 2012, 2014, 2017, Ishibashi et al. 2013, Zubovas et al. 2013a, Zubovas & King 2014). According to these models, star formation in the outflow could reach really high rates, up to SFR $\sim 100 \, \mathrm{M_\odot \, yr^{-1}}$ and have many possible important implications on galaxy formation and evolution. First, newborn stars formed in the outflow would have radial orbits and thus contribute to populate the spheroidal component of galaxies (bulges, haloes and elliptical galaxies) and shape its size and velocity dispersion (e.g. Dugan et al. 2014, Ishibashi & Fabian 2014, 2017). It has been proposed that this process could explain the problem of the size growth of massive galaxies from $z \sim 2$ to z = 0 (Ishibashi et al. 2013) and contribute to account for the mass-radius relation in early-type galaxies (Ishibashi & Fabian 2014). Moreover, the highest velocity stars would be able to escape the host galaxy or even the halo, consequently contributing to chemically enrich the circumgalactic medium (CGM) or the in-

tergalactic medium (IGM) in situ through SN explosions (e.g. Zubovas et al. 2013a), reducing the need to enrich the IGM with metals through winds from galaxy disks. These hypervelocity stars would also contribute to populate the CGM and IGM, explaining the stars and SNe observed in galaxy clusters (Ferguson et al. 1998, Gal-Yam et al. 2003). Finally, young stars ejected in the IGM within outflows may have also significantly contributed to the reionization of the early Universe.

In the recent years observations have revealed that the outflowing gas has indeed the appropriate physical conditions to host star formation. In fact, many galactic outflows are observed to host large quantities of cold molecular gas at high velocities, dominating the total outflow mass (e.g. Cicone et al. 2014, Fiore et al. 2017, Fluetsch et al. 2018; see Sect. 1.3.3 in the following for details). Moreover, a large fraction of them is also very dense ($\sim 10^6$ cm^{-3}) and clumpy, as typical of normal star-forming molecular clouds (e.g. Aalto et al. 2015, Pereira-Santaella et al. 2016).

First evidence of this new mode of star formation was found only recently by Maiolino et al. (2017), who detected star formation occurring within a prominent AGN-driven outflow in an object at $z \simeq 0.045$. Later on, a study by Gallagher et al. (2018), targeting a sample of local galactic outflows, suggested that this phenomenon is taking place in about 30% of the objects in the sample. Both studies were made possible by employing integral field spectroscopic data.

Still, further observational efforts are needed to quantify the impact that this new mode of star formation within outflows can have on galaxy formation and evolution, as we only have few examples of this phenomenon so far. In addition to that, it is not clear yet if this mechanism can occur also in starburst-driven outflows rather than in AGN-driven ones, as unambiguous observational evidence for that is still lacking.

1.3 Outflows: a multi-phase and multi-scale problem

Galactic-wide outflows driven by star formation processes (stellar winds and SNe), having velocities of a few $100 \, \mathrm{km \, s^{-1}}$ to $\lesssim 1000 \, \mathrm{km \, s^{-1}}$, have been extensively observed since many years[7] and are a basic ingredient in galaxy evolution models, as illustrated in Sect. 1.2.1 (e.g. Dalla Vecchia & Schaye 2008, Hopkins et al. 2018). Starburst winds are driven by the mechanical energy and momentum from stellar winds and SNe. Considering an instantaneous starburst episode, winds from OB stars dominate in a first phase, then Wolf-Rayet stars and, finally, core-collapse Type II SNe dominate until ~40 Myr when the least massive ones explode. The combined effect of all the ejecta from hot stars and SNe in the starburst region generates a cavity of hot, metal-enriched material, which propagates from the galaxy disk. The observed morphologies of starburst outflows are various, from nuclear superbubbles (e.g. Veilleux et al. 1994), loops

---

[7]   E.g. Heckman et al. (1990, 2015), Lehnert & Heckman (1996), Veilleux et al. (2005), Swinbank et al. (2009), Genzel et al. (2011), Newman et al. (2012), Bradshaw et al. (2013), Heckman & Thompson (2017).

(e.g. Heckman et al. 1987) and bicones (e.g. Bland & Tully 1988, Shopbell & Bland-Hawthorn 1998), to irregular and filamentary structures (e.g. Martin et al. 2002), extending from ~1 kpc up to ~20 kpc (e.g. Veilleux et al. 2003, 2005). Starburst outflows are multi-phase, being detected in hot (~10^8 K) and warm (~10^4 K) ionized gas, as well as in neutral atomic and molecular dusty gas (e.g. Heckman & Thompson 2017).

More powerful and fast outflows, accelerated by AGN activity, are predicted by radiative AGN feedback models, as introduced in Sect. 1.2.1.1, and are considered extremely important for the evolution of massive galaxies and for shaping the observed BH-host galaxy properties, as discussed in Sect. 1.1 and 1.2.1. Outflows pushed by collimated jets in the hosts of luminous radio galaxies have been observed out to $z \sim 4$ (e.g. Fu & Stockton 2009, Nesvadba et al. 2008, 2011). Outflowing winds in radio-quiet objects, where radio jet activity is negligible compared to the radiative output from the AGN, and which are associated with the radiative-mode feedback, have been instead more elusive. Only in recent years spatially resolved spectroscopic studies from optical, IR and mm facilities provided strong and conclusive evidence of the existence of AGN galaxy-wide winds, which are now routinely observed both in local galaxies (e.g. Feruglio et al. 2010, Rupke & Veilleux 2011, Sturm et al. 2011, Cicone et al. 2014) and at high-z (Maiolino et al. 2012, Harrison et al. 2012, 2016, Cano-Díaz et al. 2012, Cresci et al. 2015b, Carniani et al. 2015, Brusa et al. 2015b, 2016). Differently from starburst-driven winds, AGN outflows are in general oriented randomly relative to the major axis of the host galaxy (e.g. Kinney et al. 2000, Veilleux et al. 2005). However, despite their ubiquitous presence, it is not yet well understood and constrained how the energy released due to BH accretion on nuclear scales couples to the ISM to drive such powerful and extended galactic-scale outflows and which is their actual impact on the gas reservoir and star formation in the host galaxy. As stressed in Harrison et al. (2018), predictions for outflow physical properties from models and simulations are often based on the whole outflowing material rather than on its individual phases, while individual observations typically give information only on a specific outflow phase, making the comparison between models and observations quite challenging. That is why it is really important to study outflows in all the gas phases, as only by having a complete picture of the outflow phenomenon we can obtain information on the total energetics and impact of outflows on the host galaxies (e.g. Carniani et al. 2015, Fiore et al. 2017, Cicone et al. 2018). Different phases of the outflow relate to different spatial scales, from subpc to kpc scales, providing information on the different stages of the outflow formation and propagation throughout the galaxy. Spatially resolved spectroscopic observations are then essential to investigate in detail the spatial extension of the outflows in their various phases, their geometric and kinematic structure, their physical properties as a function of distance from the nucleus, and how and at which extent they impact on the ISM and SF processes in the host galaxies.

Table 1.1, from Cicone et al. 2018, gives a summary of some of the physical properties (tem-

Table 1.1: Main observational tracers, typical temperature and number density (either of electrons, hydrogen atoms or hydrogen molecules) of different outflow gas phases. From Cicone et al. (2018).

Outflow gas phase	Main tracers	$<T_{\text{gas}}>$ [K]	$<n_{\text{gas}}>$ [cm^{-3}]
Highly-ionized	X-ray absorption lines	10^6-10^7	10^6-10^8
Ionized	[O III], Hα	10^3-10^4	10^2-10^4
Neutral atomic	H I 21-cm, Na I D, [C II]	10^2-10^3	1-10^2
Molecular	CO, OH, [C II], H$_2$ IR lines	10-10^2	$\gtrsim 10^3$

perature and density) of outflows in their different phases as well as of the main tracers commonly used to identify each of them. We discuss them in the following.

1.3.1 Highly-ionized outflows

If AGN are able to accelerate winds by radiation pressure from the accretion disk, as predicted by models (see Sect. 1.2.1.1), we would expect to detect such nuclear winds from spectroscopic observations. Indeed, fast winds are observed from blueshifted absorption lines in the X-ray AGN continuum, due to the intervening wind material in the line of sight. The most extreme of them, called "ultra-fast outflows" (UFOs), have mildly relativistic velocities (~10000-100000 km s^{-1}), large column densities ($N_{\text{H}} \sim 10^{22}$-$10^{24}$ cm^{-2}) and high ionization ($\log \xi \sim$ 3-6 erg s^{-1} cm), being detected from iron K-band absorption lines (e.g. Pounds et al. 2003, Cappi et al. 2009, Reeves et al. 2009, Nardini et al. 2015a, Chartas et al. 2016). These winds are produced close to the BH, on sub-pc scales (e.g. Crenshaw et al. 2003, Tombesi et al. 2012). UFOs are quite ubiquitous, being observed in at least 40% of the sources (Tombesi et al. 2010, 2011, Gofford et al. 2013), they have mass outflow rates between ~0.01 and 1 M$_\odot$ yr^{-1} and their kinetic power ($\log \dot{E}_{\text{K}} \sim$ 42-45 erg s^{-1}; Tombesi et al. 2012) is higher than the minimum required by simulations for feedback from AGN winds to be effective in quenching star formation (~ 0.5-5% of the AGN bolometric luminosity, e.g. Di Matteo et al. 2005, Hopkins & Elvis 2010).

UFOs may then constitute the nuclear wind accelerated by the AGN required in many models as primary driver of galactic-scale (~1-10 kpc) outflows, as in the momentum-driven and energy-driven scenarios. Only recently Tombesi et al. (2015), Feruglio et al. (2015, 2017) were able to show examples of nuclear UFOs coupled with large-scale molecular outflows, whose energetics were consistent with an energy-conserving scenario. However, the presence of an energy-conserving expanding shell has been recently questioned even in one of these objects (Veilleux et al. 2017). Moreover, these molecular outflows are still on scales $\lesssim$ 1 kpc, too small to globally affect the host ISM. Therefore, a clear observational connection between UFOs and feedback is still lacking as well as strong evidence that the energy-conserving outflowing scenario do actually take place in nature. The topic is still under debate.

A different kind of X-ray winds in absorption are the so-called "warm absorbers" (WA),

which have lower velocities compared to UFOs (~100-1000 km s^{-1}), lower ionization param-
eter (logξ ~ 0-2 erg s^{-1} cm), being traced by K-shell ions of the lighter metals (such as C, N,
O) and Fe-L, and column densities between $N_{\rm H}$ ~ 10^{20}-10^{22} cm^{-2} (Reynolds 1997, Crenshaw
et al. 2003, Blustin et al. 2005, McKernan et al. 2007, Tombesi et al. 2013). WAs are commonly
observed in about 50% of Seyfert 1 galaxies (Reynolds 1997, Blustin et al. 2005), which host
less powerful AGN compared to quasars. WAs are associated to winds located further from the
AGN compared to UFOs, on the scale of the dusty torus[8] rather than of the accretion disk, and
they are expected to extend up to the scale of the NLR (~kpc), based on their observed ioniza-
tion parameters. UFOs and WAs may represent only different parts of a single stratified outflow
observed at different distances from the AGN and, consequently, having different ionization
states, column densities and velocities (Tombesi et al. 2013).

Winds are frequently observed also in the form of broad UV blueshifted absorption features,
in the so-called "broad absorption line" (BAL) quasars (e.g. Weymann et al. 1991, Ganguly et al.
2007). These features indicate velocities up to ~30000 km s^{-1}. BALs are generally believed to
be associated with AGN outflows from the accretion disk (e.g. Murray et al. 1995). It has been
proposed that BAL quasars are objects having a large Eddington ratio ($\gtrsim$1) and lower veloci-
ties and ionisation parameter (both are expected to decrease with increasing Eddington ratio)
compared to sources hosting UFOs (e.g. Zubovas et al. 2013b, King & Pounds 2015). Accord-
ing to this scenario, luminous AGN nuclear winds may evolve from an initial BAL phase to a
subsequent UFO phase.

1.3.2 Ionized outflows

Galactic ionized outflows are commonly observed from broad asymmetric wings in opti-
cal emission-line profiles, usually [O III]λ5007 ([O III] hereafter) in AGN. These are usually
blueshifted, indicating approaching material in the line of sight. This is interpreted as being
due to the dust in the galaxy disk that partially or totally obscures the receding (redshifted) part
of the outflow behind the disk. Being a forbidden transition, [O III] cannot originate from the
broad line region (BLR) surrounding the BH accretion disk on subpc scales, where the gas has
high densities ($n_{\rm e}$ ~ 10^9-10^{12} cm^{-3}). [O III] has been extensively used to trace ionized outflows
in larger and larger samples of AGN[9], showing that ionized outflows are prevalent, with veloci-
ties up to few ~1000 km s^{-1}. Such large-sample studies based on [O III], mostly making use of
the vast Sloan Digital Sky Survey (SDSS) optical spectra database and adopting different selec-
tion criteria (e.g. optical, radio or X-ray selection), have revealed that the incidence of ionized

---

[8] In AGN unification models (e.g. Antonucci 1993, Urry & Padovani 1995) a dusty torus surrounds the AGN on
scales of ~0.1-10 pc (Burtscher et al. 2013) and is responsible for the observational distinction between Type 1 and
Type 2 AGN, by obscuring the accretion disk continuum in the equatorial plane.
[9] E.g. Weedman (1970), Heckman et al. (1984), Veilleux (1991), Boroson (2005), Komossa et al. (2008), Zhang et al.
(2011), Bae & Woo (2014), Zakamska & Greene (2014), Balmaverde et al. (2016), Perna et al. (2017).

outflows increases with AGN luminosity and/or Eddington ratio[10]. Moreover, recent works also found that about 75% of X-ray selected, obscured, red sources show evidence of ionized outflows, indicating that they are more common in obscured and dusty sources[11]. This suggests the importance of highly obscured environments in launching outflows and is consistent with predictions from models of outflows driven by radiation pressure on dusty clouds (e.g. Costa et al. 2018). Longslit and integral field spectroscopic observations allowed to identify ionized outflows extended on ~1-10 kpc scales, both in low- and high-z AGN[12], with mass outflow rates up to ~600-700 $M_\odot$ yr^{-1}. Besides [O III], tracing medium-ionization gas, low-ionization gas outflows are also traced by broad wings in other optical emission lines such as Hα and [N II] (e.g. Rupke & Veilleux 2013, Arribas et al. 2014), or in UV and optical absorption lines (e.g. Shapley et al. 2003, Talia et al. 2012, Bordoloi et al. 2014, González-Alfonso et al. 2017).

Ionized outflows from [O III] have provided the strongest pieces of evidence of negative feedback directly in action in a few AGN around $z \sim 2$, where narrow Hα emission, tracing star formation in the host galaxy, has been found to be spatially anticorrelated with the [O III] outflowing material (Cano-Díaz et al. 2012, Cresci et al. 2015b, Carniani et al. 2016). However, in these objects the outflow seems to affect the gas reservoir only along its path, while in the rest of the galaxy star formation remains globally high, with SFRs ~100 $M_\odot$ yr^{-1}.

1.3.3 Molecular and atomic neutral outflows

Massive molecular outflows, having velocities from few 100 km s^{-1} up to ~1000 km s^{-1} and mass outflow rates of H_2 of several 100 $M_\odot$ yr^{-1} up to above 1000 $M_\odot$ yr^{-1}, are detected from faint broad features in CO emission lines in the submm/mm band[13], in [C II] emission line in FIR (e.g. Maiolino et al. 2012, Cicone et al. 2015), in emission lines from more complex molecules (such as HCN, HCO$^+$, HNC, tracing high density molecular gas, with $n > 10^4$ cm^{-3}; e.g. Aalto et al. 2012, 2015), in H_2 emission lines in the NIR and MIR bands (e.g. Dasyra & Combes 2011, Davies et al. 2014) and from characteristic P-Cygni profiles[14] of OH lines in FIR spectra (e.g. Fischer et al. 2010, Sturm et al. 2011, Veilleux et al. 2013, Spoon et al. 2013).

Molecular outflows are found to dominate the mass of AGN outflows compared to the ionized phase of about two orders of magnitude (Carniani et al. 2015, Fiore et al. 2017, Fluetsch et al. 2018). Actually this holds for AGN bolometric luminosities $<10^{46}$ erg s^{-1}. For very high-luminosity AGN ($>10^{46}$ erg s^{-1}) contradictory results have been found. Fiore et al. (2017) found

---

[10] E.g. Mullaney et al. (2013), Bae & Woo (2014), Zakamska & Greene (2014), Balmaverde et al. (2016), Woo et al. (2016), Harrison et al. (2016), Perna et al. (2017).

[11] E.g. Brusa et al. (2015a), Perna et al. (2015a), Zakamska et al. (2016), LaMassa et al. (2017), Toba et al. (2017).

[12] E.g. Holt et al. (2008), Humphrey et al. (2010), Harrison et al. (2012, 2014), Liu et al. (2013), Carniani et al. (2015), Perna et al. (2015b).

[13] E.g. Feruglio et al. (2010, 2013), Dasyra & Combes (2012), Cicone et al. (2014), Morganti et al. (2015), Dasyra et al. (2016).

[14] P-Cygni line profiles are constituted by a blueshifted absorption feature tracing approaching material and a redshifted one in emission tracing receding gas.

that the ionized outflows have mass outflow rates similar to molecular ones at these high luminosities, while Carniani et al. (2015) did not find clear evidence for this trend. However, the sample in Carniani et al. (2015) comprised outflow observations both in the molecular and ionized phase for each object, while in Fiore et al. (2017) each object had observations for only one outflow phase, either ionized or molecular. Star-forming galaxies seem to have instead comparable amounts of ionized and molecular outflow masses (e.g. Fluetsch et al. 2018).

Some caveats need to be stressed regarding molecular outflow observations. Among the various tracers presented above, most studies of molecular outflows rely on CO and OH observations, used as proxies of the total molecular gas mass, which resides mostly in the form of H_2, difficult to detect directly. Observations have mostly targeted galaxies characterised by a large molecular gas fraction and, therefore, may have been biased towards massive molecular outflows. Moreover, there is large uncertainty on outflow molecular mass estimation from CO and OH only, in absence of additional H_2 tracers. In addition to that, interferometric observations (such as those obtained with ALMA or NOEMA), if not including short antenna separations, are likely to miss the diffuse component of molecular outflows, which may carry the bulk of their mass (Cicone et al. 2018).

Cicone et al. (2014) found that the momentum rate ($\dot{P}_{out} = \dot{M}_{out} v_{out}$) of these massive molecular outflows is 20 times larger than the AGN photon momentum output, $\dot{P}_{out} \sim 20\ L_{AGN}/c$, consistently with the predictions for energy-driven outflows (e.g. Zubovas & King 2012, Faucher-Giguère & Quataert 2012), and in accordance with the results obtained from the comparison between nuclear UFOs and galactic molecular outflows in a few objects (Tombesi et al. 2015, Feruglio et al. 2015, 2017; as discussed before in Sect. 1.3.1). However, other recent works suggest that the full energy-driven mechanism may be responsible only for a few AGN outflows, as most of them fall below the above relation, pointing to a contribution of different driving mechanisms or still to an energy-driven scenario but with poor coupling between the nuclear wind and the host ISM (Fluetsch et al. 2018).

Outflows in the neutral atomic phase are traced by blueshifted wings in Na I D absorption line doublet in the optical band (Rupke et al. 2005b, Rupke & Veilleux 2011, 2015, Perna et al. 2017), in H I 21-cm absorption line in radio (e.g. Morganti et al. 2005, 2016, Schulz et al. 2018), in H I Lyα e Lyβ absorption lines and other UV low-ionisation absorption features tracing neutral atomic gas (e.g. Shapley et al. 2003, Talia et al. 2012, 2017), as well as in [C II] emission line in FIR. [C II] broad wings are found to be in fact a good tracer of both the molecular and neutral atomic phases of outflows (e.g. Janssen et al. 2016). When present, the neutral atomic outflow phase is found to dominate the total outflow mass compared to the ionized phase (e.g. Rupke & Veilleux 2013).

Neutral outflows are detected only in ~1% of nearby AGN at low z and they mainly reside in ultra-luminous infrared galaxies (ULIRGs), showing both intense SF and AGN activity (e.g.

Rupke et al. 2005a, Villar Martín et al. 2014, Cazzoli et al. 2016, Sarzi et al. 2016, Perna et al. 2017). This may suggest that neutral atomic gas outflows are mostly powered by SF and not by AGN activity (e.g. Concas et al. 2017, Bae & Woo 2018) or that they can occur only in obscured AGN hosting large quantities of cold gas to be entrained in galactic outflows (Perna et al. 2017). However, further observational studies, exploiting spatially resolved spectroscopic observations in particular, are required to better understand the nature of neutral atomic outflows and constrain their driving mechanisms.

1.4 The impact of outflows: an observational challenge

Determining the impact of outflow on host galaxies is a major observational and theoretical challenge of present-day extragalactic astrophysics. Affordable measurements of the outflow properties are in fact required in order to test predictions of feedback and outflow models and assess how and at which extent outflows are able to affect the gas reservoir and star formation in the host galaxy. Also determining which is the driving mechanism of outflows between AGN (through radiation or jets) and star formation processes in each object, or if both contribute and at which extent, is another non-secondary issue (e.g. Wylezalek & Morganti 2018).

To address these hot topics, observational works attempt to measure outflow characteristic properties such as outflow velocity, v_{out}, mass outflow rate, $\dot{M}_{out}$, kinetic energy rate, $\dot{E}_{k,out} = \dot{M}_{out}/2\left(v_{out}^2 + A\sigma_{out}^2\right)$, and momentum rate, $\dot{P}_{out} = \dot{M}_{out}v_{out}$. The factor $A\sigma_{out}^2$ is sometimes included in the calculation of the kinetic rate to account for the uncertain contribution of the velocity dispersion within the outflow, σ_{out}, regulated by the constant A (e.g. Rodríguez Zaurín et al. 2013).

A quantity which is often used to test if the AGN radiative luminosity is capable of driving the observed outflows, as well as to be compared with model expectations, is the kinetic coupling efficiency, $\dot{E}_{k,out}/L_{AGN}$. As shown in Harrison et al. (2018), various assumptions made in different works in estimating kinetic coupling efficiencies lead to a variation of four orders of magnitude in the calculated efficiencies, stressing the importance of uniformity in deriving outflow quantities.

Galactic outflows are extended structures whose properties can vary considerably throughout their extension and whose geometry also determines how they interact with the host galaxy. However, due to the large distance of the observed objects (in many cases quasars between $z \sim$ 1-3, around the peak of cosmic AGN activity) and/or to the technical limitations of the instruments, most outflow observation are unresolved, or only marginally resolved, and then only a single average value of each outflow property can be obtained (e.g. Liu et al. 2013, Fiore et al. 2017). In fact, seeing-limited ground-based spatially-resolved observations can only afford a resolution of ~1-3 kpc at $z = 0.1$ and of ~4-13 kpc at $z = 2$ (e.g. Harrison et al. 2018). Even in the best case of adaptive optics-assisted observations, only a spatial resolution of ~1 kpc can be

achieved at $z \sim 2$ (Williams et al. 2017), which is still quite poor, as a kpc-scale outflow would still be unresolved or only barely resolved.

Mass outflow rates are usually obtained from the following relation

$$\dot{M}_{\mathrm{out}} = f \frac{M_{\mathrm{out}} v_{\mathrm{out}}}{r_{\mathrm{out}}} \tag{1.4}$$

where M_{out} is the mass contained in the outflow, r_{out} its radius and the factor f, usually assumed equal to 1 or 3, depends on the assumption made on the outflow geometry and whether an instantaneous or time-averaged outflow is considered (e.g. González-Alfonso et al. 2017). First of all, the outflow velocity is defined in different ways depending on the work. Outflows are traced by broad wings in gas line profiles in integrated or low-resolution observations, resulting from the blend of the different outflow velocities in the line of sight. The outflow velocity is sometimes defined as the velocity of the most extreme part of this broad component (such as the velocity that contains 5% of the broad emission; e.g. Cano-Díaz et al. 2012) or as a combination of the velocity of the centroid of the broad component and of its width (e.g. Liu et al. 2013, Fiore et al. 2017). However, the broadening of lines due to the blend of different kinematic components resulting from poor spatial resolution, may lead to overestimated kinetic rates by one or two order of magnitudes (Husemann et al. 2016).

Another large uncertainty comes from the fact that in case of unresolved or barely-resolved observations, the size of the outflow has to be assumed and typical values are employed, though these change from object to object. Even when spatially-resolved observations are available, outflow sizes can be defined by using different criteria, such as by considering the whole observed extension of the outflow or some sort of flux-weighted effective radius (e.g. Harrison et al. 2018).

Many uncertainties are also present in the determination of outflow masses. Concentrating on warm ionized gas traced by optical emission lines, on which this thesis focuses, outflow masses are determined as $M_{\mathrm{out}} = C L_{\mathrm{out}} / n_{\mathrm{e}}$, from the luminosity of the fraction of emission line associated with the outflow, L_{out}, and the electron density of the outflowing gas, n_{e} (e.g. Osterbrock & Ferland 2006). Hydrogen recombination lines (such as Hα and Hβ) are the best choice for determining the ionized gas mass, being insensitive to gas ionization state and elemental abundances, differently from [O III] (e.g. Cano-Díaz et al. 2012). The dependence on the emission lines used is included in C, which, given these considerations, is really uncertain for [O III] but, to a much lesser extent, also for hydrogen recombination lines, for which C still depend on gas temperature (e.g. Osterbrock & Ferland 2006). On top of that, the first requirement is to be able to isolate in the spectra the luminosity of the fraction of the emission line associated with the outflow from the rest, which, especially in type 1 AGN where the broad line region strongly contributes to Hα and Hβ emission, may not be trivial and lead to further uncertainty (e.g.

Harrison et al. 2018). Correctly determining the extinction affecting the lines, so as to recover their intrinsic luminosity, may be challenging as well (e.g. Rose et al. 2018). Anyway, the largest uncertainty in determining the mass of ionized outflows comes from the electron density, usually obtained from the [S II]λ6717/λ6731 and [O II]λ3726/λ3729 diagnostic line ratios, which are reliable only in the density range ~50-5000 cm^{-3} (Osterbrock & Ferland 2006). Moreover, the small line doublet separation and the weakness of these lines compared, for example, to Hα or [O III], can complicate the isolation of the part of the emission-line profile associated to the outflow, and so the total emission-line fluxes are often directly used instead to estimate n_e (e.g. Harrison et al. 2018).

Only recently in few objects outflows have been sufficiently resolved, with enough signal-to-noise in the emission lines, so that the geometric structure of the outflow could be inferred and their physical and kinematic properties studied as a function of distance from the nucleus (e.g. Feruglio et al. 2015, Crenshaw et al. 2015, Revalski et al. 2018). Such studies have shown the importance of having spatially-resolved information to obtain a more direct assessment of outflow properties to be compared with model predictions.

1.5 Thesis aims

In this introductory Chapter we have presented the main observational results which point to the need of AGN and SN feedback during the formation and evolution of galaxies, that is, the stellar mass function of galaxies, the BH-host galaxy scaling relations and the BH and star formation cosmic histories. We have given an overview of the main types of feedback predicted by models, from negative feedback, in its radiative and kinetic modes, acting through outflows and jets, respectively, which suppress star formation in the host galaxy, to positive feedback, with outflows triggering star formation instead, either by compressing the host ISM or by forming stars within the outflowing gas itself. We then provided a description of the different gas phases and spatial scales over which outflows can manifest in observations. We finally examined the main issues and uncertainties affecting the determination of the properties of outflows and of their actual impact on host galaxies, stressing the need to have good-resolution spatially-resolved information in order to determine the size and structure of outflows as well as to measure their physical properties as a function of radius, thus avoiding many assumptions and allowing a more solid comparison with model predictions.

In this context, this work aims to investigate in detail the properties of ionized galactic outflows, the physical conditions of the ionized gas and the interplay between nuclear activity and star formation in nearby Seyfert galaxies, by employing optical spatially-resolved observations from the Multi Unit Spectroscopic Explorer (MUSE; Bacon et al. 2010) at the Very Large Telescope (VLT) in Chile. Targeting nearby galaxies with spatially-resolved observations allows us to tackle one of the major problems affecting outflow observations, that is, the lack of spatial infor-

mation with good spatial resolution. As just explained, in fact, the poor or absent spatial resolution in outflow observations introduces large uncertainties in the estimation of outflow properties or forces to directly make assumptions on some of outflow physical quantities. Though they may not host outflows as powerful as those observed in quasars around $z \sim 2$, nearby galaxies, due to their vicinity, are ideal laboratories to explore in high detail outflow properties, their formation and acceleration mechanisms, as well as the effects of AGN activity on host galaxies. MUSE operates in the optical and near-IR bands (4750-9300 Å) and has a field of view (FOV) of $1' \times 1'$ covered by 300×300 spectral pixels (spaxels) of $0.2''$/px, each one containing a spectrum (for a total of 90000 spectra per observation). MUSE has a good spectral resolution, 1770 at 4800 Å and to 3590 at 9300 Å, which allows to disentangle different kinematic components in emission lines with a velocity resolution of ~65 km s^{-1} at [O III] wavelengths and of ~50 km s^{-1} at Hα wavelengths. Moreover, MUSE exploits the large light-collecting power of an 8m-diameter telescope (VLT). MUSE is unique among the other instruments of the same kind. For example, VIMOS (Le Fèvre et al. 2003), which is considered a fairly wide integral field instrument (up to $54'' \times 54''$ FOV), only gave a total of 6400 spectra, thus having a much poorer spatial sampling compared to MUSE (as well as lower spectral resolution). The unprecedented combination of wide spatial and spectral coverage of MUSE provides a complete and detailed view of the central kiloparsecs of nearby Seyferts. This allows us to map the ionized gas in several different emission lines over galactic scales and resolve the distribution, kinematics and physical properties (such as density, extinction, ionization mechanisms) of both the gas in the host galaxy and in outflow, on scales of single clouds (~10-100 pc for distances of ~4 to 40 Mpc).

1.5.1 Thesis outline

The thesis is structured as follows. In Chapter 2 we first give an overview of our sample of nearby Seyfert galaxies observed with MUSE constituting our MAGNUM survey and present the emission-line and kinematic maps of the 10 objects that we have analyzed so far. In Chapter 3 we present our detailed multi-wavelength analysis, from MUSE in optical and *Chandra* in X-rays, of one of these sources, namely NGC 1365. Here we investigate the physical properties, the kinematics and the ionization mechanisms of the mildly- and highly-ionized phases of the gas, emitting in the optical and X-ray bands, respectively, and we compare the properties of the galactic-scale optical outflow with those of the nuclear X-ray wind. In Chapter 4 we present a study of the nearby star-forming galaxy NGC 6810 with MUSE, where we find evidence of star formation occurring within a galactic outflow. In addition to outflows in Seyferts, related to the radiative-mode feedback, MUSE allows us to inspect with unprecedented detail also the kinetic-mode AGN feedback. We conclude in fact by presenting in Chapter 5 our analysis of the radiogalaxy 3C 317 at the center of the local cluster Abell 2052, where, thanks to MUSE capabilities, we can directly measure the expansion velocity of the cavity inflated by the radio jets in the

hot gas surrounding the galaxy, and put stricter constraints on the kinematics and energetics of the kinetic feedback phenomenon.

2 MAGNUM: mapping galactic ionized outflows in nearby Seyferts with MUSE

2.1 Introduction

In this chapter we present our sample of 9 nearby active galaxies ($D < 50\,\text{Mpc}$) observed with VLT/MUSE, belonging to the MAGNUM (Measuring Active Galactic Nuclei Under MUSE Microscope) survey, namely Centaurus A, Circinus, IC 5063, NGC 1068, NGC 1365, NGC 1386, NGC 2992, NGC 4945 and NGC 5643, plus the star-forming galaxy NGC 6810. The MAGNUM survey aims at observing nearby galaxies hosting an AGN to study the physical conditions of the narrow line region (NLR), the interplay between nuclear activity and star formation, and the effects and acceleration mechanisms of outflows. We include also NGC 6810 in our analysis, which is not part of the MAGNUM sample being a star-forming galaxy, so as to study the ionized gas and outflow properties also in a star-forming galaxy and compare them with the properties observed in the other active galaxies. We first give a description of the whole MAGNUM sample selection and of the data reduction and analysis workflow, and we then present our MUSE maps of the ionized gas emission and kinematics in the central kiloparsecs of the 10 galaxies mentioned above which we have inspected so far.

2.2 MAGNUM sample selection

We selected our sources starting from the samples in Maiolino & Rieke (1995), Risaliti et al. (1999) (hereafter MR95 and R99, respectively) and Swift-BAT 70-month Hard X-ray Survey (Baumgartner et al. 2013; SB-70m).

MR95 contains 91 Seyferts with $B_T < 13.4$ either from the Revised Shapley-Ames (RSA; Sandage & Tammann 1987) catalog and from the additional list in Sandage & Tammann (1987) as well as from an integration done in MR95 itself.

R99 sample consists of 92 sources, which are the same of MR95 with the exception that only Seyfert 2 galaxies are considered (type 1.8 to 2) and with the addition of NGC 1808[1] and other 18 Seyfert galaxies found by Ho et al. (1997), which would have been included in MR95 if they had been discovered earlier.

SB-70m comprises 1171 sources detected in the 14-195 keV band in 70 months of ob-

---

[1] This source fits the selection criteria of MR95, but was missed by the original version of the sample.

Table 2.1: MAGNUM survey sample.

Name[a]	z^b	D [Mpc]^c	$F_{\text{[O III]}}{}^d$
NGC 1068[e]	0.003793	10.5 ± 1.7	15800
Circinus	0.001448	4.2 ± 0.7	6970
ESO 428-14[g]	0.005664	21 ± 7	2010
NGC 7314	0.004763	16.1 ± 1.8	1770
NGC 5643	0.003999	16 ± 7	694
NGC 2992	0.00771	32 ± 7	680
NGC 1386	0.002895	16.4 ± 0.8	655
IC 3639	0.010924	46 ± 7	620
NGC 5506	0.006181	28 ± 7	600
NGC 7582	0.005254	19.1 ± 0.9	445
NGC 4388	0.008419	21 ± 8	374
NGC 4941	0.003696	20 ± 3	355
IC 5063	0.011348	46 ± 7	353
NGC 2110	0.007789	31 ± 7	321
NGC 3081	0.007976	33 ± 7	215
NGC 5728	0.009353	30 ± 6	180
NGC 4507	0.011801	49 ± 7	158
NGC 1365	0.005457	17.29 ± 0.19	141
NGC 1808	0.003319	12 ± 2	131
NGC 3783	0.00973	40 ± 7	130[q]
NGC 4939	0.010374	38 ± 4	112
NGC 5953	0.006555	32 ± 7	86
NGC 6221	0.004999	12 ± 3	72
NGC 3227	0.003859	20 ± 3	64[q]
NGC 1320	0.008883	39 ± 7	57
NGC 3281	0.010674	45 ± 7	45
NGC 424	0.011764	48 ± 7	42[q]
NGC 4945	0.001878	3.47 ± 0.03	>40
IC 2560	0.009757	31 ± 4	>40
NGC 7743	0.005704	18.7 ± 0.8	40
ESO 138-1	0.009140	38 ± 7	36.9[s]
M 88[h]	0.007609	11.16 ± 0.10	36
NGC 7213	0.005839	24 ± 7	34.3[r]

Table 2.1: continued.

Name[a]	z^b	D [Mpc]^c	$F_{[O\,III]}{}^d$
NGC 1566	0.005017	7 ± 4	30^q
NGC 7496	0.0055	11 ± 6	29
ESO 137-34	0.009144	38 ± 7	25.4^s
NGC 6890	0.008069	35 ± 7	25
MCG -05-23-016^m	0.008486	33 ± 7	23^q
NGC 6300	0.003699	10.7 ± 0.4	20
NGC 4593	0.009	41 ± 6	17.2^q
NGC 7590	0.005255	24.5 ± 0.6	17
NGC 7479	0.007942	33 ± 4	16
NGC 7410	0.005841	35 ± 10	16
NGC 6814	0.005214	24 ± 7	13.6^q
MCG -06-30-015^n	0.007749	33 ± 7	11.4^r
M 58^i	0.00506	20.2 ± 1.8	9
M 104^j	0.003416	8.6 ± 0.2	7
NGC 5427	0.008733	38 ± 6	$>6^p$
Centaurus A^f	0.001825	3.68 ± 0.04	6
NGC 4477	0.004463	18 ± 3	4
NGC 7172	0.008683	36 ± 7	4
NGC 0676	0.005023	21 ± 7	2.9
NGC 4235	0.008039	20 ± 7	2.4^q
NGC 4698	0.003366	21 ± 3	2.4
NGC 3976	0.008329	35 ± 4	2.4
NGC 1125	0.010931	45 ± 7	2.3^s
NGC 1433	0.003589	8.5 ± 1.4	2
NGC 4639	0.003395	25.4 ± 0.3	0.9
NGC 4378	0.008536	47 ± 6	0.8
IC 1657	0.011952	49 ± 7	0.26^s
M 49^k	0.003272	16.6 ± 0.4	0.1
NGC 4168	0.007625	34 ± 5	0.1
NGC 7465	0.006538	30 ± 7	…
NGC 1097	0.00424	14.7 ± 1.7	…
ESO 377-24	0.009767	40 ± 7	…
NGC 454E	0.012125	49 ± 7	…
NGC 1052	0.005037	17.6 ± 0.9	…

Table 2.1: continued.

Name[a]	z^b	D [Mpc][c]	$F_{[O\,III]}{}^d$
ESO 362-18	0.012445	50 ± 7	...
MCG -05-14-012[l]	0.009915	39 ± 7	...
NGC 4180	0.006992	34 ± 4	...
2MASX J193-061[o]	0.010254	46 ± 7	...
ESO 234-50	0.008766	36 ± 7	...

[a] Names written in bold indicate the sources analyzed in this work. [b] Redshift, taken from NASA/IPAC EXTRA-GALACTIC DATABASE. [c] Distance (in Mpc) obtained from HyperLeda best distance modulus, i.e. the weighted average between the redshift distance modulus corrected for infall of the Local Group towards Virgo and the weighted average of the published redshift-indipendent distance measurements. [d] [O III] $\lambda 5007$ flux (from Risaliti et al. 1999 and references therein, otherwise specified) in units of $10^{-14}\,\mathrm{erg\,s^{-1}\,cm^{-2}}$, corrected for extinction as deduced from the (narrow-line) Balmer decrement. [e] Alias M 77. [f] Alias NGC 5128. [g] Alias IRS 07145. [h] Alias NGC 4501. [i] Alias NGC 4579. [j] Alias NGC 4594. [k] Alias NGC 4472. [l] Alias ESO 424-12. [m] Alias ESO 434-40. [n] Alias ESO 383-35. [o] Full name is 2MASX J19373299-0613046. [p] Not corrected for the Balmer decrement. [q] Whittle (1992); not corrected for the Balmer decrement. [r] Alonso-Herrero et al. (1997) and references therein; not corrected for Balmer decrement. [s] Gu et al. (2006); not corrected for Balmer decrement.

servations of the BAT hard X-ray detector on the Swift gamma-ray burst observatory. SB-70m is the most sensitive and uniform hard X-ray all-sky survey and reaches a flux level of $1.03 \times 10^{-11}\,\mathrm{erg\,s^{-1}\,cm^{-2}}$ over 50% of the sky and $1.34 \times 10^{-11}\,\mathrm{erg\,s^{-1}\,cm^{-2}}$ over 90% of the sky. Of its 1171 sources, 711 are confirmed to be AGN. We decided to adopt this hard X-ray selected catalogue as it includes optically-obscured AGN which are out of MR95 and R99 constraints but are detected in the hard X-rays. On the other hand a hard X-ray selection only would miss Compton-thick AGN, which are instead included in an optical selection based on gas emission lines (like the one in MR95 and R99) due to the spatially-extended nature of the optical line emission.

In order to build our sample, we selected the sources belonging to any of these three catalogues which are observable from Paranal Observatory ($-70° < \delta < 20°$), where VLT is located, and have a distance lower than 50 Mpc. The distance is obtained from HyperLeda best distance modulus, i.e. the weighted average between the redshift distance modulus corrected for infall of the Local Group towards Virgo and the weighted average of the published redshift-indipendent distance measurements. Doing so, we obtained a sample of 72 active galaxies, 14 of them present only in SB-70m and not in MR95+R99, while 28 included only in the latter and not in the former, confirming the validity of using both optically and X-ray selected sources to build our sample of local active galaxies. The 72 targets of our MAGNUM survey are then reported in Table 2.1.

Table 2.2: Basic data of the MAGNUM survey galaxies presented in this work

Name	v_z [km/s]^a	D [Mpc]^b	d_{FOV} [kpc]^c
Centaurus A	547	3.68 ± 0.04	1.14 ± 0.013
Circinus	434	4.2 ± 0.7	1.3 ± 0.2
IC 5063	3402	46 ± 7	14 ± 2
NGC 1068	1137	10.5 ± 1.7	3.3 ± 0.5
NGC 1365	1636	17.29 ± 0.19	5.33 ± 0.06
NGC 1386	868	16.4 ± 0.8	5.1 ± 0.2
NGC 2992	2311	32 ± 7	10 ± 2
NGC 4945	563	3.47 ± 0.03	1.069 ± 0.009
NGC 5643	1199	16 ± 7	5 ± 2
NGC 6810*	2031	27 ± 7	8 ± 2

Notes. $^{(a)}$ Heliocentric velocities (in km/s) calculated from redshift, taken from NASA/IPAC EXTRAGALAC-TIC DATABASE. $^{(b)}$ Distance (in Mpc) obtained from HyperLeda best distance modulus, i.e. the weighted average between the redshift distance modulus corrected for infall of the Local Group towards Virgo and the weighted average of the published redshift-indipendent distance measurements. $^{(c)}$ Size of the FOV (in kpc) covered by MUSE data used in this work (note that FOV can be slightly larger than $1' \times 1'$ of a single MUSE observation, due to dithered combined exposures). $^{(*)}$ Not part of MAGNUM survey.

2.2.1 Analyzed sources

We analyzed 9 of the galaxies belonging to our sample so far, using our own and archival MUSE data. We first concentrated on these 9 galaxies which, as explained in the following, were part of our own observing program and Science Verification data. Such galaxies have been targeted first as they have been widely studied in the past and they were likely to provide interesting results in terms of AGN activity and effects on its surroundings. Moreover, a large amount of multi-band data exist for them, allowing to extend the comparison of the ionized gas from MUSE optical data to other phases from different bands. Table 2.2 summarizes some of their characteristics (i.e. redshift, distance, physical extent of the region analyzed in this work). In this thesis we also include NGC 6810 in our MUSE data analysis, though not part of the MAGNUM sample, being not classified as AGN (e.g. Kewley et al. 2001a), so as to study the outflow properties also in a star-forming galaxy and make comparisons with outflows observed in galaxies hosting an AGN.

A large part of MUSE data studied in this work belongs to program 094.B-0321(A) (P.I. Marconi), which comprises Centaurus A, Circinus, NGC 1068, NGC 1365, NGC 1386, NGC 2992 and NGC 4945. NGC 5643 was observed as part of the above program as well, but for this work we adopted the data belonging to program 095.B-0532(A) (P.I. Carollo) due to their better seeing ($\sim 0.56''$) compared to the ones from program 094.B-0321(A). IC 5063 and NGC 6810 are part of Science Verification program 60.A-9339(A) (P.I. Marconi/Hawthorn/Salvato). Basic information about MUSE data used in this work are summarized in Table 2.3.

Table 2.3: Information about MUSE data used in this work

Name	Run/Program ID	T_{exp} [s]^a	Used OBs / OBs^b	Obs. date [yr-mm-dd]^c
Centaurus A	094.B-0321(A)	4000	2/5^d	2015-02-06
				2015-03-14
Circinus	094.B-0321(A)	2000	1/1	2015-03-11
IC 5063	60.A-9339(A)	2400	1/1	2014-06-23
NGC 1068	094.B-0321(A)	2800	2/2^e	2014-10-06
				2014-12-01
NGC 1365	094.B-0321(A)	4000	2/2	2014-10-12
				2014-10-12
NGC 1386	094.B-0321(A)	4000	2/2	2014-11-13
				2014-11-13
NGC 2992	094.B-0321(A)	4000	2/5^f	2015-01-28
				2015-02-13
NGC 4945	094.B-0321(A)	2000	1/1	2015-01-17
NGC 5643	095.B-0532(A)	3600	1/1	2015-05-12
NGC 6810	60.A-9339(A)	2400	1/1	2014-06-23

Notes. $^{(a)}$ Total exposure time on the object of all the OBs used in this work. $^{(b)}$ Number of OBs used in our analysis with respect to the total number of available OBs for each galaxy. $^{(c)}$ Observing date of each used OB, in the format year-month-day. $^{(d)}$ Three OBs were marked with grade C because of seeing or sky transparency out of requested constraints, while two OBs were marked with grade X as telescope was closed due to high humidity before they were finished; we concluded to use the two observations with best seeing, one having grade C (2015-02-06T05:41:19.170), one grade X (2015-03-14T06:33:51.807), which, despite the closure of the telescope, only lacked of two of four requested offset sky exposures and did not show any issue in the final cube with respect to the other used observation (like anomalous change of slope of the spectra or different level of signal). $^{(e)}$ The first OB presented in the central spaxels emission lines having saturated fluxes or fluxes in the non-linear response regime of the instrument. The second OB has then been acquired with shorter exposure times (8×100s instead of 4×500s) and only this second OB has been adopted for the central spaxels. $^{(f)}$ Three out of five OBs were marked with grade C because of seeing or sky transparency out of requested constraints, so we decided to use only the two OBs having grade A.

2.3 Data reduction and analysis

Depending on the galaxy, the data reduction and exposure combination have been carried out either making use of self-made scripts to execute the Common Pipeline Library (CPL) reduction recipes with EsoRex (ESO Recipe Execution Tool) or using ESO reflex, which gives a graphical and automated way to perform the reduction (still operated by EsoRex using the CPL recipes), within the Kepler workflow engine (Freudling et al. 2013). We have employed MUSE pipeline recipes v1.6 for our reduction. For a few objects we adopted the already-reduced cube provided by ESO Quality Control Group. Each Observing Block (OB) of a galaxy is composed by multiple exposures, dithered by $1''$ and/or rotated by $90°$ relative to one another.

MUSE spectral binning is 1.25Å/channel and its resolving power in Wide Field Mode (WFM) (the only available at the moment of observations) is equal to 1770 at 4800 Å and to 3590 at

9300 Å. All the observations were taken in MUSE Nominal Mode, which gives spectra spanning from 4750 Å to 9350 Å. From now on, unless specified, the given wavelengths are rest-frame. In our analysis they have been redshifted according to the redshift of each galaxy (see Table 2.2), as we have not reverted the spectra to the Earth reference frame. Galactic foreground stars, present in different quantities in the analyzed cubes, have been spatially masked when disturbing data analysis.

2.3.1   Stellar continuum fitting and subtraction

With the aim of studying the gas emission lines of interest through appropriate fits, as well as obtaining the kinematics of the stars, the stellar continuum has been fitted and removed from each single-spaxel spectrum, in order to recover the correct gas emission lines profiles. To do that, a Voronoi adaptive binning (Cappellari & Copin 2003) has first been performed, so as to achieve a minimum signal-to-noise ratio per bin for the stellar continuum, allowing to better fit it also in the fainter regions of the FOV, while preserving the maximum spatial resolution. The desired signal-to-noise ratio per bin has been set to an average value of 50 per wavelength channel, considering only the signal (and the associated noise) in the blue part of the spectrum, under 5530 Å, where stellar features are more prominent. In order to fit the stellar emission, we have employed a linear combination of Vazdekis et al. (2010) synthetic spectral energy distributions (SEDs) for single-age, single-metallicity stellar populations (SSPs) covering the full optical spectral range at moderately high resolution (FWHM = 2.3 Å), which combine theoretical isochrones with the MILES (Medium resolution INT Library of Empirical Spectra) empirical stellar spectral library (Sánchez-Blázquez et al. 2006, Falcón-Barroso et al. 2011). The models we used[2] adopt a unimodal IMF (Vazdekis et al. 1996) with slope 1.3 (i.e. a standard Salpeter IMF; Salpeter 1955) and BaSTI theoretical isochrones[3] (Pietrinferni et al. 2004, Pietrinferni et al. 2006), which have metallicities M/H spanning from -2.27 to +0.40 and ages comprised between 0.03 and 14.0 Gyr. These templates cover the interval 3540.5-7409.6 Å, but the fit has been performed at wavelengths smaller than about 6800 Å, as there were noisy sky residuals and no emission lines of interest for this work above. To speed up the fit, only the linearly independent templates have been used, as our aim is only to reproduce the shape of the stellar features and derive the bulk velocity and dispersion of the stellar population, and not to get more detailed physical information from the models, such as age, metallicities etc.

We have employed the PPXF code (Penalized PiXel-Fitting; Cappellari & Emsellem 2004), which convolves the linearly combined stellar templates with a Gaussian profile so as to reproduce the systemic velocity v and the velocity dispersion σ of the absorption lines. The main gas emission lines included in the selected range (i.e. Hβ, [O III] $\lambda\lambda$4959,5007, [O I] $\lambda\lambda$6300,6364,

---

[2]   We downloaded the models from http://www.iac.es/proyecto/miles/.
[3]   http://www.oa-teramo.inaf.it/BASTI.

Hα, [N II] $\lambda\lambda$6548,6584 and [S II] $\lambda\lambda$6716,6731) have been fitted together with the stellar continuum, so as to better constrain the underlying stellar features (especially Hα and Hβ in absorption), while other minor gas emission lines, as well as badly subtracted sky lines and other absorption features[4], have been masked not to disturb the fit. Three different fits have been performed, using respectively 1, 2 and 3 Gaussians to reproduce the (potentially asymmetric) profile of each gas emission line (from now on we will refer to these fits with 1, 2 and 3-component fit or, concisely, with 1c, 2c and 3c-fit). Some galaxies (i.e. IC 5063, NGC 1068 and NGC 6810), showing really complicated line profiles in certain areas, have required fitting with even more than 3 components. The velocity and velocity dispersion of each component has been forced to be the same for all the emission lines, while the normalization has been left free to vary (except for [O III], [N II] and [O I] line doublets, where a factor of 3 exists between [O III] λ5007 and [O III] λ4959, between [N II] λ6584 and [N II] λ6548 and between [O I] λ6300 and λ6364 line strengths; see Storey & Zeippen 2000 for example).

In case of Seyfert 1 galaxies, a single additional template - fixed in shape and velocity - has been included to reproduce the emission of the central unresolved active nucleus. Therefore, the template has been used only in those bins enclosed in a limited circular area around the center (where the nuclear emission gives a contribution in the spectra), and fixed at 0 outside. For each galaxy, this template has been obtained by fitting the spectrum extracted from a circular area of few spaxels around the nucleus. A more detailed description of how this nuclear profile has been attained is given in Sect. 2.3.1.1.

A multiplicative and an additive polynomial of degree between 7 and 10 (the former) and 2 (the latter) have been included in the fit, so as to account for deformations of the spectra with respect to the models (e.g. because of reddening).

A selection based on reduced χ^2 (χ^2/d.o.f.) has been adopted to automatically choose in each bin the optimal fit among the ones with different number of gas components. As the aim is to get the best possible subtraction under the lines of interest, χ^2/d.o.f. is calculated in narrow wavelength ranges strictly surrounding Hβ, [O III] λ5007, and Hα and the [N II] line doublet. χ^2/d.o.f. distribution is built and fitted with an asymmetric Gaussian and a Lévy distribution, the former reproducing the bulk of the χ^2/d.o.f. distribution, the latter accounting for its tail. The value of χ^2/d.o.f. corresponding to the intersection between the two fitting functions is considered as a cut, if the peak of the Levy function has a lower χ^2/d.o.f. value with respect to the intersection, otherwise the value of the peak itself is taken as cut. This is done for 1c, 2c and 3c-fit (hereafter, we will refer with 1c, 2c and 3c-χ^2/d.o.f. to the χ^2/d.o.f. values calculated for 1c, 2c and 3c-fit and, similarly, with 1c, 2c and 3c-cut to the cuts found for 1c, 2c and 3c-χ^2/d.o.f. distributions respectively.). The selection then works as follows for each single bin:

---

[4] I.e. Na I $\lambda\lambda$5890,5896 absorption doublet, due both to gas and stars, as well as, also other ISM absorption lines for galaxies near the Galactic plane.

- if 1c-χ^2/d.o.f. < 1c-cut then 1c-fit is permanently selected, otherwise:

  – if 2c-χ^2/d.o.f. < 2c-cut then 2c-fit is permanently selected, otherwise:

    a) if 2c-χ^2/d.o.f. < 1c-χ^2/d.o.f. then 2c-fit is selected, otherwise 1c-fit is selected;

    b) if 3c-χ^2/d.o.f. < 3c-cut then 3c-fit is permanently selected, otherwise:

      ◇ if 3c-χ^2/d.o.f. < χ^2/d.o.f. selected in step a) then 3c-fit is selected, otherwise the selection done in step a) is left unchanged.

In case more than 3 components are needed, the selection goes on with the same scheme just described.

The stellar and (if present) nuclear emission fitted in each Voronoi bin have then been pixel-by-pixel subtracted from the data cube, rescaling the modeled continuum emission in each j-th bin, $f_{\mathrm{mod},j}(\lambda)$, to the median of the observed continuum in each i-th spaxel belonging to that bin, $\hat{f}_i$. Thus, being $\hat{f}_{\mathrm{mod},j}$ the median of the modeled profile and $f_i(\lambda)$ the observed flux at wavelength λ, the subtracted one is the following:

$$f_{\mathrm{sub},i}(\lambda) = f_i(\lambda) - \frac{f_{\mathrm{mod},j}(\lambda)}{\hat{f}_{\mathrm{mod},j}} \hat{f}_i. \tag{2.1}$$

2.3.1.1. Nuclear BLR fitting

When dealing with Seyfert 1 galaxies, the stellar fitting procedure described in Sect. 2.3.1 has been preceded by the fit of the nuclear emission, carried out in the same wavelength range used for stars. The signal has been collapsed in a circular area around the nucleus, which contains both the emission of the nuclear source (disk continuum + BLR features) and of the gas and stars in the line of sight or immediately around the center. The following templates have been employed to reproduce all the features of the extracted spectrum:

- 1 or 2 Gaussian functions (depending from galaxy to galaxy) for each of the broad profiles of Hβ and Hα, tied with each other in velocity and velocity dispersion;

- a set of CLOUDY models and spectra for the FeII BLR emission;

- a 2-degree additive polynomial and a multiplicative one (of degree between 7 and 10) for the AGN continuum;

- 1 or 2 Gaussians per each narrow gas emission line (the same narrow lines included in the stellar fitting described in Sect. 2.3.1 have been considered here);

- the same stellar templates cited in Sect. 2.3.1.

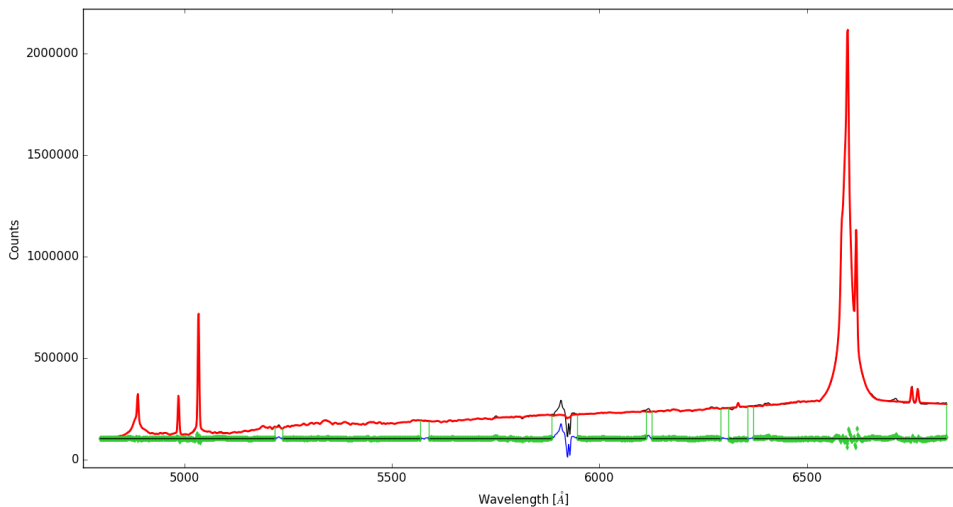Fig. 2.1 shows as an example the fit of the center done for NGC 1365.

Fig. 2.1: Black: spectrum extracted from a 9-pixels diameter circular area around the nucleus. Red: bestfit curve comprising broad Hβ and Hα, FeII broad features, AGN continuum, stellar continuum and Hβ, [O III], [O I], [N II], Hα and [S II] narrow gas emission lines. Green points: data−model residuals. Green vertical lines: spectral ranges excluded from the fit, containing other gas emission or absorption lines or sky-subtraction residuals. Blue: spectrum in the unfitted wavelength ranges.

The nuclear template, to be used when necessary (i.e. in the central pixels) in the bin-by-bin stellar fitting described in Sect. 2.3.1, has been obtained by summing together the bestfit Gaussians for broad Hβ and Hα and the bestfit FeII templates, multiplying them for the bestfit multiplicative polynomial and finally adding the bestfit additive polynomial.

2.3.2 Emission-line fitting

The fitted gas emission lines are the following: Hβ, [O III] $\lambda\lambda$4959,5007, Hα, [N II] $\lambda\lambda$6548,6584 and [S II] $\lambda\lambda$6716,6731[5]. However, before fitting the gas emission lines, two different cubes have been produced from the star-subtracted one, a spatially-smoothed cube and a Voronoi-binned one, the first to be used to get flux and kinematic maps, the second to have more quantitative information (given by the constant signal-to-noise ratio guaranteed by Voronoi binning) so as to calculate affordable line ratios in each bin to construct spatially resolved BPT diagrams (Baldwin et al. 1981, Veilleux & Osterbrock 1987). The former has been obtained by smoothing every spatial plane of the cube with a Gaussian having $\sigma_{\rm smo} = 1$ pixel (corresponding to 0.2″). Such a smoothing does not degrade much the spatial resolution, which (for a seeing of 0.8″, typical of the used MUSE observations) goes from $\sigma_{\rm seeing} = FWHM_{\rm seeing}/2.355 \simeq 0.34″$ to $\sigma \simeq 0.39″$. The latter cube has been produced by performing a Voronoi binning around the weakest line among [O III] λ5007 ([O III] from now on), Hβ, [N II] λ6584 (hereafter, [N II]) and Hα, i.e.

---

[5] Hereafter, with the expression [S II] we refer to the entire [S II] $\lambda\lambda$6716,6731 doublet.

Hβ or [O III] depending on the galaxy. The input signal and the noise for the binning have been obtained by summing over a very narrow wavelength range enclosing the chosen line (linearly the signal, quadratically the noise), requesting an average signal-to-noise ratio per wavelength channel of at least 3.

To perform the fit, we made use of MPFIT (Markwardt 2009). As done for the stellar fitting, 3 (or more, depending on the complexity of the profile in each galaxy) different fits have been carried out, both for the smoothed and for the Voronoi-binned cube, using respectively 1, 2 and 3 (or more) Gaussians to reproduce each gas emission line profile, whose flux is then the sum of the integrated fluxes of the adopted Gaussians (in case of fit with more than 1 component). Line-of-sight velocity v and velocity dispersion σ of each line are calculated respectively as the first and second-order moments in velocity space of the fitted line profile[6].

The residual continuum left after the subtraction of the stellar emission has been fitted with a constant flux value, free to vary to account for small deviations of the overall residuals from null value. For all the lines σ has been forced to be greater than MUSE spectral resolution ($\simeq$ 65 km s^{-1} at [O III]-Hβ wavelengths and $\simeq$ 50 km s^{-1} at [N II]-Hα-[S II] ones). In order to reduce degeneracy, each component has been forced to have the same velocity among all the lines, as well as the same velocity dispersion. [O III] and [N II] line doublets fluxes have been forced to obey the following constraints:

- $F_{\text{[O III]} \lambda 4959} = 1/3 \times F_{\text{[O III]} \lambda 5007}$

- $F_{\text{[N II]} \lambda 6548} = 1/3 \times F_{\text{[N II]} \lambda 6583}$,

where 1/3 is the theoretical ratio between the line strengths. The spectral range comprised between [O III]-Hβ and [N II]-Hα has been masked, not to disturb the residual continuum model with the other unfitted gas emission or absorption features or with sky residuals.

As done for stellar fitting, χ^2/d.o.f. pixel-by-pixel (or bin-by-bin, in the case of Voronoi-binned cube) selection has been employed to determine which results to adopt between the n-comp fits performed. χ^2/d.o.f. has been calculated in narrow wavelength ranges strictly including Hβ, [O III] and [N II]-Hα complex.

2.4 Results

Here we present our MUSE maps of the fitted ionized gas emission lines, specifically flux and kinematic maps, as well as stellar kinematic ones for comparison. The maps are spatially smoothed using a Gaussian kernel with $\sigma = 1$ spaxel (i.e. 0.2$''$) for a better visual output, except for the flux maps (due to their high signal-to-noise ratio) and for the stellar kinematic ones, which are obtained from the Voronoi-binned cube. In each line map, only the spaxels having a

---

[6] The line profile can be a single Gaussian, in case of 1c-fit, or the superposition of more Gaussians, when dealing with multi-component fit.

signal-to-noise ratio of 3 for the line[7] are reported. For each galaxy, we present a brief qualitative description of the reported maps. This Chapter has in fact to be intended as a presentation of the survey and of the flux and kinematic MUSE maps produced and not as a quantitative analysis of such maps, which is instead presented for specific objects, namely NGC 1365 and NGC 6810, in Chapters 3 and 4, and which will be performed on the rest of the MAGNUM galaxies in separate future works. Spatially resolved BPT diagrams and associated maps, to investigate the ionization of the gas in the outflows and disks of the MAGNUM galaxies analyzed so far, as well as maps of other physical properties such as electron density, ionization parameter and dust extinction, are presented in a parallel work of our team (Mingozzi et al. 2018).

2.4.1 Centaurus A

Centaurus A (NGC 5128)[8], located at a distance of ~3.7 Mpc from Earth ($1'' \sim 18$ pc), is the closest low-luminosity (FR I) radio galaxy ($P_{2.7\,GHz} = 1.8 \times 10^{24}$ W Hz^{-1}; Morganti et al. 1999) and one of the closest AGN. The galaxy shows evidence of being the result of a recent merger between an early-type elliptical and a spiral galaxy (e.g. Mathieu et al. 1996, Israel 1998). It is characterized by a stellar-dominated almost circular component and by a dusty and gaseous thick lane approximately in the SE-NW direction, containing the majority of molecular, ionized and neutral atomic gas (e.g. Morganti 2010; see also Fig. 2.2a). Centaurus A shows a characteristic double-sided sub-relativistic jet observed in radio and X-rays extending on a few kpc (e.g. Kraft et al. 2002, Hardcastle et al. 2003; see Fig. 2.2a), whose collimated structure has been resolved down to subpc scales with VLBI observations (e.g. Tingay et al. 1998, 2001, Horiuchi et al. 2006). The northern side of the jet is more prominent than the southern one. The jet expands in a set of radio lobes from ~5 kpc ("inner" lobes, visible in Fig. 2.2a) up to 250 kpc from the nucleus ("outer" lobes; e.g. Israel 1998, Eilek 2014), likely due to different episodes of AGN activity (e.g. Haynes et al. 1983, Morganti et al. 1999). Complex jet-ISM interaction occurs in this source (e.g. Blanco et al. 1975, Peterson et al. 1975, Sutherland et al. 1993, Santoro et al. 2015, Salomé et al. 2016), with evidence of jet-induced star formation (positive feedback) in a gas cloud at ~15 kpc from the center (well outside our MUSE FOV) found by Santoro et al. (2016). An [O III] ionization cone of ~500 pc, due to AGN photons or shocks, is found by Sharp & Bland-Hawthorn (2010) along the galaxy minor axis, that is, in the jet direction. The cone likely connects with the Paβ cone observed on small scales (few arcsecs) by Krajnović et al. (2007) in NIR. An outflow extending over ~200 pc, consistent with the ionization cone, is identified in ionized gas from FIR emission lines, as well as in neutral atomic and molecular gas from faint [C I] and CO emission, respectively (Israel et al. 2017).

---

[7] The signal-to-noise ratio for a line is calculated as the peak value of its fitted profile divided by the standard deviation of the data-model residuals around the line (within a range ~60 to 110 Å wide, depending on the line).

[8] Centaurus A indicates the radio source, while NGC 5128 is the name of the optical host galaxy. However, for simplicity, we will refer to both as Centaurus A from now on.
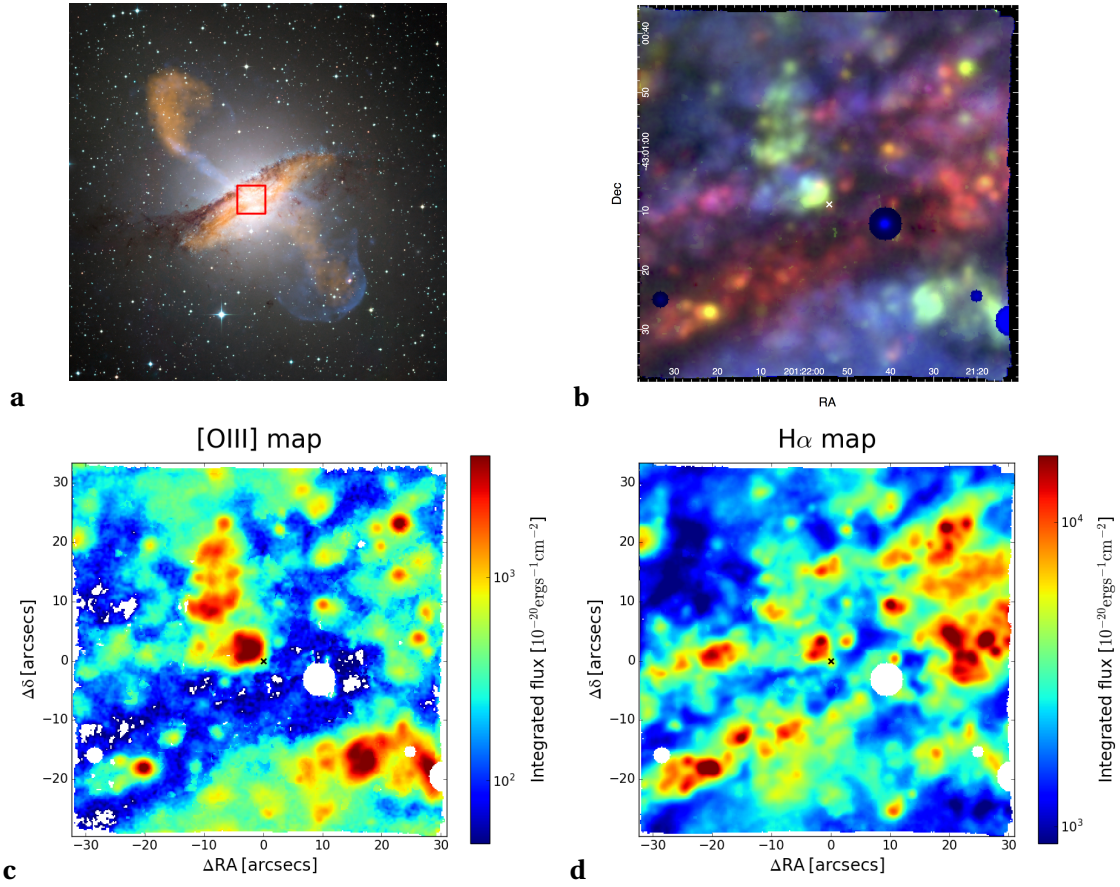
Fig. 2.2: Centaurus A. **(a)** Composite image of Centaurus A, showing 870 μm emission from LABOCA on APEX (orange), X-rays from Chandra X-ray Observatory (blue) and B, V, R (in blue, green and red, respectively) visible light from the Wide Field Imager (WFI) on the MPG/ESO 2.2 m telescope at La Silla, Chile; credit: ESO/WFI (Optical); MPIfR/ESO/APEX/A.Weiss et al. (Submm); NASA/CXC/CfA/R.Kraft et al. (X-ray). Red box represents the FOV of our MUSE maps ($\sim$1′×1′), whose side covers $\sim$1.14 kpc. **(b)** Three color image from MUSE, [O III] in green, Hα in red, stellar continuum collapsed in the spectral range $\sim$5100-5800 Å in blue. [O III] and Hα emission are obtained from the fit of the stellar continuum-subtracted, 1 spaxel-σ smoothed data cube and they are also separately reported in **(c)** and **(d)**. North is up. The reported flux is per spaxel. A signal-to-noise cut of 3 has been applied to all MUSE maps. Circular regions mark masked spaxels due to the presence of Galactic foreground stars disturbing the data analysis.

Figs. 2.2 and 2.3 display our MUSE flux and kinematic maps for Centaurus A, respectively. The composite image in Fig. 2.2a shows the stellar quasi-spherical diffuse emission (white) and the equatorial thick lane of gas and obscuring dust, together with the radio and X-ray jet (orange and blue, respectively) in the perpendicular direction, which also displaces a shell of X-ray emitting material. The FOV of our MUSE maps (red box) covers the central $\sim$1.14×1.14 kpc^2 of the galaxy, including only the inner part of the jet.

Our three-color MUSE map in Fig. 2.2b shows a lack of blue ($\sim$5100-5800 Å) stellar continuum in the approximately NW-SE diagonal direction, due to the presence of a dust lane (see

also Fig. 2.2a), where intense Hα emission (red; see also Fig. 2.2d), residing at redder wavelength, is observed, which indicates ongoing star formation activity. [O III] (green) shows a different morphology, being prominent in two elongated clumpy, roughly conical regions to the NE and SW of the center (see also Fig. 2.2c), approximately in the direction of the jet. This emission might be triggered either by the energetic AGN ionizing photons or by shock-excitation of the gas due to the jet. This is further investigated with spatially-resolved BPT diagrams and shock models in Mingozzi et al. (2018).

Fig. 2.3a displays the stellar velocity map (subtracted by the systemic velocity of the galaxy, i.e. 547 km s^{-1}), where two different components can be noticed. First, a clear thin diagonal lane blueshifted to the left and redshifted to the right with velocities $\lesssim |\pm 150|$ km s^{-1}, following the dust obscured region (see Fig. 2.2a), indicative of a rotating edge-on disk of stars. Second, a larger-scale field decentered to the N having slower velocities ($\lesssim |\pm 70|$ km s^{-1}), blueshifted velocities to the NE of the map and redshifted to the SW, likely associated to the spheroidal component of the galaxy (white light in Fig. 2.2a). The two different stellar kinematic fields then seem to be associated to the two different characteristic components of this galaxy, the edge-on disk and the large spheroid, resulting from the two progenitors, a spiral and an elliptical early-type galaxy, which merged and gave rise to Centaurus A as we see it today. The [O III] and Hα gas velocity maps (Figs. 2.3b and 2.3c) show, first of all, a thick lane having redshifted velocities to the NW and blueshifted to the SE, tracing the rotation of the gaseous, dusty thick disk (compare with its morphology in Fig. 2.2a). Interestingly, this is much thicker and also decentered compared to the stellar rotating disk. There is in fact a strong misalignment between stars and gas in Centaurus A (e.g. Morganti 2010). For this reason, in the above maps we report simply the velocity of the fitted emission lines subtracted by the systemic velocity of the galaxy, differently from the other galaxies presented in the following where we instead subtract spaxel-by-spaxel the stellar rotational velocity field from that of gas to isolate non-rotational motions of the gas. Besides the rotation in the disk, the ionized gas velocity maps show another distinctive bipolar feature to the NW and SE of the center extended over ~25″ (~450 pc) per side, in the direction of the jet and cospatial with the bipolar [O III] emission in Figs. 2.2b and 2.2c. This feature has blueshifted and redshifted velocities on both sides and clearly emerges also in the W70 linewidth maps in Figs. 2.3d and 2.3e (with values up to W70 ~ 500 km s^{-1}). The presence of such enhanced linewidths and peculiar velocities perpendicular to the rotating disk point to an outflow of ionized gas, possibly mechanically swept up by the jet, which is aligned in the same direction, or accelerated by the AGN radiation. We note that in the kinematic maps the outflowing feature is much more prominent in [O III] than in Hα, indicating that in correspondence to this region [O III] line profiles are dominated by the material in outflow, while Hα is more sensitive to the gas in the disk, thus pointing to a more energetic ionizing mechanism in the outflow than in the disk, i.e. either the AGN radiation and/or shocks.
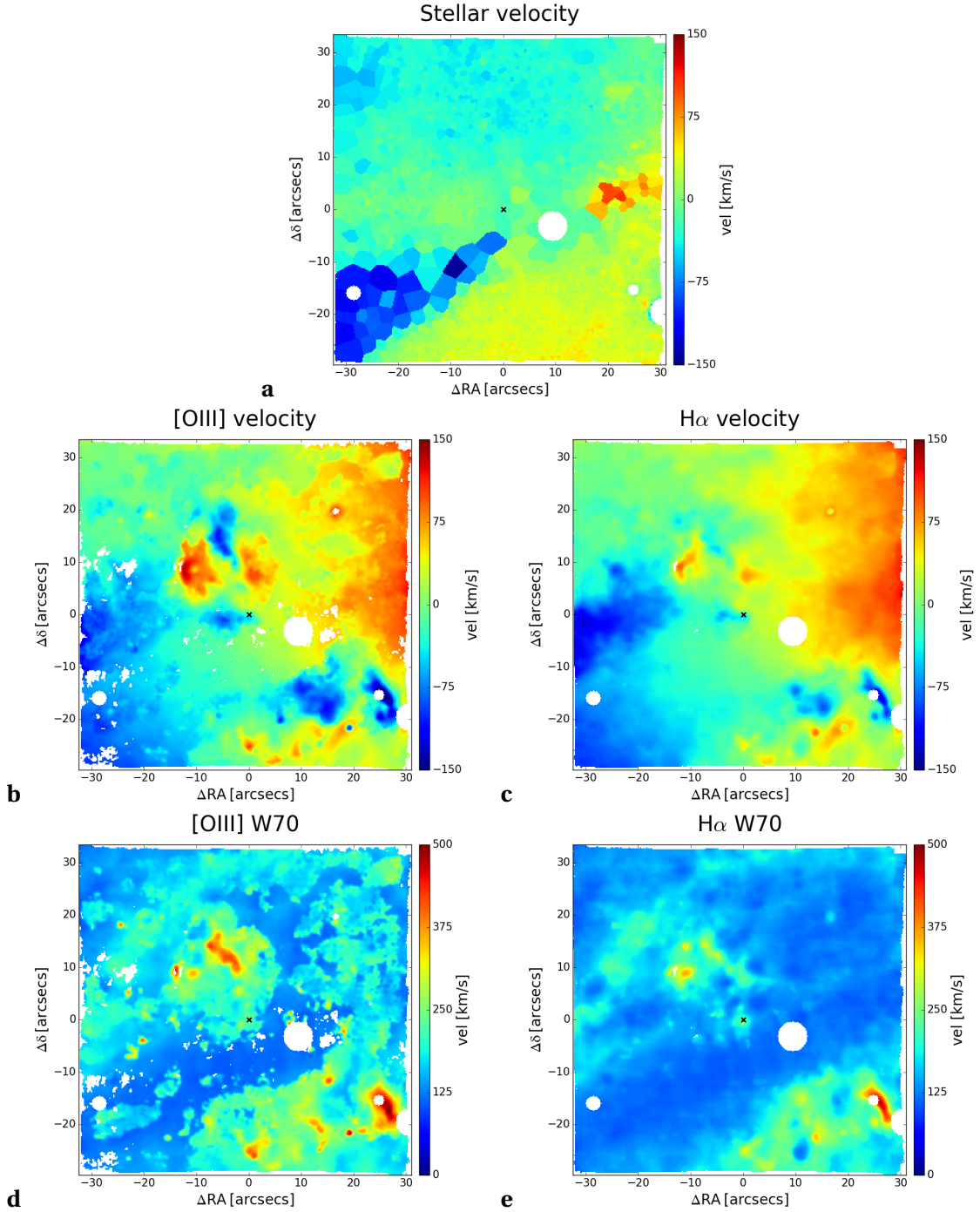
Fig. 2.3: Centaurus A. **(a)** Stellar velocity map (with respect to the systemic velocity of the galaxy), from the shift of the stellar absorption lines obtained from the fit of the stellar continuum carried out on the Voronoi-binned data cube. **(b)** [O III] and **(c)** Hα velocity maps with respect to the systemic velocity. For all the other galaxies presented, the emission line velocities are instead subtracted spaxel-by-spaxel by the stellar velocity to isolate non-rotational motions from the rotational ones in the disk. However, we have not done so in this case, as the kinematics of the stellar disk of Centaurus A is completely different from that of its gaseous disk, as can be seen in the above maps. The emission-line velocities are the 1st-order moments of the total line profile resulting from the fit of the star-subtracted smoothed (with 1 spaxel-σ Gaussian kernel) data cube. **(d)** [O iii] and **(e)** Hα W70 maps, i.e difference between the 85th-percentile and 15th-percentile velocities of the fitted line profile. All the maps have been re-smoothed with a Gaussian kernel having σ = 1 spaxel (except the stellar velocity map), for a better visual output, and a signal-to-noise cut of 3 has been applied.

2.4.2 Circinus

Circinus is a nearby gas-rich spiral ($D \sim 4.2$ Mpc, $1'' \sim 20$ pc) and a prototypical Seyfert 2 galaxy, hosting a highly obscured AGN in X-rays (Matt et al. 2000) and showing a prominent one-sided kpc-scale [O III] cone in optical to the NW of the nucleus (e.g. Marconi et al. 1994, Veilleux et al. 2003, Sharp & Bland-Hawthorn 2010) and different coronal lines in optical and IR spectra, indicating a high ionization level and complex ionization structure (Oliva et al. 1994, Moorwood et al. 1996b, Lutz et al. 2002). It also hosts starburst activity in a circumnuclear ring (e.g. Marconi et al. 1994, Wilson et al. 2000) dominating the IR emission (Matt et al. 2000). The ionization cone shows evidence of an ionized outflow (e.g. Veilleux & Bland-Hawthorn 1997). A dusty, molecular nuclear outflow is found from maser emission (Greenhill et al. 2003), along with polar MIR emission from dust (Asmus et al. 2016, Stalevski et al. 2017), both broadly consistent with the direction of the large-scale ionization cone. The presence of a large-scale molecular outflow in the same direction is suggested from ALMA CO observations (Zschaechner et al. 2016).

Figs. 2.4 and 2.5 display our MUSE flux and kinematic maps for Circinus, respectively. The FOV of our maps, covering the central $\sim 1.3 \times 1.3$ kpc^2 of the galaxy, is reported in the larger-scale composite image in Fig. 2.4a. In the three-color image in Fig. 2.4b we report the bluer part (~ 5100-5800 Å) of the stellar continuum (blue), the Hα (red) and the [O III] emission (green), which are also displayed separately in Figs. 2.4c and 2.4d. Since Circinus is low on the Galactic plane, we had to mask a great number of foreground stars (circular regions in the maps) which were disturbing the spectral analysis. [O III] traces the prominent wide-angle ionization cone, which extends out to the edge of the FOV, ~ 850 pc away from the nucleus. The deepness and spatial resolution of MUSE data allow us to reveal the fine structure of the clumpy [O III] cone, which exhibits clumpy structures and strong emission in its central part, along it axis, and smoother and fainter emission at its edges. Hα dominates in the prominent starburst ring surrounding the nucleus, encircled by a thick dust lane from W to N clockwise (see also Fig. 2.4a), which probably conceals the opposite ionization cone behind the disk.

Fig. 2.5a displays the stellar velocity field, which traces the rotation of the stars in the disk. We report the velocity maps of the emission lines spaxel-by-spaxel the stellar velocity, in order to isolate non-rotational motions of the gas in excess to the rotational field traced by the stars. The [O III] velocity map exhibits a peculiar structure in the cone, with blueshifted velocities at the edges of the cone and redshifted in the middle. Such kinematic structure might suggest a hollow conical outflow that intercepts the plane of the sky and whose axis points towards our "side" of the sky, such that the edges appear as blueshifted while along the axis our line of sight penetrates inside the hollow cone thus reaching the receding face of the cone. We investigate this possibility for the similar case of NGC 4945 in Sect. 2.5. Still, as noted by Sharp & Bland-Hawthorn (2010), the [O III] flux map indicates limb darkening rather than the limb brightening we would expect in the case of an ideal hollow conical geometry, suggesting significant emis-
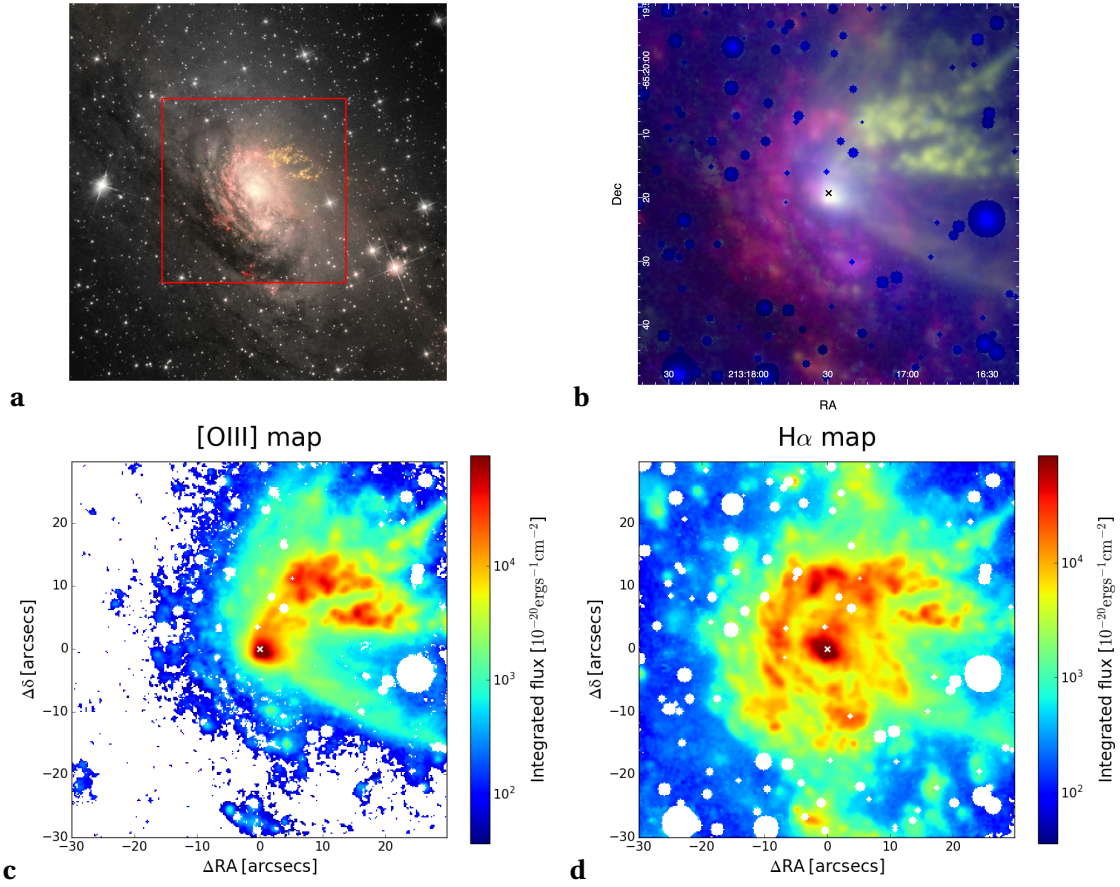
Fig. 2.4: Circinus. **(a)** Colour image combining Hubble Space Telescope WFPC2 F606W+F814W (stellar continuum; gray), F656N (Hα; red) and F502N ([O III]; green) filters; credit: J. Schmidt licensed under CC BY 2.0. The side of our MUSE maps FOV (red box) spans ~1.3 kpc. Same as in Fig. 2.2 for **(b)**, **(c)** and **(d)**.

sion from gas within the cone. Detailed kinematic modelling taking into account the observed distribution and anisotropies of the gas would be required to identify which 3D structure of the outflow is more representative of reality. Enhanced linewidths with a clumpy morphology are observed througout the whole cone in both in [O III] and Hα (Figs. 2.5d and 2.5e). The stellar velocity-subtracted Hα velocity map shows the same kinematic structure of the cone observed in [O III] though with lower absolute values of the velocity. Besides the cone, the map shows a blueshifted excess in the upper-left part of the FOV and a redshifted excess in the lower-right part, aligned with the direction of rotation of the stars (see Fig. 2.5a), thus indicating that gas in the disk rotates faster than stars.
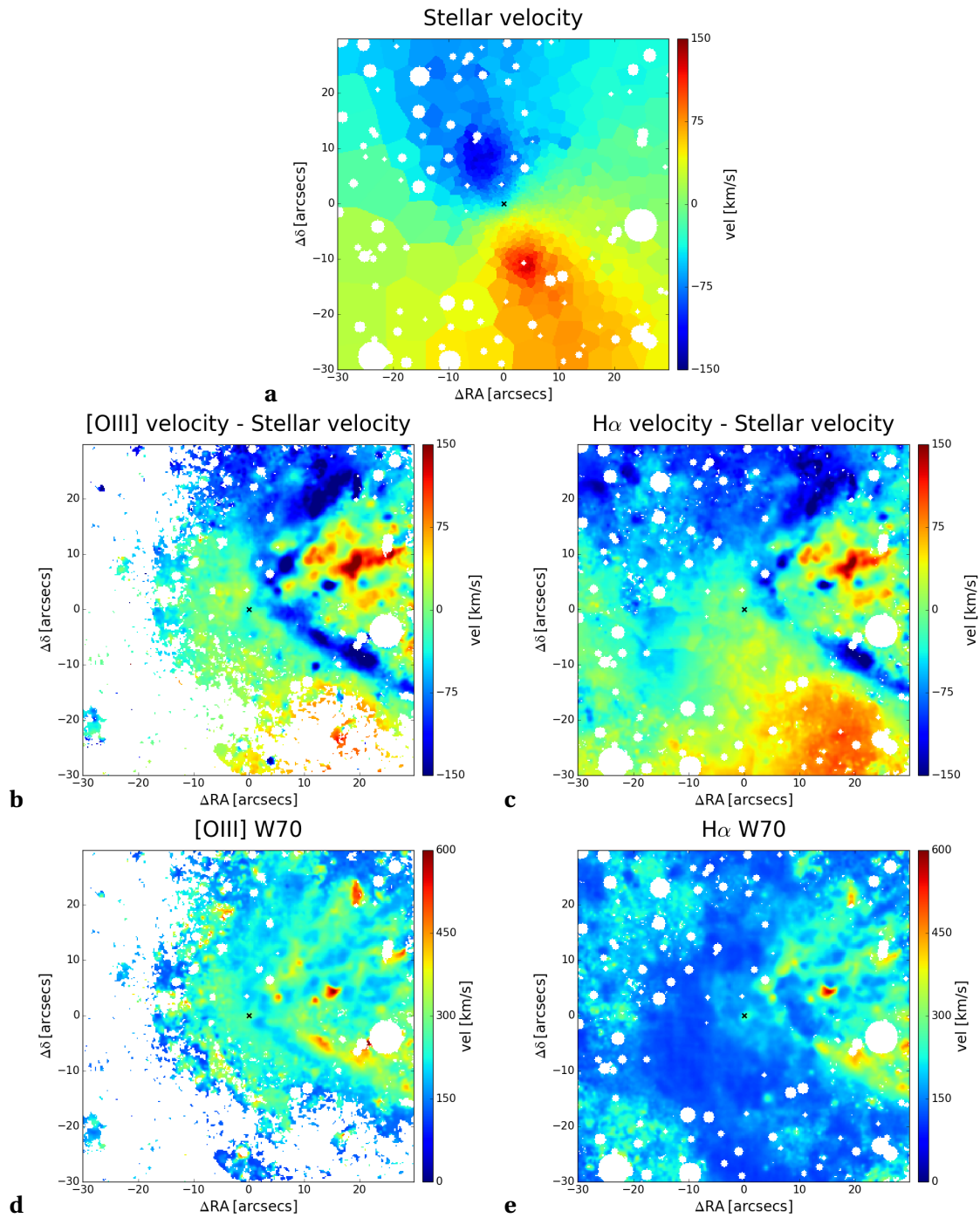
Fig. 2.5: Circinus. Same as in Fig. 2.3.

2.4.3 IC 5063

IC 5063 is an S0 early-type galaxy located at a distance of ~46 Mpc from Earth ($1''$ ~ 220 pc). The galaxy is gas rich and hosts a large-scale, regularly rotating gas disk (Bergeron et al. 1983, Morganti et al. 1998, Morganti et al. 2015). The properties of the galaxy suggest that it may be the result of a recent merger between an early-type elliptical or bulge-dominated S0 and a small gas-rich spiral (Colina et al. 1991). An extended (~20 kpc) [O III]-dominated double ionization cone with an 'X' morphology is observed (Colina et al. 1991), ubiquitously dominated by photoionization from the AGN (Sharp & Bland-Hawthorn 2010). IC 5063 hosts a radio jet limited to the inner ~1 kpc of the galaxy along its major axis, which appears to drive an outflow of neutral atomic (Morganti et al. 1998, Oosterloo et al. 2000), molecular (Morganti et al. 2013, Tadhunter et al. 2014, Morganti et al. 2015, Dasyra et al. 2016, Oosterloo et al. 2017) and ionized gas (Morganti et al. 2007, Dasyra et al. 2015, Congiu et al. 2017) on the same scales. Elongated soft X-ray emission is observed, cospatial with small-scale [OIII] emission, in the central few arcsec on the same scale and direction of the radio jet (Gómez-Guijarro et al. 2017).

Figs. 2.6 and 2.7 display our MUSE flux and kinematic maps for IC 5063, respectively. The FOV of our MUSE flux maps (red box in Fig. 2.6a) covers a large fraction of the galaxy, ~14×14 kpc^2, being IC 5063 quite distant from Earth (~46 Mpc). The three-color image in Fig. 2.6b shows the large-scale 'X'-shaped AGN ionization cone prominent in [O III], extending up to ~10 kpc per side along the galaxy major axis (also Fig. 2.6c). The shape is not actually that of an 'X', since in the NW cone a third definite lane is present between the other two. The strongest emission, both in [O III] and Hα, comes from the nucleus and from the two lobes few arcsec to the E and W of the nucleus (~500 pc per side), consistent with the location of the radio and X-ray lobes. Intense Hα emission is observed from an elongated clumpy lane to the S of the nucleus parallel to the galaxy major axis, indicating ongoing star formation.

The stellar velocity map (Fig. 2.7a) traces the rotation of the stars in the disk. The stellar-velocity subtracted [O III] and Hα maps (Figs. 2.7b and 2.7c) are complicated and their interpretation is not trivial. They show extended conical blueshifted and redshifted emission along the major axis to the NW and SE of the nucleus, respectively, spanning the whole extension of the ionization cones. At first inspection they would suggest the presence of a biconical galactic scale outflow in the ionization cones. However, except for the central few arcsec and some isolated lanes in the NW-SE direction, we do not detect double-peaked profiles indicating a separate outflow kinematic component, as shown by the fact that the linewidths are not enhanced in the two cones in the NW and SE direction (Figs. 2.7d and 2.7e). So, unless all the gas in the disk is in outflow, which seems unlikely, there must be another explanation. The other option might be that the gas is rotating faster than the stars (as observed in the case of Circinus, see Sect. 2.4.2), leaving, after the subtraction of the stellar velocity, the blueshifted and redshifted residuals that we observe. However, there are large inhomogeneities in the residual field (for
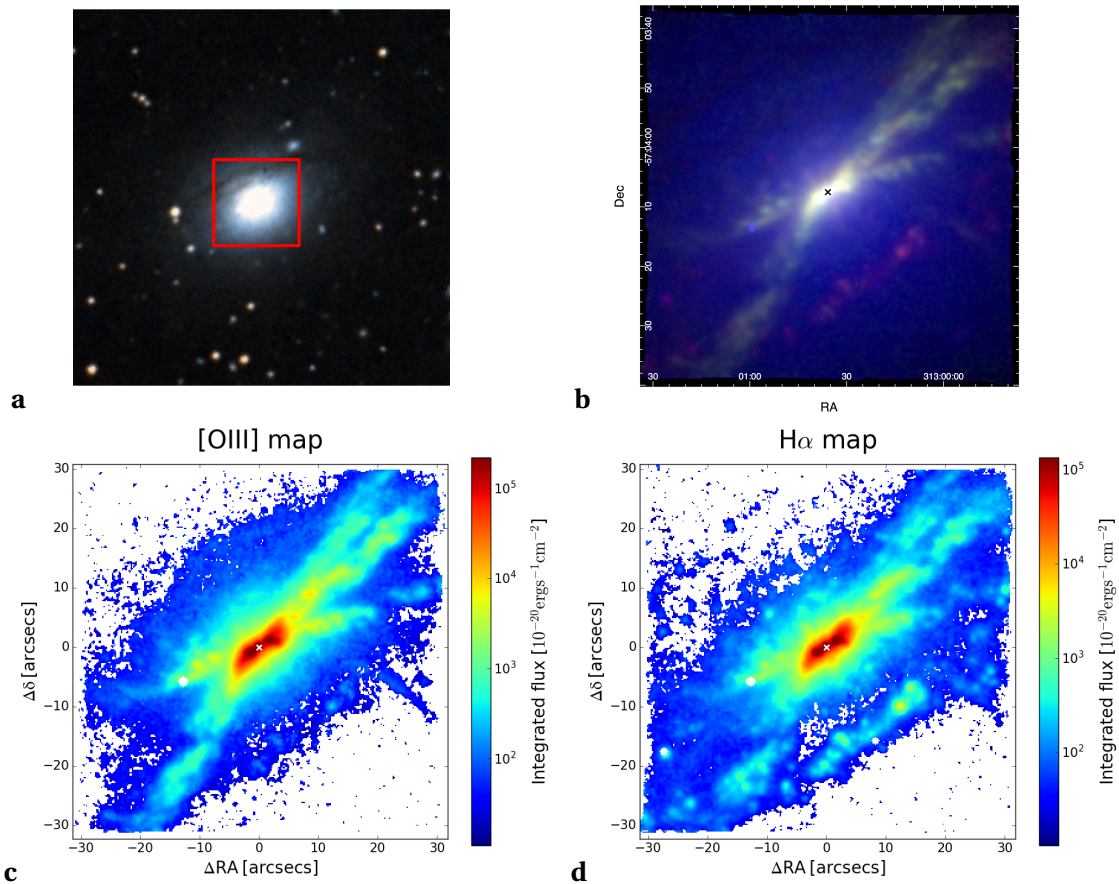
Fig. 2.6: IC 5063. **(a)** DSS colored image of IC 5063 from Digitized Sky Survey - STScI/NASA, Colored & Healpixed by CDS. The side of our MUSE maps FOV (red box) spans ~14 kpc. Same as in Fig. 2.2 for **(b)**, **(c)** and **(d)**.

example, the large green regions at almost zero-velocity in the NW cone or the extended thin lane in the right part of the FOV having blueshifted velocities), which are not expected if the gas is in simple regular rotation. The origin of the kinematics of the gas along the major axis is thus not clear.

Another intriguing feature emerges by inspecting the linewidth maps (Figs. 2.7d and 2.7e). A double conical region of enhanced linewidth, up to ~800 km s^{-1} at its center, spans several kpc along the galaxy minor axis, in the direction perpendicular to the AGN ionization cone and to the smaller-scale radio jet, X-ray emission and molecular outflow. This feature might be associated to largely turbulent or outflowing motions generated laterally in the disk by the jet in its expansion. Modelling of the jet expansion through the gas is needed to investigate the nature of this extended large linewidths. Finally, a region of enhanced Hα linewidths is present also in the top-right corner of the FOV, due to a very large plateau at the base the Hα line profile, whose physical origin is not clear.
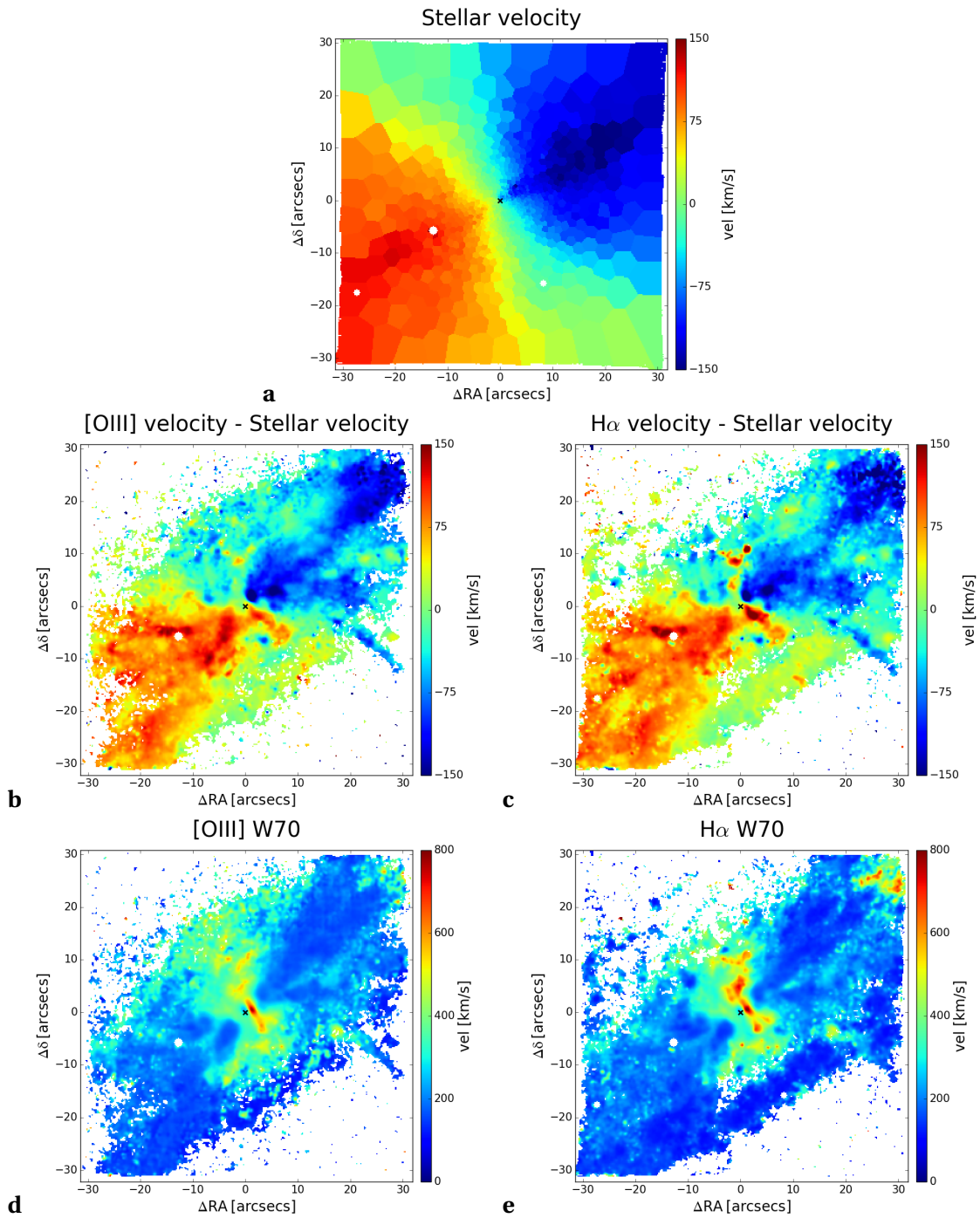
Fig. 2.7: IC 5063. Same as in Fig. 2.3.

2.4.4 NGC 1068

NGC 1068, located at a distance of ~10.5 Mpc ($1'' \sim 51$ pc), is an archetypal Seyfert 2 galaxy. The galaxy also exhibits powerful starburst activity, mainly concentrated in a prominent starburst ring of ~1-1.5 kpc radius (e.g. Schinnerer et al. 2000, García-Burillo et al. 2014), elongated in the NE-SW direction and connected by a stellar bar to a smaller circumnuclear disk in the central ~350 pc (García-Burillo et al. 2014).

NGC 1068 hosts a radio jet spanning up to ~1 kpc in the NE-SW direction (e.g. Gallimore et al. 1996, Bland-Hawthorn et al. 1997). The jet and the AGN ionization cones are inclined at ~45° to the plane of the disk, such that the AGN radiation field directly illuminates the disk (e.g. Cecil et al. 1990, Gallimore et al. 1994). There is clear evidence of an outflow in the same direction in both the ionised (e.g. Axon et al. 1997, Cecil et al. 2002, Barbosa et al. 2014) and molecular gas (García-Burillo et al. 2014, Gallimore et al. 2016), possibly driven by the radio jet intercepting the disk.

Figs. 2.8 and 2.9 display our MUSE flux and kinematic maps for NGC 1068, respectively. Fig. 2.8a shows on a large-scale image of the entire galaxy the FOV of our MUSE map (red box), covering the central ~3.3×3.3 kpc^2. Our three-color image in Fig. 2.8b displays the Hα emission (red) following the spiral pattern of the galaxy (compare with the large-scale structure in Fig. 2.8a) and its dusty features, visible from the ~5100-5800 Å stellar continuum (in blue). The Hα spiral features surrounding the center form a large star-forming ring. [O III] emission (green) is instead prominent in a bright inner cone and in a fainter elongated region extending to the NE from the inner cone out to large scales (~4.5 kpc). Its shape follows a spiralling structure spatially anticorrelated with that of Hα. A fainter, [O III] counter spiralling structure is also observed to the SW far from the center. These bipolar [O III] emissions could be explained with the AGN ionization cones pointing above (to the NE) and below the disk (to the SW) and possibly intercepting it in part as well.

The stellar velocity map (Fig. 2.9a) presents a really distorted and twisted pattern, indicating a non perfectly circular motion, likely associated to the presence of the bar. The stellar velocity-subtracted [O III] and Hα velocity maps (Figs. 2.9b and 2.9c) exhibit ubiquitous and really complicated velocity excesses. While some of them are present in both lines, as the extended spiral blueshifted feature to the NE and the redshifted one to the W, going from N to S, some others are present only in [O III]. These are the extended blueshifted emission to the W of the center, the blueshifted spiral feature to the N and the extended spiral lane going from S of the center to the NE. Strong velocity excesses, both blueshifted and redshifted, are present in both line maps close to the nucleus in the NE-SW direction, aligned with the jet, possibly tracing a jet-induced ionized outflow. It is however hard to guess from a simple visual inspection of the maps if all the velocity excesses with respect to stellar velocity present in the maps could be due to non-circular motions of the gas in the disk, inflows along the spiral arms or outflows
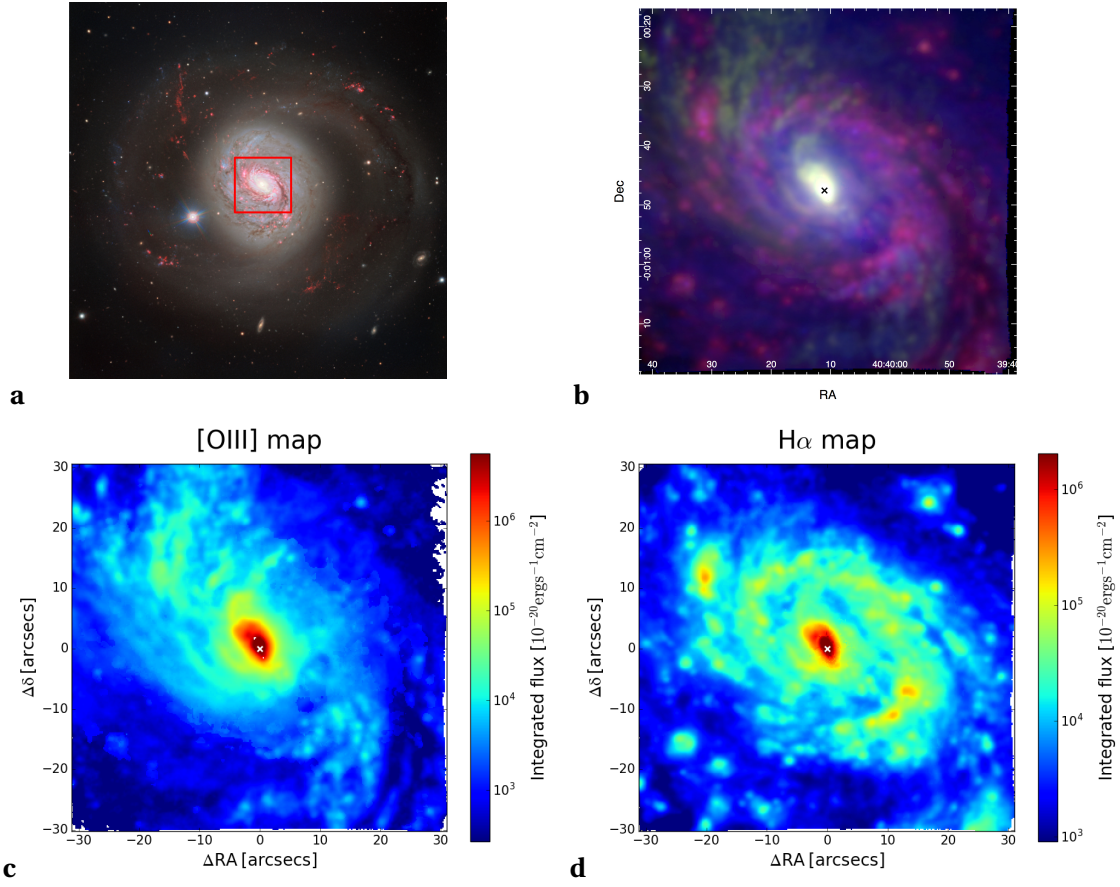
a

b

c

d

Fig. 2.8: NGC 1068. **(a)** Four-color image of NGC 1068 from FORS2 at Very Large Telescope, where emission in b, v and R filters is reported in blue, green and orange, respectively, and Hα one in red; credit: ESO. The side of our MUSE maps FOV (red box) spans ~3.3 kpc. Same as in Fig. 2.2 for **(b)**, **(c)** and **(d)**.

within or outside the disk.

The linewidht maps show and interesting behavior. The Hα linewidth (Fig. 2.9e) is en-hanced in a region slightly elongated in the NE-SW direction spanning ~1 kpc around the nucleus and reaching values above 1000 km s^{-1} in an inner biconical structure, still directed towards NE and SW, possibly associated with an inner ionized outflow pushed by the jet. In [O III] the linewidth enhancement is much more extended than in Hα and mainly elongated to the NW and SE of the center, perpendicularly to the radio jet and the [O III] ionization cone.
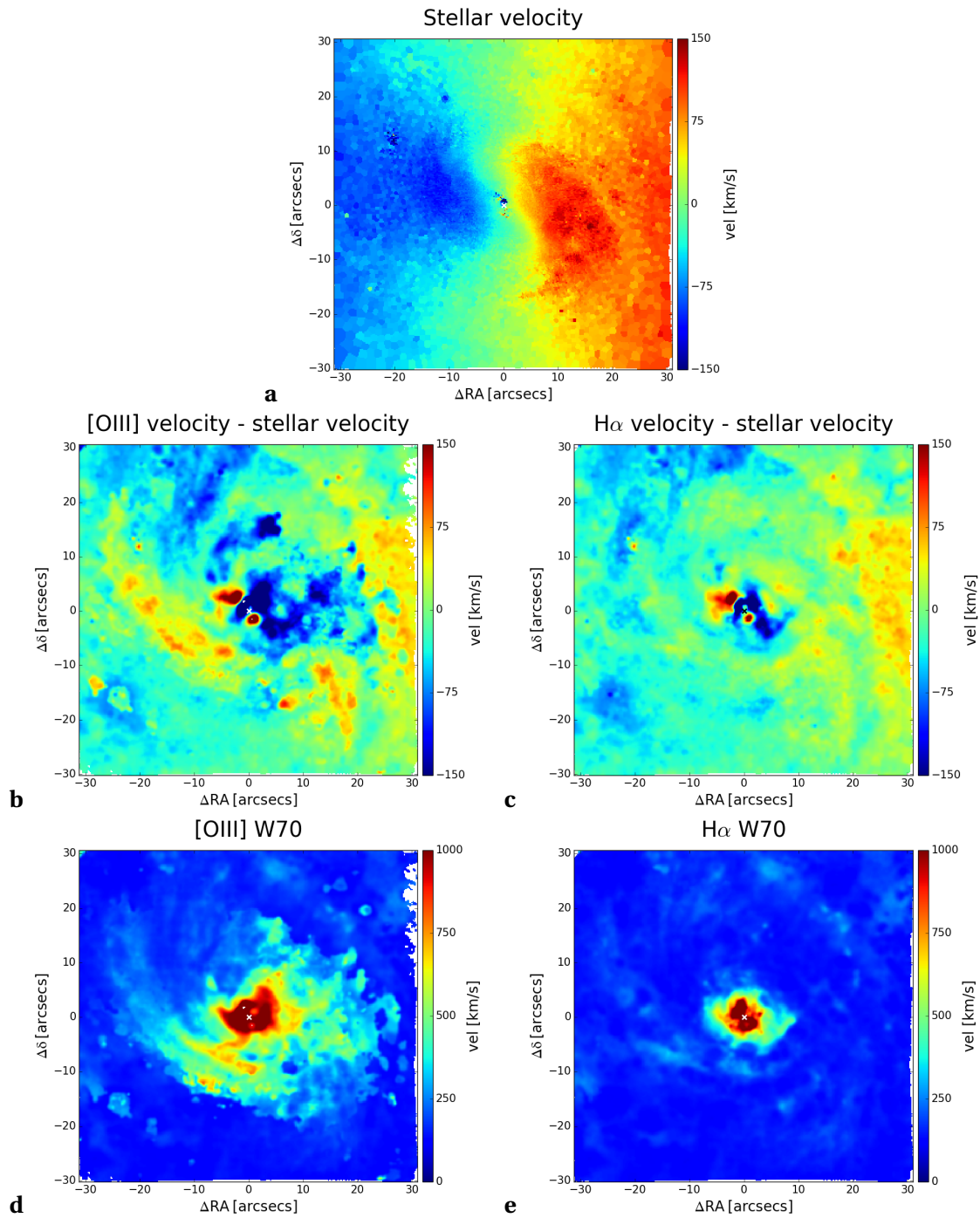
Fig. 2.9: NGC 1068. Same as in Fig. 2.3.

2.4.5 NGC 1365

NGC 1365 is a barred spiral galaxy, located at a distance of 17.3 Mpc ($1''$ ~ 84 pc) and classified as Seyfert 1.8 (Véron-Cetty & Véron 2006). It hosts a prominent star-forming ring around the nucleus, producing the bulk of star formation (e.g. Kristen et al. 1997, Forbes & Norris 1998, Stevens et al. 1999, Alonso-Herrero et al. 2012). [O III] extended (~1 kpc) conical emission is observed to the SE of the nucleus (e.g. Edmunds et al. 1988, Storchi-Bergmann & Bonatto 1991, Kristen et al. 1997) and, much fainter, also to the NW (Veilleux et al. 2003, Sharp & Bland-Hawthorn 2010), with evidence of ionized outflowing material in the direction of the cones (Phillips et al. 1983, Hjelm & Lindblad 1996, Lena et al. 2016). The nucleus exhibits a large variability in X-rays, with highly-ionized blueshifted absorption lines indicating a fast nuclear wind (e.g. Risaliti et al. 2005, Braito et al. 2014).

Figs. 2.10 and 2.11 display our MUSE flux and kinematic maps for NGC 1365, respectively. The barred structure of the galaxy with the two main spiral arms connected to it can be clearly seen in Fig. 2.10a, where we report the FOV of our MUSE maps (red box), covering the central ~5.3×5.3 kpc^2. Two main 'S'-shaped dust lanes are present along the bar, as can be seen in our three-color MUSE map in Fig. 2.10b where ~5100-5800 Å stellar continuum is reported in blue, Hα in red and [O III] in green. Hα follows the dust lanes from NE to SW parallel to the bar direction and dominates in the star-forming ring surrounding the nucleus (see also Fig. 2.10d), while [O III] has a completely different morphology (see also Fig. 2.10c), being prominent in the perpendicular direction in a clumpy double-conical ionization cone extending up to the corners of the FOV (~3.7 kpc per side). The SE cone is brigther than the NW one, especially close to the center where the NW one is obscured, indicating that the SE cone resides above the disk and the NW behind it with respect to the observer.

The stellar velocity field (Fig. 2.11a) is that of a rotating disk, with a slightly twisted shape probably associated with the presence of the bar. The spaxel-by-spaxel stellar-velocity subtracted [O III] velocity map clearly reveals the presence of a biconical outflow extended over several kpc on both sides, in correspondence to the ionization cones. The SE cone has approaching velocities and the NW one has receding velocities, consistently with the SE cone being above the disk and the NW one behind it. The biconical outflow is traced very well also by the linewidth map, both in [O III] and Hα, though it is much more prominent in [O III] than in Hα. The enhanced linewithds are in fact due to the superposition of the two different kinematics components of the gas residing in the outflow and in the disk, respectively, and [O III] line profiles are dominated by the outflow kinematic component while Hα profiles are dominated by the disk one. We note in fact that for this reason also in the stellar velocity-subtracted Hα velocity map the SE blueshifted and NW redshifted outflowing cones are much less prominent than in the [O III] map. However, in the Hα velocity map another feature clearly emerges, a redshifted thick lane and a complementary blueshifted one on the opposite side, oriented
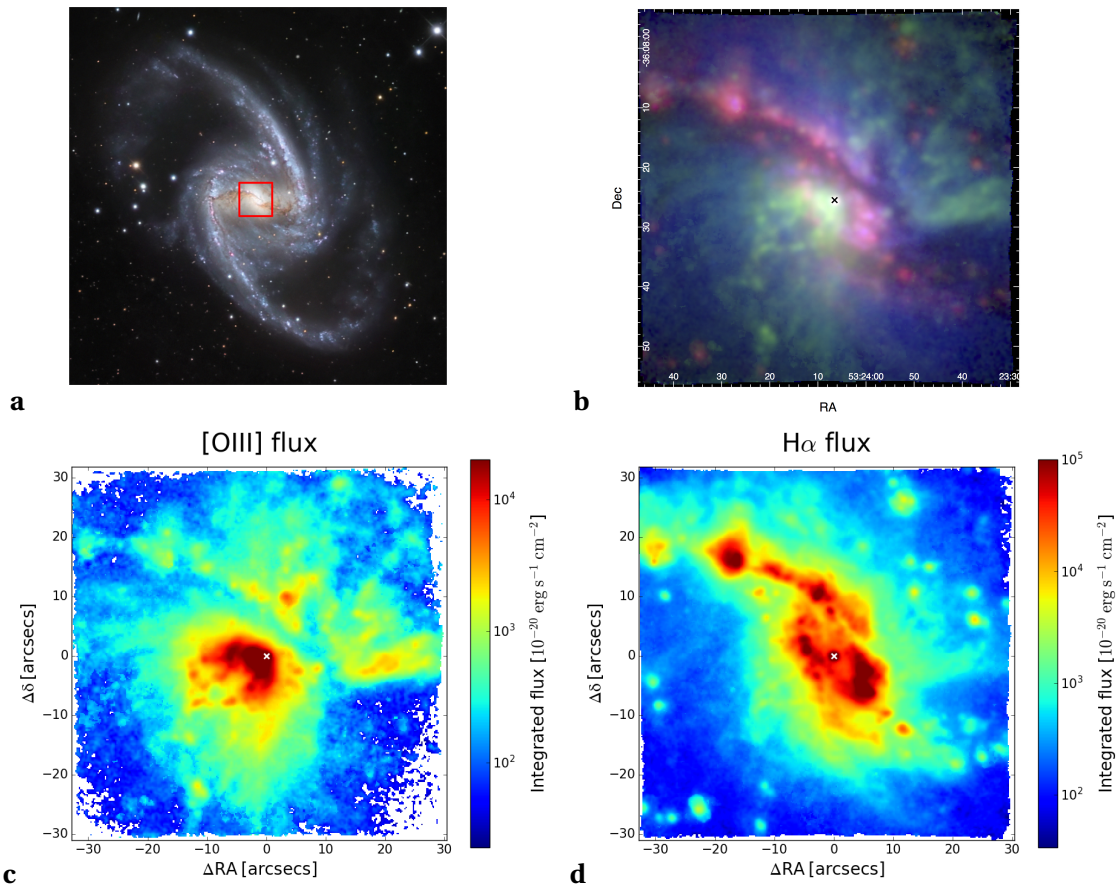
a

b

c

d

Fig. 2.10: NGC 1365. **(a)** Three-color image of NGC 1365 from observations performed through three different filters (B, V, R) with the 1.5-metre Danish telescope at the ESO La Silla Observatory; credit: ESO/IDA/Danish 1.5 m/ R. Gendler, J-E. Ovaldsen, C. Thöne, and C. Feron. The side of our MUSE maps FOV (red box) spans ~5.3 kpc. Same as in Fig. 2.2 for **(b)**, **(c)** and **(d)**.

along the bar. This opposite-velocity lane points to non-circular motions of material taking place along the bar of the galaxy.

An extensive multi-wavelength analysis of the ionized gas in NGC 1365 and of its multi-phase and multi-scale outflow, from the nucleus to galactic scales, is presented in Chapter 3 making use of the MUSE optical data introduced here and of *Chandra* ACIS-S spatially resolved X-ray observations.
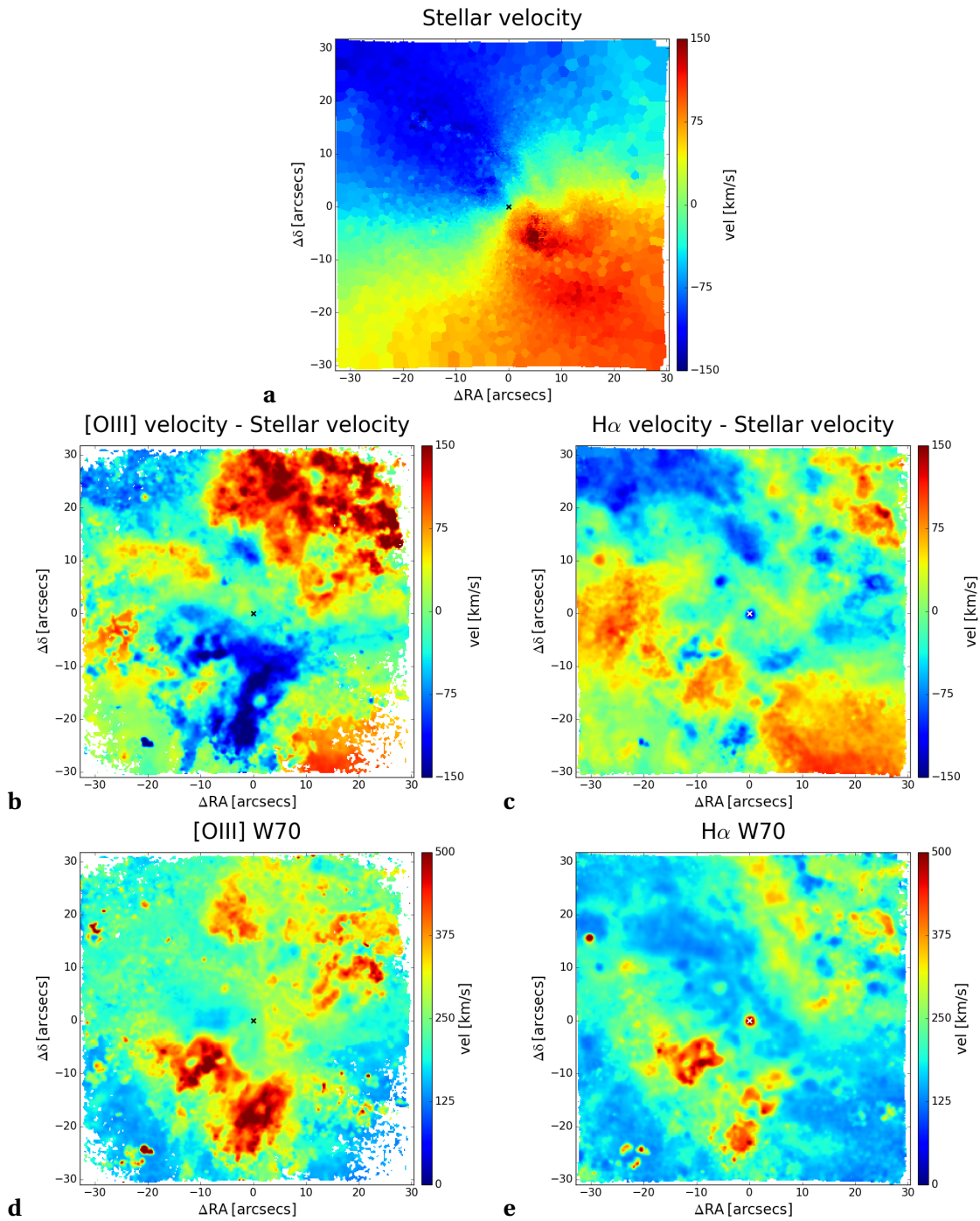
Fig. 2.11: NGC 1365. Same as in Fig. 2.3.

2.4.6   NGC 1386

NGC 1386, located at ~16.4 Mpc from Earth ($1''$ ~ 80 pc), is a Seyfert 2 spiral galaxy. The galaxy disk is highly elongated in the NE-SW direction approximately, having an inclination of ~65° with respect to the line of sight (Lena et al. 2015). Two elongated [O III] emission-line structures are observed over ~$2''$ to the N and S of the nucleus (Ferruit et al. 2000), probably due to the AGN ionizing radiation field intercepting the gas in the disk (Lena et al. 2015). Elongated radio emission, suggestive of a radio jet, is observed S to the nucleus across ~$1''$ (Nagar et al. 1999, Mundell et al. 2009), but an association between this feature and the optical ionization lobe is discarded by Mundell et al. (2009). Both soft and hard X-ray emission is found to be cospatial with the [O III] N-S ionization features (Bianchi et al. 2006, Gómez-Guijarro et al. 2017). Broad emission-line profiles are found in the perpendicular (E-W) direction across ~2-$3''$, suggesting that rotation and/or an outflow is present in this direction (Lena et al. 2015). Blueshifted and redshifted unresolved line profiles are found by Lena et al. (2015) within $1''$, suggestive of a nuclear outflow. Large-scale X-ray emission over a few kpc is observed by Li & Wang (2013) both in the N-S direction with an 'S'-shaped pattern and in the E-W direction.

Figs. 2.12 and 2.13 display our MUSE flux and kinematic maps for NGC 1386, respectively. Our MUSE maps cover the central ~5.1×5.1 kpc^2 of the galaxy disk, whose entire extension is shown in the larger scale image in Fig. 2.12a. In Fig. 2.12b we report our MUSE three-color image. The blue ~5100-5800 Å stellar continuum traces the shape of the disk elongated in the NE-SW direction, with thin dust lanes surrounding the center. A prominent circumnuclear star-forming ring is evident in Hα in red, which is absent in [O III] in green (compare also Figs. 2.12c and 2.12d). [O III] dominates instead in the two ionization lobes spanning ~200-300 pc per side N and S to the nucleus, internal to the star-forming ring. Fainter and clumpy [O III] emission extends further from the two lobes out of the ring towards the SE and NW with an 'S'-shaped pattern. A diffuse faint disk-like emission in the E-W direction is also present within a few arcsec from the nucleus, still on scales smaller than the ring.

The stellar velocity map (Fig. 2.13a) traces the rotation in the disk. Faster symmetric velocities close to the center are probably due to an inner disk aligned with the main one. The stellar-velocity subtracted [O III] and Hα maps show, more prominently in [O III], clumpy blueshifted features W-NW to the nucleus and mostly redshifted (though also blueshifted) E-SE along the minor axis of the galaxy, indicative of outflowing material. Some of this clumpy features can also be seen as faint [O III] emission in Fig. 2.12b. These kinematic features are also present in the linewidth maps (Figs. 2.13d and 2.13e), where high velocities, up to W70 $\gtrsim$ 600 km s^{-1} are observed in an elongated region W and E to the nucleus. The same clumps having excess velocities in the velocity maps have also enhanced linewidths. Moreover, [O III] linewidth map shows an extended bipolar enhancement reaching the borders of the star-forming ring, not present in Hα probably because its line profile is dominated by the rest-frame star-forming ring. We
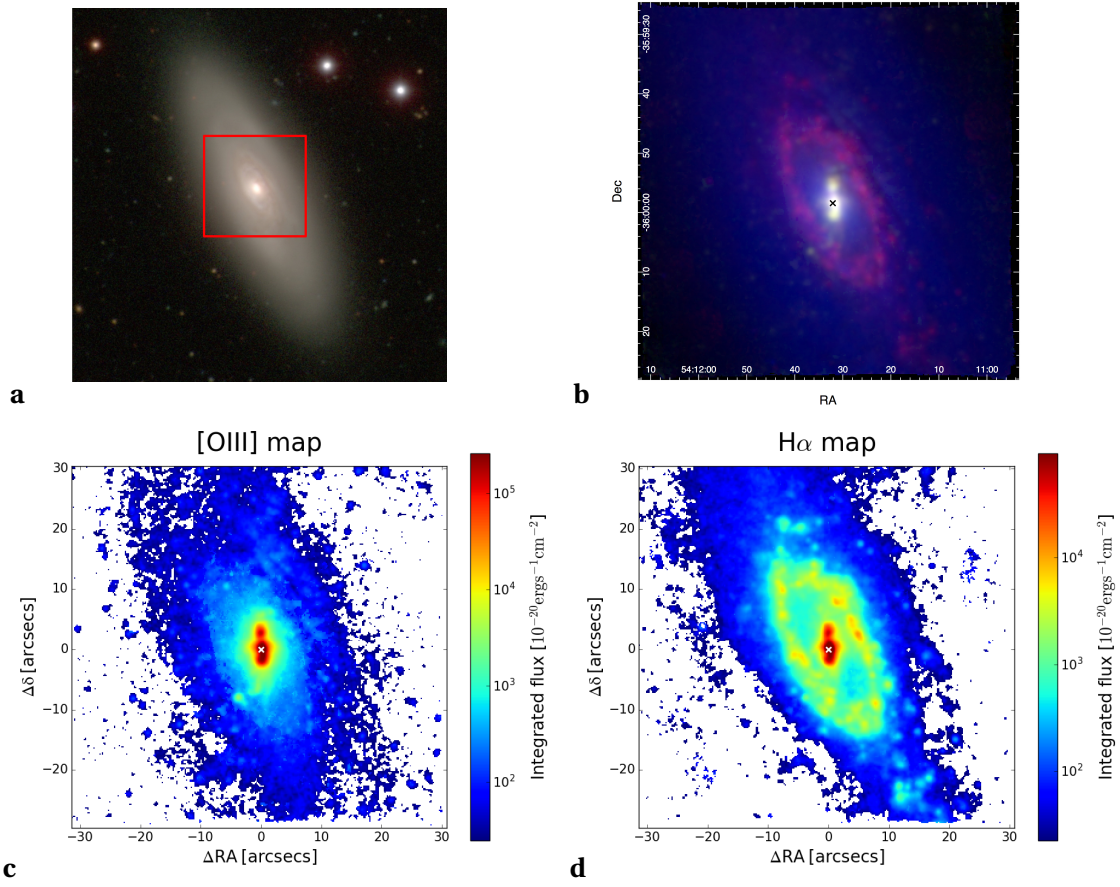
Fig. 2.12: NGC 1386. **(a)** Three-color (blue: B band; green: V band; red: I band) image of NGC 1386 obtained with the 2.5 m du Pont Telescope at Las Campanas Observatory for the Carnegie-Irvine Galaxy Survey (CGS, Ho et al. 2011). The side of our MUSE maps FOV (red box) spans ~5.1 kpc. Same as in Fig. 2.2 for **(b)**, **(c)** and **(d)**.

note that the direction of such kinematic features and enhanced linewidths is roughly perpendicular to both the ionization cone and the putative radio jet (both residing on scales of few arcsec), similarly to what we observe in IC 5063 (see Sect. 2.4.3 and Figs. 2.6a, 2.7d and 2.7e). We also note that the largest and more spatially-defined linewidth enhancement occurs within the star-forming ring while only few isolated clumps are observed outside, which might suggest that the outflowing/turbulent material is low on the disk and impacts the ring when it reaches it, with only few clumps managing to emerge at larger distances. Some minor smooth excesses with respect to stellar rotational motion in the disk ($\lesssim |\pm 50|$ km s^{-1}), following the shape of the disk, can be seen in the Hα stellar-velocity subtracted map in Fig. 2.13c. These are divided in two main spatial components, a redshifted and blueshifted excess tracing a disk shape larger than the star-forming ring, and an opposite velocity excess at the N and S edges of the FOV. These might trace components of the disk rotating at slightly different velocities compared to the stars, the inner part faster, the outer one slower.
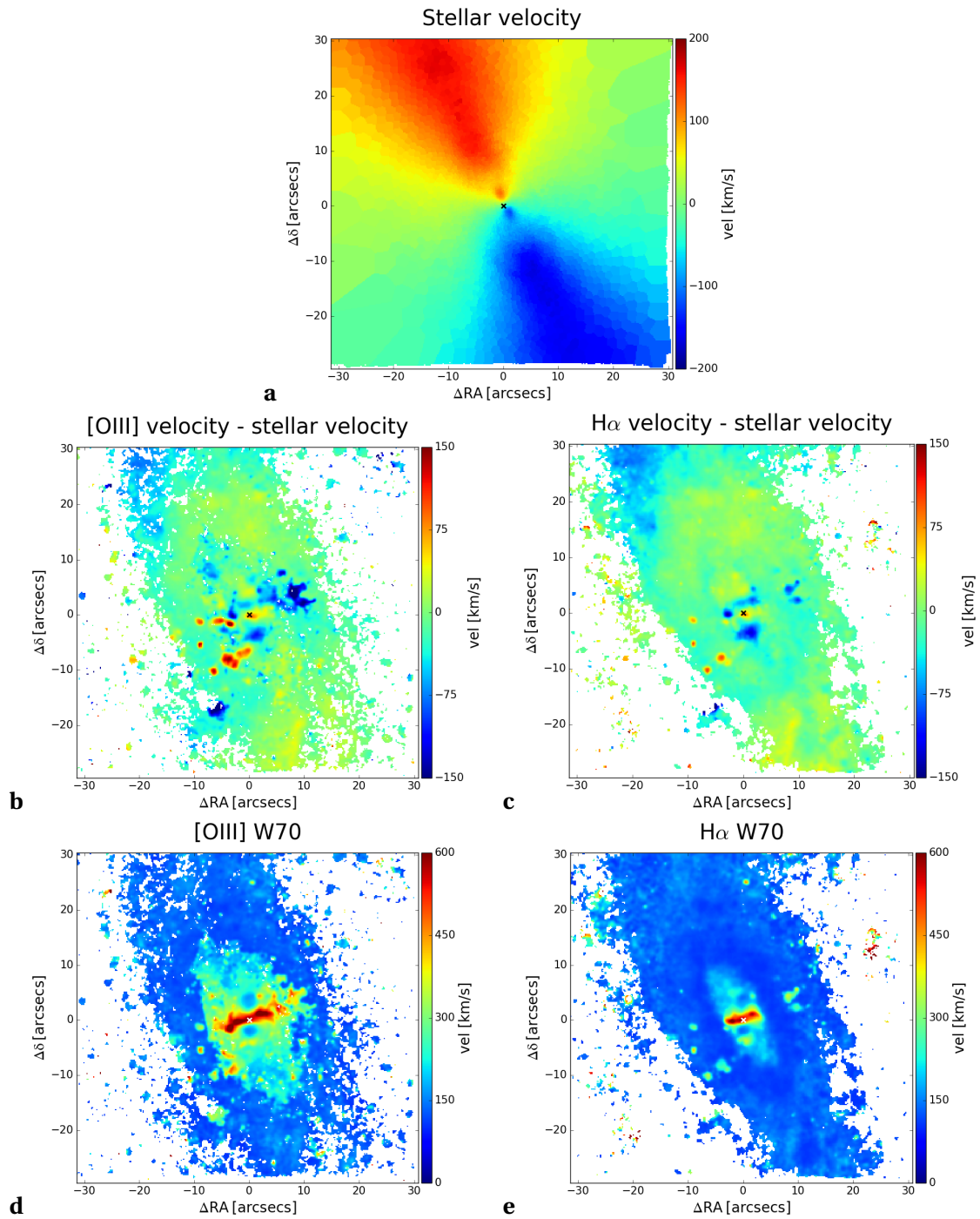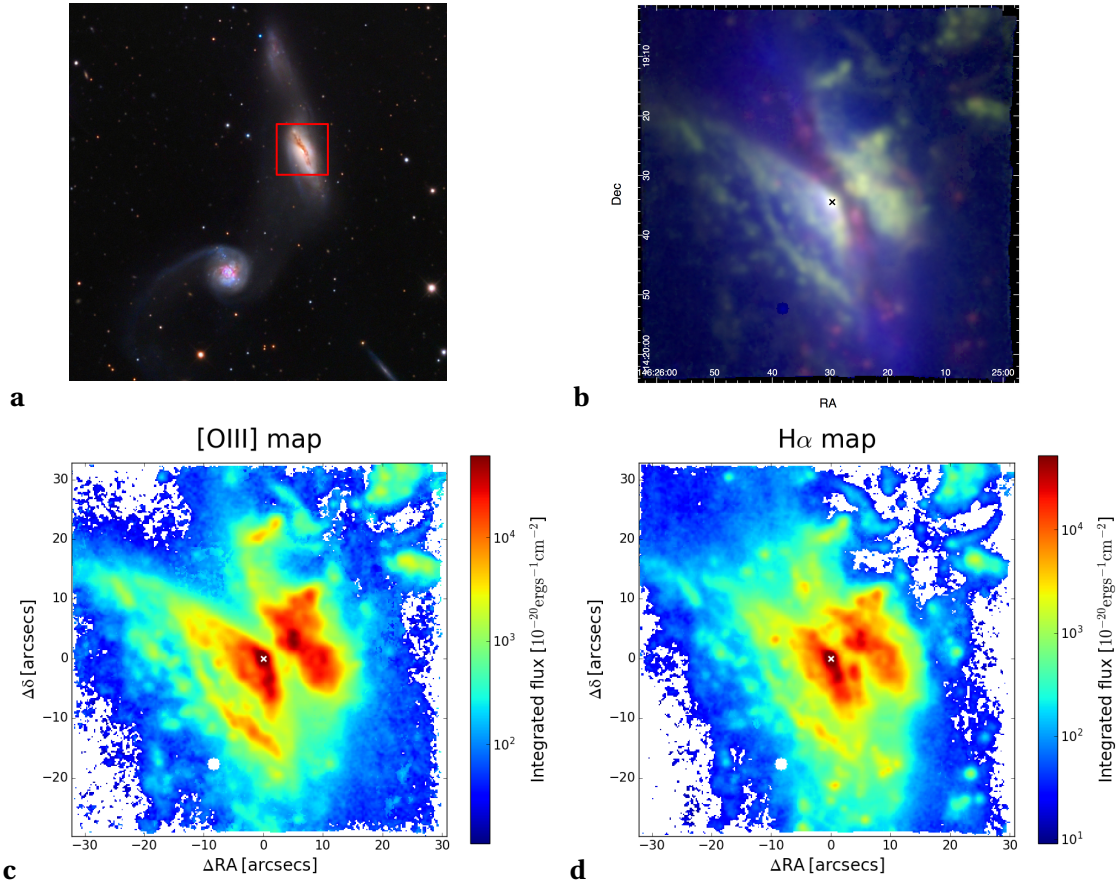
Fig. 2.13: NGC 1386. Same as in Fig. 2.3.

Fig. 2.14: NGC 2992. **(a)** Color composite image of NGC 2992 in L, R, G, B bands from 32-inch Schulman Telescope at Mount Lemmon SkyCenter; credit: Adam Block/Mount Lemmon SkyCenter/University of Arizona. The side of our MUSE maps FOV (red box) spans ~10 kpc. Same as in Fig. 2.2 for **(b)**, **(c)** and **(d)**.

2.4.7 NGC 2992

NGC 2992 is a Seyfert 1.9 spiral galaxy, located at a distance of ~32 Mpc from Earth (1"~150 pc). It is almost edge on, having an inclination angle of i = 70°. Its nucleus, showing broad Hα emission but lack of broad Hβ, is classified as Seyfert 1.9, the classification having changed over the years between 1.5 and 2 (Trippe et al. 2008). NGC 2992 is in interaction with NGC 2993 to the SE, the two galaxies being connected by a H I tidal bridge and showing two tidal tails as a result of the interaction, one to the N of of NGC 2992, the other to the SE of NGC 2993 (Ward et al. 1980). The presence of a prominent dust lane along the major axis of NGC 2992, crossing its nucleus, is known from optical continuum images (Ward et al. 1980). The galaxy presents two wide ionization cones on either side of the disk, having axis perpendicular to it and large opening angles (e.g. Allen et al. 1999). The presence of an extended bipolar outflow roughly in the same direction is inferred from Hα, [O III] and soft X-ray emission (e.g. Colina et al. 1987, Colbert et al. 1996a,b, Veilleux et al. 2001). The outflow is likely driven by the AGN rather than
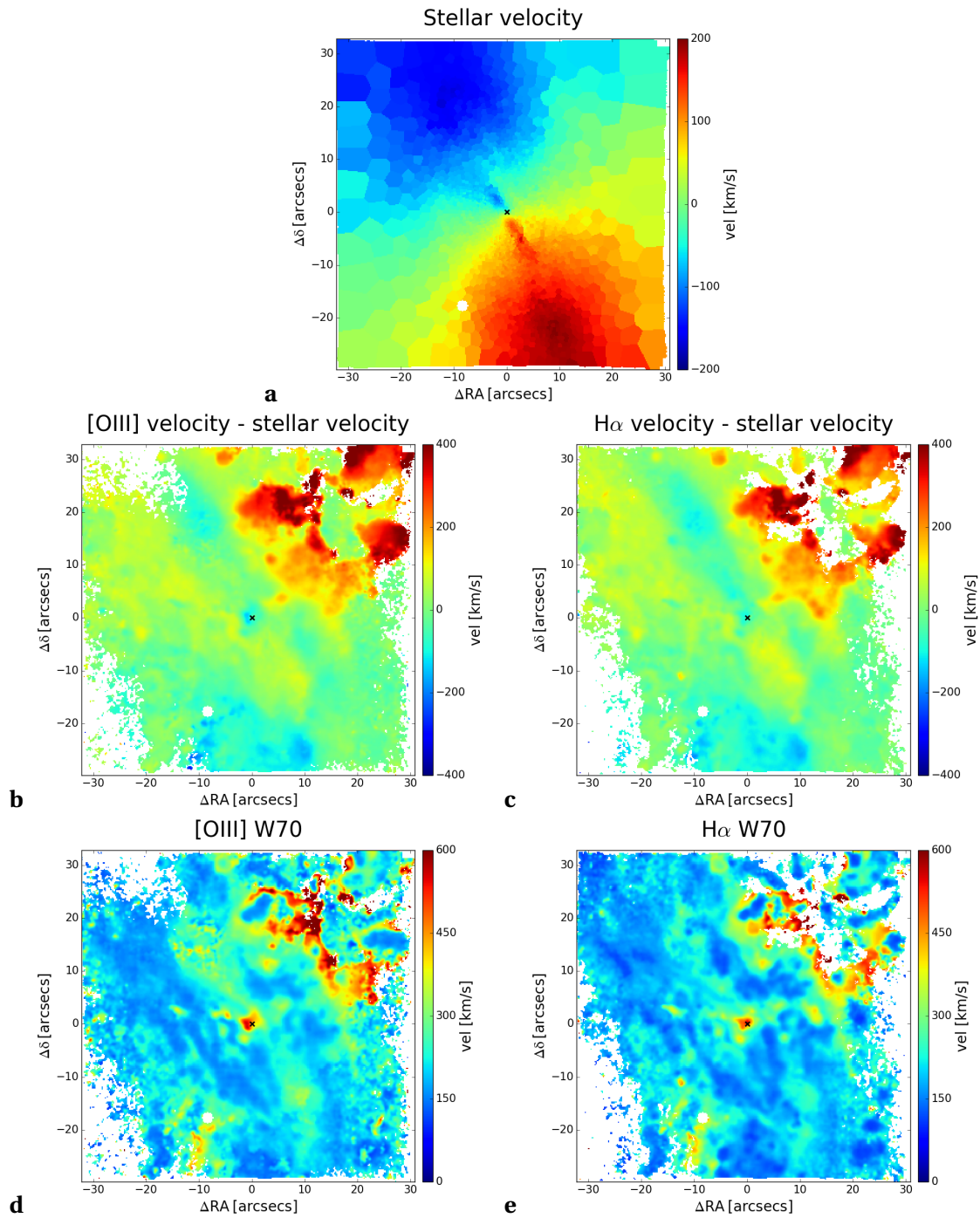
Fig. 2.15: NGC 2992. Same as in Fig. 2.3.

by starburst activity (Friedrich et al. 2010).

Figs. 2.14 and 2.15 display our MUSE flux and kinematic maps for NGC 2992, respectively. The composite image in Fig. 2.14a shows NGC 2992 (top-right) and its companion galaxy NGC 2993 (bottom-left) with which it is interacting. The FOV of our maps (red box) covers the central $\sim$10$\times$10 kpc^2 of NGC 2992. Our three-color MUSE image in Fig. 2.14b shows [O III] emission in green (see also Fig. 2.14c), dominating in double wide-angle ionization cones, Hα in red (also Fig. 2.14d), more prominent in the disk of the galaxy along the dust lane and in some scattered clumps, and the bluer part ($\sim$5100-5800 Å) of the stellar continuum in blue. The SE [O III] cone is well define in shape, with sharp edges, and presents a shell-like structure, having at least two clear shells of more intense emission at different distances from the nucleus. The SE cone is brighter than the NW, especially close to the nucleus, indicating that it resides above the disk, differently from the NW cone which instead emerges from behind the dust lane. The NW cone is less defined in shape compared to the SE one, probably because of the tidal tail due to the interaction with NGC 2993 propagating to the N of NGC 2992 (see Fig. 2.14a), and breaks up in thick and clumpy lanes in the NW part of the FOV.

The stellar kinematics (Fig. 2.15a) traces the large-scale rotation of the disk and elongates towards the center, probably due to an inner thin disk component. The stellar-velocity subtracted ionized gas kinematics (Figs. 2.15b, 2.15c, 2.15d, 2.15e) first clearly reveals receding motions strongly deviating from rotation in the NW part of the FOV (above +400 km s^{-1} and having W70 > 600 km s^{-1}), having a sort of 'X' morphology and corresponding to the features present in [O III] emission (and less evidently also in Hα). These motions may indicate a vast receding outflow with disturbed morphology extending over distances up to $\sim$7 kpc from the nucleus (and maybe above as the features reach the edge of the FOV) or tidally stripped material along the north lane due to the interaction with NGC 2993. Other minor velocity excesses with respect to stellar velocity are present in the maps, either along the disk major axis or far from the center in the SE polar direction, possibly tracing a counter outflow.

2.4.8 NGC 4945

NGC 4945 is an edge-on spiral galaxy, located at a distance of $\sim$3.5 Mpc from Earth (1$''$ $\sim$ 17 pc), making it the closest AGN known. The galaxy disk presents starburst activity and is strongly obscured by dust (e.g. Marconi et al. 2000, Pérez-Beaupuits et al. 2011), the presence of the AGN being revealed only from X-ray observations (e.g. Guainazzi et al. 2000). No clear evidence of AGN ionization of the gas is found from NIR and MIR observations (Marconi et al. 2000, Spoon et al. 2000, Pérez-Beaupuits et al. 2011), indicating that either the AGN UV radiation is completely obscured in all directions or the AGN spectrum is dominated by X-rays and lacks of UV photons. The presence of a conical cavity perpendicular to the disk is found from optical and NIR ionized and molecular emisison lines (Hα+[N II] and H$_2$) by Moorwood et al. (1996a)
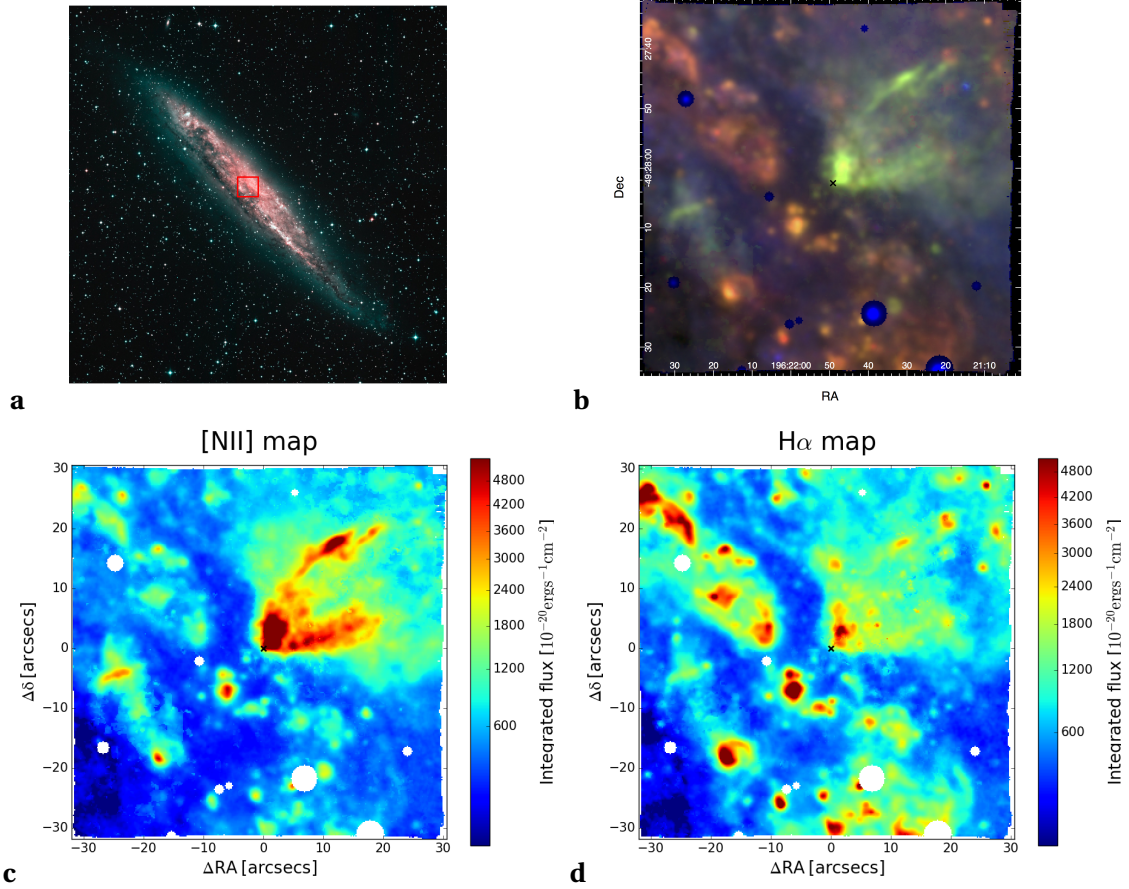
Fig. 2.16: NGC 4945. **(a)** Three-color image of NGC 4945 combining R-narrowband (red), B-band (green) and U-band observations (blue), obtained with the Wide-Field-Imager (WFI) at the MPG/ESO 2.2-m telescope at La Silla; credit: ESO. The side of our MUSE maps FOV (red box) spans ~1.1 kpc. Same as in Fig. 2.2 for **(b)**, **(c)** and **(d)**, with the exception that [N II] is reported in **(b)** in green and in **(c)**, instead of [O III], as [O III] is really faint in this galaxy due to high obscuration, while [N II] is more intense and has an analogous morphology.

and Marconi et al. (2000), who associate it to a starburst wind.

Figs. 2.16 and 2.17 display our MUSE flux and kinematic maps for NGC 4945, respectively. The FOV of our maps covers the very center of this almost-perfectly edge-on galaxy, ~1.1×1.1 kpc^2. In our three-color image in Fig. 2.16a we report the ~5100-5800 Å stellar continuum in blue, [N II] in green (also in Fig. 2.16c) and Hα in red (also in Fig. 2.16d). We have chosen to show [N II], instead of [O III], as it has a much higher signal-to-noise ratio than [O III] and traces the same morphological features, i.e. the bipolar cones perpendicular to the disk. The image shows in fact the presence of a well defined limb-enhanced conical [N II] emission to the NW emerging perpendicular to the dark obscuring dusty features in the disk, where ubiquitous Hα emission is observed. A much dimmer, partial counter cone comes out of the dust about 20″ to the SE from the base of the NW one.
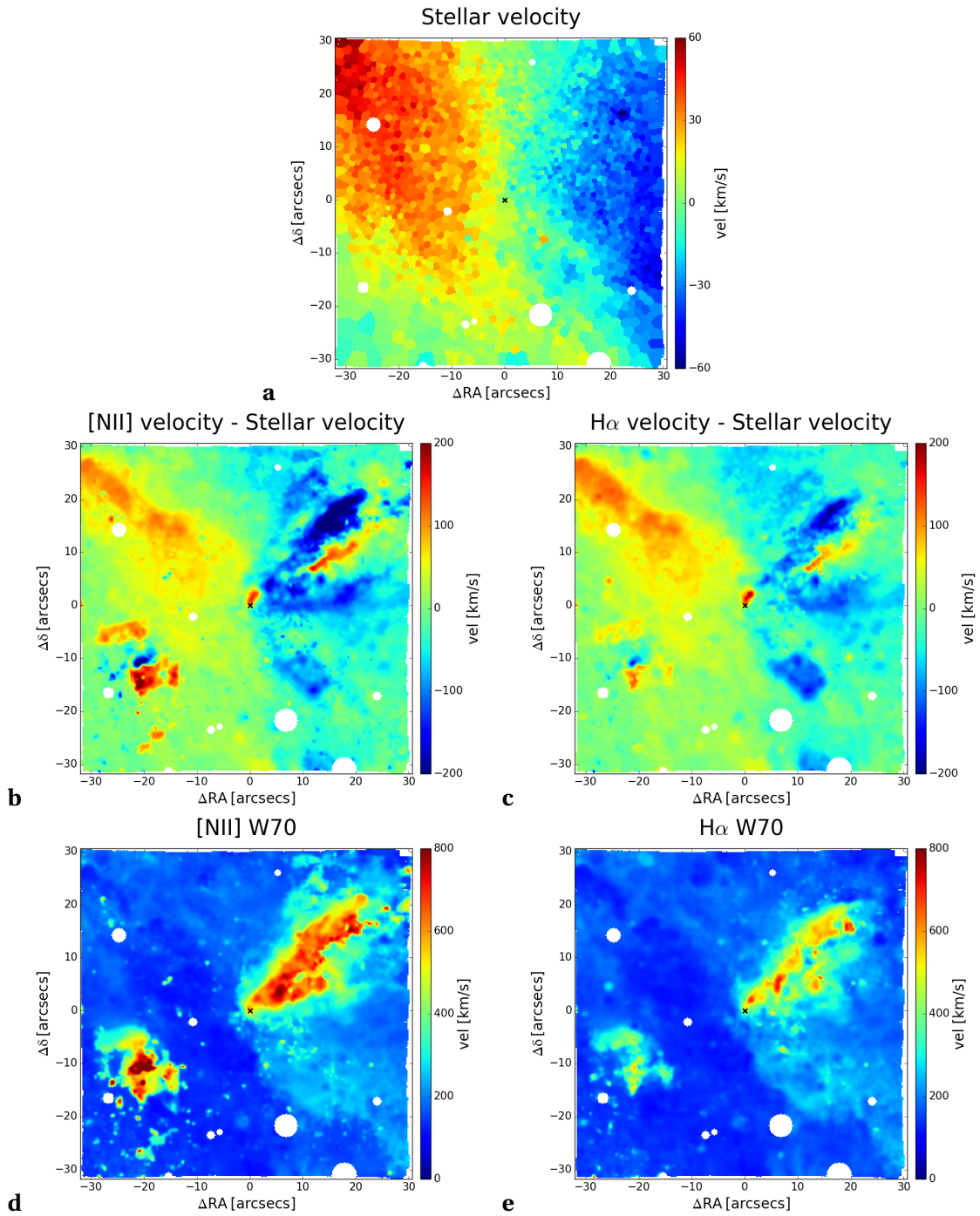
Fig. 2.17: NGC 4945. Same as in Fig. 2.3, with the exception that we report the kinematics of [N II] instead of [O III], as explained in Fig. 2.16.

The stellar velocity map (Fig. 2.17a), redshifted to the NE, blueshifted to the W, seem to trace an irregular rotation, probably because of the large and not uniform obscuration in the edge-on disk. The [N II] and Hα stellar velocity-subtracted velocity maps (Figs. 2.17b and 2.17c) and linewidth maps (Figs. 2.17d and 2.17e) clearly trace a double-conical outflow, cospatial with the double cone observed in [N II] flux map. As in the flux map, the NW lobe is more extended than the SE one, down to the ideal vertex of the cone, spanning ~600 pc. The galaxy is nearly edge on and dusty, and so the galactic plane likely resides behind the NW cone with respect to the observer, while the SE cone stands behind the disk and is obscured by dust close to the center but emerges from it at a certain distance. The velocity map of [N II] shows the kinematic structure of the two cones, the NW one having approaching velocities at its edges and receding ones around its axis, the SE lobe having an opposite behavior instead, i.e. receding velocities at its edges and approaching ones around its axis. Double-peaked and complicated line profiles are ubiquitous along the outflow. Later in Sect. 2.5 we attempt to infer the 3D structure of the outflow observed in NGC 4945 by comparing our MUSE maps with a simple toy model.

2.4.9 NGC 5643

NGC 5643, located at a distance of ~16 Mpc ($1'' \sim$ 78 pc), is a barred almost face-on Seyfert 2 galaxy. It is characterised by an ionization cone extending over a few kpc eastward of the nucleus parallel to the bar (Schmitt et al. 1994, Simpson et al. 1997, Fischer et al. 2013), along which sharp dust lanes are present. Soft X-ray emission is cospatial with the ionization cone (Bianchi et al. 2006, Gómez-Guijarro et al. 2017). The galaxy also hosts a low-luminosity radio jet aligned in the same direction, on both sides of the nucleus, spanning ~$30''$ (~2.5 kpc; Morris et al. 1985, Leipski et al. 2006). In Cresci et al. (2015a)[9], by analyzing MUSE data of NGC 5643, we detected both sides of the ionisation bicone (E and W), and found evidence of ionized out-flowing material in the E cone triggering star formation (positive feedback) in two Hα-bright clumps, located at the edge of the dust lane and which have been detected also in molecular gas from faint CO emission (Alonso-Herrero et al. 2018). Here we complement them with MUSE data from a different observing program (095.B-0532(A)) having better seeing ($FWHM$ ~ $0.56''$) than those employed in Cresci et al. (2015a) ($FWHM \sim 0.88''$; program 60.A-9339(A)).

Figs. 2.18 and 2.19 display our MUSE flux and kinematic maps for NGC 5643, respectively. The image of the entire extension of this almost face-on galaxy in Fig. 2.18a shows its spiral structure and the FOV of our MUSE maps covering the central ~5×5 kpc^2 (red box). The three-color MUSE image in Fig. 2.18b exhibits the bright [O III] double ionization cone (green), stronger to the E of the nucleus than to the W, and Hα emission (red), which traces the star formation in the spiral features outside an ideal star-forming ring a few kpc away around the nucleus and in the bright clumps at the tip of the E ionization cone where we found evidence

---

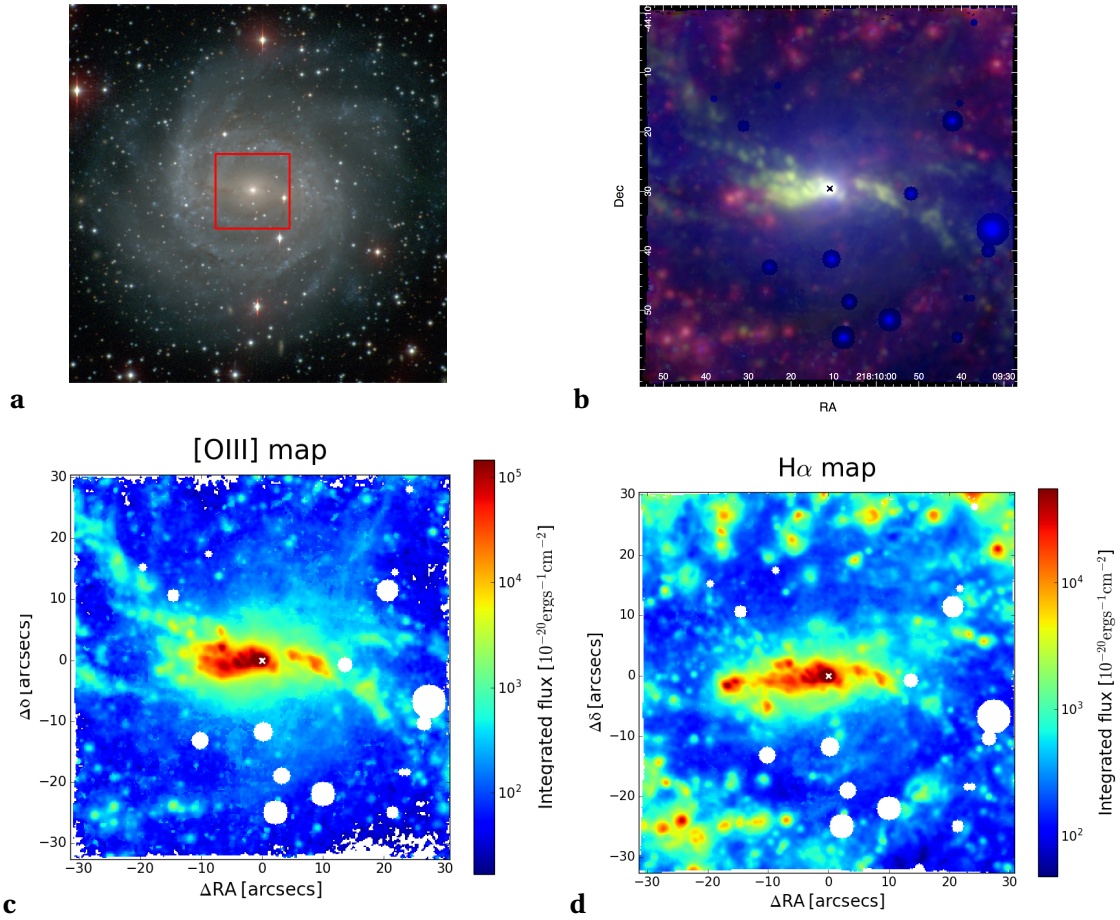[9] Further details about this work are given in Appendix.

Fig. 2.18: NGC 5643. **(a)** Three-color (blue: B band; green: V band; red: I band) image of NGC 5643 obtained with the 2.5 m du Pont Telescope at Las Campanas Observatory for the Carnegie-Irvine Galaxy Survey (CGS, Ho et al. 2011). The side of our MUSE maps FOV (red box) spans ~5 kpc. Same as in Fig. 2.2 for **(b)**, **(c)** and **(d)**.

of positive feedback in Cresci et al. (2015a). [O III] and Hα flux maps are shown separately also in Figs. 2.18c and 2.18d.

The stellar velocity map (Fig. 2.19a) follows the rotation of the disk, with trace of an inner disk component close to the nucleus, aligned with the large-scale rotation. The velocity maps of [O III] and Hα, spaxel-by-spaxel subtracted by the stellar velocity, are extremely complex (Figs. 2.19b and 2.19c). They show in fact a large variation in blueshifted and redshifted features all around the FOV in excess to stellar rotation. The ionization cones exhibit both redshifted velocities, in the inner part of the E cone close to the nucleus and in its two furthest filaments close to the edge of the FOV, and blueshifted, in the rest of the E cone and in the W cone. Other spiralling residuals remain after the subtraction of the stellar velocity field, possibly indicating peculiar gas motions in the spiral arms. A blueshifted excess also extends in the direction perpendicular to the ionization cones, to the N and S of the nucleus. A large linewidth is observed in the same
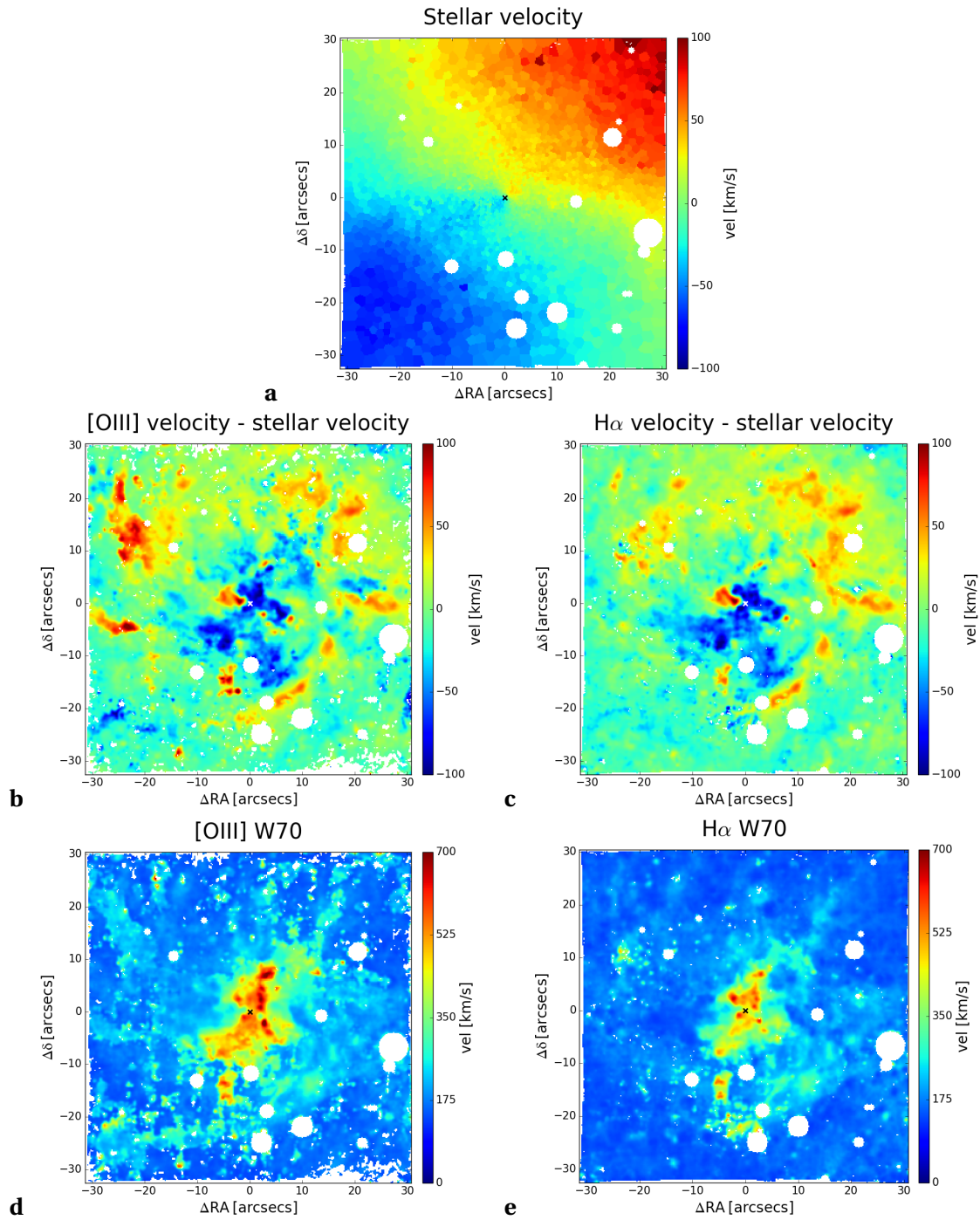
Fig. 2.19: NGC 5643. Same as in Fig. 2.3.

N-S direction perpendicularly to the ionization cones (Figs. 2.19d and 2.19e), up to W70 ~ 700 km s^{-1}, indicating a large spread in gas velocities within this extended region (up to ~2.5 kpc per side). Though less defined in shape, this feature of enhanced linewidths perpendicular to the ionization cones and radio jet is analogous to the ones that we observe in IC 5063 and NGC 1386 (see Sect. 2.4.6 and 2.4.3, respectively), suggesting a correlation between the presence of the radio jets and this perpendicular outflowing or turbulent gas motion.

2.4.10 NGC 6810

NGC 6810 is a spiral galaxy located at a distance ~27.5 Mpc from Earth ($1''$ ~ 130 pc) and having a high inclination (~74°) with respect to the line of sight. It was initially misidentified as a Seyfert 2 by Kirhakos & Steiner (1990) due to a spatial misidentification with an unrelated HEAO-1 X-ray source and because of the high emission-line widths observed, typical of Seyferts, but due instead to the presence of an outflow. The nucleus of NGC 6810 shows in fact no sign of AGN activity neither from optical diagnostics (Brightman & Nandra 2008, Yuan et al. 2010, Sharp & Bland-Hawthorn 2010, Videla et al. 2013), hard X-rays (Strickland 2007), mid-infrared (Asmus et al. 2014) nor radio emission (Kewley et al. 2000). Presence of a bipolar galactic starburst outflow perpendicular to the disk is inferred from broad and splitted line profiles observed along the minor axis (Coccato et al. 2004, Sharp & Bland-Hawthorn 2010) and from diffuse soft X-ray emission extended up to ~7 kpc per side (Strickland 2007), which spatially match with polycyclic aromatic hydrocarbon (PAH) emission from dust (McCormick et al. 2013).

Figs. 2.20 and 2.21 display our MUSE flux and kinematic maps for NGC 6810, respectively. Fig. 2.20a shows an optical image of this highly-inclined spiral galaxy, whose disk extends approximately in the N-S direction. Our MUSE FOV, covering ~8×8 kpc^2 around the center, is reported in red. Our three-color image in Fig. 2.20b shows Hα (red) and [N II] (green) emission together with the bluer part (~5100-5800 Å) of the stellar continuum (blue). Two sharp vertical dust filaments can be seen, consistently with Fig. 2.20a. [N II] and Hα emission can be seen in the disk and along the main vertical dust lane to the eastern edge of the disk. Fainter bipolar emission is observed perpendicularly to the disk, in some regions stronger in [N II] emission, in others stronger in Hα, especially in a funnel-shaped region to the W of the disk (see also their separate distribution in Figs. 2.20c and 2.20d). The enhanced linewidths to the E and W of the disk (Figs. 2.21d and 2.21e), up to ~600 km s^{-1}, indicate that a bipolar galactic outflow of ionized gas perpendicular to the disk is present, mainly blueshifted in its western side and redshifted in the eastern, as shown by the velocity maps in Figs. 2.21b and 2.21c, spaxel-by-spaxel subtracted by the stellar velocity. The outflow reaches the edges of the ~8×8 kpc^2 FOV of our maps, thus most likely extending further out. In Chapter 4 we investigate the properties of the bipolar ionized outflow that we observe in this star-forming galaxy.
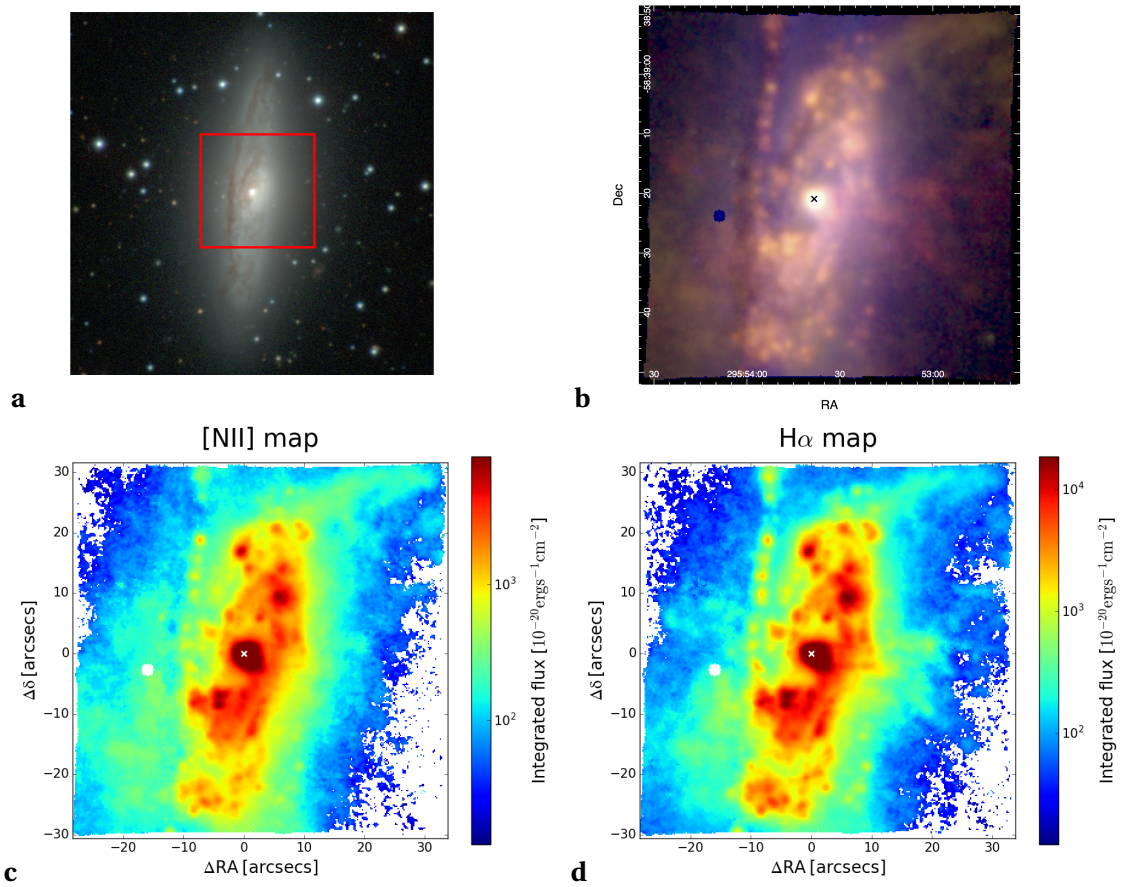
Fig. 2.20: NGC 6810. **(a)** Three-color (blue: B band; green: V band; red: I band) image of NGC 6810 obtained with the 2.5 m du Pont Telescope at Las Campanas Observatory for the Carnegie-Irvine Galaxy Survey (CGS, Ho et al. 2011). The side of our MUSE maps FOV (red box) spans ~8 kpc. Same as in Fig. 2.2 for **(b)**, **(c)** and **(d)**, with the exception that [N II] is reported in **(b)** in green and in **(c)**, instead of [O III].
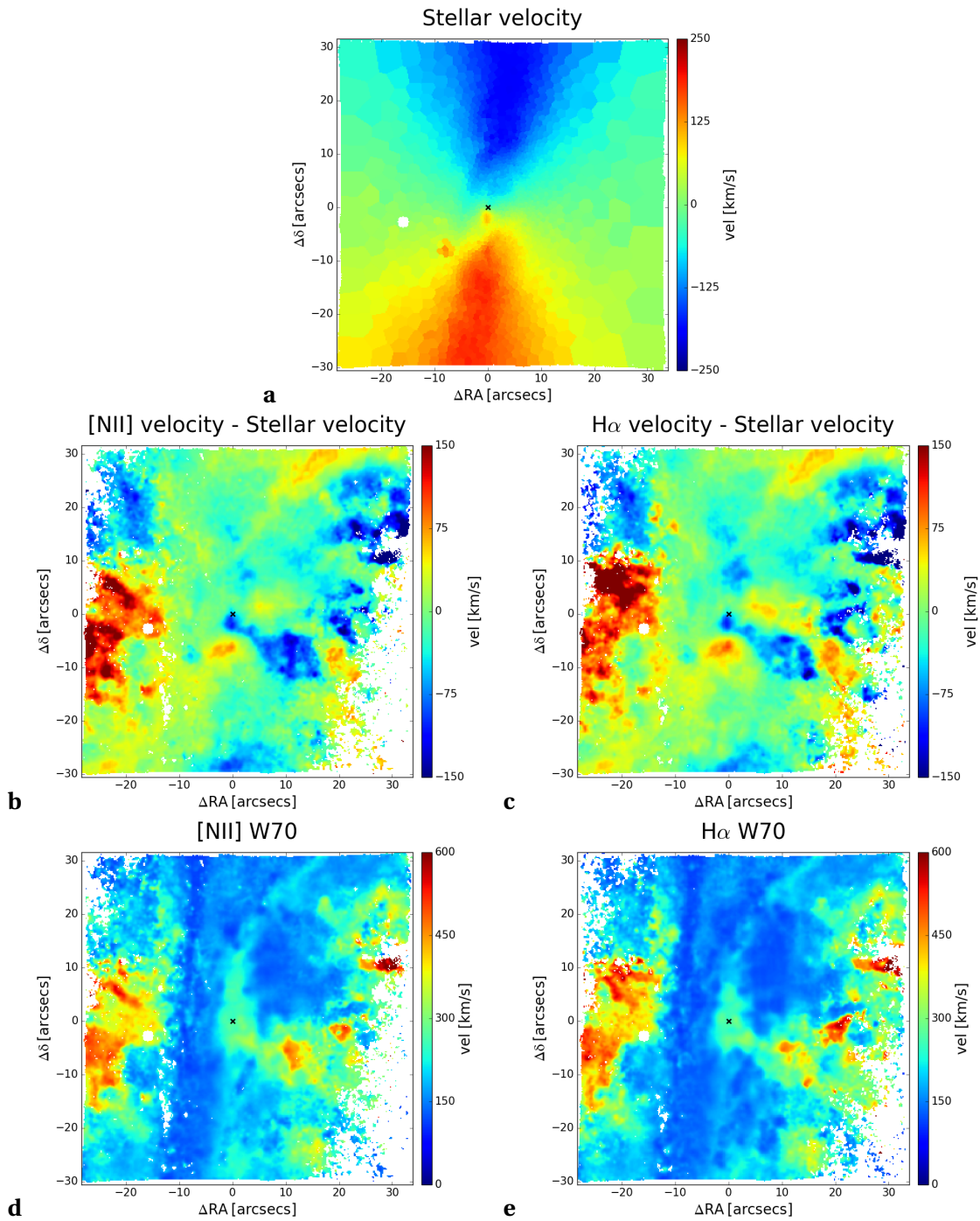
Fig. 2.21: NGC 6810. Same as in Fig. 2.3, with the exception that we report the kinematics of [N II] instead of [O III].
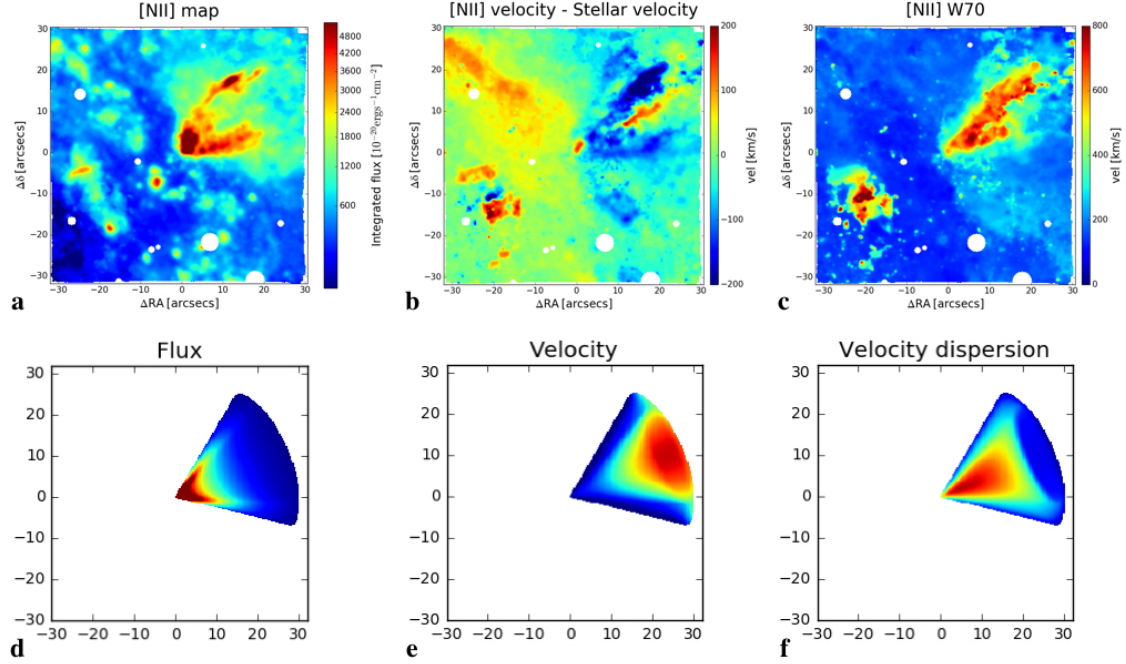
Fig. 2.22: Maps from MUSE observations of NGC 4945 (top, same as in Figs. 2.16c, 2.17b and 2.17d) and from kinematic model (bottom). **(a)** [N II] flux map. **(b)** [N II] velocity pixel-by-pixel subtracted by the stellar velocity, in order to isolate proper motions of the gas w.r.t. stars. **(c)** [N II] W70 map, i.e difference between the 85th-percentile velocity and the 15th-percentile one calculated on the fitted line profile. **(d)** Flux map from simple toy model of hollow cone having inclination of 75° with respect to line of sight, inner and outer half opening angle of 25° and 35°, respectively (thus intercepting the plane of the sky), and constant velocity field. **(e)** Velocity map from model in **(d)**. **(f)** Velocity dispersion map from model in **(d)**.

2.5   Modelling of outflow 3D structure in NGC 4945

One of the main goals of the MAGNUM survey is to study the structure and properties of the outflow. Here we attempt to infer the outflow 3D shape and kinematic properties of the outflow in NGC 4945, making use of a simple kinematic model.

[N II] fitted flux, velocity (spaxel-by-spaxel subtracted by the stellar velocity) and W70 maps of this galaxy, obtained from the fit of the star-subtracted spatially-smoothed data cube, are presented in Figs. 2.22a, 2.22b and 2.22c, respectively. These are the same reported previously in Figs. 2.16c, 2.17b and 2.17d and we display them here for a better comparison with hour toy model. As noted before, the outflowing cones have a peculiar kinematic structure, the NW one having approaching velocities at its edges and receding ones around its axis, the SE lobe having conversely receding velocities at its edges and approaching ones around its axis.

The aspect of the velocity map of the NW cone could be explained thinking to a hollow cone which has an axis inclination < 90° with respect to the line of sight and a sufficient aperture such that the far part of the cone intercepts the plane of the sky (the same holds for the

SE lobe, but with opposite geometry). Another feature supporting this scenario is the flux enhancement at the edges of [N II] cone in Fig. 2.22a, compatible with an effect of limb brightening in a hollow cone. To test this hypothesis a simple kinematic model has been realized. The model features a hollow cone having inclination of 75° with respect to line of sight, inner and outer half opening angle of 25° and 35°, respectively, a quadratic exponential radial profile for the flux ($\propto r^{-2}$) and constant velocity field. The resulting maps of flux, velocity and velocity dispersion are reported in Figs. 2.22d, 2.22e and 2.22f, respectively. The velocity map of the model approximately resembles the observed one, with approaching velocities at the edges of the cone and receding ones in the middle. Also the velocity dispersion spatial distribution well reproduces the observed one. Although this is a simple toy model aimed at qualitatively understanding the outflow kinematic structure observed in NGC 4945, and does not take into account the clumpiness of the ionized gas, it seems to be a fairly good representation of the observed maps, and thus a hollow outflowing cone intercepting the plane of the sky appears to be a promising way to explain the complex kinematics observed in NGC 4945. We are developing a more detailed and sophisticated kinematic model to actually reconstruct outflows 3D shape and intrinsic properties.

2.6 Summary and results

We presented an overview of our MAGNUM survey of nearby Seyfert galaxies, where we aim to study the physics, kinematics and ionization mechanisms of the ionized gas and carry out a detailed study of the structure and physical properties of galactic ionized outflows, by employing integral field spectroscopic data from VLT/MUSE. We described our sample selection which has made use of Maiolino & Rieke (1995) and Risaliti et al. (1999) optically-selected catalogs and of the X-ray selected Swift-BAT 70-month Hard X-ray Survey (Baumgartner et al. 2013), from which we selected the AGN closer than 50 Mpc from Earth and observable from Paranal Observatory ($-70° < \delta < 20°$). We presented our MUSE flux and kinematic maps of the 9 MAGNUM galaxies we analyzed so far, namely Centaurus A, Circinus, IC 5063, NGC 1068, NGC 1365, NGC 1386, NGC 2992, NGC 4945 and NGC 5643, to which we added the star-forming galaxy NGC 6810, to have a starburst outflow as comparison.

We find ubiquitous single or double ionization cones traced by [O III] or, in a couple of sources, by [N II], depending on which is the dominant ionization source, that is, AGN or shocks/LI(N)ER, respectively. The ionization cones span a wide range of sizes, from ~200 pc up to 10 kpc per side. Prominent starburst rings, strongly emitting in Hα, are clearly present in at least 4 of our sources, namely Circinus, NGC 1068, NGC 1365 and NGC 1386.

We mapped prominent galactic outflows associated with the ionization cones, both with clear conical shapes, such as in Circinus, NGC 1365 and NGC 4945, other with less defined shapes, like in Centaurus A, NGC 1068, NGC 2992, NGC 5643 and NGC 6810. A peculiar kine-

matic structure is observed in the outflowing cones of Circinus and NGC 4945, with blueshifted velocities at the cone edges and redshifted around the cone axis. The counter cone of NGC 4945 shows instead the opposite morphology, with redshifted velocites at the cone edges and blueshifted in the middle. Such kinematic features suggest a hollow-conical structure for the outflow, intercepting the plane of the sky. We tested if this could be the case, by attempting to infer the 3D structure of the outflow in NGC 4945 with a toy model, finding that a simple kinematic model of a uniform outflowing hollow cone intercepting the plane of the sky is indeed able to qualitatively reproduce the observed kinematic maps of both cones.

Conversely, we also detect strongly enhanced linewidths perpendicular to the ionization cones and to the radio jets in four galaxies of our sample, IC 5063, NGC 1386, NGC 5643 and, a bit less clearly, also in NGC 1068, which are the only objects hosting a jet among the ones we presented (though the presence of the jet in NGC 1386 is uncertain). Such behavior suggests a correlation between the presence of the radio jet and the enhanced linewidths perpendicular to it. This feature might be associated to outflowing or largely turbulent motions induced by the jet, creating a cocoon which displaces the gas in the disk laterally with respect to its direction of propagation. We aim to investigate this peculiar phenomenon in a future work by making use of kinematic modelling of the jet expansion in the medium. We also find evidence of gas motions in excess to the stellar velocity, such as in NGC 1365, possibly associated with the presence of a bar, suggesting non-circular motions of the gas in the disk and/or inflows.

In this Chapter, we only presented our MUSE maps and a qualitative description of the emission-line distribution and kinematic features that emerge from them, as well as an illustrative attempt to infer the outflow 3D geometry with a toy model. Our next goal is to quantitatively investigate the kinematics and nature of the outflows in separate works, by making use of complex and realistic kinematic modelling accounting for the observed distribution and clumpiness of the gas as well, so as to separate the contribution of the outflow from that of the gas at rest in the disk and to infer the intrinsic 3D geometric and kinematic structure of the outflows. In the following we illustrate our first detailed investigation of the properties of ionized gas, outflows and their interplay with star-formation in the galaxy, in two of the sources whose MUSE maps we have presented in this Chapter, namely NGC 1365 and NGC 6810.

3 A MUSE-Chandra resolved view on ionized gas and outflows in NGC 1365

3.1 Introduction

In this Chapter we present a detailed study of the ionized gas in the central regions of the nearby Seyfert galaxy NGC 1365, belonging to our MAGNUM survey. As previously discussed, although the nearby Universe mainly hosts low-luminosity AGN ($L_{\rm bol} \lesssim 10^{44}$ erg s^{-1}), likely having slower and/or less massive outflows compared to $z \sim$ 1-3 luminous AGN ($L_{\rm bol} \gtrsim 10^{46}$ erg s^{-1}), these objects are ideal laboratories to perform a spatially resolved kinematic analysis down to 10-100 parsec scales. Their vicinity allows us in fact to probe in detail the spatial structure of the outflows and to inspect their properties (such as velocity and mass outflow rate) as a function of distance from the nucleus, as well as their interplay with the star-forming processes in the host galaxy.

NGC 1365 is a local (z = 0.005457, Bureau et al. 1996) barred spiral (SB(s)b according to de Vaucouleurs et al. 1991) Seyfert 1.8 galaxy (Véron-Cetty & Véron 2006), belonging to the Fornax cluster (Jones & Jones 1980). A three-color optical image (B, V, R bands) of NGC 1365 is displayed in Fig. 3.1a, showing the two main spiral arms, connected by the bar, along which two main dust filaments can be seen. The galaxy has an angular size in the sky of $11.2' \times 6.2'$, implying an average diameter of ~44 kpc (having considered a distance of 17.3 Mpc[1]), almost twice the size of the Milky Way. NGC 1365 has an inclination of 40° with respect to the line of sight[2] (Jorsater & van Moorsel 1995).

NGC 1365 has been extensively studied over the years and a comprehensive review about the early works on this object is given in Lindblad (1999). The galaxy presents both AGN activity and star formation in its central regions. Nuclear activity emerges both at X-ray and optical wavelengths, from the unresolved hard X-ray emission and strong Fe I Kα feature (e.g., Iyomoto et al. 1997, Komossa & Schulz 1998), which are spatially coincident with the optical nucleus, characterized by broad Balmer lines (e.g., Schulz et al. 1999). Extended (~1 kpc) conical [O III] emission was observed to the SE of the nucleus (e.g., Edmunds et al. 1988, Storchi-Bergmann & Bonatto 1991, Kristen et al. 1997) and a complementary, fainter cone to the NW

---

[1] From HyperLeda best distance modulus, that is the weighted average between the redshift distance modulus corrected for infall of the Local Group toward Virgo and the weighted average of the published redshift-indipendent distance measurements.

[2] L.o.s. hereafter.

was later revealed (e.g., Veilleux et al. 2003). Sharp & Bland-Hawthorn (2010), exploiting integral field spectroscopic (IFS) observations, found enhanced [O III]- and [N II]-to-Balmer line ratios in correspondence with the two cones, suggesting that they are ionized by the AGN. This was confirmed with diagnostic diagrams only for the inner part of the SE cone, due to the limited signal-to-noise ratio available. The kinematics of [O III] in the cones from long-slit spectroscopy revealed the presence of an outflow (e.g., Phillips et al. 1983, Hjelm & Lindblad 1996), whose SE inner part has been recently mapped in [N II] by Lena et al. (2016) with $13'' \times 6''$ IFS observations.

From the X-ray point of view, the unresolved active nucleus exhibits a large variability, with highly ionized blueshifted absorption lines indicating a fast wind ($v \sim 3000$ km s^{-1}; e.g., Risaliti et al. 2005, Braito et al. 2014). The extended soft X-ray emission is dominated by thermal emission from star formation-related processes, and its spatial distribution shows a roughly biconical morphology as well (Wang et al. 2009). By using the high-resolution gratings onboard *Chandra* and *XMM-Newton*, Nardini et al. (2015b) and Whewell et al. (2016) were able to isolate the AGN-photoionized emission lines in the soft X-ray spectrum.

Star formation mostly occurs in an elongated circumnuclear ring, which was reported for instance by Kristen et al. (1997) in Hα+[N II], Forbes & Norris (1998) and Stevens et al. (1999) in radio, and has been recently studied in detail in different IR bands by Alonso-Herrero et al. (2012). The gas ionization in the corresponding region is dominated by star formation processes, as already suggested from emission-line diagnostics by Sharp & Bland-Hawthorn (2010) with their IFS observations. Non-circular motions associated with the bar were found by Teuben et al. (1986) in Hα and Jorsater & van Moorsel (1995) in H I. Using H I and optical data Lindblad et al. (1996a) inferred gas motions parallel to the bar, as found from Fabry-Perot interferometric Hα data by Zánmar Sánchez et al. (2008) and Speights & Rooke (2016). Sandqvist et al. (1995) suggested that NGC 1365 hosts a radio jet, but Stevens et al. (1999) showed that radio emission is dominated by the elongated star-forming ring in the direction NE-SW, and that the evidence of a jet emanating from the nucleus is at best marginal.

NGC 1365 was observed with MUSE (Multi Unit Spectroscopic Explorer; Bacon et al. 2010), the optical and near-IR large-field, integral-field spectrograph located at the Very Large Telescope (VLT), as part of the MAGNUM survey (Measuring Active Galactic Nuclei Under MUSE Microscope; Chapter 2). This program aims at observing nearby AGN to study the physical conditions of the narrow line region (NLR), the interplay between nuclear activity and star formation, and the effects and acceleration mechanisms of outflows.

MUSE observations of NGC 1365 have been complemented with X-ray data acquired by the Chandra X-ray Observatory (CXO). The galaxy is known to host an X-ray nuclear wind (e.g., Risaliti et al. 2005, Braito et al. 2014) and to have a complex circumnuclear medium giving rise to heterogeneous soft X-ray line emission (e.g., Guainazzi et al. 2009, Nardini et al. 2015b,
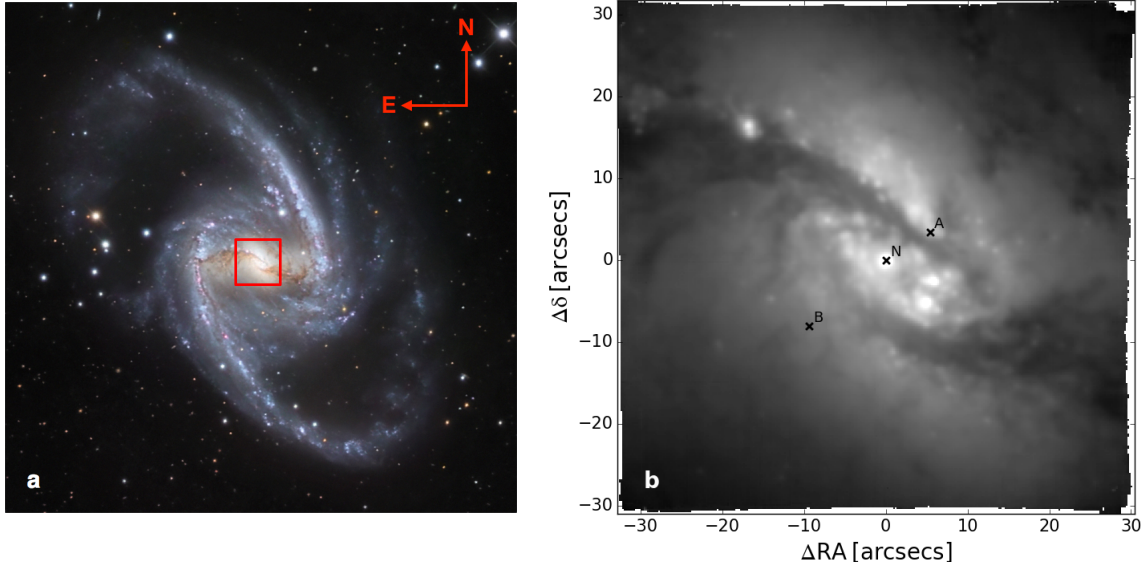
Fig. 3.1: **(a)** Three-color optical image of NGC 1365 combining observations performed through three different filters (B, V, R) with the 1.5-meter Danish telescope at the ESO La Silla Observatory in Chile. The red box indicates the region analyzed in this work, corresponding to the MUSE FOV ($\sim 1' \times 1'$). East is to the left. Credit: ESO/IDA/Danish 1.5 m/ R. Gendler, J-E. Ovaldsen, C. Thöne, and C. Feron. **(b)** Continuum emission from MUSE having collapsed the data cube in the range $\sim$5100-6470 Å, excluding emission lines and the sky residuals. The crosses mark the extraction regions of the spectra shown in Fig. 3.2.

Whewell et al. 2016). Wang et al. (2009) performed a multiband spatially resolved analysis of this galaxy employing the same *Chandra* data.

In our work we took advantage of the unprecedented capabilities of MUSE to carry out a highly detailed spatially and spectrally resolved study of the central regions of NGC 1365, both in the optical and in the X-ray band. The combination of MUSE and *Chandra* is extremely powerful, as they both provide a wide spatial coverage and a similar subarcsecond spatial resolution, as well as extensive spectral information, allowing us to study the circumnuclear gas in its different phases and compare nuclear and extended gas outflows.

In the following, wavelengths are given rest-frame. When performing our data analysis they were redshifted according to the receding velocity of the galaxy ($\sim$1630 km s^{-1}, in agreement with Jorsater & van Moorsel 1995, Zánmar Sánchez et al. 2008).

3.2 MUSE maps

3.2.1 Data description

NGC 1365 was observed with MUSE on October 12, 2014, under program 094.B-0321(A) (P.I. A. Marconi). The data consisted of two Observing Blocks (OBs) for a total of eight dithered and 90°-rotated 500s exposures of the central regions of the galaxy, together with an equal number
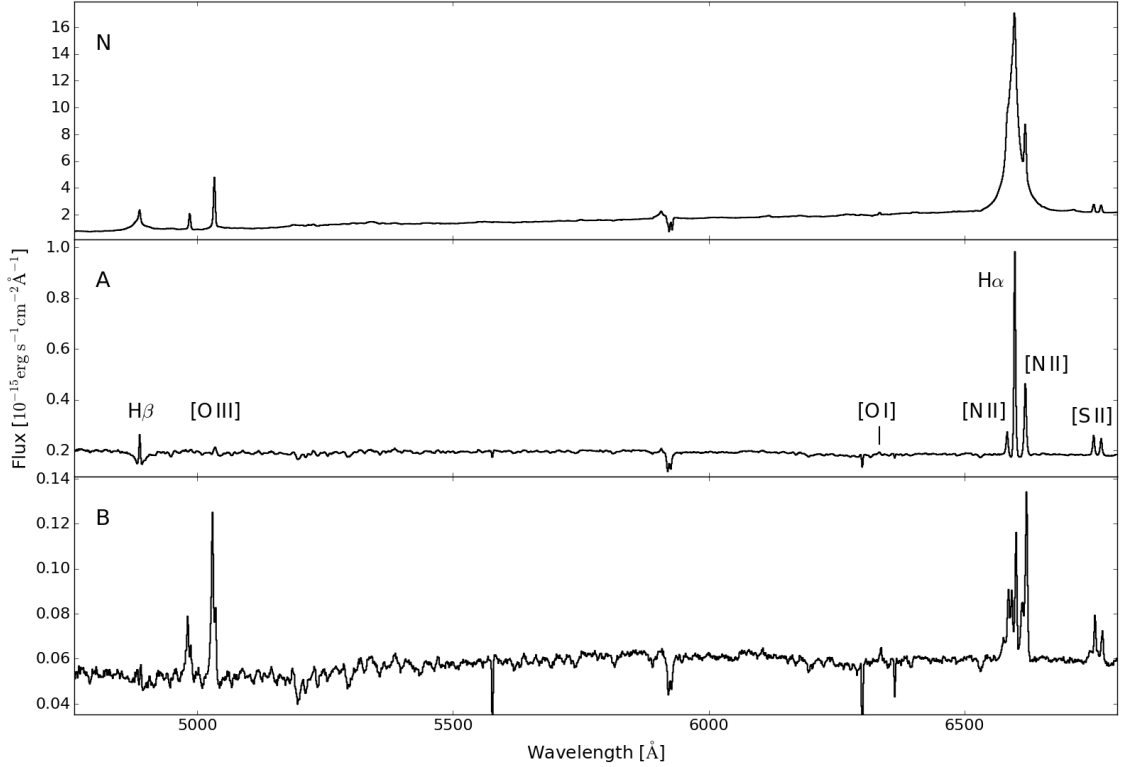
Fig. 3.2: Representative spectra extracted from circular regions with radius of 3 spaxels as defined in Fig. 3.1b. N indicates the nucleus, where broad Balmer emission is present. The spectrum of region A shows narrow emission lines on top of the stellar continuum. The spectrum of region B exhibits complicated line profiles indicative of outflowing gas. The deep narrow lines in absorption are sky residuals.

of 100s sky exposures. Each sky exposure is employed in the data reduction to create a model of the sky lines and sky continuum to be subtracted from the closest science exposure in time. The average seeing during the observations was FWHM = $0.76'' \pm 0.02''$, as derived from the unresolved nuclear Balmer line emission from the broad line region, because of the absence of foreground stars in the FOV.

The data reduction has been carried out using ESO reflex, which gives a graphical and automated way to execute with EsoRex the Common Pipeline Library (CPL) reduction recipes, within the Kepler workflow engine (Freudling et al. 2013). MUSE pipeline v1.6 has been employed for our reduction. The reduced data cube consists of 320×317 spaxels, which correspond to $64'' \times 63.4''$, spanning the central ~5.3 kpc of NGC 1365.

Fig. 3.1b shows an image of the continuum obtained by collapsing the MUSE data cube in the wavelength range ~5100-6470 Å, having masked the emission lines and the sky residuals included in the range. The continuum exhibits diffuse and clumpy emission as well as the two main dust filaments (compare with Fig. 3.1a).

Three representative spectra, extracted from circular regions having radius of 3 spaxels

whose position is indicated in Fig. 3.1b, are displayed in Fig. 3.2. The nucleus (N) clearly exhibits broad Balmer emission typical of the broad line region (BLR). The spectrum from the region of intense stellar emission A is characterized by narrow emission lines, superimposed on the stellar continuum with its absorption features, among which also the Hβ can be seen. The spectrum from region B shows instead complicated line profiles with multiple kinematic components, indicative of outflowing gas, together with clearly different emission-line ratios compared to the spectrum from A, suggesting different ionization mechanisms for the gas in the two regions.

The data analysis, aimed at fitting and subtracting the stellar continuum and then fitting the gas emission lines, has been carried out as described in Sect. 2.3 for the whole sample.

3.2.2   Flux maps and BPT diagrams

In this section we present the emission line maps of the fitted gas lines. For a better visual output, all the maps are spatially smoothed using a Gaussian kernel with $\sigma = 1\,\mathrm{px}$ (i.e., $0.2''$), except for the flux maps (due to their high signal-to-noise ratio), for the maps derived from the fit of the star-subtracted Voronoi-binned cube, and for the stellar ones obtained from the Voronoi-binned cube.

Hereafter, the cross in the maps marks the position of the nucleus, that is, of the peak of the broad Hα emission and of the continuum between ~6800-7000 Å. In all the line maps reported from now on we exclude spaxels or bins having a signal-to-noise ratio lower than 3 on any of the lines involved. We define the signal-to-noise ratio of a line as the ratio between the peak value of the fitted line profile and the standard deviation of the data–model residuals of the fit around that line (within a range about 60 to 110 Å wide, depending on the line).

[O III] $\lambda5007$ ([O III] hereafter) and Hα flux maps are reported in Fig. 3.3 and in the two-color image in Fig. 3.4a, where they are superimposed ([O III] in green and Hα in red) to better inspect their different spatial distributions, tracing the two distinct ionizing sources contributing to the line fluxes, namely the active nucleus and young stars in star-forming regions (this is quantitatively studied later on in this section). Hα dominates in an elongated region spanning from NE to SW parallel to the bar direction, while [O III] is higher in the perpendicular direction.

The [O III] emission has a clear conical shape to the SE of the center and, even though a little bit less defined in shape, to the NW, too. The SE cone is in fact the strongest one of the two by far (see also Edmunds et al. 1988, Storchi-Bergmann & Bonatto 1991, Veilleux et al. 2003, Sharp & Bland-Hawthorn 2010), being, according to Hjelm & Lindblad (1996), in the near side, above the disk.

The Hα spatial distribution is completely different from [O III], being dominant in a ~$20''\times10''$ (1.6 kpc × 0.8 kpc) elongated circumnuclear ring hosting hotspots, consistent with the star-forming ring reported for example by Kristen et al. (1997) in narrowband *HST* im-
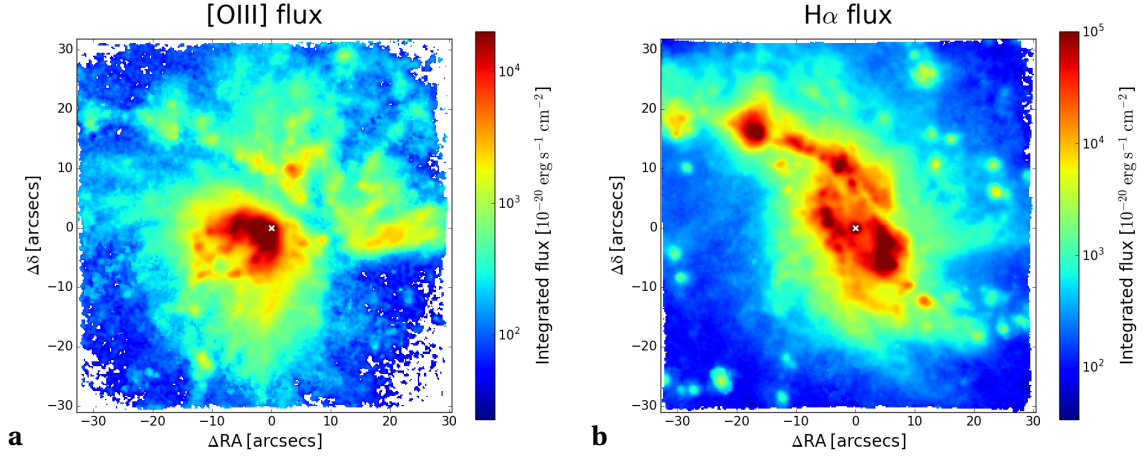
Fig. 3.3: **(a)** [O III] and **(b)** Hα emission of the total fitted line profile. Both maps have been obtained from the fit of the star-subtracted smoothed (with 1-spaxel σ gaussian kernel) data cube; a signal-to-noise cut of 3 has been applied. The FOV covers $\sim 5.3 \times 5.3$ kpc^2. The reported flux is per spaxel.

ages and by Forbes & Norris (1998) and Stevens et al. (1999) in radio. As pointed out in Lindblad (1999), circumnuclear rings of intense star formation are not infrequently observed in barred spirals and are ascribed to the presence of the inner Lindblad resonance (ILR; Binney & Tremaine 2008), with inflowing gas slowing down and accumulating between the outer and the inner ILR (having radius of $\sim 30''$ and $\sim 3''$ from the nucleus in NGC 1365, respectively; Lindblad et al. 1996b, Lindblad 1999), forming a massive ring with enhanced star formation (e.g., Shlosman 1996). Alonso-Herrero et al. (2012) also identify the starburst ring in their IR study of NGC 1365, inferring that $\sim 85\%$ of the star formation within the ILR ($r \sim 30''$, fully covered by our $\sim 60'' \times 60''$ MUSE data) is taking place in dust-obscured regions inside the star-forming ring. The effect of dust obscuration can be appreciated in Fig. 3.4b, where we report the Hα emission in red and the stellar continuum (collapsed between ~ 5100-5800 Å) in blue. Here the dust lanes can be clearly seen (see also Fig. 3.1b), as well as some stronger Hα blobs in correspondence with the lanes, indicating ongoing star formation inside them. Besides the circumnuclear ring, Hα is very strong also at the leading edge of the northern dust lane, while it is not in correspondence with the southern dust lane, which is probably obscuring the Hα emission at its leading edge on the other side with respect to the observer. There are also some isolated Hα-emitting blobs far from the central diagonal emission.

For a quantitative inspection of the dust reddening, we report in Fig. 3.4c the total extinction in V band A_V, obtained from the Balmer decrement (Hα/Hβ flux ratio) from the fit of the stellar continuum-subtracted Voronoi-binned cube. This cube provides information on regions which otherwise would have had low signal-to-noise ratio in Hβ. We employed the Calzetti et al. (2000) attenuation law for galactic diffuse ISM ($R_V = 3.12$) and an intrinsic ratio (Hα/Hβ)$_0$ = 2.86 (for an electron temperature of $T_e = 10^4$ K; Osterbrock & Ferland 2006). The nucleus has
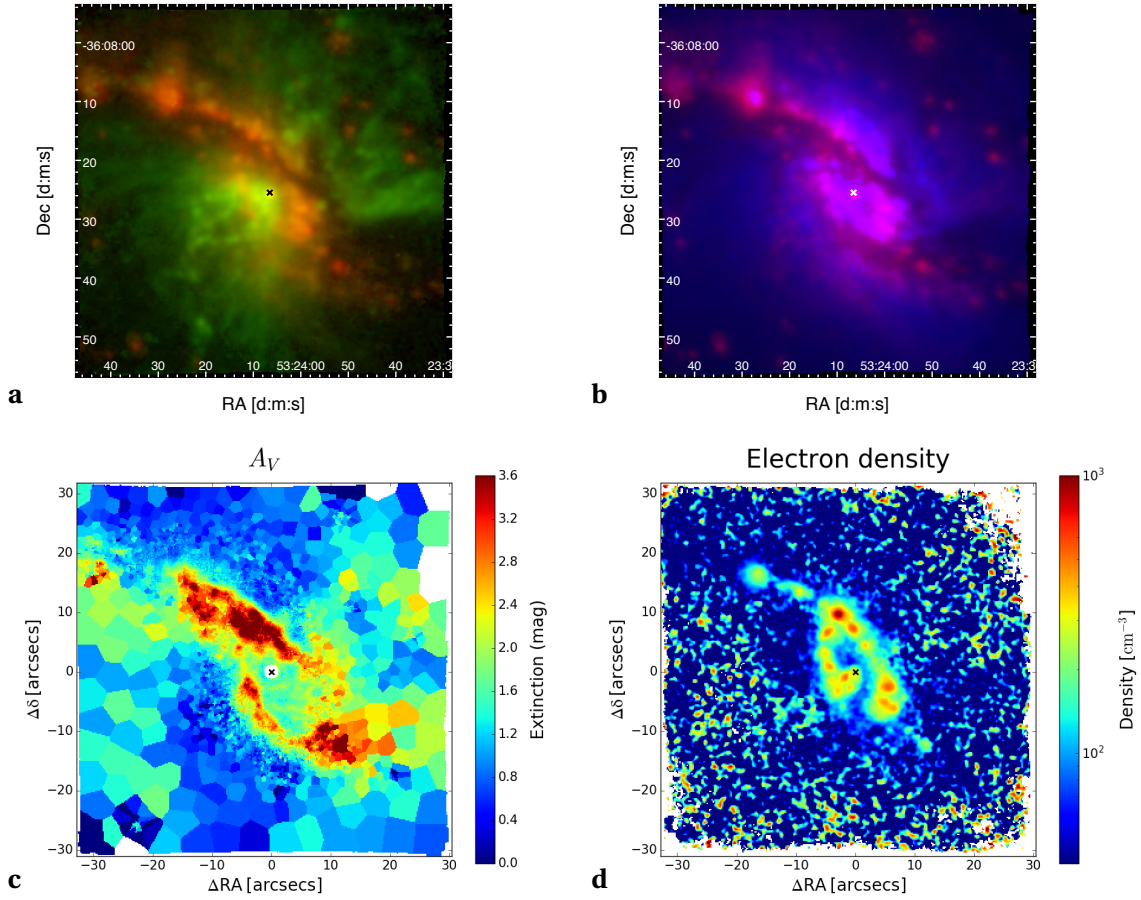
Fig. 3.4: **(a)** Two-color image of [O III] (green) and Hα (red), from the fit of the star-subtracted 1px-σ smoothed data cube. **(b)** Two-color image of Hα emission (red) and stellar continuum between ~5100-5800 Å (blue). **(c)** Map of the total dust extinction in V band A_V from the measured Balmer decrement (Hα/Hβ flux ratio), from the fit of the star-subtracted Voronoi-binned data cube (produced to have an average signal-to-noise ratio per wavelength channel around Hβ of at least 4 in each bin). **(d)** Electron density from [S II] $\lambda6716/\lambda6731$ diagnostic line ratio (a typical value of $T_e = 10^4$ K is assumed for the temperature of the gas).

been masked since the bin-by-bin fit of the broad Balmer lines in the central bins (previously described in Sect. 2.3.1.1) was not optimal, preventing a reliable estimate of the Hα/Hβ ratio for the narrow line components.

Fig. 3.4d shows the electron density map, obtained from the [S II] $\lambda6716/\lambda6731$ diagnostic line ratio (Osterbrock & Ferland 2006), assuming a typical value for the temperature of [S II]-emitting ionized gas of $T_e = 10^4$ K. As the [S II] doublet line ratio is sensitive to the electron density only for intermediate values of the density, flattening at low and high values (see Fig. 5.8 in Osterbrock & Ferland 2006), we set to 40 cm^{-3} all the measured densities falling below this value (corresponding to ~5% below the peak of the total range spanned by the ratios among the asymptotic extremes). The map shows that the circumnuclear star-forming ring has the highest
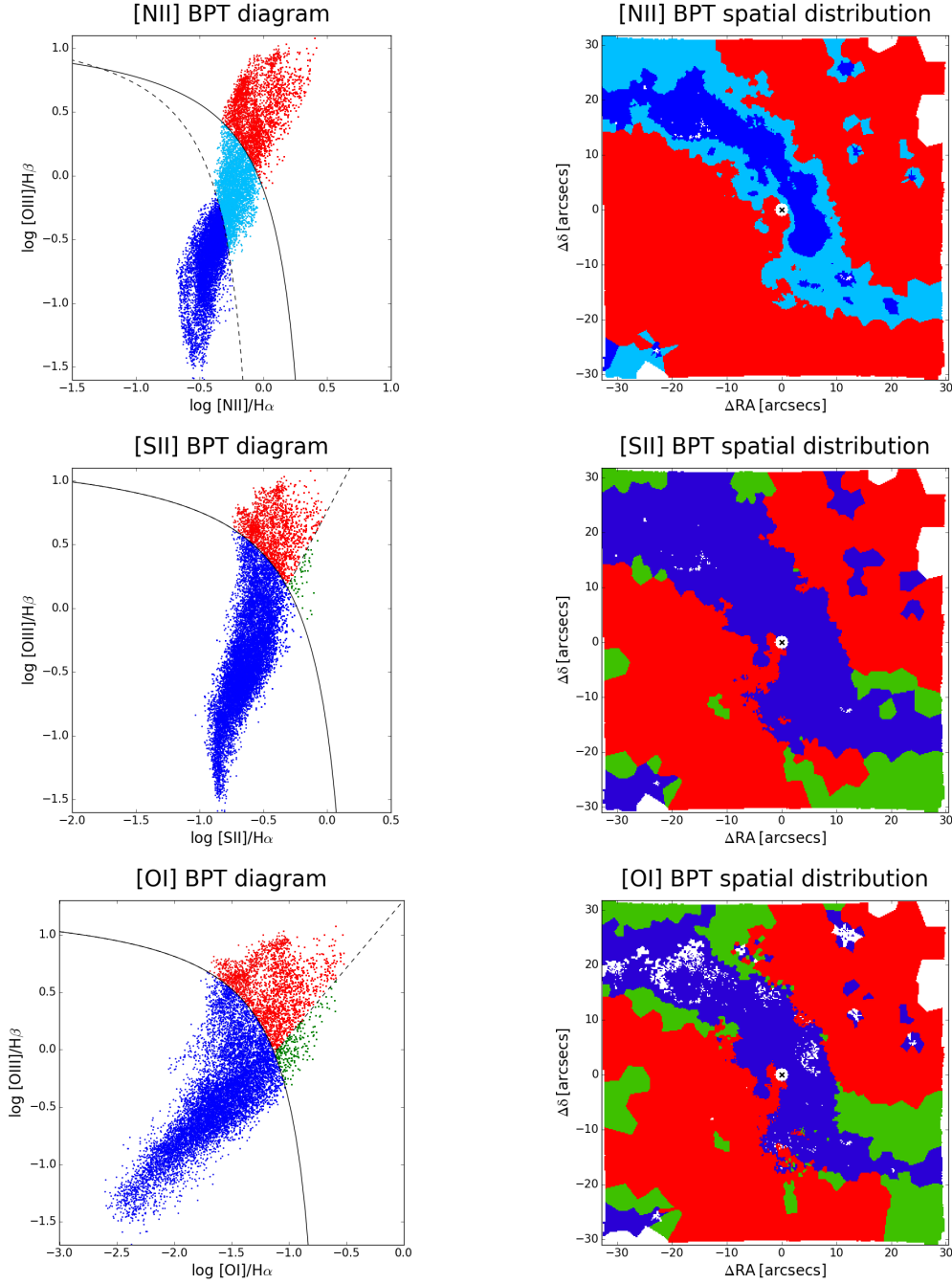
Fig. 3.5: Spatially resolved BPT diagrams (left) of NGC 1365 and corresponding spatial distribution (right), obtained from the fit of the star-subtracted Voronoi-binned cube (so as to have an average signal-to-noise ratio of at least 4 per bin in each wavelength channel around Hβ). The N-BPT ([N II]λ6584/Hα vs. [O III]λ5007/Hβ, upper panels), S-BPT ([S II]$\lambda\lambda$6716,6731/Hα vs. [O III]λ5007/Hβ, central panels), and O-BPT ([O I]λ6300/Hα vs. [O III]λ5007/Hβ, lower panels) diagrams for each bin with S/N > 3 in each line are shown on the left, while the corresponding maps are reported on the right (each bin in the maps corresponds to a single dot in the diagrams). The solid curves in the diagrams define the theoretical upper bound for pure star formation (Kewley et al. 2001b), while the dashed one in the N-BPT is the Kauffmann et al. (2003) empirical classification, and all bins under this curve are star-formation dominated. Finally, the dashed line in S-BPT and O-BPT diagrams separates Seyfert galaxies from LI(N)ERs (Kewley et al. 2006). SF-dominated regions are then marked in blue, Seyfert-type ionization is displayed in red, green marks LI(N)ER regions in the S-BPT and O-BPT, while light blue denotes composite regions in the N-BPT lying between Kewley et al. (2001b) and Kauffmann et al. (2003) curves. A 6px-radius circle around the center has been masked, because of BLR contamination (see text).

densities in the FOV, reaching a peak of $\sim 10^3$ cm^{-3} in a region to the north of the center.

Spatially resolved BPT diagnostic diagrams (Fig. 3.5) allow us to distinguish the dominant contribution to ionization in each spaxel. As suggested by Figs. 3.3 and 3.4, they show that star formation dominates gas ionization in the elongated region in the direction NE-SW, where [O III]/Hβ and [N II]/Hα are lower, while AGN dominates in a perpendicular double-conical region. This clear distinction between AGN- and SF-ionized regions is not reported in previous studies (e.g., Sharp & Bland-Hawthorn 2010) due to the lower sensitivity of their observations. We can also identify some star-forming (or composite) bins outside the main diagonal SF-dominated region, corresponding to strong Hα-emitting blobs showing up in the [O III]-dominated double cone (see Fig. 3.4a). Few bins are marked as LI(N)ER-like regions, whose line ratios can be either due to shock excitation (e.g., Dopita & Sutherland 1995) or to diffuse gas possibly ionized by hot evolved (post-asymptotic giant branch) stars (e.g., Singh et al. 2013, Belfiore et al. 2016). The circumnuclear star-forming ring seen in Hα is not completely SF-dominated in the BPT maps, but some of its parts, to the SE of the center, result to be AGN-dominated. This likely happens because the AGN-ionized cone and the SF ring belonging to the disk reside in different parts of the 3D physical space but overlap in the l.o.s. Depending on which of the two components dominates the total line profiles, each bin then occupies the SF or the AGN part of the BPT diagram.

3.2.3 Kinematic maps

MUSE data allow us to trace the kinematics of both the warm ionized gas and the stars in NGC 1365 (Fig. 3.6), from the Doppler shift of emission and absorption lines, respectively. Stellar and [O III] velocity maps are shown in Figs. 3.6a and 3.6b, respectively, and, in both cases, the velocity is reported in the galaxy rest frame. From the stellar velocity map one can clearly see the rotation of the stars in the galactic disk, approaching the observer to the NE, receding to the SW. The boundary where the velocity changes sign shows a twisted shape, likely associated to the presence of the bar. The [O III] velocity map (Fig. 3.6b) shows other complex motions in addition to the rotational field. In order to isolate and highlight these further motions of the gas with respect to stellar rotation, we report in Fig. 3.6c the map of [O III] velocity subtracted spaxel-by-spaxel by the stellar velocity. This reveals a clumpy double-conical outflow approximately in the direction SE-NW, the SE cone having approaching velocities, the NW having receding ones. The outflow shape broadly corresponds to the double cone observed in [O III] emission (Figs. 3.3a and 3.4a), which is AGN-photoionized according to the BPT diagrams (Fig. 3.5).

The shape and structure of the outflow can be well appreciated also from the map of the [O III] W70 velocity[3], where values exceeding 500 km s^{-1} are present along the outflow. The

---

[3] That is, the difference between the velocities including 85% and 15% of the flux of the total fitted line profile (without any deconvolution for the instrumental spectral resolution).
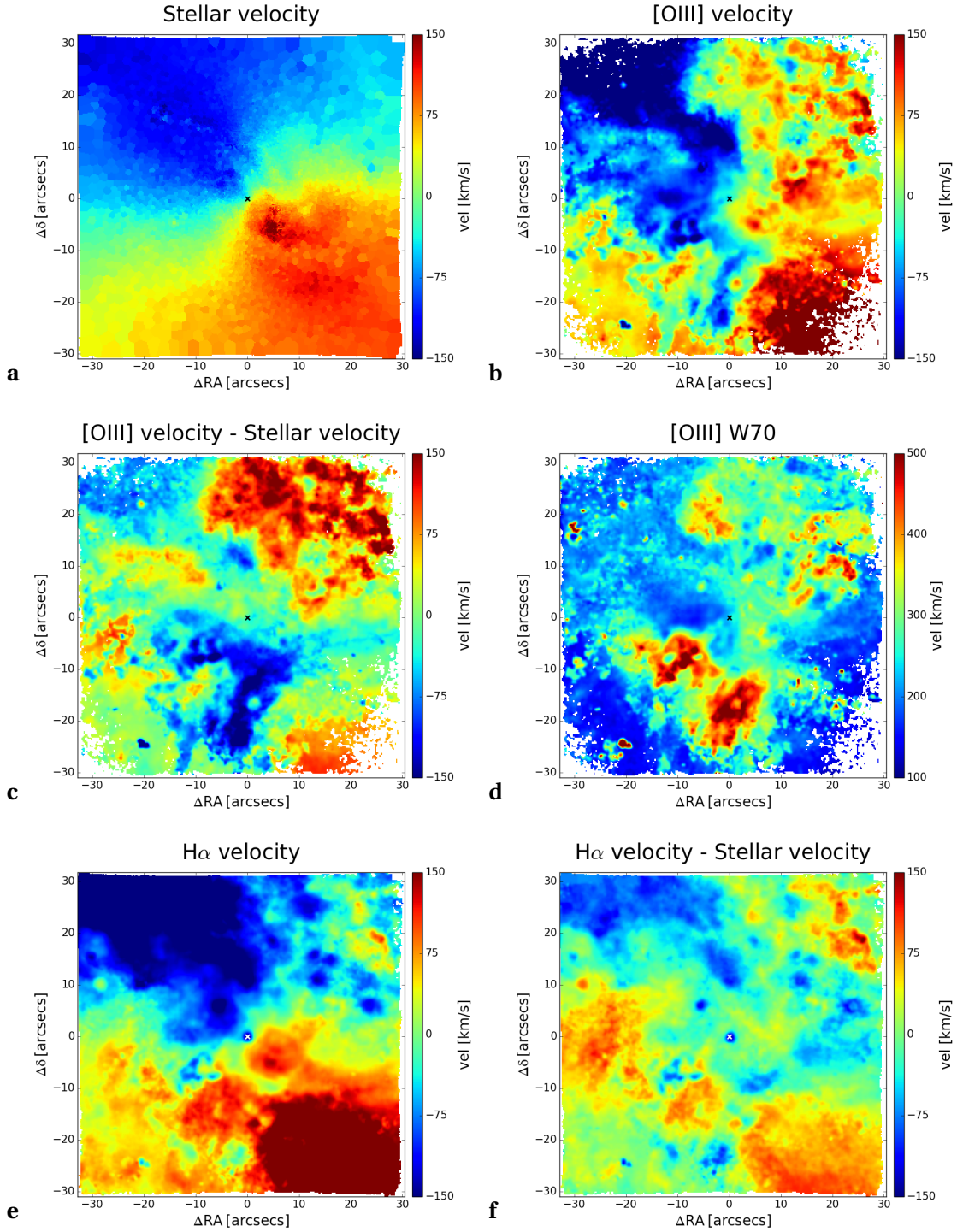
Fig. 3.6: **(a)** Stellar velocity map of NGC 1365, with respect to its systemic velocity, for which a value of 1630 km s^{-1} with respect to Earth has been considered. The map has been obtained from the fit of stellar continuum and absorption lines carried out on the Voronoi-binned data cube. **(b)** [O III] velocity map with respect to the systemic velocity. The velocities are the 1st-order moments of the total line profile resulting from the fit of the star-subtracted smoothed (with 1-spaxel σ gaussian kernel) data cube. The map has been re-smoothed with a Gaussian kernel having $\sigma = 1$ spaxel, for a better visual output, and a signal-to-noise cut of 3 has been applied (this holds for the other maps reported in panels c, d, and e of this figure, too). **(c)** [O III] velocity subtracted spaxel-by-spaxel by the stellar velocity. **(d)** [O III] W70 map, i.e difference between the 85th-percentile and 15th-percentile velocities of the fitted line profile. **(e)** Hα velocity map with respect to the systemic velocity. **(f)** Hα velocity map spaxel-by-spaxel subtracted by the stellar velocity.

high values of the W70 are due to the fact that it is calculated from the total fitted profile of [O III], which, in the regions of the outflow, is composed by the kinematic component belonging to disk and bar and by the outflowing one. Double-peaked profiles are in fact ubiquitous in our data in correspondence with the regions having higher W70 values (see e.g., the spectra in Fig. 3.8). Phillips et al. (1983) observed line splitting of [O III] for the first time to the SE of the center, proposing a model of a hollow conical outflow perpendicular to the disk to explain them. Hjelm & Lindblad (1996) suggested that line splitting could be due to two spectral components, one from the rotating disk, one from an outflow. They modeled the outflow as a wide-angle cone (50° half-opening angle), inclined of 5° with respect to the rotation axis and of 35° with respect to the l.o.s. (being the disk inclined of 40° with respect to the l.o.s.; Jorsater & van Moorsel 1995). This picture seems to be compatible with the [O III] maps presented in this work, with the approaching SE cone residing between the observer and the disk of the galaxy and the receding NW one being behind the disk, thus having a lower observed [O III] flux compared to the SE one. Recently, Lena et al. (2016) identified the inner part of the SE blueshifted outflow from [N II] kinematics maps using $13'' \times 6''$ IFS data, observing line splitting also in other low-ionization lines (Hα, [S II]) in a few nearby spaxels.

Ionized gas kinematics in the disk can be better inspected from the velocity of Hα rather than from [O III], as the total profile of Balmer lines is less affected by the outflow compared to the [O III]. This happens because the [O III]-to-Balmer lines flux ratio is higher in AGN-dominated regions than in star-forming regions and in NGC 1365 the outflowing component is much more dominated by the AGN ionization rather than the disk one (see e.g., the spectra in Fig. 3.8 from following Sect.). The Hα velocity map is reported in Figs. 3.6e and Fig. 3.6f, in the latter subtracted spaxel-by-spaxel by the stellar rotational motion. The maps show that the double-conical outflow, which is very prominent in [O III], has a much lower impact on the line profile of Hα[4]. The Hα kinematics is instead dominated by two thick lanes aligned with the bar (in the direction NE-SW; see Fig. 3.1a) having opposite velocities in excess to stellar rotation, the one in the lower-left part of the image receding, the one in the upper-right part approaching. Non-circular motions associated with the bar of NGC 1365 were already identified by Teuben et al. (1986) in Hα and then by Jorsater & van Moorsel (1995) in H I velocities, which Lindblad et al. (1996a) combined with optical ones inferring gas motions parallel to the bar, with strong velocity gradients across its leading side. Lena et al. (2016) found no obvious evidence for an inflow from their [N II] kinematic map in the central $13'' \times 6''$, but they do not exclude the possibility that gas is actually slowly migrating toward the nucleus. By using large-scale Fabry-Perot interferometric Hα data, Speights & Rooke (2016) found clear non-circular motions consistent with elliptical streaming in correspondence with the bar, compatible with what we see in our

---

[4] We stress that the gas velocity reported for a given line is the 1st-order moment of the fitted line profile and can then change from line to line depending on the shape of the profile.
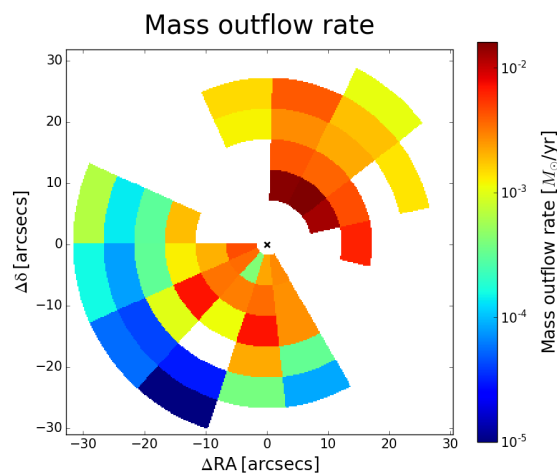
Fig. 3.7: Mass outflow rate map of the ionized gas, from the fitted Hα flux of the outflow kinematic component (see example spectra in Fig. 3.8).

Hα kinematic map. This non-circular motion likely indicates an inflow of material along the bar of NGC 1365.

3.2.4   Mass outflow rate mapping

The extension of the outflow across the FOV of MUSE allowed us to carry out a radial and angular analysis of the mass outflow rate. We grouped the spaxels in the two outflowing cones in a grid made up of radial and angular slices, excluding a circular area of radius 10 spaxels centered on the active nucleus, where the BLR contributes to Balmer line emission. The grid is made up of six radial slices per cone, 25 spaxels in size each (i.e., 5 arcsec or ≃ 420 pc) and six angular slices spanning $24''$ each for the SE cone and five spanning $25.4''$ each for the NW one (see Fig. 3.7).

We fitted [O III], Hβ, [N II], Hα, and [S II] emission lines all together using three Gaussians per line, forcing each Gaussian separately to have the same velocity and velocity dispersion among all the emission lines. One component has been dedicated to fit the outflow (blueshifted in the SE cone, redshifted in the NW one), the other two - tied to the same velocity - to fit the disk component. In fact, the disk component, despite being symmetric, was not reproduced with a simple Gaussian profile, probably because of the presence of the bar.

Due to the limited number of grid elements we could inspect the fits one-by-one and keep them under control. We immediately excluded those fits where the outflow component had null flux in Hα (as we use Hα to calculate the outflow mass) or where the line profiles showed no significant asymmetry, meaning that either no outflow is present or that it has the same l.o.s. velocity of the disk and it is thus not possible to disentangle the two.

As an example, Fig. 3.8 displays a fit for the SE blueshifted cone and a fit for the NW red-
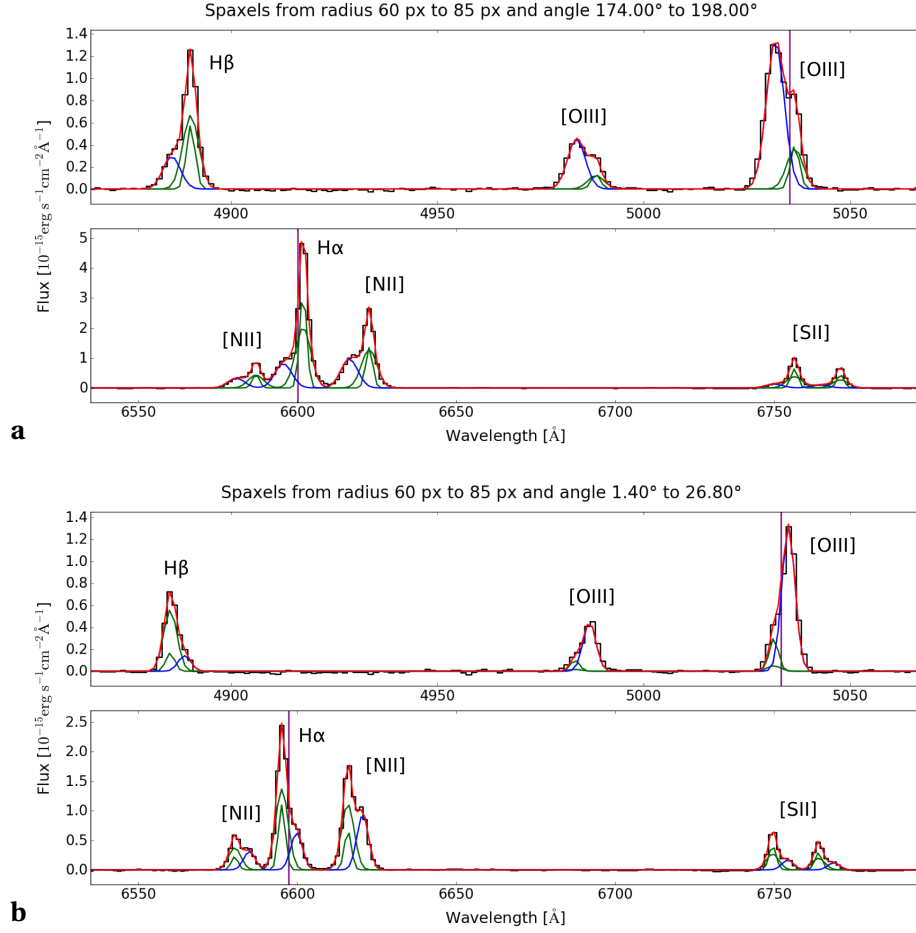
Fig. 3.8: Fit of [O III], Hβ, [N II], Hα, and [S II] lines for two elements of the grid through which we divided the out-fowing cones (see Fig. 3.7). The spectrum in **(a)** belongs to the SE blueshifted cone, the spectrum in **(b)** to the NW redshifted one. The blue Gaussian corresponds to the outflow kinematic component, the two green Gaussians (having the same velocity) to the disk; the velocity and velocity dispersion of all the Gaussians are tied between the lines. The purple vertical lines at [O III] and Hα wavelengths mark the stellar velocity for the element of the grid considered, obtained from the stellar kinematics presented in Fig. 3.6a. The reported wavelengths are in the Earth rest frame.

shifted cone. The two spectra show that the [O III] is largely dominated by the outflowing component (blue Gaussian), whereas in the other lines the dominant component is the disk one (the two green Gaussians). [O III]/Hβ is thus much higher in the outflow component compared to the disk one. [N II]/Hα is also higher in the outflow component. This holds true in general also for all the other grid elements, whose [O III]/Hβ and [N II]/Hα line ratios for the outflow component reside in the AGN-ionized part of the BPT diagrams. The disk component does not have the same velocity of the stars, indicating that, besides the outflowing gas, the gas in the disk does not follow the stellar rotation either, having redder velocities in the SE part (panel a) and bluer in the NW part (panel b). This effect is found also in the other grid elements and is exactly what emerged from the Hα velocity map subtracted by stellar velocity in Fig. 3.6f,

where non-circular motions in excess to stellar rotation came out in the direction of the bar of the galaxy, red in the SE, blue in the NW.

We calculated the outflow mass of ionized gas in each element of the grid from the flux of the outflowing component of Hα, using the following relation from Cresci et al. (2017), which assumes "Case B" recombination in fully ionized gas with electron temperature $T_e = 10^4$ K:

$$M_{\text{out}} = 3.2 \times 10^5 \, M_\odot \left(\frac{L_{\text{H}\alpha,\text{out}}}{10^{40} \text{ erg s}^{-1}} \right) \left(\frac{n_e}{100 \text{ cm}^{-3}} \right)^{-1}. \qquad (3.1)$$

In order to get the intrinsic Hα flux to be converted to luminosity, the measured Hα outflow component has been dereddened using the Balmer decrement Hα/Hβ (of the outflow component itself). However, we adopted the Balmer decrement from the entire circular shells at the same distance (separately for the two cones), rather than from the single grid elements, to increase the accuracy of the reddening correction. Indeed, the fluctuations of the Balmer decrement within each shell were consistent with being roughly constant. As expected, the outflow component results to be much more reddened in the NW cone than in the SE one, the former lying behind the galactic disk, the latter residing above the disk, with values of Hα/Hβ going from $\simeq 4.7$ to $\simeq 7.2$ ($A_V \simeq 1.3$ to $\simeq 2.5$) in the NW cone, while the SE cone has a typical ratio of 3.7 ($A_V \simeq 0.7$), with only a maximum of $\simeq 4.2$ ($A_V \simeq 1.1$). We stress that the SE outflowing cone is extincted even though it resides above the disk[5], indicating the presence of dust inside it (signatures of a dusty phase in outflows are found e.g., in Rupke & Veilleux 2015, Perna et al. 2015b; polar MIR emission from dust associated with the NLR has been observed on scales of pc up to tens of pc in some AGN, see Asmus et al. 2016, López-Gonzaga et al. 2016, Stalevski et al. 2017). This is an interesting finding as the dust might be coupled with molecular gas, which would provide the material to potentially form stars within the outflow (as observed for the first time by Maiolino et al. 2017).

The electron density n_e has been obtained from the [S II] $\lambda 6716 / \lambda 6731$ line doublet ratio of the outflow component from the fit of the whole shells (still separately for the two cones), rather than from the single elements of the grid, for the same reason of the Balmer decrement.

Both for Hα/Hβ and for n_e a few values resulting from bad fits have been replaced with the average from the two nearest shells or with the value of the nearest shell in case the shell of interest was the most internal or the most external one. Moreover, as done in Sect. 3.2.2, we set to 40 cm^{-3} all the calculated densities falling below this value, being the [S II] ratio insensitive to densities below this threshold.

We thus obtain a total ionized outflow mass from both cones of $\sim 9.2 \times 10^5 \, M_\odot$ and a total

---

[5] The SE outflowing cone has in fact approaching velocities and, in addition, the SE part of the FOV corresponds to the far part of the galactic disk, residing behind the plane of the sky (this follows from the comparison of the large-scale morphology of the galaxy in Fig. 3.1a with the stellar rotational field in Fig. 3.6a, together with the fact that the spiral arms are trailing in the rotation of the galaxy, as reported by Lindblad 1999).

kinetic energy of $\sim 4.5 \times 10^{52}$ erg, by summing the values from the single grid elements.

The mass outflow rate through a spherical surface of radius r subtended by a solid angle Ω is $\dot{M}(r) = \Omega r^2 \rho(r) v(r)$. Assuming that, within each grid element, density and outflow velocity are constant, the radial average of the outflow rate within a grid element is simply

$$\dot{M}_{\text{out}} = \frac{M_{\text{out}} v_{\text{out}}}{\Delta R}, \tag{3.2}$$

where v_{out} is the velocity of the outflow component in the galaxy rest frame and ΔR the radial width of each grid element (i.e., $\simeq 420$ pc). This outflow rate can then be interpreted as the mass of gas M_{out} flowing through each radial element of width ΔR in a time $\Delta R / v_{\text{out}}$. When using the observed outflow velocities we do not take into account geometrical projection effects and therefore our estimates are more likely lower limits. To obtain de-projected velocities a detailed 3D kinematic model is required but this is beyond the scope of this work.

The gridded map of the mass outflow rate can be inspected in Fig. 3.7. The mass outflow rate exhibits both radial and angular variations, as a consequence of the clumpiness and inhomogeneity of the outflowing gas (see kinematic maps in Fig. 3.6). We use this map to build radial profiles of the outflow physical quantities, which are presented later on in Sect. 3.4.4 where they are extensively discussed in relation with the properties of the nuclear X-ray outflow.

3.3 Chandra X-ray data analysis

NGC 1365 shows diffuse emission with roughly biconical morphology also in the soft X-rays (Wang et al. 2009), so it is worth comparing the properties of this hot gas component with those of the [O III]-emitting gas.

In this section we illustrate our analysis of six *Chandra* ACIS-S observations of NGC 1365 (ObsIDs 6868–6873). We note that *Chandra* is the only X-ray observatory affording comparable spatial resolution to our MUSE data.

3.3.1 Data description

The data have been taken with the Advanced CCD Imaging Spectrometer (ACIS; Garmire et al. 2003), positioning the galaxy inside the back-illuminated ACIS-S S3 chip, which among the ACIS-S chips has the highest energy resolution ($\simeq 74$ eV at 1.49 keV and $\simeq 147$ eV at 5.9 keV). The six snapshots, with exposure times ranging from ~13 ks to ~15 ks, for a total of ~87 ks, were acquired between April 10 and April 23, 2006. The data have been processed with the Chandra Interactive Analysis of Observations v4.6 (CIAO[6]; Fruscione et al. 2006), using the Chandra Calibration Database (CALDB[7]) v4.6.3 calibration files and following the standard reduction

---

[6] http://cxc.harvard.edu/ciao/.
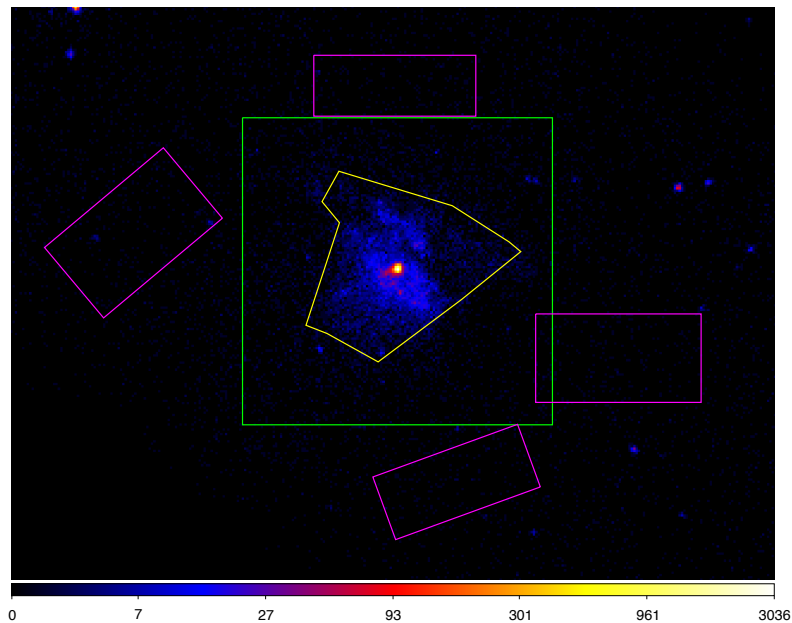[7] http://cxc.harvard.edu/caldb/.

Fig. 3.9: Full-band (0.3–8 keV) image obtained by merging the six *Chandra* ACIS-S observations of NGC 1365 of April 2006. The green box indicates the MUSE FOV. A spectrum for each of the six observations has been extracted from the yellow polygonal region, while the background has been evaluated over the magenta regions.

thread.

3.3.2 Full-band spectral fitting

In Fig. 3.9 we report the full-band (0.3–8 keV) X-ray image resulting from the combination of the six *Chandra* ACIS-S exposures of NGC 1365.

We extracted one spectrum per observation from the yellow polygonal area inside the FOV of MUSE (green box in Fig. 3.9), while the spectrum for the background-subtraction was taken from four rectangular regions free of strong point-like sources. The six spectra, which were re-binned so as to have a signal-to-noise ratio of at least 3 per energy channel, can be inspected in Fig. 3.10. The count rates in the plot are corrected for the energy-dependent effective area (this holds also for the other X-ray spectra presented in the following). We are mostly interested in the soft X-rays, as our goal is to match the extended X-ray emission with the optical one from MUSE, but we also fitted the hard X-ray part of the spectrum to isolate the unresolved emission from the active nucleus and its contribution at soft energies ($\lesssim 2$ keV). The spectra show that the hard X-ray flux varies among the observations, as the nucleus of NGC 1365 is known to alternate between obscured and unobscured states (Risaliti et al. 2007).

The spectra have been fitted using the X-ray spectral fitting package XSPEC v12.9.1 (Arnaud 1996), which is part of the NASA's HEASoft[8] release v6.20. As no variation can arise from kpc-

---

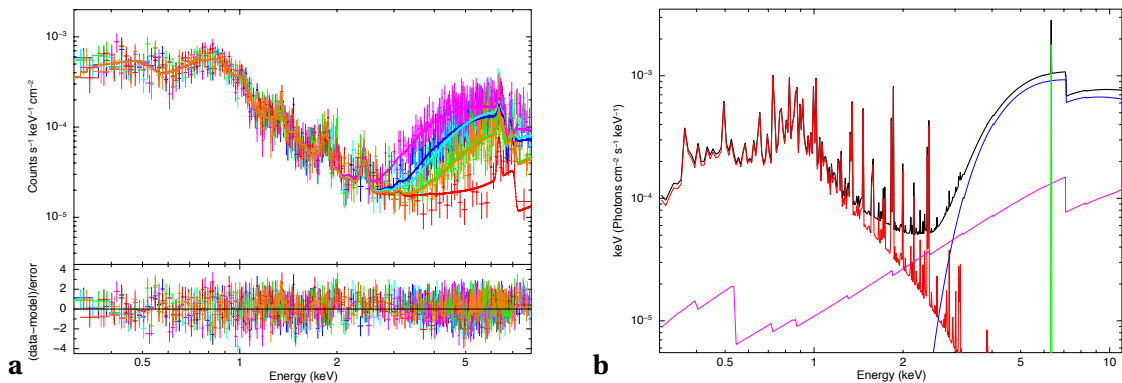[8] https://heasarc.gsfc.nasa.gov/lheasoft/.

Fig. 3.10: **(a)** Spectra of each of the six *Chandra* observations (distinguished with different colors: blue, cyan, magenta, green, red, orange in chronological order), together with the best-fitting models (solid lines of the corresponding colors). The residuals are reported in the bottom panel. **(b)** Physical model corresponding to the strongest spectrum in panel a (ObsID 6870). The single components are shown with the following color code: red for the absorbed `vapec`, thermal emission; blue for the absorbed `zpowerlaw`, primary X-ray emission; magenta for the `pexrav`, reflected continuum; green for the Gaussian emission line, fluorescent Fe I Kα at 6.4 keV. Ionized absorption barely affects the continuum and is omitted for clarity.

scale extended emission on short timescales, a constant model (red solid line in Fig. 3.10b) has been employed to reproduce the soft part of the spectrum of all the six observations, while the components adopted to fit the nuclear emission have been left free to vary among the observations. The Galactic column density, fixed to $N_H = 1.34 \times 10^{20}$ cm^{-2} (Kalberla et al. 2005), is included in each fit from now on. The total model we employed is made up of the following XSPEC components:

- `vapec:` emission spectrum from collisionally-ionized optically-thin gas calculated from the AtomDB atomic database[9], attenuated by foreground absorption (modeled with `phabs`). Following the approach of Wang et al. (2009), the abundances of O, Ne, Mg, Si, and Fe have been left free to vary, while Solar abundance has been assumed for all the other elements. This component has been introduced to fit the soft diffuse emission.

- `zpowerlw:` simple power law for the primary X-ray continuum from the AGN, in the rest frame of the galaxy. This is multiplied by `phabs` to account for the absorption due to neutral material along the line of sight. A common photon index has been used for all observations, while the normalization of the continuum and the column density of the absorber have been left free to vary to reproduce the different flux states.

- `pexrav:` power-law spectrum reprocessed by neutral material (Magdziarz & Zdziarski 1995), accounting for the fraction of X-ray continuum reflected by distant material into the line of sight.

---

[9] http://atomdb.org.

- One `zgauss`: one Gaussian profile, employed to fit the Fe I Kα fluorescent line at 6.4 keV (rest frame) produced by the distant material irradiated by the nuclear emission. The width of the line is expected to be much smaller than the energy resolution of the instrument (~150 eV), so it has been fixed to 10 eV.

- Two `zgauss`: two Gaussian profiles to fit the ionized Fe XXV and Fe XXVI Kα absorption lines (at 6.7 keV and 6.97 keV rest-frame energy, respectively) due to foreground highly-ionized gas absorbing the primary nuclear continuum, which are usually blueshifted due to their origin within an accretion-disk wind. The observed energy is forced to be the same for all the observations, while the normalizations were left free to vary.

The best-fitting models, matching in color with the respective spectra, are superimposed to the data in Fig. 3.10a, while the various components (corresponding to the highest nuclear state, in the third observation) are disentangled in Fig. 3.10b. The best fit parameters together with the associated errors (90% confidence intervals) are presented in Table 3.1, and are in good agreement with previous studies. The primary X-ray continuum from the AGN is fitted with a power-law of spectral index $\Gamma = 2.10 \pm 0.25$ and variable foreground column density, going from the lowest value of $N_H \simeq 27 \times 10^{22}$ cm^{-2} (ObsID 6870) to the highest one of $N_H \simeq 189 \times 10^{22}$ cm^{-2} (ObsID 6872), when the nucleus experienced a Compton-thick state. The Fe XXV and Fe XXVI features are blueshifted, implying an outflow velocity of $v \simeq -4540$ km s^{-1}. The best fit for the thermal model used for the soft part of the spectrum gives a temperature for the collisionally-ionized optically-thin gas of $kT \simeq 0.66$ keV (corresponding to $T \sim 8 \times 10^6$ K). Overall, the fit is very good, with $\chi^2/\nu = 1305/1281$.

In order to further inspect the nuclear outflow arising from the blueshifted Fe XXV and Fe XXVI absorption lines, we fitted them with a detailed absorption model instead of with two simple Gaussians, considering only the observations where such lines are clearly visible as the continuum is not heavily suppressed, namely ObsIDs 6868–6870. We used an XSTAR grid (Kallman & Bautista 2001) to reproduce the high-ionization absorber responsible for the two lines, multiplied to the `zpowerlaw` for the primary nuclear continuum, tying the parameters of the absorber to be the same over the three observations. We left the continuum normalization and the column of the neutral absorber free to vary, guiding the intensity of the iron lines. We obtained a velocity of the outflowing gas of -4915^{+1205}_{-1320} km s^{-1} and an intrinsic column density of the absorbing gas of $N_H \sim 3 \times 10^{24}$ cm^{-2} (for Solar abundances). The accretion-disk wind in NGC 1365 is persistent, as it regularly appears in the less obscured nuclear states, yet it is also rather variable. Both the outflow velocity and the column density derived above lie close to the upper end of the respective ranges, as observed over the years (e.g., Risaliti et al. 2005; Brenneman et al. 2013; Braito et al. 2014). While these values can certainly provide an upper limit to the mass outflow rate at subpc scales, in order to obtain a more sensible estimate to compare

Table 3.1: Best-fit parameters for the different XSPEC model components used to fit the spectra of Fig. 3.10: primary (1) and reflected (2) AGN emission, Fe I Kα (E = 6.4 keV) emission line (3), Fe XXV (4; E = 6.7 keV) and Fe XXVI (5; E = 6.97 keV) absorption lines, thermal emission (6). N_H: column density; Γ: power-law photon index; A: power-law normalization at 1 keV; F: integrated flux of the spectral line; kT: plasma temperature; Z: elemental abundance; EM: emission measure. (t) indicates tied parameters; (f) marks fixed parameters.

Model	ObsID 6868	ObsID 6869	ObsID 6870	ObsID 6871	ObsID 6872	ObsID 6873
(1) zpowerlw						
N_H (10^{22} cm^{-2})	40^{+5}_{-4}	48^{+5}_{-4}	27^{+3}_{-2}	61^{+10}_{-9}	189^{+76}_{-35}	64^{+10}_{-9}
Γ	$2.10^{+0.25}_{-0.25}$	2.10(t)	2.10(t)	2.10(t)	2.10(t)	2.10(t)
A (10^{-2} cm^{-2} s^{-1} keV^{-1})	$1.16^{+0.81}_{-0.48}$	$1.54^{+1.08}_{-0.64}$	$1.16^{+0.74}_{-0.45}$	$1.01^{+0.83}_{-0.47}$	1.07(t)	$1.03^{+0.85}_{-0.48}$
(2) pexrav						
A (10^{-2} cm^{-2} s^{-1} keV^{-1})	$1.07^{+0.42}_{-0.32}$	1.07(t)	1.07(t)	1.07(t)	1.07(t)	1.07(t)
(3) zgauss$_{(Fe\,I\,K\alpha\,em.)}$						
E (keV)	$6.38^{+0.02}_{-0.03}$	6.38(t)	6.38(t)	6.38(t)	6.38(t)	6.38(t)
F (10^{-6} cm^{-2} s^{-1})	$8.2^{+2.6}_{-2.6}$	8.2(t)	8.2(t)	8.2(t)	8.2(t)	8.2(t)
(4) zgauss$_{(Fe\,XXV\,abs.)}$						
v (km s^{-1})	-4540^{+875}_{-885}	-4540(t)	-4540(t)	-4540(t)	-4540(t)	-4540(t)
F (10^{-6} cm^{-2} s^{-1})	$-15.4^{+3.3}_{-3.3}$	-15.4(t)	-15.4(t)	> -9.06	0 (f)	> -9.06(t)
(5) zgauss$_{(Fe\,XXVI\,abs.)}$						
v (km s^{-1})	-4540(t)	-4540(t)	-4540(t)	-4540(t)	-4540(t)	-4540(t)
F (10^{-6} cm^{-2} s^{-1})	$-9.8^{+4.2}_{-4.2}$	-9.8(t)	-9.8(t)	> -6.35	0 (f)	> -6.35(t)
(6) vapec						
N_H (10^{22} cm^{-2})	$0.059^{+0.016}_{-0.020}$	0.059(t)	0.059(t)	0.059(t)	0.059(t)	0.059(t)
kT (keV)	$0.66^{+0.06}_{-0.03}$	0.66(t)	0.66(t)	0.66(t)	0.66(t)	0.66(t)
Z_O ($Z_\odot$)	$0.08^{+0.08}_{-0.05}$	0.08(t)	0.08(t)	0.08(t)	0.08(t)	0.08(t)
Z_{Ne} ($Z_\odot$)	$0.21^{+0.12}_{-0.10}$	0.21(t)	0.21(t)	0.21(t)	0.21(t)	0.21(t)
Z_{Mg} ($Z_\odot$)	$0.36^{+0.09}_{-0.08}$	0.36(t)	0.36(t)	0.36(t)	0.36(t)	0.36(t)
Z_{Si} ($Z_\odot$)	$0.49^{+0.09}_{-0.08}$	0.49(t)	0.49(t)	0.49(t)	0.49(t)	0.49(t)
Z_{Fe} ($Z_\odot$)	$0.06^{+0.01}_{-0.01}$	0.06(t)	0.06(t)	0.06(t)	0.06(t)	0.06(t)
EM (10^{63} cm^{-3})	$3.75^{+0.54}_{-0.50}$	3.75(t)	3.75(t)	3.75(t)	3.75(t)	3.75(t)

to the mass outflow rate in the optical cones we adopt the average values of $v = -3000$ km s^{-1} and $N_H = 10^{23}$ cm^{-2}. While the latter might seem too conservative, it also takes into account the possible overabundance of iron by a factor of a few with respect to Solar standards (e.g., Risaliti et al. 2013), which proportionally reduces the equivalent hydrogen column density.

We compute the mass outflow rate using equation (2) in Nardini & Zubovas (2018), which assumes that the wind covers a solid angle of 2π (comparable to the opening angle of the optical cones in a biconical geometry) and that the launch radius corresponds to the escape radius for the adopted outflow velocity. We get $\dot{M}_{out,X} \sim 0.15\ M_7\ M_\odot$ yr^{-1}, where M_7 is the mass of the central SMBH (in units of $10^7\ M_\odot$). As no reverberation mapping measure exists for NGC 1365,

there is large uncertainty on the SMBH mass, but this is most likely few times 10^6 $M_\odot$ (e.g., Risaliti et al. 2009, Davis et al. 2014, Onori et al. 2017). For $M_7 = 0.45$ (Onori et al. 2017), the mass outflow rate of the X-ray wind is $\dot{M}_{\text{out,X}} \sim 0.067$ $M_\odot$ yr^{-1} and the kinetic energy rate is $\dot{E}_{\text{k,out,X}} \sim 1.9 \times 10^{41}$ erg s^{-1}. This is about 0.9% of the bolometric luminosity of the AGN (L_{bol} $\sim 2.2 \times 10^{43}$ erg s^{-1}), which we calculated from the average de-absorbed 2-10 keV luminosity from our six observations $L_{\text{X, 2-10 keV}} \sim 1.7 \times 10^{42}$ erg s^{-1} using the median bolometric correction for Type 2 AGN $\langle k_{\text{bol}} \rangle \sim 13$ from Lusso et al. (2011).

Moreover, from $L_{\text{X, 2-10 keV}}$ we can calculate the expected [O III] luminosity in the NLR and compare it with the one we measure from MUSE. Using $L_{\text{X, 2-10 keV}}$–$L_{[\text{O III}]}^{\text{cor}}$ relation from Ueda et al. (2015) for Type 2 AGN, we obtain an extinction-corrected [O III] luminosity of $L_{[\text{O III}]}^{\text{cor}} \sim 2.6 \times 10^{40}$ erg s^{-1}, which is about a factor of three smaller than $L_{[\text{O III}]}^{\text{cor}} \sim 8 \times 10^{40}$ erg s^{-1} that we obtain from the two [O III] cones from MUSE. However, this discrepancy is well within the scatter on the $L_{\text{X, 2-10 keV}}$–$L_{[\text{O III}]}^{\text{cor}}$ relation of Ueda et al. (2015) and also consistent with the fact that in their sample all the Type 2 AGN at low $L_{\text{X, 2-10 keV}}$, on the order of 10^{42} erg s^{-1}, reside above their relation. We obtain the extinction-corrected [O III] luminosity of the cones by extracting and fitting two integrated spectra (one per cone) produced by summing up all the spaxels of each of the two cones. The spatial region covered by each cone is defined by the angles used in Fig. 3.7 extended to the margins of the FOV. We use two Gaussian components per emission line, one to reproduce the disk and one for the outflow. The obtained line flux of the outflow component is corrected for extinction using the average Balmer decrement from the fit of the radial shells in Sect. 3.2.4. We do not adopt the Hα/Hβ from these two fits because, as we integrate over the whole cones, we are taking parts of the disk and of the outflow with different velocities, which can overlap together in some areas, giving a fitted outflow component of Hα and Hβ that may be in part affected by the emission from the disk and consequently an unreliable extinction. We take the total [O III] luminosity (outflow + disk) for this comparison with Ueda et al. (2015), instead of the luminosity of the outflow component only, because the [O III] luminosities used in their work (and similar works involving $L_{[\text{O III}]}$–L_{X} relation) are the total ones, as the imaging data used did not allow them to distinguish between outflow and disk component.

Having the bolometric luminosity L_{bol}, we can also estimate the mass accretion rate as follows:

$$\dot{M}_{\text{accr}} = \frac{L_{\text{bol}}}{\eta c^2}, \tag{3.3}$$

being η the radiative efficiency and c the speed of light. Assuming $\eta = 0.1$, which is the typical value for a Shakura-Sunyaev accretion disk (Shakura & Sunyaev 1973), we get $\dot{M}_{\text{accr}} \sim 4 \times 10^{-3}$ $M_\odot$ yr^{-1}. This is a factor of 17 smaller than the nuclear mass outflow rate we obtained from the blueshifted Fe XXV and Fe XXVI absorption lines. This suggests that the X-ray outflow might have already experienced mass loading since its launch from the innermost regions close to

the BH. Indeed, the X-ray outflow in NGC 1365 is an anomalous case, as its velocity of ~3000 km s^{-1} is about one order of magnitude lower than the typical velocities of ultra fast outflows (UFOs) and at the upper limit of the velocity of warm absorbers (Tombesi et al. 2013), although having an ionization typical of UFOs. UFOs are associated to a very initial stage of the outflow close to the BH (e.g., Nardini et al. 2015a), but they might not be observable in absorption if the gas participating in them is completely ionized by the strong AGN radiation field close to the BH (Pinto et al. 2018). A UFO might then be present in NGC 1365 but not detectable, becoming observable only on a larger scale after it has done mass loading and slowed down. Another possibility to explain the UFO-like ionization of the outflow and its velocity a factor of at least 10 smaller than UFO typical velocities might be that the outflow is actually a UFO but only a little fraction of its velocity is directed in our line of sight. However, this would imply an inclination of the nuclear outflow axis close to 90° with respect to the line of sight, which is highly unlikely, either considering an accretion disk coplanar with the galaxy disk (which is inclined by 35° relative to the line of sight; Hjelm & Lindblad 1996) or the estimate of 63° for the inclination of the accretion disk from Risaliti et al. (2013).

3.4 MUSE–Chandra matching

In this section we present the spatial matching between MUSE optical data showed in Sect. 3.2 and *Chandra* ACIS-S X-ray data presented in Sect. 3.3. With the aim of comparing the distribution of the X-ray emitting ionized gas and of the optically-emitting one from MUSE, we extracted different images in selected X-ray energy bands. We also compare the properties of the nuclear X-ray wind with those of the extended ionized outflow to obtain a more comprehensive picture of the outflow in NGC 1365.

3.4.1 Diffuse emission

The smoothed contours of the 0.3–1.2 keV soft X-ray emission (compare with Fig. 3.10) are superimposed in Fig. 3.11a on the [O III] (green) and Hα (red) maps obtained from the fit of the star-subtracted smoothed MUSE data cube. The 0.3–1.2 keV contours trace very well both the [O III]-dominated regions, corresponding to the SE and NW cones, and the Hα ones, following the shape of the circumnuclear star-forming ring and of the long lane at the edge of the dust lane. The soft X-ray emission then seems to be associated in part with the AGN-ionized cone, in part with the star formation dominating in the circumnuclear ring and, in general, in the elongated diagonal region in the direction NE–SW (see the spatially resolved BPT maps in Fig. 3.5).

In order to analyze in more detail the diffuse soft X-ray emission, we merged the six spectra extracted from the polygonal region in Fig. 3.9, having constrained the nuclear X-ray emission with the full-band spectral fitting in Sect. 3.3.2. The combined spectrum was then binned to a
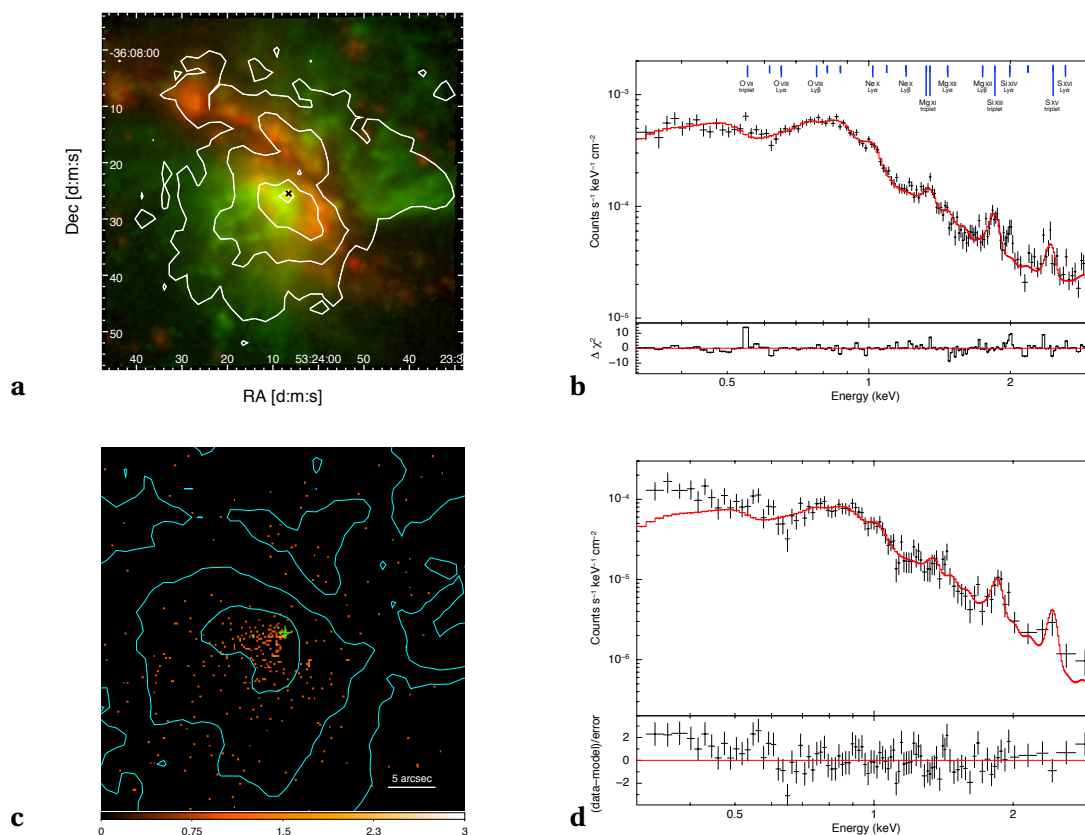
Fig. 3.11: **(a)** 0.3–1.2 keV *Chandra* ACIS-S soft X-ray emission (contours) superimposed on the [O III] (green) and Hα (red) emission fitted from the star-subtracted smoothed MUSE data cube (same as in Fig. 3.4a). **(b)** Soft X-ray emission extracted from the yellow polygonal region in Fig. 3.9. The data are in black, resulting from the merging of the six extracted spectra. Red is the best fit, having used a thermal emission model. The residuals are reported on the bottom. The labeled blue lines on top indicate the statistically significant (at 95% level) emission lines in the *Chandra* HETG spectra, after accounting for the collisional component, from Nardini et al. (2015b). **(c)** Unsmoothed 0.3–0.4 keV emission and [O III] contours from MUSE, zooming in the central regions of MUSE FOV. **(d)** Spectrum extracted from the inner contour of [O III] in panel c (excluding the nucleus).

S/N of 5 per channel. We thus performed a fit in the energy range 0.3–3 keV, fixing the parameters of the nuclear components to the values found in Sect. 3.3.2 (see Table 3.1), only allowing the normalization of the primary continuum and the column density of the neutral absorber to slightly re-adjust to fit the average spectral shape, as they both vary among the single observations. We note that the transmitted nuclear contribution becomes rapidly negligible below 3 keV, and only the faint and virtually featureless reflected component survives.

We fitted the soft X-ray emission with a single `vapec` thermal component. The best fit gave fully consistent results with the previous analysis, but the individual parameters are now better constrained, with $kT = 0.66^{+0.01}_{-0.03}$ keV and $N_H = 0.065^{+0.016}_{-0.015} \times 10^{22}$ cm^{-2}. The same holds for the elemental abundances. The fit statistics, however, is rather poor ($\chi^2/\nu = 255/135$). The merged spectrum together with the best-fit model and the relative residuals is shown in Fig. 3.11b. Fol-

lowing previous works (e.g., Wang et al. 2009, Guainazzi et al. 2009), we tried to add another collisionally-ionized component with the same abundances, but, although slightly improving the goodness of fit ($\chi^2/\nu = 212/132$), this does not return a statistically acceptable solution, indicating that a thermal model is unable to account for the main residuals. Indeed, as reported by Nardini et al. (2015b) and Whewell et al. (2016), the soft X-ray spectrum of NGC 1365 also contains a multiphase component photoionized by the AGN, producing a wealth of emission lines. The energies of the lines detected at the 95% confidence level after accounting for the collisional component in the high-resolution *Chandra* HETG spectrum by Nardini et al. (2015b) are reported in the figure. The most prominent residuals in our low resolution spectrum, at ~0.55 and 2 keV, correspond to the O VII triplet and to the Si XIII Lyα, respectively, which both have a photoionization origin. Despite the limited data quality, tentative positive residuals can be seen at the energy of several other photoionized lines.

3.4.2 Inner ionization cone

Thanks to a very deep analysis of all the available high-resolution X-ray data of NGC 1365, Whewell et al. (2016) identified two collisionally ionized and three photoionized gas phases in the soft X-ray emission-line spectrum. In their spectral decomposition, the photoionized components start to prevail below ~0.5 keV. Unfortunately, there are only few strong lines at these energies. Neglecting the N VI triplet at ~0.43 keV, which requires nitrogen abundance of 4.5 times Solar to be properly accounted for, we focused on the C VI Lyα line at ~0.37 keV, and extracted a narrowband *Chandra* image in the 0.3–0.4 keV range. Fig. 3.11c shows a zoom on the central regions of the FOV, with the unsmoothed 0.3–0.4 keV emission and the [O III] contours from MUSE superimposed on it. The figure reveals that the very soft X-ray emission, dominated by photoionized gas, perfectly traces the inner and most intense part of the [O III]-emitting AGN-dominated SE cone. We thus extracted the spectrum (one for each observation) of this region to further inspect the soft X-ray emission in the cone. The merged spectrum can be seen in Fig. 3.11d, together with the best-fit thermal model (red line) previously obtained for the extended soft X-ray emission (Fig. 3.11b), simply rescaled to the flux of this spectrum. An excess with respect to the scaled model emerges below ~0.5 keV, indicating that the emission in the inner part of the cone has an additional contribution compared to the extended thermal emission. We also tried to refit the model (an absorbed `vapec`) to the data, but it was still not able to reproduce the observed excess, which can then be attributed to a blend of emission lines (due to low resolution and limited statistics) photoionized by the AGN.

In order to obtain a rough guess of the luminosity of this excess component, we fitted it with a simple blackbody model, getting a luminosity of $\sim 2 \times 10^{39}$ erg s^{-1}. We get an [O III] luminosity over the same region of $\sim 5 \times 10^{39}$ erg s^{-1} from MUSE data, which is of the same order of magnitude, thus supporting the scenario of a common energy input for the two emissions,
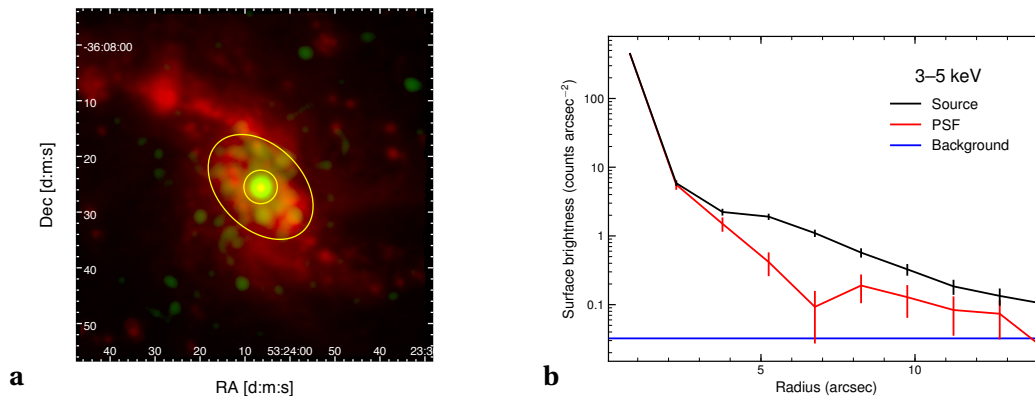
Fig. 3.12: **(a)** 3–5 keV emission (green) together with Hα emission (red) from MUSE. **(b)** Radial profile of the surface brightness in the energy range 3–5 keV (black) versus the simulated PSF of the nucleus (red) from the brightest, less obscured state of the AGN (ObsID 6870); the level of the background is also reported (blue).

that is, the AGN photoionization. This is expected for Sy2 galaxies (see e.g., Bianchi et al. 2006), but it is not straightforward for NGC 1365, being the soft (0.3–2 keV) X-ray band dominated by thermal emission due to the intense star formation. Nevertheless, we have shown that using the appropriate strategy the photoionized component can be isolated. While Nardini et al. (2015b) were able to reveal the diluted photoionized emission by adopting a narrow extraction region close to the nucleus, here we have reached the same results by choosing the proper energy band, which allowed us to find the cospatiality of the X-ray photoionized component with the [O III]. NGC 1365 is then a standard obscured AGN, whose peculiar spectral properties (such as thermal emission dominating over photoionization in the soft X-rays) are most likely due to the much higher star-formation compared to normal Sy2s.

3.4.3 Star-forming ring

While the AGN radiation field clearly dominates the photoionization in the cones, the circumnuclear starburst ring can, in principle, contribute to the driving of the outflow. Soft X-ray emission from collisionally-ionized gas is typical of shock heating associated with starburst winds (e.g., Veilleux et al. 2005, and references therein). In general, one should expect that the larger the gas temperature, the faster the shocks and the larger the injection of mechanical energy (e.g., McKee & Hollenbach 1980). Even if we were able to obtain a good fit of the soft X-ray continuum with a single `vapec` component of $kT \simeq 0.66$ keV, this is just a phenomenological approximation of the emission from a multitemperature gas known to be present in the circumnuclear environment. In Fig. 3.12a the 3–5 keV smoothed hard X-ray emission (green) can be compared with Hα emission (red). Besides the nuclear point source, there is an extended component that is cospatial with the elongated star-forming ring traced by the strong Hα emission, suggesting that the diffuse 3–5 keV emission is associated with the star-forming processes

occurring in the ring. This can be due to hotter diffuse gas and/or X-ray binaries.

The extended nature of the 3–5 keV emission is confirmed by the radial profile of the surface brightness in this band reported in Fig. 3.12b (black curve), compared to the simulated PSF of the nucleus (red) generated with the *Chandra* Ray Tracer[10] and MARX[11] suites. The brightest, less obscured state of the AGN (ObsID 6870) was considered to be as much conservative as possible. Still, there is a significant excess in the surface brightness with respect to the wings of nuclear PSF at the scale of the ring, confirming that there is extended local emission in addition to the unresolved source. In order to evaluate the spectral properties of this component, we selected an elliptical region encompassing the ring, and excising the central 3 arcsec (in radius) around the nucleus (Fig. 3.12a). This ensures that any contribution from the wings of the nuclear PSF is minimized. The combined spectrum of the ring from the six observations was fitted with the same model of Sect. 3.3.2, including an absorbed `pshock` component to account for any emission from hot, shocked gas (following Wang et al. 2014). The collisionally-ionized and nuclear components were fixed to the best fit values of Table 3.1, simply rescaled through constant factors. From the former, we get that about 40% of the thermal emission arises in the ring, while the latter implies that the nuclear PSF leakage amounts to only 2%, in excellent agreement with the simulated PSF. The shock component, absorbed by a column of $(5 \pm 2) \times 10^{21}$ cm^{-2}, improves the χ^2/ν from 341/182 to 213/179, but its temperature is poorly constrained. Taking the nominal best-fit value of 4.8 keV as the post-shock temperature in a fully ionized, monoatomic gas, we would derive a shock velocity of ~2000 km s^{-1}. The intrinsic luminosity of this component is $\approx 1.5 \times 10^{40}$ erg s^{-1} (this is most likely an upper limit, as a similar contribution is expected from the high-mass X-ray binary population of the ring, based on the SFR of the ring of ~5.6 $M_\odot$ yr^{-1} from Alonso-Herrero et al. 2012 and the predictions from Mineo et al. 2012), to be compared to the expected rate of energy injection from SNe of ~ 2×10^{41} erg s^{-1}, assuming the standard 10^{51} erg per SN and 10% efficiency, and a SN rate in the ring of 0.07 yr^{-1} (Wang et al. 2009). In order to achieve a kinetic energy rate comparable to the one previously estimated for the AGN wind (~ 2×10^{41} erg s^{-1}), 2 $M_\odot$ per SN would be required to be entrained in such a fast outflow from the SF ring.

From an energetic point of view this SNe shock might then be capable of driving the extended optical outflow. Moreover, the highest values of the mass outflow rate are observed on the scale of the SF ring (Fig. 3.13a), which might suggest a correlation between the ring and the outflow, even though the mass outflow rate remains still high at larger distances compared to the ring scale, before dropping.

So, the SNe shock in the ring, if actually present, might contribute in principle to the kpc-scale wind we observe from MUSE, but it is not clear to which extent or how (if by directly

---

[10] http://cxc.harvard.edu/chart/.
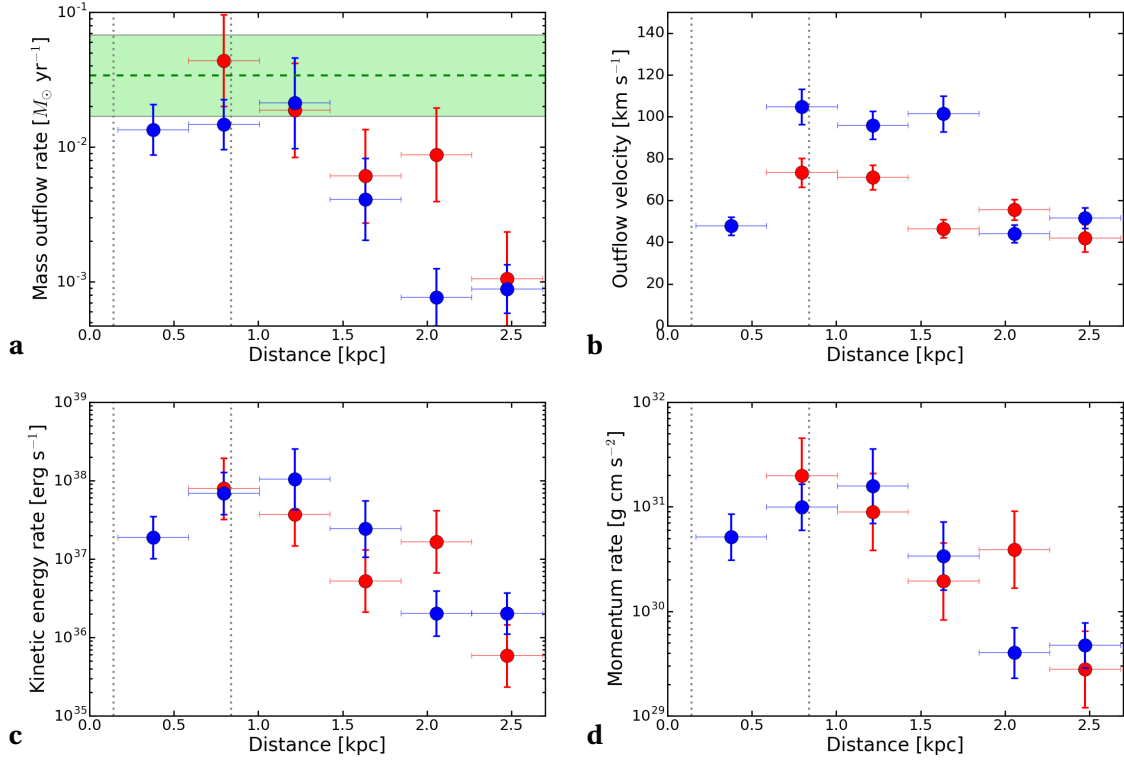[11] http://space.mit.edu/cxc/marx/.

Fig. 3.13: **(a)** Mass outflow rate of the ionized gas as a function of distance from the active nucleus, obtained from the gridded map in Fig. 3.7; blue and red points indicate the sum of the mass outflow rates of all the grid elements at a certain distance, for the SE (blueshifted) cone and for the NW (redshifted) one, respectively. The error bars on the distance indicate the width of the radial shells. The green dashed line is the mass outflow rate obtained for the nuclear outflow from Fe XXV and Fe XXVI absorption lines from *Chandra* X-ray data (Sect. 3.3), together with its typical uncertainty in shaded green; the two dotted gray lines mark the scale of the inner minor semi-axis and of the outer major semi-axis of the circumnuclear SF ring, respectively. **(b)** Absolute value of the outflow velocity; the points indicate the average velocity at the given distance. **(c)** Kinetic energy rate radial profile. **(d)** Momentum rate radial profile.

pushing out material to large distances or only by adding additional mass to the passing AGN outflow). With the present X-ray data quality, it is therefore impossible to quantify the additional contribution of the starburst to the AGN outflow.

3.4.4 Multiphase outflow properties

Here we present an extensive analysis of the outflow in NGC 1365, by comparing the properties and energetics of the extended ionized phase with those of the nuclear X-ray phase.

In Fig. 3.13 we show the mass outflow rate, the outflow velocity, the kinetic energy rate, and the momentum rate as a function of distance from the active nucleus. These are obtained from the gridded map of the mass outflow rate (Fig. 3.7) that we have produced in Sect. 3.2.4. The kinetic energy rate and the momentum rate are defined as $\dot{E}_{\mathrm{k,out}} = 1/2\,\dot{M}_{\mathrm{out}}\,v_{\mathrm{out}}^2$ and $\dot{p}_{\mathrm{out}} = \dot{M}_{\mathrm{out}}\,v_{\mathrm{out}}$, respectively. The plotted points of mass outflow rate, kinetic energy rate, and momentum rate are the sum of the values of these quantities in the grid elements at the same

Table 3.2: Mass outflow rate ($\dot{M}_{\text{out}}$), outflow velocity (v_{out}), kinetic energy rate ($\dot{E}_{\text{k,out}}$), and momentum rate ($\dot{p}_{\text{out}}$) of the ionized gas as a function of distance from the center for both the SE (blueshifted) and the NW (redshifted) cone, as reported in Fig. 3.13.

Distance [kpc]	Cone	0.38	0.80	1.22	1.64	2.06	2.48
$\dot{M}_{\text{out}}$ [$10^{-2}\ M_\odot\ \text{yr}^{-1}$]	SE	$1.3^{+0.7}_{-0.5}$	$1.5^{+0.8}_{-0.5}$	$2.1^{+2.5}_{-1.1}$	$0.4^{+0.4}_{-0.2}$	$0.08^{+0.05}_{-0.03}$	$0.09^{+0.05}_{-0.03}$
	NW	–	4^{+5}_{-2}	$1.9^{+2.3}_{-1.0}$	$0.6^{+0.7}_{-0.3}$	$0.9^{+1.1}_{-0.5}$	$0.11^{+0.13}_{-0.06}$
v_{out} [km s^{-1}]	SE	-48 ± 4	-105 ± 8	-96 ± 7	-101 ± 9	-44 ± 4	-52 ± 5
	NW	–	$+73 \pm 7$	$+71 \pm 6$	$+47 \pm 4$	$+56 \pm 5$	$+42 \pm 7$
$\dot{E}_{\text{k,out}}$ [10^{37} erg s^{-1}]	SE	$1.9^{+1.6}_{-0.9}$	7^{+6}_{-3}	10^{+15}_{-6}	$2.4^{+3.1}_{-1.4}$	$0.20^{+0.19}_{-0.10}$	$0.20^{+0.17}_{-0.09}$
	NW	–	8^{+12}_{-5}	4^{+6}_{-2}	$0.5^{+0.8}_{-0.3}$	$1.7^{+2.5}_{-1.0}$	$0.006^{+0.009}_{-0.004}$
$\dot{p}_{\text{out}}$ [10^{30} g cm s^{-2}]	SE	5^{+3}_{-2}	10^{+7}_{-4}	16^{+20}_{-9}	$3.4^{+3.8}_{-1.8}$	$0.40^{+0.30}_{-0.17}$	$0.47^{+0.30}_{-0.18}$
	NW	–	20^{+26}_{-11}	9^{+12}_{-5}	$1.9^{+2.6}_{-1.1}$	4^{+5}_{-2}	$0.28^{+0.37}_{-0.16}$

distance, while in the case of the outflow velocity they are the average of the velocities at the given distance. The values reported in the plots are tabulated in Table 3.2. The uncertainties have been estimated through a Monte Carlo simulation[12].

By inspecting the mass outflow rate in the two cones as a function of distance (Fig. 3.13a) we see that, especially in the SE blueshifted cone, there is an initial almost constant or slightly increasing trend up to ~1 kpc, followed by a sharp drop of up to an order of magnitude at larger distances, from $>10^{-2}\ M_\odot\ \text{yr}^{-1}$ to $\sim 10^{-3}\ M_\odot\ \text{yr}^{-1}$. The decreasing trend is more irregular in the NW redshifted cone but still clearly present. The constant or slightly increasing values at smaller distances seen in the SE cone are not evident in the NW one, but the shell at the smallest distance is absent in the latter. Moreover, the second shell has the highest values of reddening, which could have been slightly overestimated, resulting in an overestimated mass outflow rate. At any rate, the red points (NW cone) are generally consistent with the blue ones (SE cone) within the uncertainties.

The green dashed line in Fig. 3.13a indicates the estimate of the nuclear mass outflow rate from the *Chandra* X-ray data from the Fe XXV and Fe XXVI absorption lines (Sect. 3.3), divided by 2 to be compared to the optical mass outflow rates of the single cones, giving 0.034 $M_\odot\ \text{yr}^{-1}$ for $M_7 = 0.45$ (Onori et al. 2017). The nuclear X-ray mass outflow rate is consistent with the optical one in the inner three radial shells (after which the mass outflow rate in the cones drops).

However, we stress that, while the X-ray mass outflow rate is an instantaneous quantity, the

---

[12] We have generated mock spectra from the observed data by perturbing the flux value of each spectral channel from its real value according to its statistical variance. We have then performed a spectral fitting of each mock spectrum, giving the estimates of the free parameters. This simulation results in a distribution for all free parameters, from which we have derived the various uncertainties, that we propagated.

optical mass outflow rate of the extended gas traces the time-averaged past activity, and this aspect has to be kept in mind when comparing them (although the mass outflow rate calculated in Eq. 3.2 is defined as instantaneous according to the usual conventions for extended outflows; e.g., González-Alfonso et al. 2017). In addition, the velocities we measure for the two outflows may also be subject to different projection effects, due to the different nature of the two signatures (absorption lines for the X-ray outflow, emission lines for the optical one). Moreover, the mass outflow rate measured from the X-rays is the total nuclear mass outflow rate, as all the gas belonging to the nuclear outflow is expected to be in a highly ionized phase, while the optical outflow we observe from MUSE only samples the ionized gas, thus missing the contribution to the outflow mass from the neutral atomic and molecular phases. Therefore, the total mass outflow rate of the kpc-scale outflow is expected to be larger than the sky-projected one we measure only for the ionized gas and, consequently, larger than the nuclear one.

As just emphasized, we are only measuring the ionized phase of the gas, whose fraction at a given distance from the ionizing source (which in case of the outflow in NGC 1365 is the AGN) depends on the fraction of ionizing photons intercepting the gas clouds at that distance, which is, in turn, determined by the covering factor of the clouds and by the shading of the AGN flux by the gas from smaller distances. The putative case that the mass outflow rate is constant with distance (when considering all the gas phases) might then result in an ionized mass outflow rate which radially decreases if the gas at larger distances receives less ionizing photons than the gas at smaller distances. Assuming that the total gas mass in each radial shell is conserved, this would imply that velocity would also remain constant with distance. Overall, this explanation does not seem to apply to NGC 1365, since the outflow velocity clearly varies with distance over the radial extent of the outflow (Fig. 3.13b). However, we cannot rule out that this occurs locally, as the velocity stays roughly constant over two to three consecutive radial shells both in the SE and in the NW cone. The radial profile of the velocity reflects in general that of the mass outflow rate, as there is a decrease of the velocity in the outer two-three points compared to the inner ones. However, there are some differences between the two, as the innermost shell of the SE cone has almost half the velocity of the three following ones and the NW cone has lower maximum velocities (of about 20-30 km s^{-1}) compared to those of the SE cone. Moreover, the velocity of the NW cone has already declined to about 40-50 km s^{-1} at ~1.5 kpc, where the velocity of the SE cone is instead still as high as in the inner shells (~100 km s^{-1}).

The radial profile of kinetic energy rate and momentum rate reflects that of mass outflow rate and velocity (being a by-product of those quantities), though the rising and dropping trend with distance is more regular in this case. Decreasing trends with distance of either outflow velocity, mass outflow rate, and outflow energetics are observed in AGN also for example by Cicone et al. (2015), Karouzos et al. (2016a), Karouzos et al. (2016b), Bae et al. (2017). Crenshaw et al. (2015) and Revalski et al. (2018) performed a grid- or shell-like analysis of the outflow

similar to ours on two single galaxies (NGC 4151 and Mrk 573, respectively), both finding a rising and dropping trend of mass outflow rate, kinetic rate, and momentum rate as we do, but on scales smaller than ours. They cover in fact a radial distance smaller than ~140 pc and ~600 pc, respectively, against the ~2.5 kpc of our case, and the above outflow quantities peak at ~70-90 pc and ~210 pc in their respective cases, while they peak at ~1 kpc in our work.

To compare the energetics of nuclear and extended outflow in NGC 1365, we consider their kinetic energy rate and momentum rate, which are $\dot{E}_{k,out,X} \sim 1.9 \times 10^{41}$ erg s^{-1} and $\dot{p}_{out,X} \sim 1.3 \times 10^{33}$ g cm s^{-2} for the X-ray outflow and $\dot{E}_{k,out} \lesssim 2 \times 10^{38}$ erg s^{-1} and $\dot{p}_{out} \lesssim 3 \times 10^{31}$ g cm s^{-2} for the optical outflow (these are the peak values of the optical outflow, corresponding to the second and third radial shell; Figs. 3.13c and 3.13d). In order to have momentum conservation between the nuclear X-ray outflow and the large scale outflow in all its phases (ionized, neutral atomic, and molecular), a mass of neutral atomic and molecular gas a factor of at least ~40 larger than the ionized one would be required, supposing that all the three gas phases have the same velocity (which is found for ionized and molecular outflows e.g., by Carniani et al. 2015, Fiore et al. 2017). This threshold is consistent with the molecular versus ionized mass outflow rate ratios found by Carniani et al. (2015), Fiore et al. (2017), Fluetsch et al. (2018). Energy conservation would instead require a fraction of neutral atomic and molecular gas a factor of at least ~10^3 larger than the ionized gas for the large scale kinetic rate to match the nuclear one, which is unlikely. Therefore, a momentum-conserving outflow seems to be the favored scenario for NGC 1365. However, momentum-driven outflows are predicted to occur on scales $\lesssim$kpc (e.g., King & Pounds 2015), while we are dealing with distances $\gtrsim$kpc in our case. Direct AGN radiation pressure on dusty clouds could be potentially capable of driving the outflow, as the AGN photon momentum $L_{bol}/c \sim 7 \times 10^{32}$ g cm s^{-2} is a factor ~20 greater than the peak value of the optical extended outflow ($\sim 3 \times 10^{31}$ g cm s^{-2}). Momentum rates ranging from ~ 1 up to 5 L_{bol}/c are expected on ~kpc scales in this regime (Thompson et al. 2015, Ishibashi et al. 2018), implying that a fraction of neutral atomic and molecular gas a factor at least ~ 20 up to 100 larger than the optical one would be required, still broadly compatible with what Carniani et al. (2015), Fiore et al. (2017), Fluetsch et al. (2018) find.

In order to derive integrated estimates of the outflow quantities, to be compared with our spatially resolved measurements, we followed the same approach adopted in Sect. 3.3.2 to obtain the total [O III] luminosity of the two cones, by fitting the two integrated spectra of the cones with two Gaussians per line, one for the outflow and one for the disk. We then obtain a total outflow mass from the luminosity of the Hα outflow component of $M_{out} \sim 4 \times 10^6\ M_\odot$ and a total kinetic energy of the outflow of $E_{k,out} = 1/2\ M_{out}\ v_{out}^2 \sim 1.2 \times 10^{53}$ erg. They are, respectively, a factor of ~ 4.3 and ~ 2.7 larger than the total outflow mass $M_{out} \sim 9.2 \times 10^5\ M_\odot$ and kinetic energy $E_{k,out} \sim 4.5 \times 10^{52}$ erg we previously measured by summing the single outflow masses and kinetic energies of the grid elements. This can be partly due to the fact that we are

now integrating over a wider area (a factor ~1.7 larger than that covered by the grid elements) and to a contamination by Hα emission from the disk. Therefore, the values just obtained have to be taken as rough estimates of the total kinetic energy and of the total outflow mass.

We can estimate the dynamical timescale of the optical outflow by dividing the distance of the most external shell (~2.5 kpc) by its velocity (~47 km s^{-1}, average between the blueshifted and the redshifted cone; see Fig. 3.13b). We then get $t_{\rm dyn} \sim 5.2 \times 10^7$ yr. However, this is an upper limit, as the outflow might have been faster at smaller distances in the past. A constant deceleration is a more reasonable assumption, and, considering as initial velocity of the outflow that of the nuclear X-ray wind (~3000 km s^{-1}), we obtain $t_{\rm dyn} \sim 1.6 \times 10^6$ yr. We can also calculate the time that would be needed by the AGN at its present-day rate to inject in the system the total amount of kinetic energy observed from the two optical outflowing cones, as $t_{\rm out} = 1/2$ $M_{\rm out} v_{\rm out}^2 / \dot{E}_{\rm k,out,X}$. With $\dot{E}_{\rm k,out,X} \sim 1.9 \times 10^{41}$ erg s^{-1} (from Sect. 3.3), we obtain $t_{\rm out} \sim 1.9 \times 10^4$ yr or $t_{\rm out} \sim 7.5 \times 10^3$ yr, by adopting the kinetic energy from the two fits of the integrated spectra of the cones in the first case and the sum of kinetic energies of the grid elements in the second case. Anyway, the two values have the same order of magnitude of ~10^4 yr. This is quite a short timescale for AGN activity and also compared to $t_{\rm dyn}$ calculated above. It is worth noting that, even in the energy-conserving case, simulations predict a coupling efficiency of 10-20% between the nuclear wind and the extended outflow (e.g., Richings & Faucher-Giguère 2018), so we should not expect $t_{\rm out} \sim t_{\rm dyn}$ (e.g., Nardini & Zubovas 2018). However, even considering our most conservative estimation of $t_{\rm dyn}$ given above, we obtain $t_{\rm out}/t_{\rm dyn} < 10^{-2}$, which is far too small. This might indicate that the AGN is now in a phase of more intense activity compared to the time-averaged past one from the optical outflow. The fact that both the outflow velocity and the mass outflow rate are lower at larger distances seems to enforce this possibility. In principle, the decrease of the mass outflow rate at larger distances could be also ascribed to the radial density profile. We do not find, however, any clear trend in this sense from our [S II]-based estimates, and the same clumpy nature of the outflow seems to rule out such a simple explanation. Anyway, the total kinetic energy of all the gas phases rather than of the ionized gas only would be needed for a more significant estimation of $t_{\rm out}$.

Fiore et al. (2017) studied the dependence of the outflow characteristic quantities (velocity, mass outflow rate, kinetic energy rate) on AGN bolometric luminosity. Their sample of ionized outflows covers bolometric luminosities ranging from ~2 × 10^{44} erg s^{-1} to ~10^{48} erg s^{-1}. As we estimate a bolometric luminosity of $L_{\rm bol} \sim 2.2 \times 10^{43}$ erg s^{-1} for NGC 1365 (see Sect. 3.3.2), we are then able to extend the work by Fiore et al. (2017) down by an order of magnitude in bolometric luminosity. As the results in their work come from integrated spectra, we adopt $M_{\rm out}$ and $v_{\rm out}$ from our fit of the entire cones previously mentioned. Moreover, while in our work we measure the outflow velocity $v_{\rm out}$ from the position of the centroid of the outflow component, in Fiore et al. (2017) the outflow velocity is defined as $v_{\rm max} = v_{\rm out} + 2\sigma$ (as e.g., in Rupke &
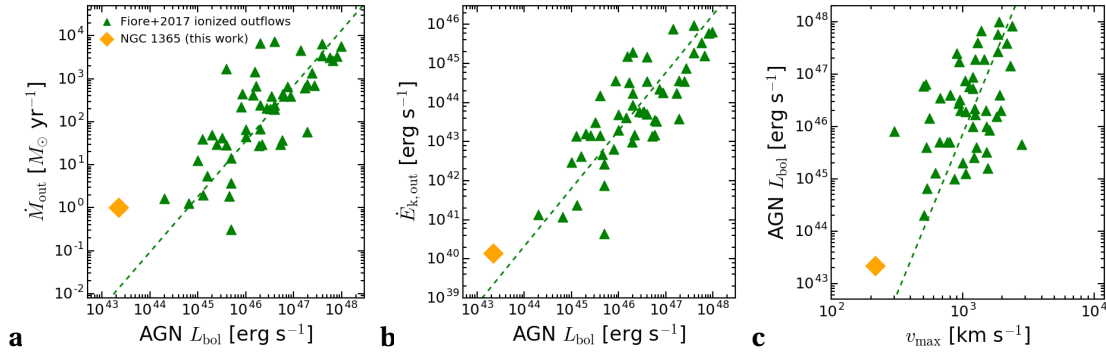
Fig. 3.14: **(a)** Mass outflow rate as a function of the AGN bolometric luminosity. The green symbols mark the ionized outflow measurements from Fiore et al. (2017), while the orange diamond is our estimate for the ionized outflow in NGC 1365, having calculated the mass outflow rate and the maximum outflow velocity consistently with Fiore et al. (2017) from the integrated spectra of the two outflowing cones (see text). The green dashed line is the best-fit correlation from Fiore et al. (2017) for their ionized outflow sample. **(b)** Kinetic energy rate as a function of the AGN bolometric luminosity. **(c)** AGN bolometric luminosity as a function of the maximum outflow velocity.

Veilleux 2013, Feruglio et al. 2015, Bischetti et al. 2017), being σ the velocity dispersion of the outflow component. We thus calculate the velocity in the above way to make the comparison. The mass outflow rate is obtained from Eq. 3.2, where v_{max} is used instead of v_{out} and ΔR is now the extension of the entire outflow, namely $\sim 30''$ (~ 2.7 kpc) per cone as the outflow reaches the margins of MUSE FOV. Moreover, the mass outflow rate is multiplied by 3 to be consistent with the relation adopted in Fiore et al. (2017) for a spherical or multiconical outflow uniformly filled with clumps.

The resulting ionized mass outflow rate ($\dot{M}_{\mathrm{out}} \sim 1\ M_{\odot}\ \mathrm{yr}^{-1}$) is two orders of magnitude larger compared to the the extrapolation at $L_{\mathrm{bol}} \sim 2.2 \times 10^{43}\ \mathrm{erg\ s}^{-1}$ of Fiore et al. (2017) best fit for ionized outflows ($\sim 0.01\ M_{\odot}\ \mathrm{yr}^{-1}$; Fig. 3.14a). However, the scatter in their points is large, spanning up to almost three orders of magnitude at high bolometric luminosities and thus the extrapolation at low luminosities is quite uncertain. We obtain a kinetic energy rate $\dot{E}_{\mathrm{k,out}} \sim 1.4 \times 10^{40}\ \mathrm{erg\ s}^{-1}$, which is one order of magnitude larger than the extrapolated value from Fiore et al. (2017) ($1.4 \times 10^{39}\ \mathrm{erg\ s}^{-1}$), but within the scatter of their points (Fig. 3.14b). The velocity that we get ($v_{\mathrm{max}} \sim 215\ \mathrm{km\ s}^{-1}$) is also consistent with the extrapolation at low luminosities from their best fit ($\sim 370\ \mathrm{km\ s}^{-1}$) within the scatter (Fig. 3.14c).

We emphasize that the integrated mass outflow rate obtained following Fiore et al. (2017) prescriptions is much higher (by a factor >20) than the radial values we mapped with our own method (Fig. 3.13a). This highlights that different methods for calculating the outflow quantities give a large scatter in the results and underlines the importance of having spatially resolved information to properly disentangle the outflows from the disk motions.

3.5 Conclusions

We have presented a study of the ionized gas in the central ~5.3 kpc of the nearby Seyfert galaxy NGC 1365, both in its warm and hot phase, using spatially resolved optical VLT/MUSE observations and *Chandra* ACIS-S X-ray data. Thanks to the capabilities of MUSE, we could map the spatial distribution of the optical emission lines to an unprecedented detail, and obtained unique insights by comparing them with the hot gas from *Chandra*.

The main results of our analysis are summarized below:

- We detect a biconical outflow prominent in [O III] and extended out to about 2.5 kpc in both directions, with line-of-sight velocities up to ±170 km s^{-1}. We resolve the clumpy structure of the outflow down to a scale of ~70 pc. The cone to the SE of the nucleus has approaching velocities, while the NW one recedes and is located behind the disk, being partly obscured by the dust in the disk, especially closer to the center. The SE cone, despite residing above the disk, has a typical extinction of $A_V \simeq 0.7$, indicating that the outflow contains dust, in agreement with the polar extra-disk dust features observed on smaller scales in some AGN. Moreover, the dust might be coupled with cold molecular gas which would be potentially capable of forming stars within the outflow.

- The AGN ionizes the outflowing cones as inferred from the spatially resolved BPT diagnostic diagrams. The AGN origin of the ionization in the two cones is further supported by the fact that the extinction-corrected [O III] emission measured in the cones is compatible with the value that we get from the 2-10 keV X-ray emission using the latest $L_{\text{X, 2-10 keV}}-L_{\text{[O III]}}^{\text{cor}}$ correlation for Type 2 AGN.

- Star formation dominates the disk and the bar of the galaxy (which extends in the direction SW-NE, perpendicular to the biconical outflow), where a strong Hα emitting circumnuclear star-forming ring is observed, residing between the outer and the inner Inner Lindblad Resonances. The ring is also traced by the density map (from the [S II] line doublet ratio), where values up to 10^3 cm^{-3} are found in correspondence with it. The Hα emission also nicely follows the leading edges of two dust lanes in the bar in an S-shaped pattern wrapping the circumnuclear ring.

- The soft X-rays in NGC 1365 are dominated by thermal emission due to star-forming processes, with about 40% of the soft X-ray emission originating from the SF ring. However, by selecting appropriate X-ray energy intervals we are able to recover the AGN-photoionized component, which spatially matches the [O III] optical AGN-photoionized emission from MUSE.

- The mass outflow rate of the kpc-scale ionized outflow from the MUSE optical emission lines is of the same order of magnitude as the one obtained for the nuclear highly-ionized

outflow from the Fe XXV and Fe XXVI absorption lines from *Chandra* X-ray data ($\approx$0.067 $M_\odot$ yr^{-1}). This, together with the fact that the AGN ionizes the double-conical outflow, suggests that the AGN is the driver of the wind. We observe a decrease of the mass outflow rate with distance, which might either imply that the outflow slows down at larger distances ($\sim$1.5 kpc) or that the AGN pushing the wind has become more powerful recently. An energy-driven scenario for the extended outflow is unlikely, as a fraction of neutral atomic and molecular gas $\gtrsim 10^3$ than the ionized one would be required to have energy conservation, which is too large compared to what is observed in other AGN. A lower fraction ($\gtrsim$40) would be required for momentum conservation, but models predict that the momentum-driven mode operates on scales $\lesssim$1 kpc, while the outflow in NGC 1365 extends on few kpc. We note that the constraints of $\gtrsim 10^3$ and $\gtrsim$40 on the gas fraction are partially relaxed in the hypothesis that the AGN (and so the X-ray wind) is more powerful at present time than in the past. Finally, direct acceleration by the AGN radiation pressure on dusty clouds could be a possible driver of the outflow.

- The integrated mass outflow rate, kinetic energy rate, and outflow velocity are broadly consistent with the extrapolation at low AGN bolometric luminosities of Fiore et al. (2017) relations for more luminous AGN ($10^{44} \lesssim L_{\rm bol} \lesssim 10^{48}$ erg s^{-1}), being the AGN bolometric luminosity of NGC 1365 $\sim$2.2 $\times$ 10^{43} erg s^{-1}. However, we note that the integrated mass outflow rate, calculated according to Fiore et al. (2017) prescriptions, is 20 times larger than the values that we obtain from our radial analysis of the outflowing shells. This indicates that different methods may lead to a large discrepancy in estimating the outflow quantities and stresses the importance of having spatially resolved information to properly disentangle outflow and disk kinematics.

- We observe an excess of hard X-ray (3-5 keV) extended emission cospatial with the SF ring in Hα. This could be tentatively associated with a hotter gas component due to SNe in the ring driving a shocked wind, which might contribute in principle to the kpc-scale outflow. However, higher quality X-ray data are needed to discern if star formation actually contributes to the observed optical outflow and, if it does, to which extent.

4 Star formation inside a starburst-driven galactic outflow

4.1 Introduction

Recent models predict that formation of stars can take place within galactic outflows (e.g. Ishibashi & Fabian 2012, 2014, 2017, Zubovas et al. 2013a, Ishibashi et al. 2013, Zubovas & King 2014), with important potential implications on galaxy evolution. The high-velocity newborn stars would have radial orbits and may contribute to populate the spheroidal component of the host galaxy and shape its size and velocity dispersion (e.g. Ishibashi & Fabian 2014, Dugan et al. 2014) as well as chemically enrich the circumgalactic medium (e.g. Zubovas et al. 2013a). The first pieces of evidence of this new mode of star formation in action were recently found in a galaxy hosting an AGN by Maiolino et al. (2017) and in a sample of objects from the SDSS IV MaNGA survey by Gallagher et al. (2018), including both galaxies optically classified as active and as composite/star-forming. However, the spatial resolution of these observations is quite poor (~2.5 kpc), so objects classified as star-forming might actually host an active nucleus at their centres, whose signature is lost in the optical diagnostics due to the poor spatial resolution. Therefore, we still miss a clear evidence that this in-outflow star formation mode can actually take place also in starburst-driven outflows, besides in AGN-driven ones.

In this work we employ VLT/MUSE optical integral field spectroscopic observations to study the distribution, kinematics and ionization of the warm ionized gas ($T \sim 10^4$ K) in the nearby galaxy NGC 6810, which has a distance of 27.5 ± 4.6 Mpc[1] from Earth. NGC 6810 is a spiral galaxy having an inclination of 74° with respect to the line of sight (McCormick et al. 2013), a stellar mass of ~8×10^{10} $M_\odot$ and a star formation rate of 2-3 $M_\odot$ yr^{-1} (Strickland 2007). It was initially classified as a Seyfert 2 by Kirhakos & Steiner (1990), both because of the high emission-line widths observed, typical of Seyferts, and because it was misidentified as the optical counterpart of a HEAO-1 hard X-ray source that would have had an X-ray luminosity of a Seyfert 2, if it was located at the distance of NGC 6810. However, NGC 6810 lied outside the 95 per cent confidence error box of this HEAO-1 source and it then turned out that there had been a misidentification and the two objects were not related (Strickland 2007). In fact, the nucleus of NGC 6810 shows no sign of AGN activity neither from optical diagnostics (Brightman & Nandra 2008, Yuan et al. 2010, Sharp & Bland-Hawthorn 2010, Videla et al. 2013), hard X-rays

---

[1] Mean of redshift-independent distances from NASA/IPAC Extragalactic Database (NED).

(Strickland 2007), mid-infrared (Asmus et al. 2014) nor radio emission (Kewley et al. 2000). The presence of a starburst galactic-wide ionized outflow perpendicular to the disk was inferred from the high velocity dispersion along the minor axis (Coccato et al. 2004, Sharp & Bland-Hawthorn 2010) and from the soft X-ray emission extending up to ~7 kpc above the disk on both sides (Strickland 2007). Moreover, the soft X-ray emission spatially matches with extraplanar polycyclic aromatic hydrocarbon (PAH) emission, indicating presence of dust entrained in the outflow (McCormick et al. 2013).

4.2   Data description and analysis

For this work, we employed optical integral field data from the Multi Unit Spectroscopic Explorer (MUSE; Bacon et al. 2010) at the Very Large Telescope (VLT), located at the Paranal Observatory, in Chile. The data were observed under program ID 60.A-9339(A) (P.I. Marconi/Hawthorn/Salvato). MUSE observations were acquired in Nominal Mode (4750-9350 Å) for a total of four 500s seeing-limited Wide Field Mode (having a field of view of $\sim 1' \times 1'$) exposures, dithered by $1''$ and/or rotated by 90° relative to one another. The dataset included four 100s offset sky exposures for the sky background subtraction. We adopted the already-reduced data cube provided by ESO Quality Control Group. The spectral resolution of MUSE is ~65 km s^{-1} at ~5000 Å (around [O III]) and ~50 km s^{-1} at ~6600 Å (around Hα). The average seeing during the observations was $\sim 1''$, corresponding to ~130 pc. For the data analysis, that is, stellar continuum fitting and subtraction and multi-component emission-line fitting, we used our own suite of python scripts, following the same scheme described in Sect. 2.3.

4.3   Emission-line maps

The three color image in Fig. 4.1a shows Hα (red) and [N II] (green) line emission from ionized gas together with the stellar continuum (blue). The disk of the galaxy, whose major axis extends approximately in the North-South direction, shows both Hα and [N II] emission. Besides the disk, [N II] dominates to the South-East of the disk and in a plume to the North-West of the disk. Hα emission is instead dominant both to the East of the disk and, above all, in an elongated funnel-shaped region to the West of the centre of the galaxy, extending over ~4.5 kpc perpendicularly to the disk. The linewidth of the total Hα line profile is enhanced perpendicularly to the disk in both directions, to the East and to the West in correspondence to the funnel-shaped emission ($W70$ up to 500-600 km s^{-1}; Fig. 4.1b), compared to the disk where the linewidth is instead much lower ($W70 \lesssim 150$ km s^{-1}). We interpret this enhanced Hα linewidth perpendicularly to the disk on both sides as a bipolar outflow of ionized gas. Its spatial distribution is in fact consistent with the galactic-scale starburst-driven wind found from the soft X-rays by Strickland (2007).
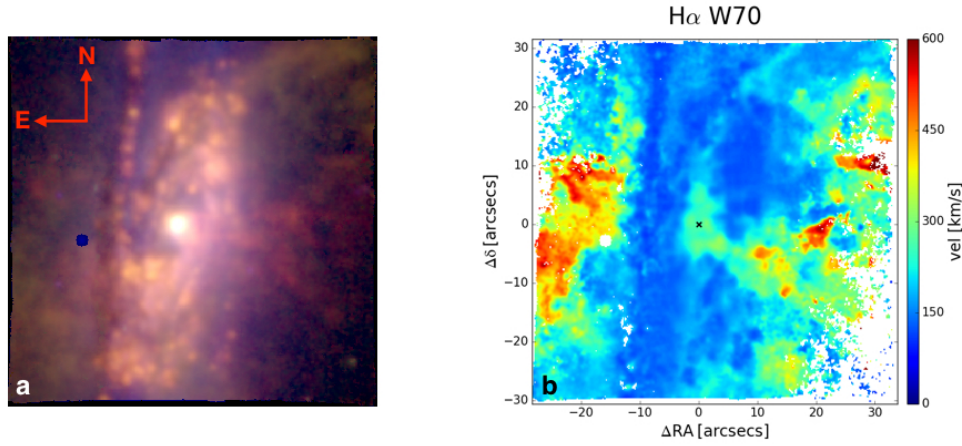
Fig. 4.1: Flux and kinematic maps of ionized gas and stars in NGC 6810 from VLT/MUSE observations. **(a)** Three color image of NGC 6810 from VLT/MUSE observations, displaying Hα (red) and [N II] (green) integrated line emission and stellar continuum in the range ~5100-5800 Å (blue). **(b)** Linewidth ($W70$) of the Hα total line profile.

In Fig. 4.2 we present the spatially-resolved [N II] and [S II] BPT diagrams of NGC 6810 obtained from the total emission-line profiles, together with their associated spatial distributions, which we employ to discriminate the dominant source of ionization throughout NGC 6810. They show that young stars, besides in the disk, are the dominant ionization mechanism in the funnel-shaped outflow and also partially to the East of the disk, suggesting that star formation is taking place there. LI(N)ER-like line ratios, generally associated either with shocks or hot evolved stars or (low-surface brightness areas) surround the star formation-dominated area.

However, the projected line emission that we observe in correspondence to the outflowing regions is the sum of the emissions in the line of sight from the outflow and the disk, where stars are known to form. So, a possibility might be that the star-forming line ratios observed in correspondence with the outflow are simply due to the fact that the star-forming disk dominates the line emission in the line of sight and the outflow is actually ionized by some other mechanism (e.g. shocks). To exclude this possibility, we performed an accurate spatial and spectral disentanglement of disk and outflow emission within the region corresponding to the outflow, as discussed in the following.

4.4 Star formation in the outflow?

In order to spatially and spectrally isolate the outflow kinematic component from that belonging to the disk of the galaxy and remove any effect due to projection in our BPT diagnostic maps for gas ionization, we divided the area corresponding to the bipolar outflow in a grid of elements of fixed radius and angle on both sides, West and East.

The grid consists of up to eight radial slices per cone, 20 spaxels in size each (i.e. 4 arcsec or ~500 pc) and seven angular slices spanning 14.9″ each. We fitted the spectrum belonging to
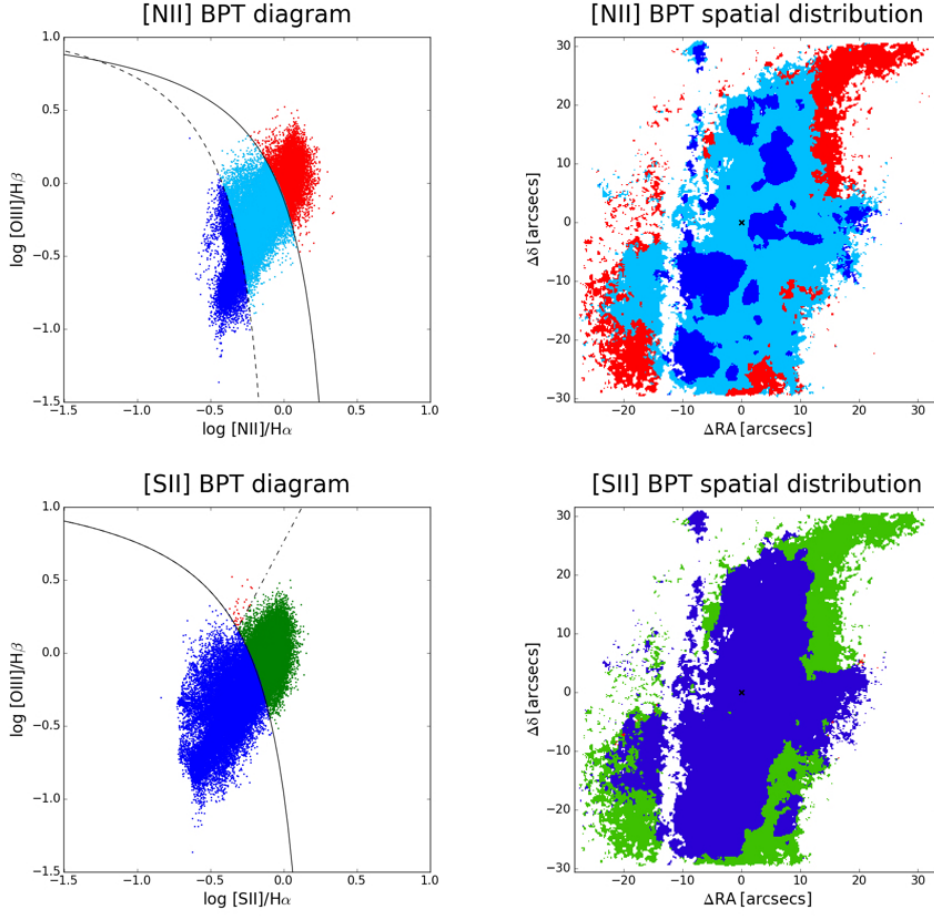
Fig. 4.2: Spatially resolved diagnostic diagrams (BPT) for dominant ionization source of the gas in NGC 6810, making use of emission-line ratios. Each point in the diagrams to the left corresponds to a spaxel in the associated maps to the right. A signal-to-noise cut of 3 on the lines involved in each diagram is adopted. The Kewley et al. (2001a) solid curve divides regions dominated by ionization from star formation processes, colored in blue or light-blue, from areas having AGN- or LI(N)ER-like ionization, lying above and below the Kewley et al. (2006) dashed-dotted line and colored in red and green, respectively.

each grid element, obtained by summing together the spaxels within it, using two Gaussians per emission line, one associated to the outflow kinematic component, one to the disk one. Such gridding also increases the signal-to-noise ratio on the emission lines, allowing to explore regions which are too faint in the single-spaxel BPT diagrams in Fig. 4.2. As for the spaxel-by-spaxel fit, the velocity shift and velocity dispersion of each component were tied among the lines. The disk kinematic component is traced by the stellar velocity, which generally corresponds to the peak of the Hα line profile. The outflow is traced by wings in the line profiles and is mostly blueshifted in the West cone while it is redshifted in the East cone. We thus forced the velocity of the disk component to stay within ± 50 km s^{-1} around the stellar velocity in each grid element. The velocity of the outflow component has been forced to be shifted of at least
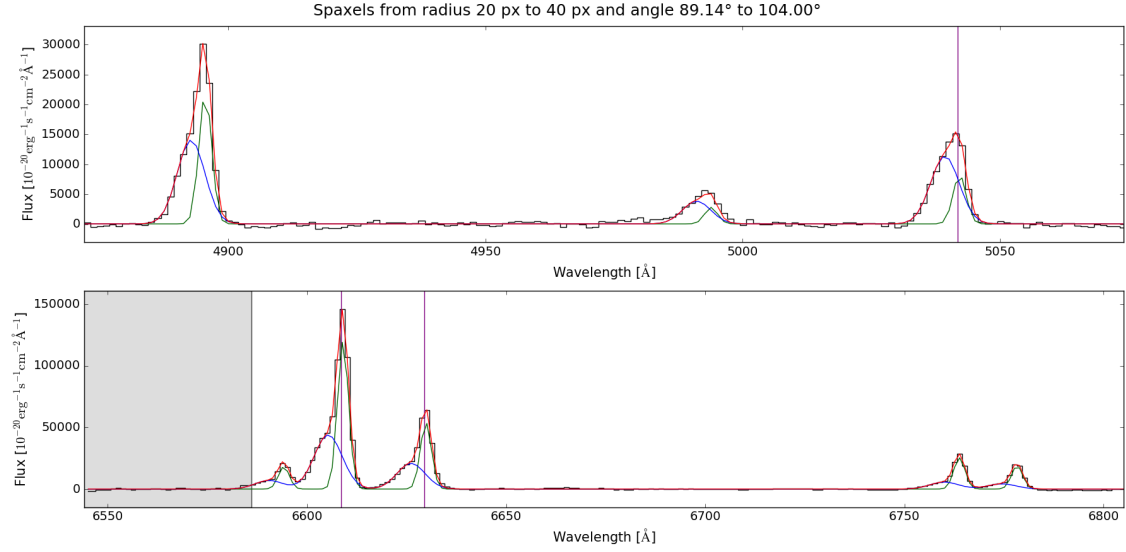
Fig. 4.3: Fitted spectrum from one of the elements of the radial and angular grid through which we divided the stellar continuum-subtracted data cube in correspondence to the outflowing regions. The outflow (blueshifted) kinematic component is shown in blue while the disk component in green. The purple vertical line marks the velocity of the stars, obtained from the shift of the absorption lines in the fitted stellar continuum. The emission lines reported are, from left to right, the Hβ and the [O III] doublet in the upper panel, the Hα and the [N II] and [S II] doublets in the lower panel.

-50 km s^{-1} or $+50$ km s^{-1} relative to the disk component, the former for the West cone, the latter for the East cone. An upper limit of $\sim$70 km s^{-1} has been set on the velocity dispersion (intrinsic, deconvolved for the spectral resolution) of the disk component and a lower limit of $\sim$70 km s^{-1} on that of the outflow component.

We excluded those grid elements where the flux of one of the fitted lines was zero or under the noise, either in the disk or in the outflow component, or which showed no significant asymmetries in the total Hα profile. We quantify the line asymmetry by using the following dimensionless quantity (Zakamska & Greene 2014): $R = ((v_{95} - v_{50}) - (v_{50} - v_{05}))/(v_{95} - v_{05})$, being v_{p} the velocity at the p-th percentile of the total line profile. We excluded those grid elements whose fit gave an Hα line profile having $|R| < 0.05$, that is, where the outflow was not present or spectrally undistinguishable from the disk.

In Fig. 4.3 we report, as an example, the fitted spectrum from one of the grid elements. The outflow kinematic component (blueshifted) is shown in blue while the green Gaussian marks the disk component, having a velocity similar to that of the stars (purple vertical line; obtained from the shift of the absorption lines in the fitted stellar continuum).

The resulting spatially resolved BPT diagrams for the outflow spectral component only are reported in Fig. 4.4 together with their associated spatial distribution. They show that the outflow has mostly star forming-like line ratios, indicating that the gas participating in the outflow is indeed ionized by young stars from star-forming regions.
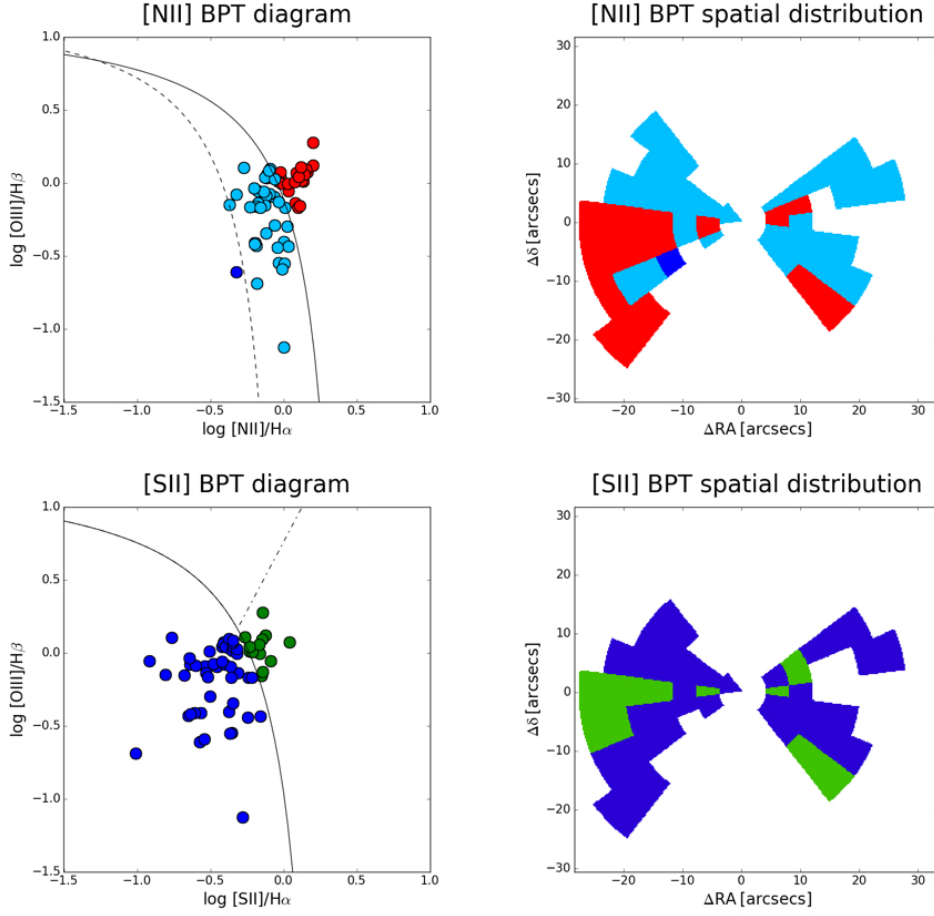
Fig. 4.4: Spatially resolved BPT diagnostic diagrams and associated maps (same as in Fig. 4.2) for outflow kinematic component only. The outflowing cones have been sliced in a grid to more robustly separate the outflow from the disk kinematic component in the gas emission lines.

However, the ionization might not be taking place in situ, but the ionizing photons might instead come from the star-forming regions inside the disk, illuminating the outflow. To check if this is the case or not, we made use of the $[\mathrm{O\,III}]\lambda5007/[\mathrm{S\,II}](\lambda6716+\lambda6731)$ $([\mathrm{O\,III}]/[\mathrm{S\,II}])$ ratio as a tracer of the ionization parameter U. Usually $[\mathrm{O\,III}]\lambda5007/[\mathrm{O\,II}]\lambda3727$ $([\mathrm{O\,III}]/[\mathrm{O\,II}])$ or $[\mathrm{S\,III}](\lambda9069+\lambda9532)/[\mathrm{S\,II}](\lambda6716+\lambda6731)$ are used instead as indicators of the ionization parameter (e.g. Díaz et al. 2000). However, in our case, $[\mathrm{O\,II}]\lambda3727$ lies outside the wavelength range covered by MUSE, while $[\mathrm{S\,III}]\lambda9069$ is too faint to be detected in correspondence to the outflow of NGC 6810. That is why we employed $[\mathrm{O\,III}]/[\mathrm{S\,II}]$ which, as shown in Fig. 4.5 where we report such ratio versus $[\mathrm{O\,III}]/[\mathrm{O\,II}]$ for local star-forming galaxies from the MaNGA survey (Bundy et al. 2015), is proportional to $[\mathrm{O\,III}]/[\mathrm{O\,II}]$ and is then a good tracer of the ionization parameter.

We reported our points for the outflow component in the $[\mathrm{O\,III}]/[\mathrm{S\,II}]$ versus
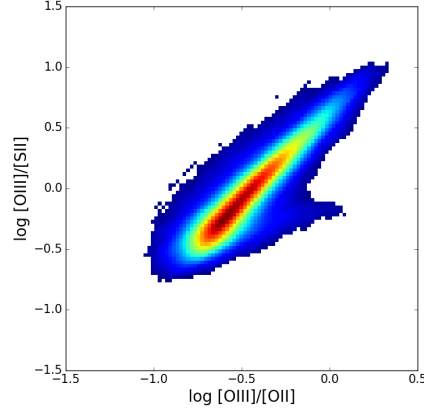
Fig. 4.5: [O III]/[S II] versus [O III]/[O II], sensitive to the ionization parameter (Díaz et al. 2000), for local star-forming galaxies from the MaNGA survey (Bundy et al. 2015). The two ratios are proportional, implying that [O III]/[S II] traces the ionization parameter as well.

([O III]+[S II])/Hα plot in Fig. 4.6a, superimposing them over the contours of local star-forming galaxies from the MaNGA survey. As the lines involved in these ratios are not close in wavelength (differently from the ones featuring in the BPT diagrams) and the extinction affecting them is thus not comparable, we corrected their fluxes for extinction before producing the plot. To do so we exploited the so-called Balmer decrement Hα/Hβ, which traces the extinction due to dust, and employed a Calzetti et al. (2000) attenuation law for galactic diffuse interstellar medium ($R_V = 3.12$) and an intrinsic ratio (Hα/Hβ)$_0$ = 2.86 (for an electron temperature of $T_e = 10^4$ K; Osterbrock & Ferland 2006). The gas in outflow spans distances from the disk from ~500 pc to ~4 kpc, approximating the galaxy as being edge-on and assuming that the outflow is perpendicular to the disk, so that the observer sees all its extension. The [O III]/[S II] line ratio traces the ionization parameter, so we would expect that if the ionizing photons come from the disk, located at such large distances from the gas in outflow, this ratio would be much lower compared to the contours of the MaNGA star-forming galaxies. Fig. 4.6a shows instead that our points are consistent with the contours of the MaNGA star-forming galaxies, indicating that they have comparable ionization parameter.

Still, the same ionization parameter of star-forming galaxies might be achieved anyway in the outflow in the case that the ionizing photons come from the disk, if the gas density in the outflow is lower enough compared to the typical gas densities in star-forming galaxies, so as to balance the lower ionizing flux received. In fact, the ionization parameter is defined as the ratio of the ionizing photon density to the electron density (e.g. Osterbrock & Ferland 2006) and it is thus inversely proportional to the square of the distance r from the ionizing source and to the electron density n_e. We thus estimated the gas electron density in the outflow, from the [S II] λ6716/λ6731 diagnostic ratio (Osterbrock & Ferland 2006), which is sensitive in the range

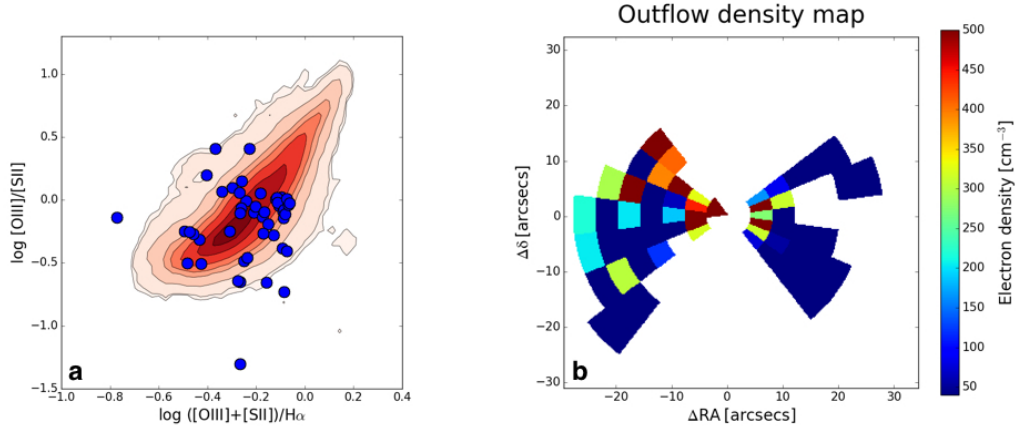Fig. 4.6: Diagnostic diagram of ionization parameter of the gas for the outflow in NGC 6810 (a) and outflow electron density map (b). [O III]/[S II] in (a) is sensitive to the ionization parameter. The contours represent local star-forming galaxies from the MaNGA survey.

~40-5000 cm^{-3}, outside which the line ratio saturates. We thus set to 40 cm^{-3} all the densities falling below this value, corresponding to ~5% below the peak of the total range spanned by the line ratio. We thus found (Fig. 4.6b) that a large part of the outflow exhibits densities even larger (up to few hundreds cm^{-3}) than the typical values of 20-30 cm^{-3} found for local star-forming galaxies (Sanders et al. 2016, Bian et al. 2016, Kaasinen et al. 2017), while in the rest of the outflow the density is under our minimum threshold of 40 cm^{-3}. However, it is not excluded that also in this regions the density may still be larger or comparable with 20-30 cm^{-3}.

So, the fact that we observe an ionization parameter in the outflow comparable to that of star-forming galaxies and gas densities even larger than in such objects excludes the possibility that the ionizing photons giving star forming-like line ratios in the outflow come from the disk. We thus conclude that, without any doubt, star formation is actually taking place in situ within the outflow. Our result is further enforced by the fact that PAH emission is observed in correspondence to the outflow (McCormick et al. 2013), tracing the presence of dust, a key ingredient to have the molecular gas needed to form stars.

We estimate the star formation rate (SFR) in the outflow from the extinction-corrected luminosity of the Hα outflow fitted kinematic component, taking into account only the grid elements showing star formation-like line ratios in the [S II]-BPT (see Fig. 4.4). We stress that the actual SFR in the outflow is likely to be higher than the estimated one as we are potentially excluding the contribution to the SFR from the grid elements not defined as star-forming in the BPT and also from those excluded due to bad fits where the outflow is spectrally indistinguishable from the disk. The SFR is obtained by using the following calibration from Kennicutt & Evans (2012):

$$\log\left(\frac{\text{SFR}}{M_\odot\,\text{yr}^{-1}}\right) = \log\left(\frac{L_{\text{H}\alpha}}{\text{erg}\,\text{s}^{-1}}\right) - 41.27 \qquad (4.1)$$

We then obtain a SFR in the outflow of $\sim 10^{-1}$ $M_\odot$ yr^{-1}. We also estimate the total SFR in the galaxy from the extinction-corrected spectrally-integrated Hα luminosity summed over all spaxels in the field of view having star forming-like line ratios in the [S II]-BPT (Fig. 4.2), obtaining a total SFR ~ 2.3 $M_\odot$ yr^{-1}, consistent with previous works (Strickland 2007). The SFR in the outflow thus constitutes only ~4 per cent of the total SFR in NGC 6810. The outflow does not then seem to deeply contribute to the star formation in the galaxy, but may still contribute to enrich the circumgalactic medium perpendicularly to the disk of NGC 6810 with young stars and metals due to exploding supernovae, as well as to populate the spheroidal component of the galaxy.

4.5 Conclusions

We presented an analysis of the gas kinematics and ionization in the nearby star-forming galaxy NGC 6810 with the integral field optical spectrograph MUSE at VLT. Our maps revealed a bipolar outflow of ionized gas down to spatial scales of ~130 pc. The bipolar outflow, roughly perpendicular to the disk of the galaxy, is spatially consistent with that found by Strickland (2007) in the soft X-rays. We kinematically isolated the outflow from the disk and we found strong evidence of star formation taking place within part of the outflow, dominated by ionization from young stars. By inspecting ionization parameter tracers, we excluded the possibility that the ionizing photons stem from star-forming regions in the disk rather than in-situ within the outflow. This is the first evidence of star formation occurring within an outflow in a galaxy unambiguously identified as star-forming, resolving the ionized gas entrained in the starburst-driven outflow down to a spatial scale of ~130 pc. Our result represents a pilot study and suggests that by investigating star-forming galaxies in detail and at high spatial resolution, many other cases of in-outflow star formation might emerge, potentially constituting another key element to add to the complex puzzle of galaxy evolution.

5 The VLT/MUSE view of the central galaxy in Abell 2052: Ionized gas swept by the expanding radio source

5.1 Introduction

The exchange of matter and energy between active galactic nuclei (AGN), their host galaxies, and clusters of galaxies–known as the AGN feedback process–is a fundamental ingredient in the formation and evolution of astrophysical structures. As illustrated in Chapter 1, the AGN feedback, through the exchange of matter and energy between AGN, their host galaxies and clusters of galaxies is considered a fundamental ingredient in the development of astrophysical structures and is in fact routinely included in models of galaxy formation and evolution. Such models consider two modes of AGN feedback: the radiative (quasar) mode, which operates during a luminous nuclear phase and produces winds powered by radiation pressure, and the kinetic (radio) mode, in which kinetic energy is released through relativistic jets. Though powerful outflows are now routinely observed at both low and high redshift (see 1.3), the observational evidence that they have a relevant impact on the star formation of their host galaxies remains elusive.

So far, the clearest evidence of AGN feedback has been found in its kinetic mode in the local Universe, where X-ray images of galaxy clusters revealed cavities in the hot ionized medium (HIM) ($10^6 - 10^7$ K), often filled by the radio emitting plasma. The radio sources hosted in the brightest cluster galaxies (BCGs) were able to displace the low-density gas forming the hot phase of the ISM while expanding (McNamara et al. 2000, Bîrzan et al. 2004, Bîrzan et al. 2012).

The X-ray image of the galaxy cluster A2052 from the Chandra satellite provides one of the clearest examples of such cavities: a pair of symmetric depressions in the X-ray surface brightness is closely correlated with the presence of radio emission (Blanton et al. 2001). In A2052 the estimate of the total energy required to inflate the cavity is a few 10^{57} erg (Bîrzan et al. 2004). Since gas speed cannot be measured from X-ray observations, it is assumed that the bubble moves outward at the sound speed (~ 500 km s^{-1} for an external gas temperature of 10^7 K, Blanton et al. 2011) or, alternatively, that its motion is driven by buoyancy forces (Panagoulia et al. 2014), resulting in a cavity age of $\sim 1 - 2 \times 10^7$ years.

The presence of warm ionized medium (WIM) producing optical emission lines in the cen-

tral region of A2052 (Baum et al. 1988, Heckman et al. 1989, McDonald et al. 2010) offers the unique possibility of studying the dynamics of the expanding cavity and the energy exchange between the active nucleus and the surrounding medium, an essential ingredient for a better understanding of the feedback process.

We observed the central brightest cluster galaxy, UGC 9799, in the optical band with the VLT/MUSE integral field spectrograph. UGC 9799 is an elliptical galaxy (z=0.0345 where 1" corresponds to 0.69 kpc) associated with the radio source 3C 317. The mass of its central supermassive black hole, estimated from the central stellar velocity dispersion (σ_{star} = 190 km s^{-1}, Smith et al. 2004), and the relation of σ_{star} with M_{BH} (Kormendy & Ho 2013) is M_{BH} =$10^8 M_\odot$. Source 3C 317 shows an amorphous radio halo, elongated in the NS direction and extended over ~60 kpc (Morganti et al. 1993), with a radio luminosity of P=1.3 10^{33}erg s^{-1} Hz^{-1} at 178 MHz (Spinrad et al. 1985); the radio core is coincident with the optical center of the galaxy. The optical nucleus has emission line ratios typical of low-ionization nuclear emission line regions (LINERs, Heckman 1980, Buttiglione et al. 2010).

5.2   Observation and data reduction

We pointed the telescope at A2052 and we took advantage of the large field of view ($\sim 1' \times 1'$) of the instrument to observe both the northern and southern X-ray cavities. The observations were obtained with the VLT/MUSE spectrograph on 13 April, 13 May, and 28 May 2016 for about two hours split between five exposures of ~25 minutes each, taken with different seeing conditions (between 0.6″ to 2.0″). Four datasets were affected by bad sky conditions, resulting in strong reddening and uncertainties in the flux calibration or poor seeing conditions. We thus decided to limit our analysis to the exposure with the highest spatial resolution (0.6″) and best sky conditions, namely MUSE.2016-05-13T05:19:36.833. We used the ESO MUSE pipeline (version 1.6.2) to obtain a fully reduced and calibrated data cube. No correction for the small Galactic reddening, E(B-V)=0.03, is applied.

To subtract the stellar continuum, we need to optimally bin the data to detect the stellar absorption features in the spectra, preserving the highest possible spatial resolution. Therefore, we performed a Voronoi adaptive spatial binning of the cube data, requiring an average signal-to-noise ratio per wavelength channel of at least 50 in the range 4500-7000 Å. We used the Penalized Pixel-Fitting code (pPXF, Cappellari & Copin 2003) to fit the absorption stellar features with a linearly independent subset of stellar templates from Vazdekis et al. 2010 that combine theoretical isochrones with the full MILES empirical stellar library (Falcón-Barroso et al. 2011). We adopt a 10th order additive polynomial correction for the continuum and included the emission lines in the fit instead of masking them. From this analysis we also estimated the recession velocity for UGC 9799 of 10330±10 km s^{-1}, in good agreement with previous optical measurements (Katgert et al. 1998, Wegner et al. 1999, Smith et al. 2000).
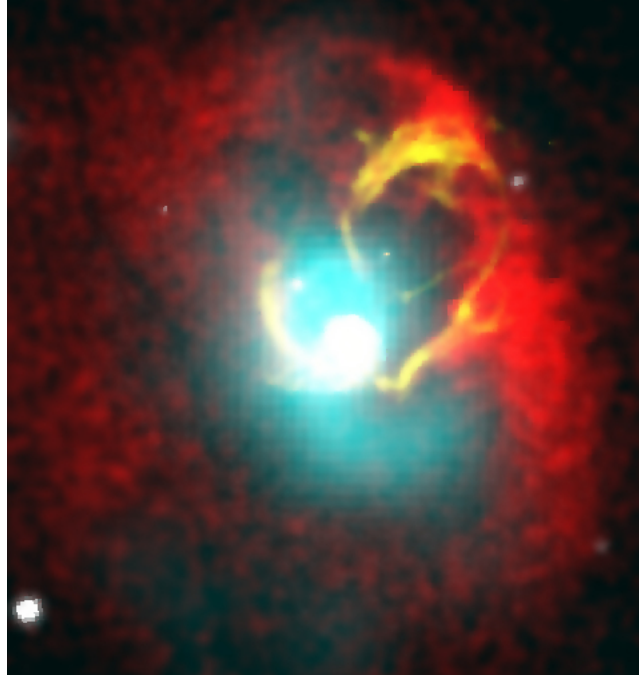
Fig. 5.1: Multiwavelength composite image of the central regions of the A2052 cluster. Optical continuum image in the r band from the the Sloan Digital Sky Survey (white), radio map from the Very Large Array (cyan), X-ray emission from Chandra (red) and the Hα+[N II] emitting filaments we observed with VLT/MUSE (yellow). The image covers the MUSE field of view, i.e., $60'' \times 60''$, 41.4×41.4 kpc^2.
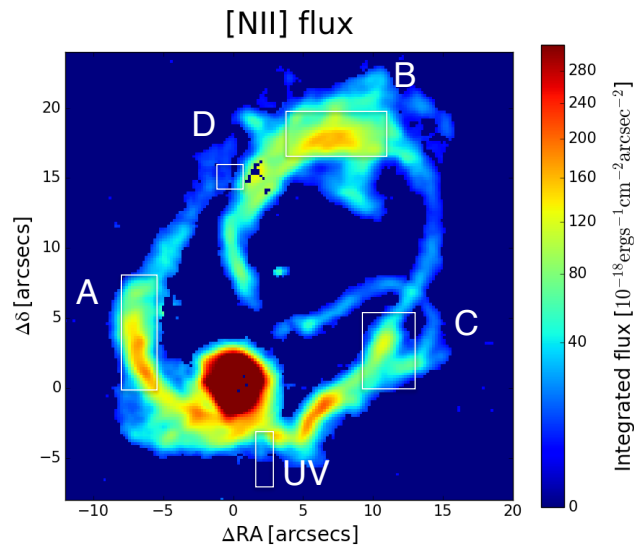

Fig. 5.2: Surface brightness of the [N II]λ6584 emission line. The image covers the $33'' \times 33''$, 22.8×22.8 kpc^2.
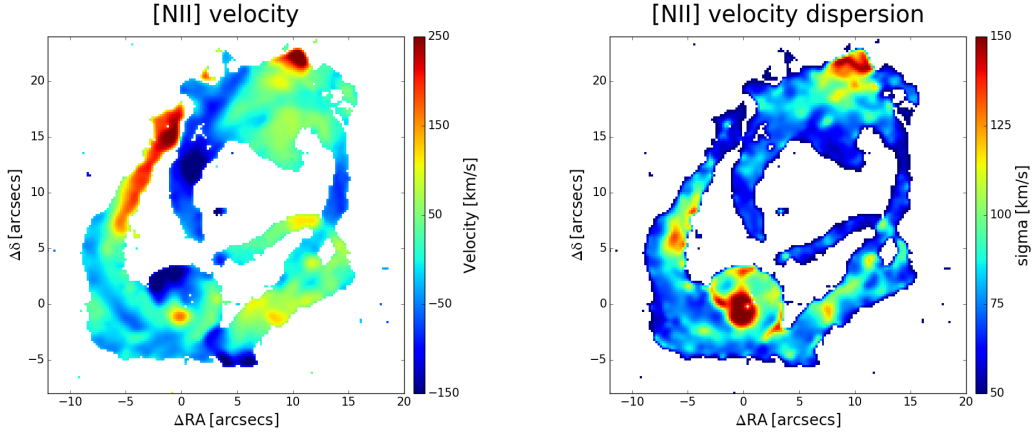
Fig. 5.3: Gas velocity (left panel) and velocity dispersion (right panel) derived from the [N II] line.
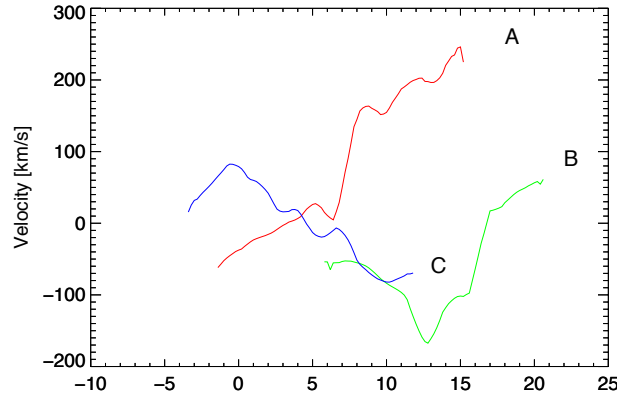
Fig. 5.4: Position–velocity diagram for the three main emission line filaments. At each given height, we measured the velocity at the brightness peak, i.e., following the filament's ridge line.

We fit simultaneously all emission lines in the red portion of the spectrum (from 6000 to 7000 Å) with a single Gaussian profile, one for each line. The line wavelength separation is fixed to the theoretical value, while the intensities are free to vary (except for the [N II] $\lambda\lambda 6584,6548$ ratio, which is fixed to 3). We repeated the reduction procedure for the blue spectrum to measure the Hβ and [O III] $\lambda\lambda 4959,5007$ lines. In a few regions, the emission lines show two well-separated peaks and, in these cases, we included a second Gaussian component.

5.3 Results

The resulting image obtained in the forbidden [N II] line at 6584 Å, the strongest line in our spectra, shows a complex network of filaments enshrouding the northern X-ray cavity (Figs. 5.1 and 5.2). The emission line filaments are co-spatial with those traced by the hot gas and by the dust features seen in the Hubble Space Telescope images (Sparks et al. 2000), while they are anti-correlated with the radio emitting plasma. No lines are detected from the southern cavity.

We integrated over two $20'' \times 20''$ square regions centered at $13''$ NW and SE from the nucleus, and found a flux asymmetry higher than 75.

The velocity field of the warm gas mapped by the [N II] emission (Fig. 5.3, left panel) is rather complex, but the hallmarks of the cavity's expansion are clearly visible. Starting immediately south of the central galaxy, a bright filament (A in Fig. 5.2) shows a velocity gradient starting from a null velocity and reaching a redshift of 265 ± 8 km s^{-1} (see Fig. 5.4). This is likely due to the gradual increase in the projected velocity along the line of sight as the filament wraps around the cavity. Filament A intersects another emission line structure (B in Fig. 5.2) that shows a similar but opposite behavior, reaching a maximum blueshift of -180 ± 2 km s^{-1}. The emission from these two filaments (A behind the cavity, B in front of it) is projected onto the same location in the sky producing a region of split-lines (D in Fig. 5.2), with a velocity separation of 290 ± 10 km s^{-1} (Fig. 5.6), an effect that also occurs in other regions of the nebula. This is the characteristic signature of an expanding bubble when both sides are simultaneously visible.

The overall gas kinematics is well reproduced by the toy model of an expanding bubble presented in Fig. 5.5. The bubble is surrounded by line-emitting filaments modeled as parts of thick polar rings with the same radius but different orientations. The model confirms that, in general, we see only one of the two velocity components of an expanding filament (partial ring). In a cartesian coordinate system (x, y, z) we consider spherical coordinates (r, θ, ϕ). We simulate each filament considering a ring with thickness r, r+dr with null velocity in the galactic nucleus (in x=0, y=0, z=-r). We assume that in each filament the intrinsic expansion velocity is higher toward the pole and decreases at lower latitudes to produce the quasi-spherical shape $v = v_0 * \cos\theta$, with θ being the angle between the z-axis and the direction from the galaxy nucleus (x=0, y=0, z=-r) to the point on the sphere. To project onto the plane of the sky (X,Y) taking into account the orientation with respect to the line of sight, we consider a rotation of the system around the three Euler angles α, β, γ obtaining a new system of reference (X,Y, Z) in which the Z-axis is oriented along the line of sight. We locate the origin of the reference frame at the center of the cavity. We obtain a good match to the observation assuming α=30°, β=70°, γ=35° with different ϕ ranges for all three filaments. The velocities along the line of sight of the receding and approaching halves are shown in red and blue. Several of the observed features are accounted for, such as the increase in velocity along filament A, the highly negative velocity at the pole, the velocity structure of filament B (reaching the maximum speed at the bubble's center), and the general shallower gradients along the west with respect to the east side.

The line widths (Fig. 5.3, right panel) are generally between 50 and 100 km s^{-1}, consistent with MUSE instrumental resolution; higher values are found, besides the central ~1 kpc of the host, only over rather small regions and notably at the cavity's NW tip where line widths up to 150 km s^{-1} are reached.
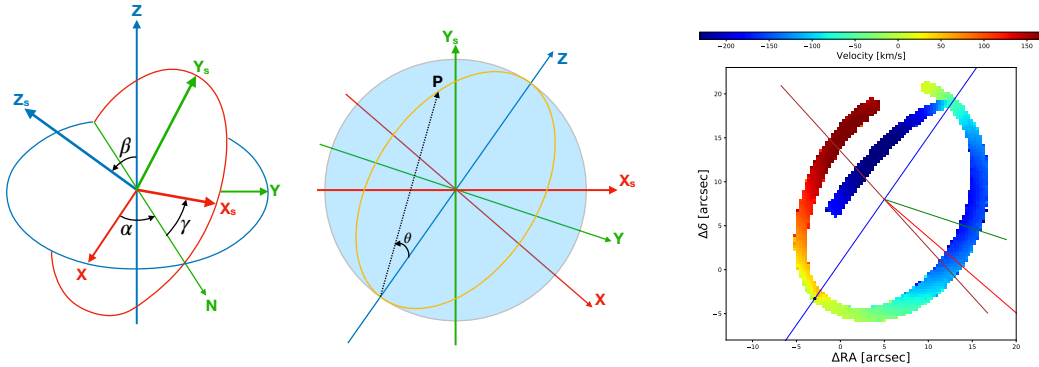
Fig. 5.5: Left and middle panel: Reference coordinate systems and rotation angles used in the kinematical model. Right panel: Toy model of a spherical expanding bubble. The origin of the reference coordinates is the center of the cavity. The velocities of the receding and approaching halves are reproduced in red and blue. The black dot marks the location of the bubble origin. The three reference axes in each figure are the X-axis (in red), the Y-axis (in green), and Z-axis (in blue). We plot the ring axis in the XY-plane (in brown).
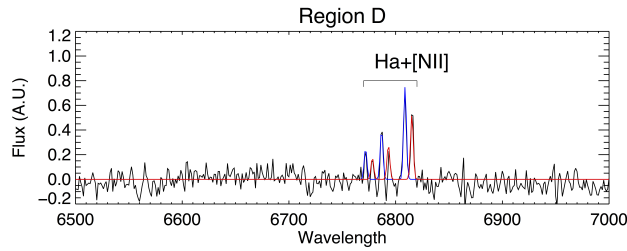
Fig. 5.6: Red spectra of region D showing one of the locations of split emission lines where we performed a fit with two Gaussians, represented by the blue and red curves.

The emission line intensity ratios can be used to distinguish between different ionization mechanism of the nebular gas: H II regions, AGN, or shocks (Baldwin et al. 1981, Dopita & Sutherland 1995). To explore the physical conditions of the WIM, we modeled the other weaker emission lines present in the spectra, i.e., $H\beta$, $H\alpha$, [O III]$\lambda5007$, [O I]$\lambda6300$, and the [S II] doublet at $\lambda\lambda6716,6731$.

In Fig. 5.7 we show the spectra of regions A, B, and C. In the plane defined by the [N II]/$H\alpha$ and [O III]/$H\beta$ ratio (Fig. 5.8), their representative points fall into a region not populated by any of the emission line galaxies extracted from the SDSS DR7 data (Kewley et al. 2006, Capetti 2011): in these objects the dominant ionization mechanism is due to the high-energy photon field produced by young stars or by the active nucleus. The inconsistency with the properties of photoionized gas in 3C 317 is confirmed by the other two diagrams where a contradictory classification would be obtained, as star-forming H II regions from the [S II]/$H\alpha$ ratio and as LINER from [O I]/$H\alpha$. This suggests that the gas is ionized by a different mechanism.

This result is confirmed overall across the nebula because we measured rather constant
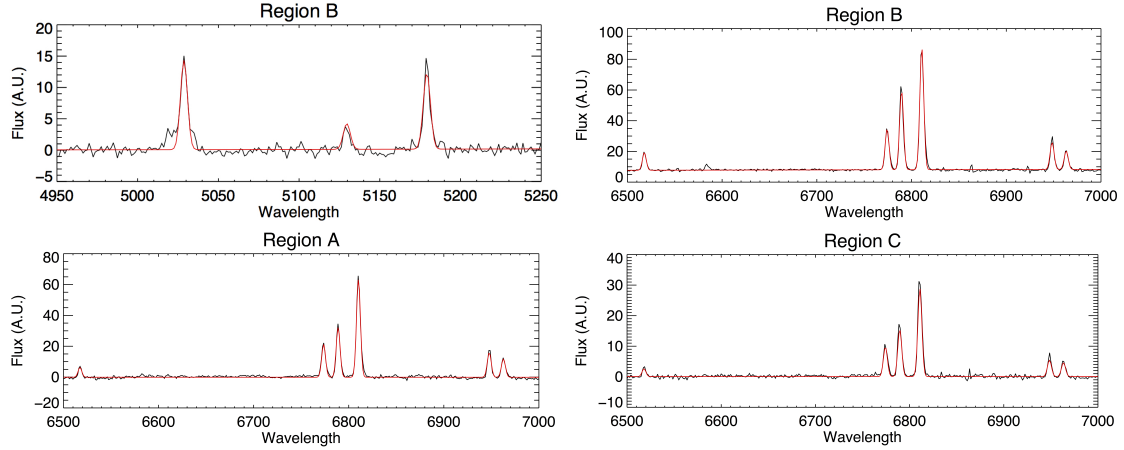
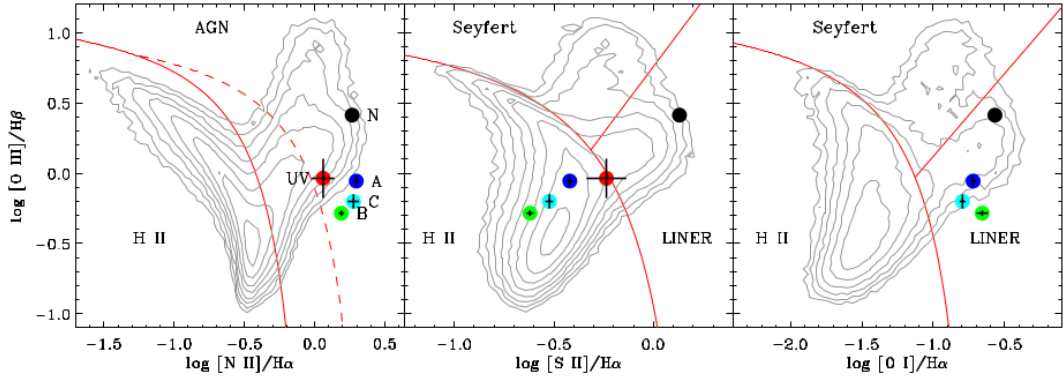Fig. 5.7: Top panels: Blue and red spectra of region B. Bottom panels: Red spectra of regions A and C.

Fig. 5.8: Location of regions A, B, C, nucleus (N), and UV filament (green, cyan, blue, black, and red dots, respectively) in the spectroscopic diagnostic diagrams. The solid lines separate star-forming galaxies, LINERs, and Seyferts (Kewley et al. 2006). Contours represent the iso-densities of all SDSS/DR7 emission line galaxies (Capetti 2011).

values ([O III]/Hβ ~ 0.5 − 0.9, [N II]/Hα ~ 1.5 − 2.0, [S II]/Hα ~ 0.2 − 0.4, and [O I]/Hα ~ 0.15 − 0.25), which again rules out the AGN or young stars as the dominant sources of ionization of the gas. In particular the ratio [N II]/Hα is everywhere higher than 1.2 (see Fig. 5.9), inconsistently with the values predicted for and observed in star-forming regions (Kewley et al. 2001b). The only exception is a small area (located $2''$ S and $4''$ W of the host where [N II]/Hα is ~ 0.8), which we discuss in more detail in Sect. 5.4.

We also estimated the gas density from the ratio $R_{[S II]}$ of the [S II] lines at 6716 and 6731 Å (Osterbrock & Ferland 2006) in the same three regions of the nebula considered above, obtaining $R_{[S II],A} = 1.34 \pm 0.05$ in region A, $R_{[S II],B} = 1.41 \pm 0.04$ in region B, and $R_{[S II],C} = 1.18 \pm 0.05$ in region C. By adopting a temperature of 10^4 K, the corresponding gas densities are $n_e = 270^{+70}_{-70}$ cm^{-3} and $n_e = 80^{+50}_{-45}$ cm^{-3} in C and A, respectively, while only an upper limit of $n_e = 50$ cm^{-3} can be set on region B.
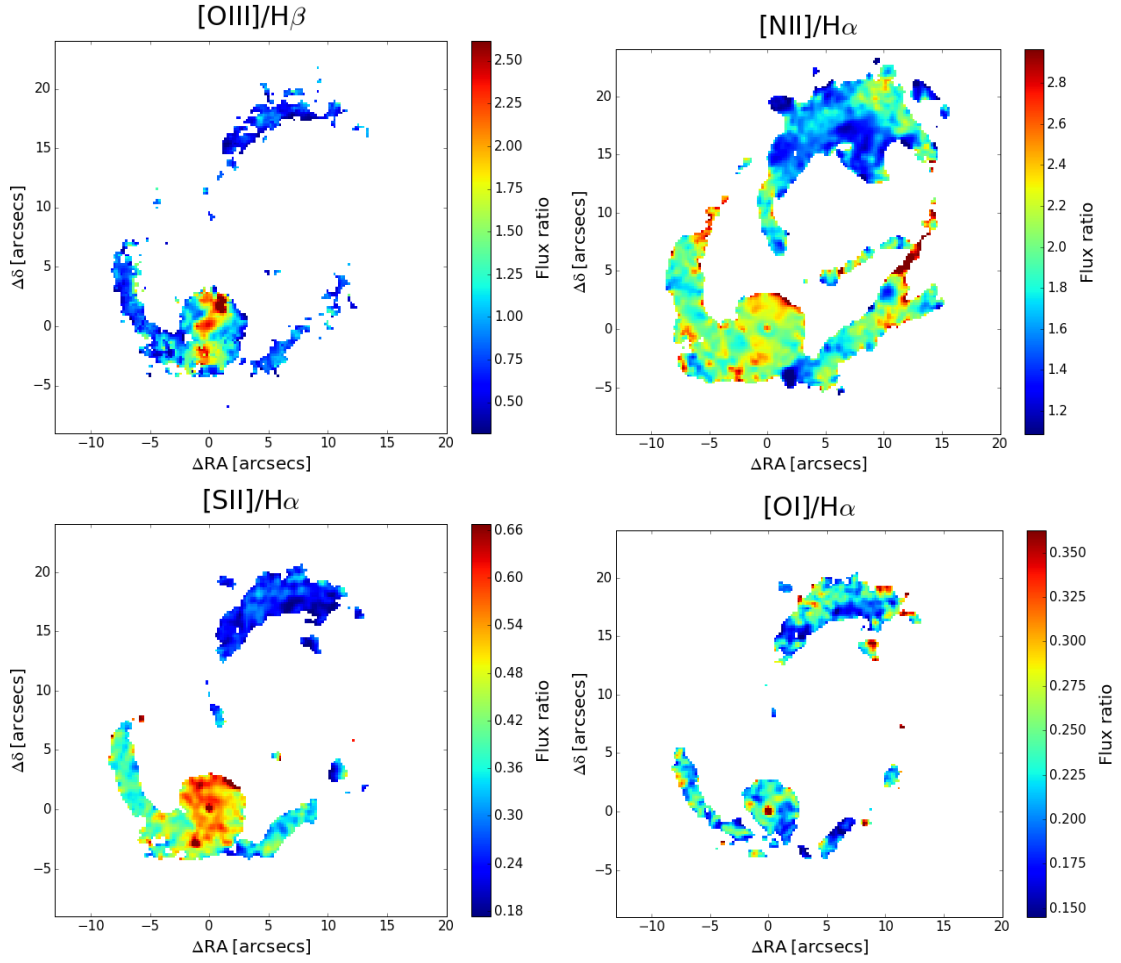
Fig. 5.9: Spatial map of the diagnostic line ratios.

The total mass of the ionized gas can be estimated as

$$M = 7.5 \times 10^{-3} \left(\frac{10^4}{n_e} \frac{L_{H\beta}}{L_\odot} \right) M_\odot,$$

where $L_{H\beta}$ is the luminosity of the Hβ emission line (Osterbrock & Ferland 2006). Adopting a density of $n_e = 100 \, \text{cm}^{-3}$ we integrated the Hα emission line map (excluding a circular region of 4'' of radius centered on the host galaxy and assuming $\frac{F_{H\beta}}{F_{H\alpha}} = 3$), finding a total mass of $M_{\text{tot}} = 1.3 \times 10^6 \, M_\odot$. We then estimated the total kinetic energy of the gas as $\frac{1}{2} M v^2$, where M is the mass estimated in each spatial bin and v is the corresponding observed velocity. Integrating all over the nebula we derive a total kinetic energy in the WIM of 1.6×10^{53} erg. In this calculation there are two main sources of uncertainty: 1) the effects of projection on the velocity field and 2) the assumption on the gas density value because in some regions the [S II] doublet lines ratio is close to the low-density limit value and only returns to upper limits for the density in region

B. The reported gas mass and kinetic energy are likely to be underestimated and should only be considered an order of magnitude estimate. These values indicate that the acceleration of the WIM gas only requires the conversion of a small fraction ($\sim 10^{-4}$) of the total energy injected into the ISM by the AGN ($\sim 10^{57}$ erg, Bîrzan et al. 2004), thus not representing a significant demand for the efficiency of the process of energy exchange. However, the gas in the warm phase represents only a very small fraction of the ISM, which is by far dominated by the hot phase and, in many brightest cluster galaxies (BCGs), also has an important contribution of molecular gas (e.g., Salomé & Combes 2003).

5.4 Discussion

The expansion rate of the cavities inflated by the radio lobes cannot be measured from X-ray observations: both the age and the power required are derived from indirect and model-dependent methods. MUSE observations instead enable us to directly measure the expansion speed of the cavity in A2052. The line emitting gas is located at the edges of the northern cavity and it moves with an ordered velocity field tracing a quasi-spherical outflow. The maximum observed speed is 265 km s^{-1} measured at the location of the A filament, 10 kpc from the nucleus. This value is lower with respect to the estimates obtained from X-ray observations, $\sim 600 - 700$ km s^{-1} (Bîrzan et al. 2004). However, since the optical nebula only partly covers the cavity we might still suffer from projection effects. Furthermore, the X-ray data return an average of the expansion speed over its lifetime, while the optical data are instantaneous measurements and the expansion of over-pressured radio lobes slows with time (Begelman & Cioffi 1989). A similar comparison between optical and X-ray observations should be extended to other similar sources to further explore this issue.

We found that while the emission line ratios on the nucleus are typical of a LINER, in the filaments they are inconsistent with ionization from the AGN or young stars. The transition from the nuclear LINER spectrum to that typical of the nebula occurs at the very onset of the filaments, at ~ 3 kpc from the nucleus. This is clearly marked by a decrease in [O III]/Hβ from the central value of ~ 3 to $\lesssim 1$ and in [S II]/Hα from ~ 0.6 to ~ 0.3. At this distance the AGN ionization leaves place for a different mechanism. There are two possible alternatives: ionization due to slow shocks (Dopita & Sutherland 1995) or collisional heating from cosmic rays (Ferland et al. 2008, 2009, Fabian et al. 2011). The small width of the emission lines, $\sim 50 - 100$ km s^{-1}, argues against the importance of shocks particularly noting that the broader lines are found in regions of large velocity gradients and where different filaments intersect, thus favoring ionization from energetic particles.

Various techniques provide similar indications for a modest level of star formation ($\sim 1 M_\odot \text{yr}^{-1}$) in the central regions of UGC 9799 (Crawford et al. 1999, Blanton et al. 2003, O'Dea et al. 2008). In addition, a filament of UV emission extending from 4 to 6 kpc SW of the nucleus

is interpreted as a star-forming region with a rate of $\sim 10^{-3} M_\odot \mathrm{yr}^{-1}$ (Martel et al. 2002). Based on our results, we can conclude that star formation does not have a significant impact on the line ratios and on the gas physical conditions. Nonetheless, the lowest value of [N II]/Hα over the whole nebula, ~ 0.8, is found at the location of the brightest UV knots. The integrated spectrum of this region is still characteristic of LINERs, but its representative point in the diagnostic diagrams is located close to the boundary of [H II] objects, likely due to the contribution of this star-forming region.

The depth of the MUSE observations of A2052 allowed us to set stringent limits on any line flux from the southern side of the galaxy, with an asymmetry higher than a factor ~ 75 with respect to the northern side. This result has implications on the origin and evolution of the warm and cold phases of its ISM because the extreme differences in line emission contrast with the symmetry of the radio and starlight. In X-rays the morphology is also rather symmetric: within the same regions on which we estimated the line asymmetry, the number counts in the Chandra image returns a ratio of 1.5. The northern cavity also shows a temperature a factor of ~ 2 lower than on the south side, with the lowest temperature found cospatial with the brightest line and X-ray regions (Blanton et al. 2011). Our results represent a significant new ingredient for modeling the interaction between the outflowing plasma and the external medium.

ALMA observations of central cluster galaxies have revealed a close association between the X-ray cavities, Hα emission, and the molecular gas (McNamara et al. 2014, Russell et al. 2017, McDonald et al. 2012). A large amount of cold molecular gas ($10^9 - 10^{10} M_\odot$) is common in BCG galaxies (e.g., Edge 2001, Salomé & Combes 2003), but the origin of this gas is uncertain. A possible explanation is that it is produced by the cooling of the hot plasma compressed and uplifted by the expanding bubbles. Alternative scenarios exist, for example the lifting of dense gas out of the galaxy or the deposition of cold gas as a result of a merger or a fly-by encounter. The last possibility seems unlikely because it requires an almost radial orbit at low velocity. The information on the distribution of the cold molecular gas in 3C 317 would be of great importance in this respect, but it is still currently not available.

5.5   Summary and conclusion

MUSE data have provided new and detailed insights into the physical properties of the WIM of UGC 9799, the central galaxy in the Abell cluster 2052, with full 3D coverage of the X-ray cavities. The ionized gas forms a filamentary structure surrounding the northern radio lobe. No emission is seen instead on the southern side with an asymmetry between the sides higher than a factor 75.

The gas velocity field is indicative of an expanding nebula and we found regions where the emission lines are split, marking the locations where the two sides project onto each other. The maximum observed velocity is 265 km s^{-1}. The expansion speed of the nebula derived from

these observations is a factor of ~ 2 lower than previous indirect estimates based on X-ray data. However, our measurement represents the instantaneous velocity instead of the value averaged across its whole lifetime.

From optical emission lines we also measured gas density (up to 270 cm^{-3}), estimated its mass (on the order of one million solar masses) across the cavity and kinetic energy (on the order of 10^{53} erg). The emission line ratios reveal that the warm gas is photoionized by the AGN only within the central ~ 3 kpc, while they are inconsistent with AGN or ionization of young stars at greater distances. Because the emission lines are generally quite narrow, 50 – 100 km s^{-1}, shock ionization appears unlikely, favoring ionization from cosmic rays instead.

The kinematics of the WIM described above clearly indicates that the radio source has a profound impact on the external medium, confirming that radio mode feedback is operating in A2052. However, the WIM is just the tip of the iceberg of the various ISM phases. The X-ray data indicate that ~ $10^{10} M_\odot$ of the tenuous hot gas have been displaced. Furthermore, it is likely that UGC 9799 harbors a large amount of cold and molecular gas ($10^8 – 10^9 M_\odot$), as commonly observed in the galaxies at the center of cluster. The interplay between all phases of the ISM and the relativistic radio plasma is a very complex phenomenon. The MUSE data provide us with detailed information on the ionized gas. When coupled with those that can be derived in the other observing bands these observations can be used to proceed toward a comprehensive description of the energy exchange between the AGN and the surrounding gas, tackling the issues of the origin, acceleration, and ultimate fate of the cold and warm gas clouds.

Summary and Conclusions

A feedback mechanism from active galactic nuclei (AGN) and supernovae (SNe) on their host galaxies is invoked to explain many observational properties of galaxies and supermassive black holes (BHs) at their centers. The main ones are the following: the discrepancy between the observed stellar mass function of galaxies and that predicted by ΛCDM models, both at low and high galaxy masses; the observed tight relations, spanning several orders of magnitude, between the mass of BHs and the velocity dispersion, mass and luminosity of the host galaxy spheroid (or bulge) or of the entire galaxy, in case of ellipticals; the similarity between the cosmic histories of BH growth and star formation activity. The first suggests that with secular processes alone, there would be much more low-mass and high-mass galaxies compared to what we observe, and there must then be a mechanism suppressing the formation of stars during the life of galaxies at those masses. The latter two point to a coevolution mechanism between the BH and the host galaxy, which regulates in parallel the BH growth and the star formation in the galaxy and shapes their physical properties, giving rise to the observed scaling relations. Such mechanism needs to be non-gravitational, since the BH gravitational sphere of influence is negligible compared to the size of the host galaxy. AGN and stellar feedback are nowadays commonly included in models of galaxy formation and evolution as they successfully reconcile the stellar mass function of galaxy predicted by models with the observed one. AGN feedback from accreting BHs, acting through outflows and jets, accounts for the lack of high-mass galaxies, while stellar feedback, through SN explosions and stellar winds, accounts for the lack of low-mass galaxies.

Models predict two mechanisms of AGN feedback, radiative mode and kinetic mode, acting through outflows and jets, respectively. In the standard simple picture, radiative feedback operates during a first intense and rapid phase, in which outflows accelerated by the AGN radiation pressure suppress star formation in the host galaxy and expel the gas reservoir out of it, dampening at the same time the accretion on the BH. During this phase the BH-host galaxy scaling relations are established. In a second slower and stable phase kinetic mode feedback, through jets launched by the now low-accreting AGN, maintains the gas in the galaxy halo hot, preventing it from recollapsing onto the galaxy and reigniting star formation. However, while there is strong evidence of kinetic mode feedback preventing, the collapse of gas in the halo onto the central galaxies in cool core clusters, through the mechanical action of radio jets, radiative mode feedback from outflows remains more elusive. Outflows are now routinely detected in many gas phases (highly-ionized, mildly-ionized, neutral atomic, molecular) related

to different spatial scales (from subpc to tens of kpc), from X-ray to radio observations. Despite star formation suppression from outflows has been witnessed in action in a few objects recently, it is not yet clear which is their actual impact on the whole star formation and gas reservoir in the host galaxy. This comes in part from the high uncertainties and degeneracies associated with the measurements of the outflow physical and kinematic properties and energetics, which complicate the comparison with models. Most observations, addressing powerful quasars around the peak of cosmic AGN activity ($z \sim$ 1-3), are in fact spatially unresolved or have low-resolution, thus giving integrated information on the outflow properties (e.g. velocity, density, mass) and forcing to make many assumptions, for example on the outflow geometry and extension, which lead to large uncertainties on outflow energetics and in evaluating their impact on the host galaxy.

For this reason, we targeted nearby Seyfert galaxies with spatially-resolved observations. Due to their vicinity, nearby Seyferts are ideal laboratories to explore in high detail outflow properties, their formation and acceleration mechanisms, as well as the effects of AGN activity on the host galaxy. Specifically, we made use of observations from the optical and near-infrared integral field spectrograph MUSE at VLT, which provides an unprecendented combination of wide spatial and spectral coverage, together with the light-collecting power of an 8m-diameter telescope and with good spectral resolution, making of MUSE a unique instrument among the other integral field spectrographs.

We first presented in Chapter 2 our MAGNUM survey, comprising a total of 72 nearby AGN (<50 Mpc) observable with VLT/MUSE from Paranal Observatory, extracted from both optically- and X-ray selected AGN samples. We described the 9 sources whose MUSE data we already analyzed, namely Centaurus A, Circinus, IC 5063, NGC 1068, NGC 1365, NGC 1386, NGC 2992, NGC 4945, NGC 5643, to which we also added the star-forming galaxy NGC 6810, to compare the properties of outflows in AGN with those of a starburst outflow.

MUSE allowed us to map the ionized gas in several different optical emission lines over galactic scales and resolve the distribution, kinematics and physical properties of the ionized gas on spatial scales as low as ~10 to 100 pc, for galaxy distances of ~4 to 40 Mpc, respectively. We could then resolve, down to this small scales, on the order of single gas clouds, the structure of [O III] and [N II] ionization cones and outflows, as well as Hα star forming rings and spiral arms. Star-formation in the disk dominates in fact Hα emission, while the ionization cones stand out in [O III] (or, in a couple of sources, [N II]), resulting from a more energetic ionizing mechanism, either the AGN radiation and/or shocks. We find ubiquitous one- or double-sided ionization cones spanning a wide range of sizes, from ~200 pc up to 10 kpc per side. We map prominent galactic outflows associated with the ionization cones, both with clear conical shapes, or with less defined shapes. A peculiar kinematic structure is observed in the outflowing cones of two sources, Circinus and NGC 4945, with blueshifted velocities at the cone edges

and redshifted around the cone axis, and an opposite morphology in the counter cone, that is, redshifted velocities at the cone edges and blueshifted in the middle. We compared our maps of NGC 4945 with a toy kinematic model of a hollow conical outflow intercepting the plane of the sky, which qualitatively reproduces the features observed in the cones of NGC 4945. A hollow conical outflow intercepting the plane of the sky then seems to be a promising way to explain the peculiar kinematic features observed in these two galaxies. We detect strongly enhanced linewidths perpendicular to the ionization cones and to the radio jets in four galaxies of our sample, IC 5063, NGC 1386, NGC 5643 and, less clearly, also in NGC 1068, which are the only objects hosting a jet among the ones we presented. Such aspect suggests a correlation between the presence of the radio jet and the enhanced linewidths perpendicular to it, which might stem from outflowing or turbulent motions induced laterally by the jet expansion.

We then concentrated on single objects. In Chapter 3 we presented a detailed study of the ionized gas in the central ~5.3 kpc of the MAGNUM galaxy NGC 1365, both in its warm and hot phase, using our spatially resolved optical VLT/MUSE observations and *Chandra* ACIS-S X-ray data. Here we observe a biconical outflow prominent in [O III] extending out to about 2.5 kpc in both directions, with line-of-sight velocities up to ± 170 km s^{-1}. We resolve its clumpy structure down to a scale of ~70 pc. One cone is brighter and has approaching velocities, while the other recedes and is fainter, the former residing above the galaxy disk and the latter behind, partially obscured by dust in the disk. The cones are ionized by the AGN while star formation dominates along the dust lanes aligned with the bar enclosing a prominent star forming ring, where densities up to 10^3 cm^{-3} are observed. The soft X-rays in NGC 1365 are dominated by thermal emission due to star-forming processes, with about 40% of the soft X-ray emission originating from the star-forming ring. However, by selecting appropriate X-ray energy intervals we are able to recover the AGN-photoionized component, which spatially matches the [O III] optical AGN-photoionized cone from MUSE. NGC 1365 hosts a nuclear unresolved outflow, revealed from blueshifted Fe XXV and Fe XXVI absorption lines in the hard X-rays, which indicate a velocity of ~3000 km s^{-1} and a mass outflow rate of the same order of magnitude as that of the galactic outflow from MUSE. The mass outflow rate of the ionized galactic outflow, which we could map thanks to MUSE, decreases with distance, which might either imply that the outflow slows down at larger distances or that the AGN pushing the wind has become more powerful recently (or it is also due to the fact that the AGN ionizing flux decreases as r^{-2}). By comparing the properties of the X-ray wind with those of the galactic ionized outflow we can investigate the feasibility of different driving mechanism for the outflow. An energy-driven scenario for the extended outflow is unlikely, as a fraction of neutral atomic and molecular gas $\gtrsim 10^3$ larger than the ionized one would be required for energy conservation, which is too large compared to what is observed in other AGN. A lower fraction ($\gtrsim 40$) would be required for momentum conservation, but models predict that the momentum-driven mode operates on scales $\lesssim 1$ kpc,

while the outflow in NGC 1365 extends on few kpc. However, these constraints on the gas frac-
tion are partially relaxed in the hypothesis that the AGN (and so the X-ray wind) is more pow-
erful at present time than in the past. Finally, direct acceleration by the AGN radiation pressure
on dusty clouds could be a possible driver of the outflow in principle. We find that the inte-
grated mass outflow rate, kinetic energy rate, and outflow velocity of the galactic outflow of
NGC 1365 are broadly consistent with the relations observed in more luminous AGN. How-
ever, we note that the integrated mass outflow rate, calculated following the prescriptions for
integrated analyses, is 20 times larger than the values that we obtain from our radial analysis,
indicating that different methods may lead to a large discrepancy in the derived outflow quan-
tities and stresses the importance of having spatially resolved information. Finally, we detect a
hard X-ray (3-5 keV) excess cospatial with the star-forming ring prominent in Hα, tentatively
associated with a hotter gas component due to SNe in the ring driving a shocked wind, which
might contribute in principle to the kpc-scale outflow.

Recent models predict that galactic outflows, besides suppressing star formation, can also
give birth to stars within the outflow itself, with important potential implications on galaxy
evolution. According to these models, the high-velocity newborn stars with radial orbits may
contribute to populate the spheroid of the host galaxy and shape its size and velocity dispersion
as well as chemically enrich the circumgalactic medium. The first evidences of this new mode
of star formation in action were recently found in a few objects. However, we still miss a clear
evidence that this in-outflow star formation can actually take place also in starburst-driven
outflows, besides in AGN-driven ones. In Chapter 4 we presented our MUSE detailed study of
the galactic ionized outflow in the star-forming galaxy NGC 6810. By kinematically isolating the
outflowing gas from that in the galaxy disk, we found that the gas within the outflow is ionized
by young stars and has an ionization parameter typical of star-forming regions, indicating on-
going star formation in situ. We thus found the first evidence of star formation occurring within
an outflow in a galaxy unambiguously identified as star-forming. Our result represents a pilot
study and demonstrates that by investigating galactic outflows in detail and at high spatial res-
olution, both in star-forming galaxies and AGN, we may unveil this new in-outflow mode of
star formation, otherwise hidden, in many other objects, potentially constituting another key
element to add to the complex puzzle of galaxy evolution.

The clearest observational evidence of feedback comes in its kinetic mode from massive
brightest cluster galaxies (BCGs) at the center of cool core clusters in the local Universe. Here
X-ray images revealed cavities in the hot ionized medium surrounding the BCG, filled by the ra-
dio jets, which provide the mechanical energy input to keep the gas in the halo hot, preventing
it to cool and recollapse on the galaxy to form stars. Still, since gas speed cannot be measured
from X-ray observations, the expansion velocity of the bubble has to be assumed or derived
from indirect and model-dependent methods. In Chapter 5 we show that, by exploiting MUSE

integral field optical data, we are able to measure the expansion velocity of the northern cavity around the the radio source 3C 317 at the center of the cluster Abell 2052, by mapping the warm gas filaments enshrouding the bubble. The expansion speed of the nebula derived from MUSE observations ($\simeq$265 km s^{-1}) is a factor of ~ 2 lower than previous indirect estimates based on X-ray data. We also measure gas density (up to 270 cm^{-3}), estimate its mass (on the order of one million solar masses) across the cavity and kinetic energy (on the order of 10^{53} erg). While AGN dominates gas photoionization within the central ~ 3 kpc, we exclude ionization either from the AGN, young stars or shocks at larger distances, based on optical emission-line ratios and linewidths, favoring ionization from cosmic rays instead. No line emission is detected instead from the southern cavity. Such strong asymmetry between the northern and southern cavities observed in the warm ionized gas contrasts with the much less pronounced differences between the two sides in the hot X-ray emitting gas and represents a significant new ingredient for our understanding of the process of energy exchange between the relativistic radio-emitting plasma and the external medium. The kinematics of the warm ionized gas found from MUSE indicates that the radio source has a profound impact on the external medium, confirming that radio mode feedback is operating in A2052.

Future developments

Our next goal is to fully exploit the possibilities offered by MUSE data in the framework of our MAGNUM survey. We have recently finalized an extensive analysis of the ionization and physical properties of the gas in the 9 galaxies we presented, by exploiting optical emission-line ratios available in MUSE cubes (Mingozzi et al. 2018). We then want to carry out a detailed study of the galactic outflows and of their interplay with the gas and star formation in the host galaxy, in each of these 9 objects. We also aim to investigate the nature of the common properties that we observe in the analyzed sources, such as the peculiar kinematic maps suggesting a hollow-conical structure for the outflows in NGC 4945 and Circinus, or the enhanced linewidths perpendicular to the ionization cones and radio jets in IC 5063, NGC 1386, NGC 5643 and NGC 1068. We will make use of physically-motivated models of realistic clumpy outflows, based on the observed flux and kinematic distribution of the gas, and of jet expansion in the gas medium.

Similarly to what we did for NGC 1365, we want to compare MUSE optical line-emission with X-ray emission in AGN ionization cones in other MAGNUM galaxies for which *Chandra* ACIS-S data are available, so as to obtain further insights on the kinematics, ionization and energetics of the ionized gas. We aim to fully exploit our MUSE cubes to study, in addition to the ionized phase of outflows, also their neutral phase from Na I D absorption doublet, and compare their distribution, kinematics and masses. We also have an ongoing observing program with the mm and sub-mm interferometer Atacama Large Millimeter Array (ALMA) targeting some of the galaxies we analyzed with MUSE. Our goal is to investigate the presence of molec-

ular outflows and compare their properties, extension, structure, kinematics, masses and energetics with those of the ionized outflows from MUSE.

We plan to extend our analysis to the whole MAGNUM sample of 72 nearby AGN we selected, by exploiting archival MUSE, ALMA and other multi-wavelength ancillary data (e.g. *Chandra* X-ray data), when present, and by asking for observation for the other targets. By having information on galactic ionized and neutral atomic outflows from MUSE, molecular outflows from ALMA and highly-ionized nuclear outflows from hard X-rays, we will encompass all outflow gas phases in our nearby targets with an extremely high detail. This will give us a comprehensive view of the outflow phenomenon, allowing us to investigate the distribution of outflows on various spatial scales and their different contribution to the total mass budget. We will determine the total energetics of outflows, instead of a single phase only, from nuclear to galactic scales, allowing solid comparisons with models, which generally give predictions on all the total outflow budget rather than on single phases. We will thus be able to obtain a clear view on the driving engine of outflows, if AGN, star formation or both, on the acceleration mechanisms, if momentum-driven, energy-driven, radiation-pressure driven, a mix of them or some other mechanism, and to put tighter constraints on the interaction processes with the host galaxy.

Bibliography

Aalto S., Garcia-Burillo S., Muller S., Winters J. M., van der Werf P., Henkel C., Costagliola F., Neri R., 2012, A&A, 537, A44

Aalto S., et al., 2015, A&A, 574, A85

Aird J., et al., 2010, MNRAS, 401, 2531

Aird J., Coil A. L., Georgakakis A., Nandra K., Barro G., Pérez-González P. G., 2015, MNRAS, 451, 1892

Alexander D. M., Hickox R. C., 2012, New A Rev., 56, 93

Allen M. G., Dopita M. A., Tsvetanov Z. I., Sutherland R. S., 1999, ApJ, 511, 686

Alonso-Herrero A., Ward M. J., Kotilainen J. K., 1997, MNRAS, 288, 977

Alonso-Herrero A., et al., 2012, MNRAS, 425, 311

Alonso-Herrero A., et al., 2018, ApJ, 859, 144

Anglés-Alcázar D., Davé R., Faucher-Giguère C.-A., Özel F., Hopkins P. F., 2017, MNRAS, 464, 2840

Antonucci R., 1993, ARA&A, 31, 473

Arnaud K. A., 1996, in Jacoby G. H., Barnes J., eds, Astronomical Society of the Pacific Conference Series Vol. 101, Astronomical Data Analysis Software and Systems V. p. 17

Arribas S., Colina L., Bellocchi E., Maiolino R., Villar-Martín M., 2014, A&A, 568, A14

Asmus D., Hönig S. F., Gandhi P., Smette A., Duschl W. J., 2014, MNRAS, 439, 1648

Asmus D., Hönig S. F., Gandhi P., 2016, ApJ, 822, 109

Axon D. J., Marconi A., Macchetto F. D., Capetti A., Robinson A., 1997, Ap&SS, 248, 69

Bacon R., et al., 2010, in Society of Photo-Optical Instrumentation Engineers (SPIE) Conference Series. p. 773508, doi:10.1117/12.856027

Bae H.-J., Woo J.-H., 2014, ApJ, 795, 30

Bae H.-J., Woo J.-H., 2018, ApJ, 853, 185

Bae H.-J., Woo J.-H., Karouzos M., Gallo E., Flohic H., Shen Y., Yoon S.-J., 2017, ApJ, 837, 91

Baldwin J. A., Phillips M. M., Terlevich R., 1981, PASP, 93, 5

Balmaverde B., et al., 2016, A&A, 585, A148

Barbosa F. K. B., Storchi-Bergmann T., McGregor P., Vale T. B., Rogemar Riffel A., 2014, MNRAS, 445, 2353

Baum S. A., Heckman T. M., Bridle A., van Breugel W. J. M., Miley G. K., 1988, ApJS, 68, 643

Baumgartner W. H., Tueller J., Markwardt C. B., Skinner G. K., Barthelmy S., Mushotzky R. F., Evans P. A., Gehrels N., 2013, ApJS, 207, 19

Begelman M. C., Cioffi D. F., 1989, ApJ, 345, L21

Beifiori A., Courteau S., Corsini E. M., Zhu Y., 2012, MNRAS, 419, 2497

Belfiore F., et al., 2016, MNRAS, 461, 3111

Bell E. F., McIntosh D. H., Katz N., Weinberg M. D., 2003, ApJS, 149, 289

Benson A. J., Bower R. G., Frenk C. S., Lacey C. G., Baugh C. M., Cole S., 2003, ApJ, 599, 38

Bergeron J., Durret F., Boksenberg A., 1983, A&A, 127, 322

Bian F., Kewley L. J., Dopita M. A., Juneau S., 2016, ApJ, 822, 62

Bianchi S., Guainazzi M., Chiaberge M., 2006, A&A, 448, 499

Binney J., Tremaine S., 2008, Galactic Dynamics: Second Edition. Princeton University Press

Bîrzan L., Rafferty D. A., McNamara B. R., Wise M. W., Nulsen P. E. J., 2004, ApJ, 607, 800

Bîrzan L., Rafferty D. A., Nulsen P. E. J., McNamara B. R., Röttgering H. J. A., Wise M. W., Mittal R., 2012, MNRAS, 427, 3468

Bischetti M., et al., 2017, A&A, 598, A122

Blanco V. M., Graham J. A., Lasker B. M., Osmer P. S., 1975, ApJ, 198, L63

Bland J., Tully B., 1988, Nature, 334, 43

Bland-Hawthorn J., Lumsden S. L., Voit G. M., Cecil G. N., Weisheit J. C., 1997, Ap&SS, 248, 177

Blanton E. L., Sarazin C. L., McNamara B. R., Wise M. W., 2001, ApJ, 558, L15

Blanton E. L., Sarazin C. L., McNamara B. R., 2003, ApJ, 585, 227

Blanton E. L., Randall S. W., Clarke T. E., Sarazin C. L., McNamara B. R., Douglass E. M., McDonald M., 2011, ApJ, 737, 99

Blustin A. J., Page M. J., Fuerst S. V., Branduardi-Raymont G., Ashton C. E., 2005, A&A, 431, 111

Boehringer H., Voges W., Fabian A. C., Edge A. C., Neumann D. M., 1993, MNRAS, 264, L25

Bordoloi R., et al., 2014, ApJ, 794, 130

Boroson T., 2005, AJ, 130, 381

Bower R. G., Benson A. J., Malbon R., Helly J. C., Frenk C. S., Baugh C. M., Cole S., Lacey C. G., 2006, MNRAS, 370, 645

Bower R. G., Benson A. J., Crain R. A., 2012, MNRAS, 422, 2816

Boyle B. J., Shanks T., Croom S. M., Smith R. J., Miller L., Loaring N., Heymans C., 2000, MNRAS, 317, 1014

Bradshaw E. J., et al., 2013, MNRAS, 433, 194

Braito V., Reeves J. N., Gofford J., Nardini E., Porquet D., Risaliti G., 2014, ApJ, 795, 87

Brenneman L. W., Risaliti G., Elvis M., Nardini E., 2013, MNRAS, 429, 2662

Brightman M., Nandra K., 2008, MNRAS, 390, 1241

Brusa M., et al., 2015a, MNRAS, 446, 2394

Brusa M., et al., 2015b, A&A, 578, A11

Brusa M., et al., 2016, A&A, 588, A58

Bundy K., et al., 2015, ApJ, 798, 7

Bureau M., Mould J. R., Staveley-Smith L., 1996, ApJ, 463, 60

Burtscher L., et al., 2013, A&A, 558, A149

Buttiglione S., Capetti A., Celotti A., Axon D. J., Chiaberge M., Macchetto F. D., Sparks W. B., 2010, A&A, 509, A6

Calzetti D., Armus L., Bohlin R. C., Kinney A. L., Koornneef J., Storchi-Bergmann T., 2000, ApJ, 533, 682

Cano-Díaz M., Maiolino R., Marconi A., Netzer H., Shemmer O., Cresci G., 2012, A&A, 537, L8

Capetti A., 2011, A&A, 535, A28

Cappellari M., Copin Y., 2003, MNRAS, 342, 345

Cappellari M., Emsellem E., 2004, PASP, 116, 138

Cappi M., et al., 2009, A&A, 504, 401

Carilli C. L., Perley R. A., Harris D. E., 1994, MNRAS, 270, 173

Carniani S., et al., 2015, A&A, 580, A102

Carniani S., et al., 2016, A&A, 591, A28

Cattaneo A., et al., 2009, Nature, 460, 213

Cazzoli S., Arribas S., Maiolino R., Colina L., 2016, A&A, 590, A125

Cecil G., Bland J., Tully R. B., 1990, ApJ, 355, 70

Cecil G., Dopita M. A., Groves B., Wilson A. S., Ferruit P., Pécontal E., Binette L., 2002, ApJ, 568, 627

Chartas G., Cappi M., Hamann F., Eracleous M., Strickland S., Giustini M., Misawa T., 2016, ApJ, 824, 53

Cicone C., et al., 2014, A&A, 562, A21

Cicone C., et al., 2015, A&A, 574, A14

Cicone C., Brusa M., Ramos Almeida C., Cresci G., Husemann B., Mainieri V., 2018, Nature Astronomy, 2, 176

Ciotti L., Ostriker J. P., Proga D., 2010, ApJ, 717, 708

Coccato L., Corsini E. M., Pizzella A., Morelli L., Funes J. G., Bertola F., 2004, A&A, 416, 507

Colbert E. J. M., Baum S. A., Gallimore J. F., O'Dea C. P., Lehnert M. D., Tsvetanov Z. I., Mulchaey J. S., Caganoff S., 1996a, ApJS, 105, 75

Colbert E. J. M., Baum S. A., Gallimore J. F., O'Dea C. P., Christensen J. A., 1996b, ApJ, 467, 551

Cole S., Lacey C. G., Baugh C. M., Frenk C. S., 2000, MNRAS, 319, 168

Colina L., Fricke K. J., Kollatschny W., Perryman M. A. C., 1987, A&A, 178, 51

Colina L., Sparks W. B., Macchetto F., 1991, ApJ, 370, 102

Concas A., Popesso P., Brusa M., Mainieri V., Thomas D., 2017, preprint, (arXiv:1710.08423)

Congiu E., et al., 2017, MNRAS, 471, 562

Costa T., Sijacki D., Haehnelt M. G., 2014, MNRAS, 444, 2355

Costa T., Sijacki D., Haehnelt M. G., 2015, MNRAS, 448, L30

Costa T., Rosdahl J., Sijacki D., Haehnelt M. G., 2018, MNRAS, 479, 2079

Crawford C. S., Allen S. W., Ebeling H., Edge A. C., Fabian A. C., 1999, MNRAS, 306, 857

Crenshaw D. M., Kraemer S. B., George I. M., 2003, ARA&A, 41, 117

Crenshaw D. M., Fischer T. C., Kraemer S. B., Schmitt H. R., 2015, ApJ, 799, 83

Cresci G., et al., 2015a, A&A, 582, A63

Cresci G., et al., 2015b, ApJ, 799, 82

Cresci G., Vanzi L., Telles E., Lanzuisi G., Brusa M., Mingozzi M., Sauvage M., Johnson K., 2017, A&A, 604, A101

Crockett R. M., et al., 2012, MNRAS, 421, 1603

Croft S., et al., 2006, ApJ, 647, 1040

Croton D. J., et al., 2006, MNRAS, 365, 11

Dalla Vecchia C., Schaye J., 2008, MNRAS, 387, 1431

Dasyra K. M., Combes F., 2011, A&A, 533, L10

Dasyra K. M., Combes F., 2012, A&A, 541, L7

Dasyra K. M., Bostrom A. C., Combes F., Vlahakis N., 2015, ApJ, 815, 34

Dasyra K. M., Combes F., Oosterloo T., Oonk J. B. R., Morganti R., Salomé P., Vlahakis N., 2016, A&A, 595, L7

Davies R. I., et al., 2014, ApJ, 792, 101

Davis B. L., et al., 2014, ApJ, 789, 124

Dekel A., Silk J., 1986, ApJ, 303, 39

Di Matteo T., Springel V., Hernquist L., 2005, Nature, 433, 604

Díaz A. I., Castellanos M., Terlevich E., Luisa García-Vargas M., 2000, MNRAS, 318, 462

Dopita M. A., Sutherland R. S., 1995, ApJ, 455, 468

Dressler A., 1989, in Osterbrock D. E., Miller J. S., eds, IAU Symposium Vol. 134, Active Galactic Nuclei. p. 217

Dugan Z., Bryan S., Gaibler V., Silk J., Haas M., 2014, ApJ, 796, 113

Dunn R. J. H., Fabian A. C., 2008, MNRAS, 385, 757

Edge A. C., 2001, MNRAS, 328, 762

Edmunds M. G., Taylor K., Turtle A. J., 1988, MNRAS, 234, 155

Eilek J. A., 2014, New Journal of Physics, 16, 045001

Elbaz D., Jahnke K., Pantin E., Le Borgne D., Letawe G., 2009, A&A, 507, 1359

Fabian A. C., 1999, MNRAS, 308, L39

Fabian A. C., 2012, ARA&A, 50, 455

Fabian A. C., Wilman R. J., Crawford C. S., 2002, MNRAS, 329, L18

Fabian A. C., Vasudevan R. V., Gandhi P., 2008, MNRAS, 385, L43

Fabian A. C., Sanders J. S., Williams R. J. R., Lazarian A., Ferland G. J., Johnstone R. M., 2011, MNRAS, 417, 172

Falcón-Barroso J., Sánchez-Blázquez P., Vazdekis A., Ricciardelli E., Cardiel N., Cenarro A. J., Gorgas J., Peletier R. F., 2011, A&A, 532, A95

Faucher-Giguère C.-A., Quataert E., 2012, MNRAS, 425, 605

Feain I. J., Papadopoulos P. P., Ekers R. D., Middelberg E., 2007, ApJ, 662, 872

Ferguson H. C., Tanvir N. R., von Hippel T., 1998, Nature, 391, 461

Ferland G. J., Fabian A. C., Hatch N. A., Johnstone R. M., Porter R. L., van Hoof P. A. M., Williams R. J. R., 2008, MNRAS, 386, L72

Ferland G. J., Fabian A. C., Hatch N. A., Johnstone R. M., Porter R. L., van Hoof P. A. M., Williams R. J. R., 2009, MNRAS, 392, 1475

Ferrarese L., Ford H., 2005, Space Sci. Rev. , 116, 523

Ferrarese L., Merritt D., 2000, ApJ, 539, L9

Ferruit P., Wilson A. S., Mulchaey J., 2000, ApJS, 128, 139

Feruglio C., Maiolino R., Piconcelli E., Menci N., Aussel H., Lamastra A., Fiore F., 2010, A&A, 518, L155

Feruglio C., Fiore F., Piconcelli E., Cicone C., Maiolino R., Davies R., Sturm E., 2013, A&A, 558, A87

Feruglio C., et al., 2015, A&A, 583, A99

Feruglio C., et al., 2017, A&A, 608, A30

Fiore F., et al., 2017, A&A, 601, A143

Fischer J., et al., 2010, A&A, 518, L41

Fischer T. C., Crenshaw D. M., Kraemer S. B., Schmitt H. R., 2013, ApJS, 209, 1

Fluetsch A., et al., 2018, preprint, (arXiv:1805.05352)

Forbes D. A., Norris R. P., 1998, MNRAS, 300, 757

Freudling W., Romaniello M., Bramich D. M., Ballester P., Forchi V., García-Dabló C. E., Moehler S., Neeser M. J., 2013, A&A, 559, A96

Friedrich S., Davies R. I., Hicks E. K. S., Engel H., Müller-Sánchez F., Genzel R., Tacconi L. J., 2010, A&A, 519, A79

Fruscione A., et al., 2006, in Society of Photo-Optical Instrumentation Engineers (SPIE) Conference Series. p. 62701V, doi:10.1117/12.671760

Fu H., Stockton A., 2009, ApJ, 690, 953

Gabor J. M., Davé R., Oppenheimer B. D., Finlator K., 2011, MNRAS, 417, 2676

Gal-Yam A., Maoz D., Guhathakurta P., Filippenko A. V., 2003, AJ, 125, 1087

Gallagher R., Maiolino R., Belfiore F., Drory N., Riffel R., Riffel R. A., 2018, preprint, (arXiv:1806.03311)

Gallimore J. F., Baum S. A., O'Dea C. P., Brinks E., Pedlar A., 1994, ApJ, 422, L13

Gallimore J. F., Baum S. A., O'Dea C. P., Pedlar A., 1996, ApJ, 458, 136

Gallimore J. F., et al., 2016, ApJ, 829, L7

Ganguly R., Brotherton M. S., Cales S., Scoggins B., Shang Z., Vestergaard M., 2007, ApJ, 665, 990

García-Burillo S., et al., 2014, A&A, 567, A125

Garmire G. P., Bautz M. W., Ford P. G., Nousek J. A., Ricker Jr. G. R., 2003, in Truemper J. E., Tananbaum H. D., eds, Society of Photo-Optical Instrumentation Engineers (SPIE) Conference Series Vol. 4851, X-Ray and Gamma-Ray Telescopes and Instruments for Astronomy.. pp 28–44, doi:10.1117/12.461599

Gebhardt K., et al., 2000, ApJ, 539, L13

Genzel R., et al., 2011, ApJ, 733, 101

Gofford J., Reeves J. N., Tombesi F., Braito V., Turner T. J., Miller L., Cappi M., 2013, MNRAS, 430, 60

Gómez-Guijarro C., González-Martín O., Ramos Almeida C., Rodríguez-Espinosa J. M., Gallego J., 2017, MNRAS, 469, 2720

González-Alfonso E., et al., 2017, ApJ, 836, 11

Graham A. W., 2007, MNRAS, 379, 711

Graham A. W., 2008a, PASA, 25, 167

Graham A. W., 2008b, ApJ, 680, 143

Graham A. W., Scott N., 2013, ApJ, 764, 151

Graham A. W., Onken C. A., Athanassoula E., Combes F., 2011, MNRAS, 412, 2211

Granato G. L., De Zotti G., Silva L., Bressan A., Danese L., 2004, ApJ, 600, 580

Greene J. E., et al., 2010, ApJ, 721, 26

Greenhill L. J., et al., 2003, ApJ, 590, 162

Gu Q., Melnick J., Cid Fernandes R., Kunth D., Terlevich E., Terlevich R., 2006, MNRAS, 366, 480

Guainazzi M., Matt G., Brandt W. N., Antonelli L. A., Barr P., Bassani L., 2000, A&A, 356, 463

Guainazzi M., Risaliti G., Nucita A., Wang J., Bianchi S., Soria R., Zezas A., 2009, A&A, 505, 589

Gültekin K., et al., 2009, ApJ, 698, 198

Hardcastle M. J., Worrall D. M., Kraft R. P., Forman W. R., Jones C., Murray S. S., 2003, ApJ, 593, 169

Häring N., Rix H.-W., 2004, ApJ, 604, L89

Harrison C. M., et al., 2012, MNRAS, 426, 1073

Harrison C. M., Alexander D. M., Mullaney J. R., Swinbank A. M., 2014, MNRAS, 441, 3306

Harrison C. M., et al., 2016, MNRAS, 456, 1195

Harrison C. M., Costa T., Tadhunter C. N., Flütsch A., Kakkad D., Perna M., Vietri G., 2018, Nature Astronomy, 2, 198

Haynes R. F., Cannon R. D., Ekers R. D., 1983, Proceedings of the Astronomical Society of Australia, 5, 241

Heckman T. M., 1980, A&A, 87, 152

Heckman T. M., Best P. N., 2014, ARA&A, 52, 589

Heckman T. M., Thompson T. A., 2017, preprint, (arXiv:1701.09062)

Heckman T. M., Miley G. K., Green R. F., 1984, ApJ, 281, 525

Heckman T. M., Armus L., Miley G. K., 1987, AJ, 93, 276

Heckman T. M., Baum S. A., van Breugel W. J. M., McCarthy P., 1989, ApJ, 338, 48

Heckman T. M., Armus L., Miley G. K., 1990, ApJS, 74, 833

Heckman T. M., Alexandroff R. M., Borthakur S., Overzier R., Leitherer C., 2015, ApJ, 809, 147

Hinshaw G., et al., 2013, ApJS, 208, 19

Hjelm M., Lindblad P. O., 1996, A&A, 305, 727

Hlavacek-Larrondo J., Fabian A. C., Edge A. C., Ebeling H., Sanders J. S., Hogan M. T., Taylor G. B., 2012, MNRAS, 421, 1360

Hlavacek-Larrondo J., et al., 2013, ApJ, 777, 163

Ho L., 1999, in Chakrabarti S. K., ed., Astrophysics and Space Science Library Vol. 234, Observational Evidence for the Black Holes in the Universe. p. 157, doi:10.1007/978-94-011-4750-7_11

Ho L. C., Filippenko A. V., Sargent W. L. W., 1997, ApJS, 112, 315

Ho L. C., Li Z.-Y., Barth A. J., Seigar M. S., Peng C. Y., 2011, ApJS, 197, 21

Holt J., Tadhunter C. N., Morganti R., 2008, MNRAS, 387, 639

Hopkins P. F., Elvis M., 2010, MNRAS, 401, 7

Hopkins P. F., Hernquist L., Cox T. J., Di Matteo T., Robertson B., Springel V., 2006, ApJS, 163, 1

Hopkins P. F., et al., 2018, MNRAS, 480, 800

Horiuchi S., Meier D. L., Preston R. A., Tingay S. J., 2006, PASJ, 58, 211

Hu J., 2008, MNRAS, 386, 2242

Humphrey A., Villar-Martín M., Sánchez S. F., Martínez-Sansigre A., Delgado R. G., Pérez E., Tadhunter C., Pérez-Torres M. A., 2010, MNRAS, 408, L1

Husemann B., Scharwächter J., Bennert V. N., Mainieri V., Woo J.-H., Kakkad D., 2016, A&A, 594, A44

Ishibashi W., Fabian A. C., 2012, MNRAS, 427, 2998

Ishibashi W., Fabian A. C., 2014, MNRAS, 441, 1474

Ishibashi W., Fabian A. C., 2015, MNRAS, 451, 93

Ishibashi W., Fabian A. C., 2017, MNRAS, 472, 2768

Ishibashi W., Fabian A. C., Canning R. E. A., 2013, MNRAS, 431, 2350

Ishibashi W., Fabian A. C., Maiolino R., 2018, MNRAS, 476, 512

Israel F. P., 1998, A&A Rev., 8, 237

Israel F. P., Güsten R., Meijerink R., Requena-Torres M. A., Stutzki J., 2017, A&A, 599, A53

Iyomoto N., Makishima K., Fukazawa Y., Tashiro M., Ishisaki Y., 1997, PASJ, 49, 425

Janssen A. W., et al., 2016, ApJ, 822, 43

Jones J. E., Jones B. J. T., 1980, MNRAS, 191, 685

Jorsater S., van Moorsel G. A., 1995, AJ, 110, 2037

Kaasinen M., Bian F., Groves B., Kewley L. J., Gupta A., 2017, MNRAS, 465, 3220

Kalberla P. M. W., Burton W. B., Hartmann D., Arnal E. M., Bajaja E., Morras R., Pöppel W. G. L., 2005, A&A, 440, 775

Kallman T., Bautista M., 2001, ApJS, 133, 221

Karouzos M., Woo J.-H., Bae H.-J., 2016a, ApJ, 819, 148

Karouzos M., Woo J.-H., Bae H.-J., 2016b, ApJ, 833, 171

Katgert P., Mazure A., den Hartog R., Adami C., Biviano A., Perea J., 1998, A&A, 129, 399

Kauffmann G., Haehnelt M., 2000, MNRAS, 311, 576

Kauffmann G., White S. D. M., Guiderdoni B., 1993, MNRAS, 264, 201

Kauffmann G., et al., 2003, MNRAS, 346, 1055

Kennicutt R. C., Evans N. J., 2012, ARA&A, 50, 531

Kewley L. J., Heisler C. A., Dopita M. A., Sutherland R., Norris R. P., Reynolds J., Lumsden S., 2000, ApJ, 530, 704

Kewley L. J., Heisler C. A., Dopita M. A., Lumsden S., 2001a, ApJS, 132, 37

Kewley L. J., Dopita M. A., Sutherland R. S., Heisler C. A., Trevena J., 2001b, ApJ, 556, 121

Kewley L. J., Groves B., Kauffmann G., Heckman T., 2006, MNRAS, 372, 961

King A., 2003, ApJ, 596, L27

King A., 2005, ApJ, 635, L121

King A., Pounds K., 2015, ARA&A, 53, 115

King A. R., Zubovas K., Power C., 2011, MNRAS, 415, L6

Kinney A. L., Schmitt H. R., Clarke C. J., Pringle J. E., Ulvestad J. S., Antonucci R. R. J., 2000, ApJ, 537, 152

Kirhakos S. D., Steiner J. E., 1990, AJ, 99, 1722

Komossa S., Schulz H., 1998, A&A, 339, 345

Komossa S., Xu D., Zhou H., Storchi-Bergmann T., Binette L., 2008, ApJ, 680, 926

Kormendy J., 1993, in Beckman J., Colina L., Netzer H., eds, The Nearest Active Galaxies. pp 197–218

Kormendy J., Bender R., 2009, ApJ, 691, L142

Kormendy J., Bender R., 2011, Nature, 469, 377

Kormendy J., Gebhardt K., 2001, in Wheeler J. C., Martel H., eds, American Institute of Physics Conference Series Vol. 586, 20th Texas Symposium on relativistic astrophysics. pp 363–381 (arXiv:astro-ph/0105230), doi:10.1063/1.1419581

Kormendy J., Ho L. C., 2013, ARA&A, 51, 511

Kraft R. P., Forman W. R., Jones C., Murray S. S., Hardcastle M. J., Worrall D. M., 2002, ApJ, 569, 54

Krajnović D., Sharp R., Thatte N., 2007, MNRAS, 374, 385

Kristen H., Jorsater S., Lindblad P. O., Boksenberg A., 1997, A&A, 328, 483

LaMassa S. M., et al., 2017, ApJ, 847, 100

Laor A., 2001, ApJ, 553, 677

Le Fèvre O., et al., 2003, in Iye M., Moorwood A. F. M., eds, Society of Photo-Optical Instrumentation Engineers (SPIE) Conference Series Vol. 4841, Instrument Design and Performance for Optical/Infrared Ground-based Telescopes. pp 1670–1681, doi:10.1117/12.460959

Lehnert M. D., Heckman T. M., 1996, ApJ, 462, 651

Leipski C., Falcke H., Bennert N., Hüttemeister S., 2006, A&A, 455, 161

Lena D., et al., 2015, ApJ, 806, 84

Lena D., Robinson A., Storchi-Bergmann T., Couto G. S., Schnorr-Müller A., Riffel R. A., 2016, MNRAS, 459, 4485

Li J.-T., Wang Q. D., 2013, MNRAS, 428, 2085

Lilly S. J., Eales S. A., Gear W. K. P., Hammer F., Le Fèvre O., Crampton D., Bond J. R., Dunne L., 1999, ApJ, 518, 641

Lindblad P. O., 1999, A&A Rev., 9, 221

Lindblad P. O., Hjelm M., Hoegbom J., Joersaeter S., Lindblad P. A. B., Santos-Lleo M., 1996a, A&A, 120, 403

Lindblad P. A. B., Lindblad P. O., Athanassoula E., 1996b, A&A, 313, 65

Liu G., Zakamska N. L., Greene J. E., Nesvadba N. P. H., Liu X., 2013, MNRAS, 436, 2576

López-Gonzaga N., Burtscher L., Tristram K. R. W., Meisenheimer K., Schartmann M., 2016, A&A, 591, A47

Lusso E., et al., 2011, A&A, 534, A110

Lutz D., Maiolino R., Moorwood A. F. M., Netzer H., Wagner S. J., Sturm E., Genzel R., 2002, A&A, 396, 439

Madau P., Dickinson M., 2014, ARA&A, 52, 415

Madau P., Ferguson H. C., Dickinson M. E., Giavalisco M., Steidel C. C., Fruchter A., 1996, MN-RAS, 283, 1388

Magdziarz P., Zdziarski A. A., 1995, MNRAS, 273, 837

Magorrian J., et al., 1998, AJ, 115, 2285

Maiolino R., Rieke G. H., 1995, ApJ, 454, 95

Maiolino R., et al., 2012, MNRAS, 425, L66

Maiolino R., et al., 2017, Nature, 544, 202

Marconi A., Hunt L. K., 2003, ApJ, 589, L21

Marconi A., Moorwood A. F. M., Origlia L., Oliva E., 1994, The Messenger, 78, 20

Marconi A., Oliva E., van der Werf P. P., Maiolino R., Schreier E. J., Macchetto F., Moorwood A. F. M., 2000, A&A, 357, 24

Marconi A., Risaliti G., Gilli R., Hunt L. K., Maiolino R., Salvati M., 2004, MNRAS, 351, 169

Markwardt C. B., 2009, in Bohlender D. A., Durand D., Dowler P., eds, Astronomical Society of the Pacific Conference Series Vol. 411, Astronomical Data Analysis Software and Systems XVIII. p. 251 (arXiv:0902.2850)

Martel A. R., Sparks W. B., Allen M. G., Koekemoer A. M., Baum S. A., 2002, AJ, 123, 1357

Martin C. L., Kobulnicky H. A., Heckman T. M., 2002, ApJ, 574, 663

Mathieu A., Dejonghe H., Hui X., 1996, in Bender R., Davies R. L., eds, IAU Symposium Vol. 171, New Light on Galaxy Evolution. p. 411

Matt G., Fabian A. C., Guainazzi M., Iwasawa K., Bassani L., Malaguti G., 2000, MNRAS, 318, 173

McConnell N. J., Ma C.-P., 2013, ApJ, 764, 184

McConnell N. J., Ma C.-P., Gebhardt K., Wright S. A., Murphy J. D., Lauer T. R., Graham J. R., Richstone D. O., 2011, Nature, 480, 215

McCormick A., Veilleux S., Rupke D. S. N., 2013, ApJ, 774, 126

McDonald M., Veilleux S., Rupke D. S. N., Mushotzky R., 2010, ApJ, 721, 1262

McDonald M., Veilleux S., Rupke D. S. N., 2012, ApJ, 746, 153

McKee C. F., Hollenbach D. J., 1980, ARA&A, 18, 219

McKernan B., Yaqoob T., Reynolds C. S., 2007, MNRAS, 379, 1359

McLure R. J., Dunlop J. S., 2002, MNRAS, 331, 795

McNamara B. R., Nulsen P. E. J., 2007, ARA&A, 45, 117

McNamara B. R., Nulsen P. E. J., 2012, New Journal of Physics, 14, 055023

McNamara B. R., et al., 2000, ApJ, 534, L135

McNamara B. R., et al., 2014, ApJ, 785, 44

Merritt D., Ferrarese L., 2001, MNRAS, 320, L30

Mineo S., Gilfanov M., Sunyaev R., 2012, MNRAS, 419, 2095

Mingozzi M., et al., 2018, preprint, (arXiv:1811.07935)

Moorwood A. F. M., van der Werf P. P., Kotilainen J. K., Marconi A., Oliva E., 1996a, A&A, 308, L1

Moorwood A. F. M., Lutz D., Oliva E., Marconi A., Netzer H., Genzel R., Sturm E., de Graauw T., 1996b, A&A, 315, L109

Morganti R., 2010, PASA, 27, 463

Morganti R., Killeen N. E. B., Tadhunter C. N., 1993, MNRAS, 263, 1023

Morganti R., Oosterloo T., Tsvetanov Z., 1998, AJ, 115, 915

Morganti R., Killeen N. E. B., Ekers R. D., Oosterloo T. A., 1999, MNRAS, 307, 750

Morganti R., Oosterloo T. A., Tadhunter C. N., van Moorsel G., Emonts B., 2005, A&A, 439, 521

Morganti R., Holt J., Saripalli L., Oosterloo T. A., Tadhunter C. N., 2007, A&A, 476, 735

Morganti R., Frieswijk W., Oonk R. J. B., Oosterloo T., Tadhunter C., 2013, A&A, 552, L4

Morganti R., Oosterloo T., Oonk J. B. R., Frieswijk W., Tadhunter C., 2015, A&A, 580, A1

Morganti R., Veilleux S., Oosterloo T., Teng S. H., Rupke D., 2016, A&A, 593, A30

Morris S., Ward M., Whittle M., Wilson A. S., Taylor K., 1985, MNRAS, 216, 193

Mullaney J. R., Alexander D. M., Fine S., Goulding A. D., Harrison C. M., Hickox R. C., 2013, MNRAS, 433, 622

Mundell C. G., Ferruit P., Nagar N., Wilson A. S., 2009, ApJ, 703, 802

Murray N., Chiang J., Grossman S. A., Voit G. M., 1995, ApJ, 451, 498

Murray N., Quataert E., Thompson T. A., 2005, ApJ, 618, 569

Nagar N. M., Wilson A. S., Mulchaey J. S., Gallimore J. F., 1999, ApJS, 120, 209

Nardini E., Zubovas K., 2018, preprint, (arXiv:1805.00040)

Nardini E., et al., 2015a, Science, 347, 860

Nardini E., Gofford J., Reeves J. N., Braito V., Risaliti G., Costa M., 2015b, MNRAS, 453, 2558

Nayakshin S., 2014, MNRAS, 437, 2404

Nayakshin S., Zubovas K., 2012, MNRAS, 427, 372

Nesvadba N. P. H., Lehnert M. D., De Breuck C., Gilbert A. M., van Breugel W., 2008, A&A, 491, 407

Nesvadba N. P. H., De Breuck C., Lehnert M. D., Best P. N., Binette L., Proga D., 2011, A&A, 525, A43

Newman S. F., et al., 2012, ApJ, 761, 43

O'Dea C. P., et al., 2008, ApJ, 681, 1035

Oliva E., Salvati M., Moorwood A. F. M., Marconi A., 1994, A&A, 288, 457

Onori F., et al., 2017, MNRAS, 468, L97

Oosterloo T. A., Morganti R., Tzioumis A., Reynolds J., King E., McCulloch P., Tsvetanov Z., 2000, AJ, 119, 2085

Oosterloo T., Raymond Oonk J. B., Morganti R., Combes F., Dasyra K., Salomé P., Vlahakis N., Tadhunter C., 2017, A&A, 608, A38

Osterbrock D. E., Ferland G. J., 2006, Astrophysics of gaseous nebulae and active galactic nuclei

Panagoulia E. K., Fabian A. C., Sanders J. S., Hlavacek-Larrondo J., 2014, MNRAS, 444, 1236

Peng C. Y., 2007, ApJ, 671, 1098

Pereira-Santaella M., et al., 2016, A&A, 594, A81

Pérez-Beaupuits J. P., Spoon H. W. W., Spaans M., Smith J. D., 2011, A&A, 533, A56

Perna M., et al., 2015a, A&A, 574, A82

Perna M., et al., 2015b, A&A, 583, A72

Perna M., Lanzuisi G., Brusa M., Mignoli M., Cresci G., 2017, A&A, 603, A99

Peterson J. R., Fabian A. C., 2006, Phys. Rep., 427, 1

Peterson B. A., Dickens R. J., Cannon R. D., 1975, Proceedings of the Astronomical Society of Australia, 2, 366

Phillips M. M., Edmunds M. G., Pagel B. E. J., Turtle A. J., 1983, MNRAS, 203, 759

Pietrinferni A., Cassisi S., Salaris M., Castelli F., 2004, ApJ, 612, 168

Pietrinferni A., Cassisi S., Salaris M., Castelli F., 2006, ApJ, 642, 797

Pinto C., et al., 2018, MNRAS, 476, 1021

Pounds K. A., Reeves J. N., King A. R., Page K. L., O'Brien P. T., Turner M. J. L., 2003, MNRAS, 345, 705

Rafferty D. A., McNamara B. R., Nulsen P. E. J., Wise M. W., 2006, ApJ, 652, 216

Rafferty D. A., McNamara B. R., Nulsen P. E. J., 2008, ApJ, 687, 899

Read J. I., Trentham N., 2005, Philosophical Transactions of the Royal Society of London Series A, 363

Reeves J. N., et al., 2009, ApJ, 701, 493

Revalski M., Crenshaw D. M., Kraemer S. B., Fischer T. C., Schmitt H. R., Machuca C., 2018, ApJ, 856, 46

Reynolds C. S., 1997, in Arav N., Shlosman I., Weymann R. J., eds, Astronomical Society of the Pacific Conference Series Vol. 128, Mass Ejection from Active Galactic Nuclei. p. 173 (arXiv:astro-ph/9704131)

Richards G. T., et al., 2006, AJ, 131, 2766

Richings A. J., Faucher-Giguère C.-A., 2018, MNRAS, 478, 3100

Risaliti G., Maiolino R., Salvati M., 1999, ApJ, 522, 157

Risaliti G., Bianchi S., Matt G., Baldi A., Elvis M., Fabbiano G., Zezas A., 2005, ApJ, 630, L129

Risaliti G., Elvis M., Fabbiano G., Baldi A., Zezas A., Salvati M., 2007, ApJ, 659, L111

Risaliti G., et al., 2009, ApJ, 696, 160

Risaliti G., et al., 2013, Nature, 494, 449

Rizza E., Loken C., Bliton M., Roettiger K., Burns J. O., Owen F. N., 2000, AJ, 119, 21

Rodríguez Zaurín J., Tadhunter C. N., Rose M., Holt J., 2013, MNRAS, 432, 138

Rose M., Tadhunter C., Ramos Almeida C., Rodríguez Zaurín J., Santoro F., Spence R., 2018, MNRAS, 474, 128

Rupke D. S. N., Veilleux S., 2011, ApJ, 729, L27

Rupke D. S. N., Veilleux S., 2013, ApJ, 768, 75

Rupke D. S. N., Veilleux S., 2015, ApJ, 801, 126

Rupke D. S., Veilleux S., Sanders D. B., 2005a, ApJS, 160, 87

Rupke D. S., Veilleux S., Sanders D. B., 2005b, ApJ, 632, 751

Russell H. R., et al., 2017, ApJ, 836, 130

Salomé P., Combes F., 2003, A&A, 412, 657

Salomé Q., Salomé P., Combes F., Hamer S., 2016, A&A, 595, A65

Salpeter E. E., 1955, ApJ, 121, 161

Sánchez-Blázquez P., et al., 2006, MNRAS, 371, 703

Sandage A., Tammann G. A., 1987, A revised Shapley-Ames Catalog of bright galaxies

Sanders R. L., et al., 2016, ApJ, 816, 23

Sandqvist A., Joersaeter S., Lindblad P. O., 1995, A&A, 295, 585

Sani E., Marconi A., Hunt L. K., Risaliti G., 2011, MNRAS, 413, 1479

Santoro F., Oonk J. B. R., Morganti R., Oosterloo T., 2015, A&A, 574, A89

Santoro F., Oonk J. B. R., Morganti R., Oosterloo T. A., Tadhunter C., 2016, A&A, 590, A37

Sarzi M., Kaviraj S., Nedelchev B., Tiffany J., Shabala S. S., Deller A. T., Middelberg E., 2016, MNRAS, 456, L25

Scannapieco C., et al., 2012, MNRAS, 423, 1726

Schaye J., et al., 2015, MNRAS, 446, 521

Schechter P., 1976, ApJ, 203, 297

Schinnerer E., Eckart A., Tacconi L. J., Genzel R., Downes D., 2000, ApJ, 533, 850

Schmitt H. R., Storchi-Bergmann T., Baldwin J. A., 1994, ApJ, 423, 237

Schulz H., Komossa S., Schmitz C., Mücke A., 1999, A&A, 346, 764

Schulz R., Morganti R., Nyland K., Paragi Z., Mahony E. K., Oosterloo T., 2018, A&A, 617, A38

Shakura N. I., Sunyaev R. A., 1973, A&A, 24, 337

Shankar F., Weinberg D. H., Miralda-Escudé J., 2009, ApJ, 690, 20

Shapley A. E., Steidel C. C., Pettini M., Adelberger K. L., 2003, ApJ, 588, 65

Sharp R. G., Bland-Hawthorn J., 2010, ApJ, 711, 818

Shlosman I., 1996, in Sandqvist A., Lindblad P. O., eds, Lecture Notes in Physics, Berlin Springer Verlag Vol. 474, Lecture Notes in Physics, Berlin Springer Verlag. p. 141 (arXiv:astro-ph/9602151), doi:10.1007/BFb0101973

Shopbell P. L., Bland-Hawthorn J., 1998, ApJ, 493, 129

Sijacki D., Vogelsberger M., Genel S., Springel V., Torrey P., Snyder G. F., Nelson D., Hernquist L., 2015, MNRAS, 452, 575

Silk J., 2013, ApJ, 772, 112

Silk J., Norman C., 2009, ApJ, 700, 262

Silk J., Rees M. J., 1998, A&A, 331, L1

Simpson C., Wilson A. S., Bower G., Heckman T. M., Krolik J. H., Miley G. K., 1997, ApJ, 474, 121

Singh R., et al., 2013, A&A, 558, A43

Smith R. J., Lucey J. R., Hudson M. J., Schlegel D. J., Davies R. L., 2000, MNRAS, 313, 469

Smith R. J., et al., 2004, AJ, 128, 1558

Sparks W. B., Baum S. A., Biretta J., Macchetto F. D., Martel A. R., 2000, ApJ, 542, 667

Speights J. C., Rooke P. C., 2016, ApJ, 826, 2

Spinrad H., Djorgovski S., Marr J., Aguilar L., 1985, PASP, 97, 932

Spoon H. W. W., Koornneef J., Moorwood A. F. M., Lutz D., Tielens A. G. G. M., 2000, A&A, 357, 898

Spoon H. W. W., et al., 2013, ApJ, 775, 127

Springel V., Di Matteo T., Hernquist L., 2005, MNRAS, 361, 776

Stalevski M., Asmus D., Tristram K. R. W., 2017, MNRAS, 472, 3854

Stevens I. R., Forbes D. A., Norris R. P., 1999, MNRAS, 306, 479

Storchi-Bergmann T., Bonatto C. J., 1991, MNRAS, 250, 138

Storey P. J., Zeippen C. J., 2000, MNRAS, 312, 813

Strickland D. K., 2007, MNRAS, 376, 523

Sturm E., et al., 2011, ApJ, 733, L16

Sutherland R. S., Bicknell G. V., Dopita M. A., 1993, ApJ, 414, 510

Swinbank A. M., et al., 2009, MNRAS, 400, 1121

Swinbank A. M., et al., 2015, MNRAS, 449, 1298

Tadhunter C., Morganti R., Rose M., Oonk J. B. R., Oosterloo T., 2014, Nature, 511, 440

Talia M., et al., 2012, A&A, 539, A61

Talia M., et al., 2017, MNRAS, 471, 4527

Teuben P. J., Sanders R. H., Atherton P. D., van Albada G. D., 1986, MNRAS, 221, 1

Thompson T. A., Fabian A. C., Quataert E., Murray N., 2015, MNRAS, 449, 147

Tingay S. J., et al., 1998, AJ, 115, 960

Tingay S. J., Preston R. A., Jauncey D. L., 2001, AJ, 122, 1697

Toba Y., Bae H.-J., Nagao T., Woo J.-H., Wang W.-H., Wagner A. Y., Sun A.-L., Chang Y.-Y., 2017, ApJ, 850, 140

Tombesi F., Cappi M., Reeves J. N., Palumbo G. G. C., Yaqoob T., Braito V., Dadina M., 2010, A&A, 521, A57

Tombesi F., Cappi M., Reeves J. N., Palumbo G. G. C., Braito V., Dadina M., 2011, ApJ, 742, 44

Tombesi F., Cappi M., Reeves J. N., Braito V., 2012, MNRAS, 422, L1

Tombesi F., Cappi M., Reeves J. N., Nemmen R. S., Braito V., Gaspari M., Reynolds C. S., 2013, MNRAS, 430, 1102

Tombesi F., Meléndez M., Veilleux S., Reeves J. N., González-Alfonso E., Reynolds C. S., 2015, Nature, 519, 436

Tremaine S., et al., 2002, ApJ, 574, 740

Trippe M. L., Crenshaw D. M., Deo R., Dietrich M., 2008, AJ, 135, 2048

Ueda Y., Akiyama M., Ohta K., Miyaji T., 2003, ApJ, 598, 886

Ueda Y., et al., 2015, ApJ, 815, 1

Urry C. M., Padovani P., 1995, PASP, 107, 803

Vazdekis A., Casuso E., Peletier R. F., Beckman J. E., 1996, ApJS, 106, 307

Vazdekis A., Sánchez-Blázquez P., Falcón-Barroso J., Cenarro A. J., Beasley M. A., Cardiel N., Gorgas J., Peletier R. F., 2010, MNRAS, 404, 1639

Veilleux S., 1991, ApJS, 75, 383

Veilleux S., Bland-Hawthorn J., 1997, ApJ, 479, L105

Veilleux S., Osterbrock D. E., 1987, ApJS, 63, 295

Veilleux S., Cecil G., Bland-Hawthorn J., Tully R. B., Filippenko A. V., Sargent W. L. W., 1994, ApJ, 433, 48

Veilleux S., Shopbell P. L., Miller S. T., 2001, AJ, 121, 198

Veilleux S., Shopbell P. L., Rupke D. S., Bland-Hawthorn J., Cecil G., 2003, AJ, 126, 2185

Veilleux S., Cecil G., Bland-Hawthorn J., 2005, ARA&A, 43, 769

Veilleux S., et al., 2013, ApJ, 776, 27

Veilleux S., Bolatto A., Tombesi F., Meléndez M., Sturm E., González-Alfonso E., Fischer J., Rupke D. S. N., 2017, ApJ, 843, 18

Véron-Cetty M.-P., Véron P., 2006, A&A, 455, 773

Videla L., Lira P., Andrews H., Alonso-Herrero A., Alexander D. M., Ward M., 2013, ApJS, 204, 23

Vika M., Driver S. P., Cameron E., Kelvin L., Robotham A., 2012, MNRAS, 419, 2264

Villar Martín M., Emonts B., Humphrey A., Cabrera Lavers A., Binette L., 2014, MNRAS, 440, 3202

Vogelsberger M., et al., 2014, MNRAS, 444, 1518

Wang J., Fabbiano G., Elvis M., Risaliti G., Mazzarella J. M., Howell J. H., Lord S., 2009, ApJ, 694, 718

Wang J., et al., 2014, ApJ, 781, 55

Ward M., Penston M. V., Blades J. C., Turtle A. J., 1980, MNRAS, 193, 563

Weedman D. W., 1970, ApJ, 159, 405

Wegner G., Colless M., Saglia R. P., McMahan R. K., Davies R. L., Burstein D., Baggley G., 1999, MNRAS, 305, 259

Weller J., Ostriker J. P., Bode P., Shaw L., 2005, MNRAS, 364, 823

Weymann R. J., Morris S. L., Foltz C. B., Hewett P. C., 1991, ApJ, 373, 23

Whewell M., Branduardi-Raymont G., Page M. J., 2016, A&A, 595, A85

Whittle M., 1992, ApJS, 79, 49

Williams R. J., Maiolino R., Krongold Y., Carniani S., Cresci G., Mannucci F., Marconi A., 2017, MNRAS, 467, 3399

Wilson A. S., Shopbell P. L., Simpson C., Storchi-Bergmann T., Barbosa F. K. B., Ward M. J., 2000, AJ, 120, 1325

Woo J.-H., Bae H.-J., Son D., Karouzos M., 2016, ApJ, 817, 108

Wyithe J. S. B., 2006, MNRAS, 365, 1082

Wylezalek D., Morganti R., 2018, Nature Astronomy, 2, 181

Yuan T.-T., Kewley L. J., Sanders D. B., 2010, ApJ, 709, 884

Zakamska N. L., Greene J. E., 2014, MNRAS, 442, 784

Zakamska N. L., et al., 2016, MNRAS, 459, 3144

Zánmar Sánchez R., Sellwood J. A., Weiner B. J., Williams T. B., 2008, ApJ, 674, 797

Zhang D., Thompson T. A., 2012, MNRAS, 424, 1170

Zhang K., Dong X.-B., Wang T.-G., Gaskell C. M., 2011, ApJ, 737, 71

Zschaechner L. K., et al., 2016, ApJ, 832, 142

Zubovas K., King A., 2012, ApJ, 745, L34

Zubovas K., King A. R., 2014, MNRAS, 439, 400

Zubovas K., Nayakshin S., Sazonov S., Sunyaev R., 2013a, MNRAS, 431, 793

Zubovas K., Nayakshin S., King A., Wilkinson M., 2013b, MNRAS, 433, 3079

de Vaucouleurs G., de Vaucouleurs A., Corwin Jr. H. G., Buta R. J., Paturel G., Fouqué P., 1991,
Third Reference Catalogue of Bright Galaxies. Volume I: Explanations and references. Volume
II: Data for galaxies between 0^h and 12^h. Volume III: Data for galaxies between 12^h and 24^h.

Appendix

In the following we give a brief description of each work in which the author has been involved and that is not included in this thesis.

The MAGNUM survey: positive feedback in the nuclear region of NGC 5643 suggested by MUSE

Cresci, G., Marconi, A., Zibetti, S., Risaliti, G., Carniani, S., Mannucci, F., Gallazzi, A., Maiolino, R., Balmaverde, B., Brusa, M., Capetti, A., Cicone, C., Feruglio, C., Bland-Hawthorn, J., Nagao, T., Oliva, E., Salvato, M., Sani, E., Tozzi, P., Urrutia, T., and **Venturi, G.**, 2015, A&A, 582, A63

We study the ionization and kinematics of the ionized gas in the nuclear region of the barred Seyfert 2 galaxy NGC 5643 using MUSE integral field observations in the framework of the Measuring Active Galactic Nuclei Under MUSE Microscope (MAGNUM) survey. The data were used to identify regions with different ionization conditions and to map the gas density and the dust extinction. We find evidence for a double-sided ionization cone, possibly collimated by a dusty structure surrounding the nucleus. At the center of the ionization cone, outflowing ionized gas is revealed as a blueshifted, asymmetric wing of the [O III] emission line, up to projected velocity $v_{10} \sim -450$ km s^{-1}. The outflow is also seen as a diffuse, low-luminosity radio and X-ray jet, with similar extension. The outflowing material points in the direction of two clumps characterized by prominent line emission with spectra typical of H II regions, located at the edge of the dust lane of the bar. We propose that the star formation in the clumps is due to positive feedback induced by gas compression by the nuclear outflow, providing the first candidate for outflow-induced star formation in a Seyfert-like, radio-quiet AGN. This suggests that positive feedback may be a relevant mechanism in shaping the black hole-host galaxy coevolution.

The MURALES survey. I. A dual AGN in the radio galaxy 3C459?

Balmaverde, B., Capetti, A., Marconi, A., **Venturi, G.**, Chiaberge, M., Baldi, R. D., Baum, S., Gilli, R., Grandi, P., Meyer, E., Miley, G., O'Dea, C., Sparks, W., Torresi, E., and Tremblay, G., 2018, A&A, 619, A83

We observed the FRII radio galaxy 3C459 (z=0.22) with the MUSE spectrograph at the Very Large Telescope (VLT) as part of the MURALES project (a MUse RAdio Loud Emission line Snapshot survey). We detected diffuse nuclear emission and a filamentary ionized gas structure forming a one-sided, triangular-shaped region extending out to ~80 kpc. The central emission line region is dominated by two compact knots of similar flux: the first (N1) cospatial with the

radio core and the (N2) second located 1.2″ (5.3 kpc) to the SE. The two regions differ dramatically from the point of view of velocity (with an offset of ~400 km/s), line widths, and line ratios. This suggests that we are observing a dual AGN system formed by a radio loud AGN and type 2 QSO companion, which is the result of the recent merger that also produced its disturbed host morphology. The alternative possibility that N2 is just a bright emission line knot resulting from, for example, a jet-cloud interaction, is disfavored because of 1) the presence of a high ionization bicone whose apex is located at N2; 2) the observed narrow line widths; 3) its line luminosity (~10^42 erg s^{-1}) typical of luminous QSOs; and 4) its location, which is offset from the jet path. The putative secondary AGN must be highly obscured, since we do not detect any emission in the Chandra and infrared Hubble Space Telescope images.

The MAGNUM survey: different gas properties in the outflowing and disk components in nearby active galaxies with MUSE

Mingozzi M., Cresci, G., **Venturi, G.**, Marconi, A., Mannucci, F., Perna, M., Belfiore, F., Carniani, S., Balmaverde, B., Brusa, M., Cicone, C., Feruglio, C., Gallazzi, A., Mainieri, V., Maiolino, R., Nagao, T., Nardini, E., Sani, E., Tozzi, P., and Zibetti, S., 2018, A&A in press, arXiv:1811.07935

We investigate the interstellar medium (ISM) properties of the disk and outflowing gas in the central regions of nine nearby Seyfert galaxies, all characterised by prominent single- or bi-conical outflows. These objects are part of the MAGNUM (Measuring Active Galactic Nuclei Under MUSE Microscope) survey, that aims at probing their physical conditions and ionisation mechanism, by exploiting the unprecedented sensitivity of the Multi Unit Spectroscopic Explorer (MUSE), combined with its spatial and spectral coverage. Specifically, we study the different properties of the gas in the disk and in the outflow with spatially and kinematically resolved maps, by dividing the strongest emission lines in velocity bins. We associate the core of the lines to the disk, consistent with the stellar velocity, and the redshifted and the blueshifted wings to the outflow, measuring the reddening, density, ionisation parameter and dominant ionisation source of the emitting gas for both components in each galaxy. We find that the outflowing gas is characterised by higher values of density and ionisation parameter than the disk, which presents a higher dust extinction. Moreover, we distinguish high- and low-ionisation regions across the spatially resolved narrow line region (NLR) traced by the outflowing gas. The high ionisation regions characterised by the lowest [N II]/Hα and [S II]/Hα line ratios, generally trace the innermost parts along the axis of the emitting cones, where the [S III]/[S II] line ratio is enhanced, while the low ionisation ones follow the cone edges and/or the regions perpendicular to the axis of the outflows, characterised also by a higher [O III] velocity dispersion. A possible scenario to explain these features relies on the presence of two distinct population of line emitting clouds: one is optically thin to the radiation and characterised by the highest excitation, while the other, optically thick, is impinged by a filtered – and thus harder – radiation

field, which generates strong low-excitation lines. The highest values of [N II]/Hα and [S II]/Hα line ratios may be due to shocks and/or hard, filtered radiation field from the AGN.

Cold Molecular Outflows in the Local Universe

Fluetsch, A., Maiolino, R., Carniani, S., Marconi, A., Cicone, C., Bourne, M. A., Costa, T., Fabian, A. C., Ishibashi, W., and **Venturi, G.**, 2018, subm. to MNRAS, arXiv:1805.05352

We study molecular outflows in a sample of 45 local galaxies, both star forming and AGN, primarily by using CO data from the ALMA archive and from the literature. For a subsample we also compare the molecular outflow with the ionized and neutral atomic phases. We infer an empirical analytical function relating the outflow rate simultaneously to the SFR, L_{AGN}, and galaxy stellar mass; this relation is much tighter than the relations with the individual quantities. The outflow kinetic power shows a larger scatter than in previous studies, spanning from 0.1 to 5 per cent of L_{AGN}, while the momentum rate ranges from 1 to 30 times L_{AGN}/c, indicating that these outflows can be both energy-driven, but with a broad range of coupling efficiencies with the ISM, and radiation pressure-driven. For about 10 per cent of the objects the outflow properties significantly exceed the maximum theoretical values; we interpret these as "fossil outflows" resulting from activity of a past strong AGN, which has now faded. We estimate that, in the stellar mass range probed here ($> 10^{10}$ M$_\odot$), less than 5 per cent of the outflowing gas escapes the galaxy. The molecular gas depletion time associated with the outflow can be as short as a few million years in powerful AGNs, however the total gas (H_2+H I) depletion times are much longer. Altogether, our findings suggest that even AGN-driven outflows might be relatively ineffective in clearing galaxies of their entire gas content, although they are likely capable of clearing and quenching the central region. Finally, we find no correlation between molecular outflow rate and radio power, suggesting that on average radio jets do not play a major role in driving massive molecular outflows in the luminosity range ($\log(L_{AGN})$ = 41-46 erg s^{-1}) probed here.

Acknowledgements

I wish to thank my supervisor Prof. Alessandro Marconi for having guided and assisted me along my academic path from my Master's Thesis to my PhD degree, providing me with many opportunities to progress as a researcher. I also want to thank the members of the extragalactic group in Arcetri who were interested in my work and helped me in carrying it out, in particular Matilde Mingozzi, Giovanni Cresci, Emanuele Nardini, Filippo Mannucci, Michele Perna and Guido Risaliti, as well as all the coauthors of my papers.

Many thanks also to all my friends in Arcetri with whom I shared the path starting from my Master's thesis, constantly supporting each other.

I would like to thank Roberto Maiolino and Stefano Carniani for having guided me and widened my scientific interests during my period at the Kavli Institute for Cosmology in Cambridge, UK, allowing me to join a stimulating and lively scientific environment. I also want to thank all the people I met there for the good time we had together.

I wish to thank Eleonora Sani for having given me the unique opportunity to work with her at the European Southern Observatory in Santiago, Chile, and up to the Paranal Observatory in the Atacama Desert. I would like to thank the people I met at ESO for the fun I had with them.

I would also like to thank Barbara Balmaverde and Alessandro Capetti for having brought me in the realm of radiogalaxies, allowing me to jump into this additional interesting field of astronomy.

I want to thank the referees of my thesis, Prof. Francesco Massaro and Prof. Stefano Bianchi, for their useful comments and suggestions that improved my thesis work.

I also wish to thank all my dear friends that I had the luck to meet throughout my life and who accompanied me with interest along my path up to this point.

I deeply thank all my family, in particular my parents, who have always supported me since I was a child and allowed me to reach this goal.

Finally, I want to thank Alessia for having constantly been at my side and sustained me tenderly and with patience during these three years.